SKULL BONE MARROW EMERGES AS A KEY NEUROIMMUNE PLAYER THROUGH DISCO-CLEARING AND MULTI-OMICS

Graduate School of Systemic Neurosciences

LMU Munich

Dissertation der Graduate School of Systemic Neurosciences

der Ludwig-Maximilians-Universität München

Zeynep Ilgın Kolabaş

August 15, 2023

Date of submission: August 15, 2023
Date of defense: January 30, 2024

First supervisor and reviewer: Prof. Dr. Ali Maximilian Ertürk
Institute for Tissue Engineering and Regenerative Medicine, Helmholtz Munich, Munich, Germany

Second reviewer: Prof. Dr. Ilona Grunwald Kadow
Institute of Physiology II at the Faculty of Medicine, University of Bonn, Germany

CONTENTS

SUMMARY ..... **V**

ABBREVIATIONS OF INTRODUCTION AND GENERAL DISCUSSION ..... **VII**

1. INTRODUCTION **9**

1.1 Inflammation: a physiological and defense response 12

1.2. Neuroimmune axis players in health and pathology 15

1.2.1 CNS pathologies 18

1.3 Skull marrow and its contribution to the neuroimmune axis 19

1.4 Imaging modalities and blood biomarkers for understanding CNS pathologies 21

1.5 Optical tissue clearing to investigate intact specimens 23

1.5.1 History of optical tissue clearing technology 24

1.5.2 Applications of tissue clearing 26

1.6 Omics technologies to understand cellular heterogeneity 27

1.6.1 RNA Technologies in cellular heterogeneity 28

1.6.2 Analysing RNA technologies 29

1.6.2 Protein-based technologies in cellular heterogeneity 30

1.6.2 Analysing protein-based technologies 31

2. AIM **32**

3. STUDIES **33**

3.1 Study I: Distinct molecular profiles of skull bone marrow in health and neurological disorders 33

3.2 Study II: Whole-mouse clearing and imaging at the cellular level with vDISCO 84

4. GENERAL DISCUSSION **147**

4.1. Main findings 147

4.2. Key implications 148

4.2.1 Bone marrow cell composition in the skull differs from other bones in mice and humans 148

4.2.1.1 Unique aspects of human skull proteome 149

4.2.1.2 Human skull is highly connected with the meningeal layers through SMCs 150

4.2.1.3 Structural detail of human SMCs 151

4.2.1.4 Optimized pipeline for bone processing and clearing 153

4.2.1.5 Skull TSPO-PET imaging: A proof-of-concept for mirroring brain inflammation 154
4.2.2 vDISCO whole-body immunolabeling, clearing, and imaging pipeline 154
4.3. Limitations 155
4.3.1 Technical limitations 155
4.3.2 Biological limitations 156
4.4. Future directions 157
4.4.1. Leveraging Skull in monitoring brain pathologies in Humans 158
4.4.2. Using vDISCO clearing technology to assess whole-body pathology response in mice 159
4.5. Conclusion 159

5. REFERENCES OF INTRODUCTION AND GENERAL DISCUSSION 161

ACKNOWLEDGEMENTS VIII

CURRICULUM VITAE X

LIST OF PUBLICATIONS XI

AFFIDAVIT XIII

DECLARATION OF AUTHOR CONTRIBUTIONS XIV

SUMMARY

The bone marrow plays a central role in the interconnected web of biological systems. It contributes to multiple systems, such as hematopoietic, immune, skeletal, circulatory, lymphatic, and nervous systems. Inflammation, a typical response to injury, infection, or tissue damage, often originates from the bone marrow and affects multiple systems. Remarkably, the immune and nervous systems interact complexly, forming the neuroimmune systems. The brain is considered immune-privileged by being protected by physical and immunological barriers such as the blood-brain barrier, blood-cerebrospinal fluid barrier, and meninges, limiting the entry of immune cells and antigens into the brain parenchyma. However, recent research showed that the various barriers surrounding the brain have active roles in immune regulation, thereby questioning the concept of immune privilege. Traditionally, the immune and nervous systems have been studied separately by focusing on primary organs like the bone marrow, thymus, or brain. However, examining organisms as a whole is essential to grasp the interconnectedness. More recently, there has been growing interest in exploring the skull bone marrow and its microscopic channels connecting it to the meningeal layers, primarily facilitated by various microscopy techniques.

This thesis integrates advanced imaging technology with molecular data obtained through omics technologies to provide an in-depth understanding of the bone marrow cellular and molecular heterogeneity in various bones in healthy and brain-associated disease conditions, emphasizing skull bone[1]. Our results demonstrate that skull bone marrow's transcriptome and proteome differ markedly from other bone marrow in mice and humans, mainly exhibiting a unique neutrophil profile. Furthermore, we uncover previously unknown details about the human SMCs: we demonstrate that the SMCs are uniformly distributed throughout the frontal, parietal, and temporal regions of the human skull with size variations. Remarkably, SMCs often traverse the dura and extend into the subdural space, potentially containing lipids and featuring a fibroblastic lining integral to their structure. Finally, our evidence indicates that the skull elicits a spatially and temporally resolved immune reaction, mirroring the brain's inflammatory state in various neurological diseases. This discovery positions the skull as a promising candidate for developing new tools to diagnose, monitor, and potentially treat brain diseases.

The second study is dedicated to broadening the scope of systems biology inquiries using the vDISCO protocol, a pivotal tool for investigating the skull in health and disease[2]. We share the setup, execution, and analysis pipeline of tissue clearing and imaging experiments, presenting

light sheet and confocal imaging approaches for transgenic mice bodies, whole organs, and virus-traced samples.

This work collectively conveys the remarkable power of systems biology to advance biomedical sciences.

ABBREVIATIONS OF INTRODUCTION AND GENERAL DISCUSSION

3D	3-dimensional
3DISCO	3D imaging of solvent-cleared organs
4RT	4-repeat tauopathy
AD	Alzheimer's disease
Aβ	Amyloid-beta
ALS	Amyotrophic lateral sclerosis
BBB	Blood-brain barrier
BCSFB	Blood cerebrospinal fluid barrier
BABB	1:2 Benzyl alcohol-benzyl benzoate
CNS	Central nervous system
ChP	Choroid plexus
CLARITY	Clear lipid exchanged acrylamide-hybridized rigid imaging/immunostaining/in situ hybridization-compatible tissue hydrogel
CSF	Cerebrospinal fluid
CT	Computed tomography
CXCL12-CXCR4	CXCL12 ligand and CXCR4 receptor
CUBIC	clear, unobstructed brain/body imaging cocktails and computational analysis
cDNA	Copy DNA
DAMP	Damage-associated molecular pattern
DISCO-MS	DISCO clearing protocol coupled with mass spectrometry
ECi	Ethyl cinnamate clearing protocol
EDTA	Ethylenediaminetetraacetic acid
GFAP	Glial fibrillary acidic protein
HCl	Hydrochloric acid
ICH	Intracerebral hemorrhage
iDISCO	Immunolabeling-enabled imaging of solvent-cleared organs
ISF	Interstitial fluid
KikGR	Kikume Green-Red photoconvertible fluorescent protein-expressing mouse line
LSFM	Light sheet fluorescent microscopy
LysM	Lysozyme M
mRNA	Messenger RNA
MS	Multiple sclerosis
MRI	Magnetic resonance imaging

NfL	Neurofilament Light Chain
PACT	Passive CLARITY technique
PARS	Perfusion-assisted agent release in situ
PCR	Polymerase chain reaction
PDGRRB	Platelet-derived growth factor receptor beta
PEGASOS	Polyethylene glycol (PEG)-associated solvent system
PAMPs	Pathogen-associated molecular patterns
PET	Positron emission tomography
PPMS	Primary progressive multiple sclerosis
PRR	Pattern recognition receptors
RI	Refractive index
RNA	Ribonucleic acid
RRMS	Relapsing-remitting multiple sclerosis
SDF-1	Stromal cell-derived factor 1
Scale	Sorbitol-based optical clearing method
scRNAseq	Single-cell RNA sequencing
SeeDB	See deep brain-clearing protocol
SHANEL	Small-micelle-mediated human organ efficient clearing and labeling
SMC	Skull-meninges connection
S100B	S100 calcium-binding protein B
THF	Tetrahydrofuran
TSPO	Translocator protein
TSPO-PET	Translocator protein – positron emission tomography
uDISCO	Ultimate imaging of solvent-cleared organs
vDISCO	Nanobody(VHH)-boosted 3D imaging of solvent-cleared organs

1. INTRODUCTION

Science aims to acquire knowledge and understanding of the natural world through systematic observation, experimentation, and analysis. Systems biology is a branch of science that aims to improve the quality of life, initially by understanding and later by manipulating the interconnected systems in living organisms. These systems include but are not limited to the circulatory, respiratory, digestive, musculoskeletal, endocrine, nervous, and immune systems, which work together in harmony, where each system relies on one another to maintain homeostasis. Ultimately, the scientific pursuit of improving quality of life necessitates a comprehensive understanding of intact systems, with results measured objectively and unbiasedly.

The bone marrow occupies a central position in the intricate web of biological interconnections, as it is integral to multiple systems, including hematopoietic, immune, skeletal, circulatory, lymphatic, and even partially the nervous system (Illustration 1). Bone marrow corresponds to the soft, spongy tissue found inside the bones of vertebrates in two types: red marrow and yellow marrow. Red marrow is found in the spongy part of larger bones such as the skull, vertebrae, pelvis, and ends of long bones, whereas yellow marrow is found in the central cavity of long bones in the majority and consists mainly of fat cells. Overall, bone marrow's primary function is to produce cells. More specifically, the bone marrow produces bone cells of the skeletal system and immune cells comprising the immune system. It also contributes to the circulatory system by continuously providing new blood cells, where red blood cells carry oxygen to the tissues, and white blood cells maintain homeostasis or defend against disease. The lymphatic system also relies on the production of lymphocytes, the B and T cells from the bone marrow, and the nervous system is heavily affected by marrow-produced immune cells in both health and disease [3–5].

Bone marrow actively participates in the immune response against injury, infection, or tissue damage, affecting multiple systems. This immune response, commonly called inflammation, aims to eliminate the source of damage, initiate the healing process, and restore normal tissue function. It is important to note that while inflammation is a beneficial mechanism, it can sometimes exacerbate the condition.

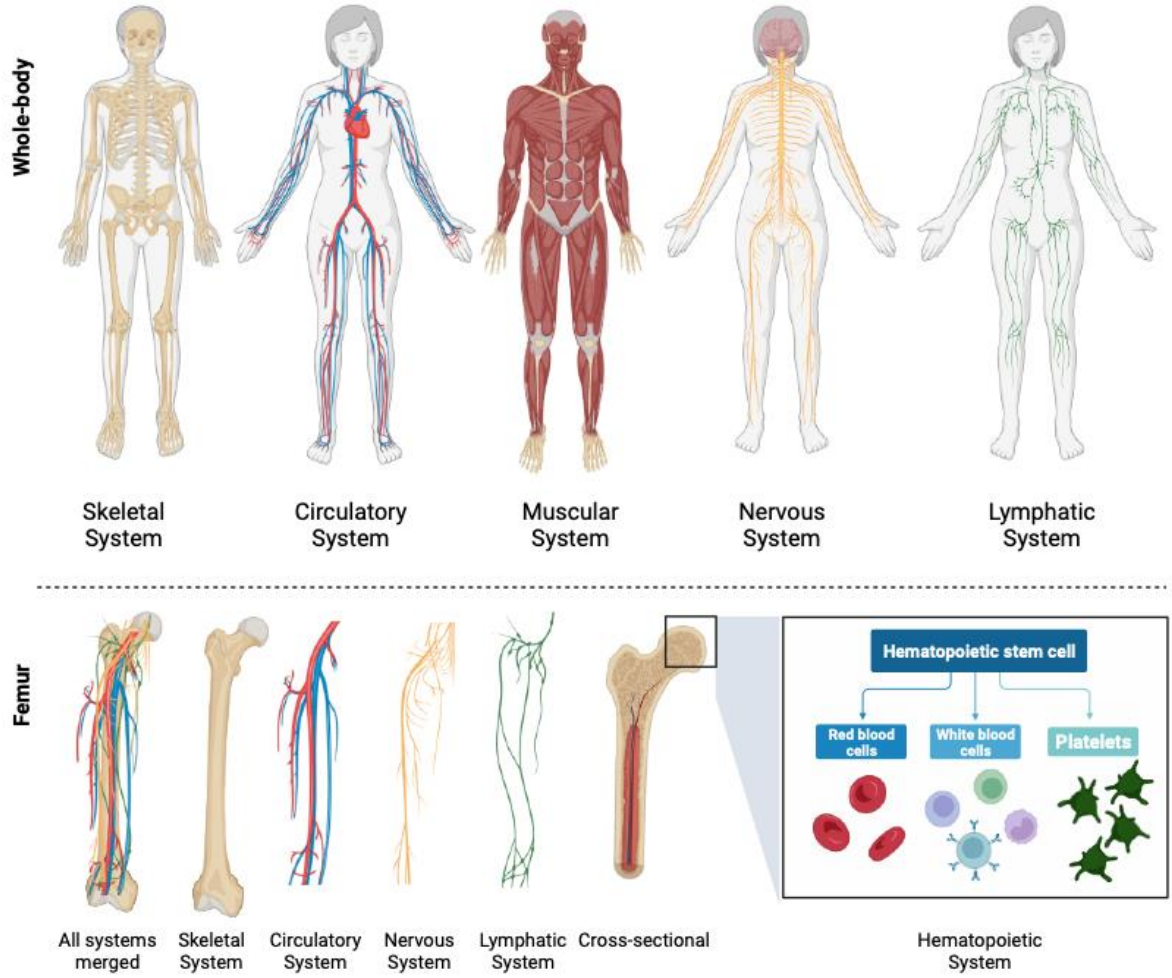

Illustration 1: Interconnectedness of Human Systems
The human body consists of highly complex and interconnected systems. Among these systems, the bone marrow holds a central position within the intricate web of biological connections. It serves as a hub for various crucial systems, including the skeletal, circulatory, nervous, lymphatic, and hematopoietic systems.

The nervous system is an important system affected by the immune system in health and disease. The interaction between these two systems, referred to as the neuroimmune system, has been proven to be highly complex and is a rapidly growing field. This interest stems from the brain's so-called immune privilege: the physical and immunological barriers that protect it from the body's immune response by limiting the entry of immune cells and outside antigens to the brain parenchyma[6]. Although the immune privilege has been recently challenged from many different angles, it is undeniable that the barriers the nervous system lays in front of the immune system require it to function in a distinct way than it does in the rest of the body.

One well-known barrier in the neuroimmune axis equation is the blood-brain barrier (BBB), formed by tight junctions between endothelial cells that line the vessel wall[7]. Blood-cerebro spinal fluid- barrier (BCSFB) is another barrier to maintaining the CNS. Moreover, the choroid plexus (ChP) is a highly vascularized structure that produces cerebrospinal fluid (CSF) via the filtering of blood plasma, followed by secreting it into the ventricles to be circulated to the brain

parenchyma. Like the endothelial cells of the BBB, the epithelial cells in the ChP have tight junctions that allow strict substance filtering, leaving most immune cells and large molecules in the blood circulation[8]. Furthermore, the meninges have initially been understood as an additional layer for physical brain protection. At the same time, recent research has shown that this three-layered membrane's functions extend beyond its role as a physical barrier to encompass the intricate involvement in maintaining the health and function of the central nervous system (CNS), both in normal physiological and pathological states[9]. Lastly, the recent discovery of skull-meninges connections (SMCs) using tissue clearing and other modalities has put the immunological contribution of the skull bone marrow in the equation of the neuroimmune axis, which was previously thought to be only a physical barrier[10,11], which will be extensively explained in the upcoming chapters of this thesis (Section 1,2).

The immune system and the nervous system have been investigated as separate entities by dissecting the primary organs of each system, such as bone marrow, thymus, or the brain, for respective fields. However, the above examples solidify the need to examine an organism as a whole, as evidence shows that these systems are not isolated and heavily influence each other. The lack of holistic investigation has been due to constraints in examination modalities and a traditional siloed perspective on interconnected systems. However, technological advancements and the recognition of systems biology offer opportunities to overcome these limitations and deepen our understanding of complex interactions between the nervous and immune systems.

One attempt to visualize the entire body is imaging techniques, such as CT, PET, or MRI in humans and CT, PET, MRI, and bioluminescence imaging in rodents. Although these modalities can provide preliminary structural understanding or metabolism information on the whole-body level, they have been limited to gross-anatomical results, often lacking the necessary resolution[12]. On the other hand, the possibility of investigating high-resolution specimens via histological tissue sectioning, staining, and imaging has limited the field of view that could be studied in a high-throughput manner. These imaging modalities often rely on the penetration of light through the tissue of interest. However, due to the complicated nature of biological specimens, the light gets refracted and scattered, forcing the samples to be in the range of 1-100 μms.

Challenges arise from various tissue types in biological tissue, like lipids, nucleic acids, proteins, and water, each with distinct refractive indices (RIs), were tackled by tissue-clearing technologies by reducing refraction effects and harmonizing the RI, thereby enabling deeper

penetration of light into the tissue. Samples becoming transparent expands the field of view that microscopes could image. LSFM, developed in 2007 by Dodt et al.[13], in addition to the advancement of tissue clearing, has been instrumental in allowing whole-mouse body and whole-human organ imaging, addressing the challenges in the field. As a result, many discoveries have been made in a short period due to their high versatility ranging from but not limited to studying the development of organs, monitoring the progression of cancer, detecting single-cell metastasis in the whole mouse body, interaction of different cell types within tissues, generating atlases of different systems and allowing a more intricate examination of the structural details of the brain, its circuitry and its immune system: discovery of SMCs[2,10,14–19]. A short history and applications of tissue clearing can be found in the following chapters (Section 1,5).

Imaging technology is undeniably powerful; however, its potential is maximized with molecular data. Bridging imaging with molecular information enables the identification of functional correlations within specific biological systems, providing a powerful approach to examining cellular heterogeneity. Omics technologies play a crucial role in integrating molecular data by encompassing various levels of biological function, including genomics, epigenomics, transcriptomics, proteomics, and metabolomics. These omics approach provide comprehensive insights into the molecular underpinnings of biological processes, facilitating a more comprehensive understanding of complex biological systems[20].

This thesis describes a comprehensive investigation of the skull through omics and optical tissue clearing, how it is distinct compared to other bone marrow on the transcriptomic and proteomic levels, and how its strategic location contributes to the immune regulation of the nervous system. Moreover, we present the vDISCO protocol, an in-depth extension of one of the main tissue-clearing techniques used in skull exploration, which offers a thorough explanation of the protocol and showcases its broad range of potential applications.

1.1 Inflammation: a physiological and defense response

Inflammation is a typical response observed in various pathological conditions, regardless of whether they are caused by viral infections or sterile insults[21–23]. The underlying source of inflammation can be attributed to immune cells, primarily produced in the bone marrow. Immune cells, including macrophages, neutrophils, and lymphocytes, play crucial roles in orchestrating the inflammatory response. Upon activation, these immune cells release various pro-inflammatory mediators, such as cytokines, chemokines, and reactive oxygen species,

contributing to the characteristic signs of inflammation[24]. The bone marrow serves as a key site for the production and maturation of these immune cells, ensuring a constant supply to combat invading pathogens or respond to tissue damage[24].

In addition to the immune cells produced in the bone marrow, inflammation involves the coordinated efforts of innate and adaptive immune responses. The innate immune system acts as the first line of defense, providing immediate, non-specific defense mechanisms against pathogens or tissue injury. Macrophages and neutrophils, derived from the bone marrow, are important components of the innate immune system and play crucial roles in initiating and amplifying the inflammatory response. They recognize PAMPs and DAMPs through PRRs, triggering the release of pro-inflammatory mediators[25–27] (Illustration 2).

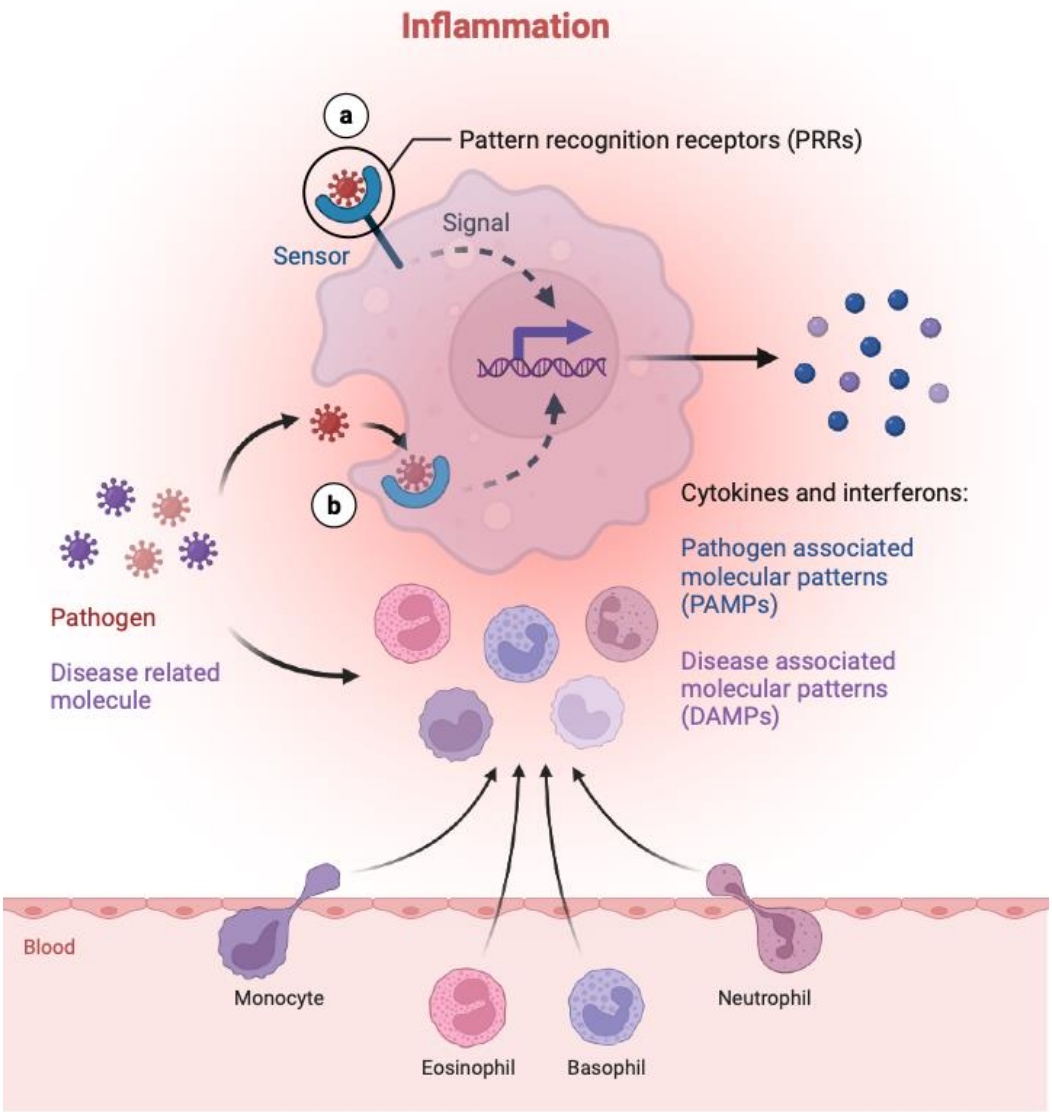

Illustration 2: Components of Inflammation
Inflammation plays a vital role in the immune response. The recognition of threats is facilitated by Pattern Recognition Receptors (PRRs). Upon recognition, cells within the inflamed tissue release either Pathogen-Associated Molecular Patterns (PAMPs) or Damage-Associated Molecular Patterns (DAMPs) based on the nature of the threat. These molecules serve to attract and recruit additional immune cells to the site of inflammation.

Furthermore, the adaptive immune system, which includes lymphocytes such as T cells and B cells, complements the innate response by mounting a specific and tailored immune response. T cells, produced in the bone marrow and matured in the thymus, recognize specific antigens presented by antigen-presenting cells, contributing to the regulation and coordination of the inflammatory process. B cells, also derived from the bone marrow, produce antibodies that bind to pathogens, marking them for destruction and promoting their clearance[28].

The crosstalk between innate and adaptive immunity is essential for effective inflammation resolution and the restoration of tissue homeostasis. Activation of the adaptive immune response leads to the formation of memory cells, enabling a faster and more specific immune response upon subsequent encounters with the same pathogen[29]. The bone marrow's continuous production of immune cells ensures a well-coordinated and efficient inflammatory response involving innate and adaptive immunity to protect against pathogens and promote tissue healing.

On the other hand, immune cells are also produced outside the bone marrow (Illustration 3). These cells are called resident immune cells of most organs, which play crucial roles in regulating the local immune milieu. For example, macrophages may be referred to with a variety of names depending on the location of where they are found[30]. Bones, lungs, liver, and skin all have specific resident macrophages called osteoclasts, alveolar macrophages, Kupffer cells, and Langerhans cells, respectively[31]. The resident immune cell of the brain, microglia, is also an immune cell that does not originate from the bone marrow[32]. Microglia have been the primary focus of understanding brain immunity as it was the sole known resident immune cell in the brain housed in homeostatic condition. Recent research has expanded microglial function in the brain and enlarged the constituents of the brain’s immune regulation.

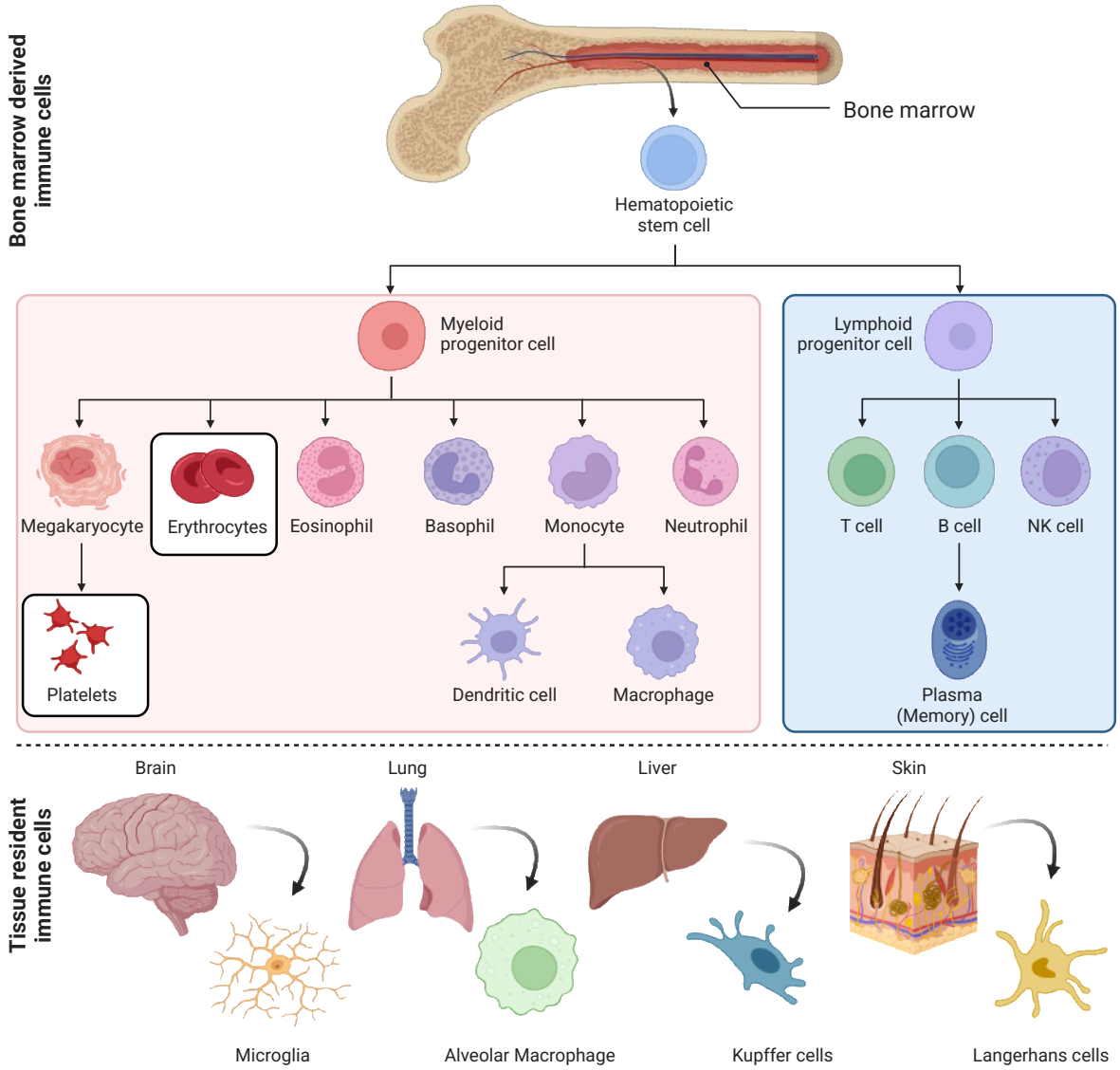

Illustration 3: Overview of Immune Cell Types
In the bone marrow, immune cells undergo differentiation from hematopoietic stem cells. Initially, these cells differentiate into either myeloid or lymphoid progenitors. Myeloid cells, excluding platelets and erythrocytes, contribute to the innate immune response (depicted in pink), while lymphoid immune cells (shown in blue) generate components of the adaptive immune system. Additionally, tissue resident immune cells play a crucial role in injury response and maintaining homeostasis, providing an additional layer of defense.

1.2. Neuroimmune axis players in health and pathology

The brain is considered an immune-privileged organ, meaning the conventional immune system does not function within the brain. The brain's label as an immune-privileged organ was due to several aspects of brain architecture, such as the presence of BBB and the BCSFB and the absence of a lymphatic system to drain the antigens and the brain's unique resident immune cells, previously known as microglia[33]. Although recent discoveries have debilitated the immune privilege[34], the barriers mentioned above provide an extra layer of seclusion within the brain and its antigens. Moreover, the recent expansion of the field with several other border

tissues participating in the brain immune response has provided a different aspect of immune privilege, in the sense that the communication between the immune and the nervous system was much more intricate than previously imagined[35].

Specialized myeloid cells originating in the yolk sac migrate into the CNS during embryonic development and reside within the parenchyma. These cells are called microglia in the parenchyma and CNS-associated macrophages or border-associated macrophages due to their presence near the brain borders[36,37]. Microglia have several functions in brain homeostasis, including controlling neurogenesis and myelin formation in development[38]. On the other hand, aged microglia have been linked with impaired metabolism, reducing their motility and increasing the production of proinflammatory cytokines, increasing neuroinflammation and leading to BBB disruption[39].

The BBB is a unit formed by many different cell types layering to restrict the passage of substances and cells into the brain tissue while allowing required molecules to pass. The blood vessels within the brain are covered with a layer of endothelial cells that are joined together with tight junctions, pericytes cover the blood vessel as a second layer to regulate the functioning of the BBB, and lastly, the astrocyte end feet form the outermost layer of the BBB further accommodating the functioning of the BBB. This subunit thus prohibits the immune system from surveilling the brain. Thus, its function is critical to maintaining the brain in homeostasis.

The second barrier that protects the brain from outside cells is the BCSFB. The BCSFB is present in the places where cerebrospinal fluid circulates, which is a current field of discovery. Cerebrospinal fluid is generated in the choroid plexus, composed of specialized choroid plexus epithelial cells. ChP is found in the ventricles of the brain. Like the endothelial cells of the BBB, these epithelial cells are also connected with tight junctions, filtering out harmful substances and maintaining the balance within the CNS[35].

CSF is a colorless fluid that circulates in the sub-arachnoid space of the meninges participating in a number of functions such as protection: by acting as a cushion between the skull and the brain, support: via providing buoyancy to the brain, reducing the weight of the brain and allowing it to float within the skull bones, immune function: by hosting several immune cells within itself and lastly for waste removal: where CSF drains brain’s waste products such as neurotransmitters and other metabolites into either the lymphatic vessels in the dural layer of the meninges or the arachnoid granulations of the meninges which eventually leads to the

cervical lymph nodes[40,41]. Cervical lymph nodes are located in the neck region, where the CSF is filtered to the lymphatic system. The antigens collected during the CSF-interstitial fluid (ISF) exchange drain in the dural sinuses in the meninges, densely populated regions with adaptive immune cells. It has been traditionally thought that cervical lymph nodes provide the first adaptive immune response when foreign particles are filtered from the CSF, allowing for encounters with brain-specific antigens. However, this idea has been reshaped with recent discoveries. After the filtration into the lymphatic system, CSF is returned to the bloodstream via the thoracic duct, the largest lymphatic vessel in the body. CSF is then emptied into the subclavian vein, which returns the blood to the heart (Illustration 4). Thus, CSF access gives an essential advantage in brain immune response surveillance. As previously mentioned, recent literature has significantly expanded our understanding of the regions through which CSF flows. Initially, it was accepted that CSF was flowing within the subarachnoid space of the meninges and draining into the cervical lymph nodes. However, with the recent improvements in imaging technologies, first, the meningeal lymphatics were re-discovered, and second, CSF was reported in the skull bone marrow via the recently discovered SMCs. However, it is still unknown how the CSF flows through the dura and how it happens into the skull marrow niches[42,43].

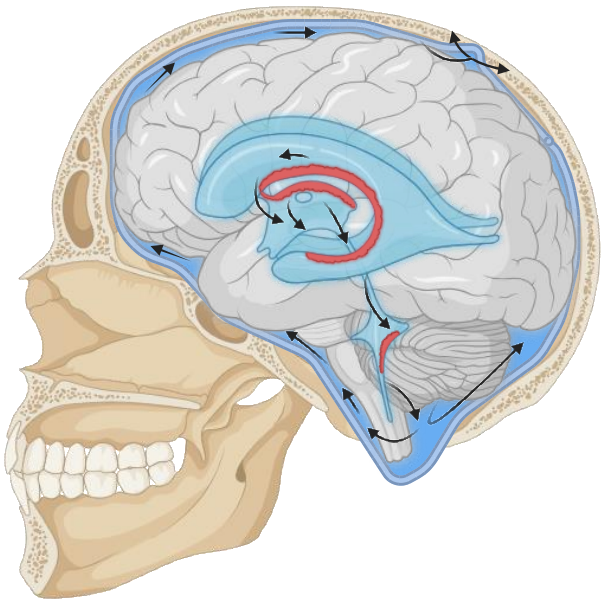

Illustration 4: Conventional CSF flow diagram
CSF is produced at the choroid plexus (shown here in red) and is released to the ventricles of the brain (shown here in light blue). CSF follows within the sub-arachnoid space (dark blue membrane encapsulating the brain), directionality is depicted with the arrowheads.

CSF reaches the brain tissue via the perivascular spaces surrounding the small blood vessels within the parenchyma. These perivascular regions are Virchow-Robin spaces and can be considered within the BBB subunit[43]. The perivascular space is the region where the previously mentioned CNS-associated macrophages reside in addition to peripheral immune cells. Thus, this area is the brain's ‘first line of defense.’ Moreover, through the astrocytic end feet expressing aquaporin-4, the glymphatic system is described where additional drainage of brain metabolite happens in addition to the recently termed lymphatic system in the meninges[44]. Here

too, perivascular space plays a fundamental role, as the glymphatic system functions via the influx of the CSF to the brain parenchyma through these spaces, is exchanged with ISF and collected by the perivenular space with the efflux of ISF/CSF mixture and is drained to the cervical lymph nodes by the meningeal lymphatic system[45].

The meninges are a protective covering between the skull and the brain. However, recent studies have expanded its role in the immune regulation of the brain. Structurally, the meninges are composed of several membranes: the dural layer is the outmost meningeal layer, composed of mainly fibroblasts and connective tissue. It houses the venous sinuses, numerous immune cells, and the lymphatic vessels that drain the brain's waste into the cervical lymph nodes[33]. The arachnoid barrier lays underneath the dura. Beneath the dural layer is the subarachnoid space composed of web-like structures that allow the CSF flow. The CSF is supplied by connecting the brain's fourth ventricle through the median aperture and paired lateral apertures. Recent studies have reported an additional layer within the subarachnoid membrane, limiting the solute passage into the parenchyma[46]. However, due to contradictory reports, it is too early to consider the reported layer as a separate fourth layer of the meninges. Lastly, the meninges' pia mater is highly vascularized above the brain parenchyma. Each meningeal layer has been attributed a particular immunological function from cognitive, memory, or inflammatory functions in healthy and injured states[47]. Currently, the meninges are the fundamental immunological niche of the brain.

1.2.1 CNS pathologies

CNS pathologies span a wide range of conditions, and the prevalence depends on many factors, such as sex, age, and geographic region. However, CNS pathologies, regardless of pathology type, are predicted to affect around 1 billion people worldwide and are listed as the leading cause of disability and ranking second for causes of death worldwide[48,49]. CNS pathologies can be broadly categorized into several groups: neurodevelopmental, neurogenerative, traumatic brain injury, stroke, inflammatory and infectious diseases, brain tumors, some genetic disorders, movement disorders, and psychiatric disorders[50]. In all of these pathologies, immune regulation is an important parameter that alters the disease progression in addition to neuronal dysregulation. For example, although neurodevelopmental disorders have not been characterized based on immune regulation, there has been increasing literature on the critical role of the immune system[51]. Microglia have been shown to control neurogenesis and affect neuronal survival via phagocytosing cellular debris[52]. Neurodegenerative diseases are often categorized based on the progressive loss of function and death of neurons where the

aggregation of proteins due to vascular limitations or in the waste clearance pipelines of the brain are not optimally functioning[53]. These events may also trigger neuroinflammatory processes where cells infiltrating the cells may be damaging or healing[54]. Although participating immune cell types may vary in type or activation pathway: such as myeloid or lymphocyte-based or PAMP, DAMP or complement-activated mechanisms, traumatic brain injury, stroke, infectious diseases, and brain tumors are highly involved with the brain's immune response as these injuries and diseases often lead to breakage in one or more barriers that protect the brain from outside antigens[55]. Lastly, neuropsychiatric diseases have also been reported to generate neuroinflammatory processes[56]. Other than pathologies, simply aging can increase inflammation in the brain due to cellular aging or decrease the efficiency of waste clearance pipelines of the brain[57].

Therefore, it is critical to monitor the brain, especially for the neuroinflammatory reaction pattern during pathology, to better diagnose, monitor and potentially treat any pathologies.

1.3 Skull marrow and its contribution to the neuroimmune axis

Although the meninges is considered the brain's fundamental immunological niche, its strategic closeness to bone marrow, a reservoir whose primary function is to supply immune cells, has been neglected until recent years. The discovery of microscopic channels connecting the dura mater of the meninges to the skull bone marrow in mice provided a new perspective on the meninges' immune supply[58,59]. Subsequent studies further explored the connection between these two compartments, although mainly using animal models.

Two publications identified these channels using different imaging modalities, such as ex-vivo confocal microscopy, micro CT, tissue clearing, and 3-dimensional (3D) imaging. One study showed preferential immune cell trafficking from the skull bone marrow to the brain parenchyma compared with distal bone marrow sites[11]. They also showed the release of more neutrophils and monocytes from the skull upon a stroke compared to the tibia, although they did not report any significant bone marrow permeability differences of the skull bone marrow when comparing between 6h after a 30 min occlusion, mimicking stroke vs. its sham control nor in the tibia. Nevertheless, SDF-1, a known factor in retaining leukocytes, which was previously shown to increase in the brain upon stroke[60], was significantly lower in the skull. In contrast, no difference was reported in the tibia, which suggested molecular differences between the recruitment cues in the two sites. Following the cues on differential recruitment of the immune cells from different bone marrow, the authors reported direct vascular channels

connecting the skull's bone marrow which trafficked more neutrophils upon a stroke compared to its sham control using ex vivo confocal microscopy. Moreover, they provided information on channel size and their relative frequencies, suggesting that 15-20µm size is the most prevalent in mice. Lastly, they reported the presence of these channels in humans using micro CT from three patients and quantified the 60 detected channel's diameter from the inner and outer skull to be around 100µm[11].

The second study that came about at the same time investigated channels by injecting a CSF tracer into the cisterna magna of mice and observing that the tracer did not only travel into the meningeal lymphatic vessels but that it also traveled into the skull bone marrow via the channel which they termed as SMCs[10]. CSF flow through the channels was later confirmed and expanded by two other publications[58,59]. Additionally, Cai et al. confirmed two findings from the initial study: first, the size of the channels reported in this study was also around 20µm, and second, they also quantified more immune cells in these channels upon a stroke compared to its sham control[10].

Two other articles were published back-to-back focusing on two different cell types in the skull-meninges axis: myeloid and B cells. The authors used methods spanning from calvaria bone-flap transplantation and parabiosis to scRNAseq. Their experiments concluded that the calvaria supplies myelomonocytic and B cells to the dura without the conventional blood route and that injury causes differential molecular signatures between the skull bone marrow and the blood-derived leukocytes in an animal model of MS[58,59].

Moreover, the authors also demonstrated that the dura harbors developing B cells[59]. Previous literature suggests that B cells mature in the bone marrow before they are released into circulation. During the maturation phase, they also go through central tolerance, in which B cells that recognize self-antigens are eliminated to prevent autoimmune diseases[61]. The presence of developing B cells in the dura was also confirmed in other articles published, in which it was also shown that the central tolerance could take place in the dura, further underlining the dura's unique role and contribution to the brain's immune system[62]. T cells, on the other hand, were also shown to be involved in the brain-bone marrow axis in multiple sclerosis settings[4]. The authors showed that using the CXCL12-CXCR4 axis, autoreactive T cells migrate into the bone marrow, which in turn causes myelopoiesis and infiltration of the CNS by myeloid cells. The infiltration then exacerbated the injury. Several different bone marrow were used in this study: the skull, vertebra, and femur, although contributions from different bone marrow (CNS-surrounding vs. femur, for example) were not examined.

Similarly, bone marrow influence is well-established in ICH patients and ICH experimental models where the authors showed a skew to myelopoiesis upon injury, where they investigated the skull and the femur[5]. They showed beta3-adrenergic innervation involvement promoting myeloid cell expansion, which suppressed neuroinflammation. It was also inconclusive whether the skull effect differed from the femur effect, which requires further investigation.

Nevertheless, with the recapitulation of CSF-skull interaction by two more reports, it is clear that skull bone marrow is in a strategic position where no other bone marrow reservoir has access to [63,64]. In bacterial meningitis and spinal cord injury, authors report that skull bone marrow can access brain antigens via the CSF before the tibia. Mazzitelli et al. also report limited transcriptomic differences between the tibia and the skull in healthy conditions.

Hence, these reports and previous reports suggest that skull bone marrow is a site that requires further investigation on the molecular and structural level and in its potential for diagnosing and monitoring brain diseases. In order to do so, it is crucial to understand and utilize current technologies to reflect brain pathologies.

1.4 Imaging modalities and blood biomarkers for understanding CNS pathologies

Brain pathologies can be lethal, so brain health must be monitored best to our abilities. Diagnosing a brain pathology may involve clinical evaluation, medical history, diagnostic test, biopsy, blood biomarker detection, and imaging after potentially aberrant behavior. Although, behavior is often affected when a pathology's onset has been set. Ideally, non-invasive brain imaging to observe neuroinflammation, often a byproduct of brain pathology, may provide early diagnosis options[55]. On the other hand, further experiments using animal models *in vivo* settings and post-mortem settings help understand pathologies in a controlled environment, unlike experiments with humans.

Currently, blood biomarkers provide an alternative to non-invasive brain health investigation. Some markers have been proposed to reflect specific disease phenotypes when found in the blood, which is relatively more accessible than the CSF via a lumbar puncture or the brain itself. Neurofilament Light Chain (NfL), tau protein, amyloid-beta (Aβ) peptides, glial fibrillary acidic protein (GFAP), and S100B are under investigation about whether an in which circumstances they could help diagnose and monitor CNS pathologies[65–67]. To exemplify, elevated levels of NfL in the blood have been associated with neurodegenerative diseases such as AD, Parkinson's disease, MS, and amyotrophic lateral sclerosis (ALS)[67]. NfL is a protein

component of neurons, and its release into the bloodstream reflects neuronal damage or degeneration. Tau protein abnormalities, including increased levels or altered forms, are seen in conditions such as Alzheimer's disease and certain types of dementia[65]. Blood-based assays measuring specific tau isoforms or total tau levels are being explored as potential biomarkers for these disorders. Aβ Peptides are implicated in the development of Alzheimer's disease. Blood-based assays measuring different forms of Aβ, such as Aβ42 and Aβ40, are being studied as potential markers for Alzheimer's disease risk and progression[68]. GFAP is a protein primarily found in astrocytes, a type of brain cell. Elevated levels of GFAP in the blood have been associated with acute brain injuries, including traumatic brain injury and stroke[66]. Blood-based GFAP assays are being explored as tools for detecting and monitoring brain damage. Lastly, S100B is a protein released by astrocytes following brain injury. Elevated blood levels of S100B have been associated with traumatic brain injury, stroke, and neurodegenerative diseases[69]. S100B assays are being investigated for their potential as blood-based biomarkers for CNS pathologies. Although these markers are promising, the challenge of standardizing the highly dynamic blood remains. Moreover, disease phenotypes may yield similar biomarkers leading to further challenges in identifying a specific disease or a disease state. Thus, further work is necessary for blood biomarkers to reflect brain pathology.

Brain imaging studies are another approach to follow brain health, and human imaging modalities span from CT, MRI, and PET. CT scans rely on X-rays and generate a cross-sectional image of the brain based on measuring the density of the tissues. CT imaging is often used to diagnose bleeds in the brain stemming from a stroke or a traumatic brain injury, as it is a fast-imaging modality. However, the scans are not very high in resolution and subject the patient to ionizing radiation[70]. MRI utilizes a magnetic field and radio waves to generate higher resolution brain images that also provide information on abnormal brain tissue, especially for detecting brain tumors[71] and AD and dementia due to the detection of shrinkage in the hippocampus[72] and dark matter states[73], among others. Although MRI has many sequences that generate information on different aspects, it is based on measuring the brain's response to hydrogen atoms. It is safer compared to CT; however, it also takes more time to acquire. PET imaging utilizes radioactive agents and tracers to measure brain functions and metabolism. Tracers can measure glucose metabolism (such as ^{18}F-FDG PET)[74] and AD-related protein deposition such as amyloid (such as ^{11}C-PiB PET) or Tau tracers (such as ^{18}F-Flortaucipir PET)[75]. Dopamine tracers are used to measure dopamine levels, which is critical to assess in Parkinson's disease (such as [18F]FDOPA)[76]. Serotonin tracers help diagnose depression and anxiety (5-HT1AR antagonist PET tracers such as [*carbonyl*-11C]WAY100635)[76,77]. Some

tracers are designed to detect neuroinflammation via TSPO protein, which targets microglia, monocytes that participate in a neuroinflammatory process in the brain[76]. Different TSPO tracers are available depending on practical considerations such as approval and availability and considerations such as the binding specificity, half-life, and lipophilicity (as this parameter is essential to determine the crossing of the BBB)[78]. Although PET imaging modality also exposes patients to ionizing radiation, the high sensitivity that allows the detection of even small changes in neuroinflammation is an essential advantage over other modalities. However, all of these imaging modalities are, unfortunately, either in terms of resolution or invasiveness.

As portrayed by the wide variety of imaging techniques present in previously presented papers and the limitations posed by human imaging experiments, it is essential to further examine neuroinflammatory processes in experimental settings using animal models. Some examples of how CNS pathologies can be imaged are confocal microscopy, 2-photon microscopy, and LSFM. Confocal microscopy is useful for imaging *in vivo* cells in high-resolution or small tissue volumes *ex vivo*. 2-photon imaging, on the other hand, allows live imaging *in vivo*. However, it is limited in imaging depth and time due to the phototoxicity of the laser in living specimens. Also, the field of view that can be imaged in this imaging modality is relatively low, limiting a holistic understanding of the tissue of interest [79]. LSFM, on the other hand, combined with tissue clearing, becomes a powerful tool to investigate large pieces of tissue in its intact state[79]. However, with LSFM, examining large tissues *in vivo* is impossible.

1.5 Optical tissue clearing to investigate intact specimens

Optical tissue-clearing technology is a relatively new and rapidly developing field that has revolutionized how biological tissues are studied. Tissue clearing is a process that aims to make biological tissues transparent by removing opaque or light-scattering components, such as lipids and water while preserving the structural integrity and spatial organization of cells and biomolecules[16]. This process allows for the imaging of intact tissues at a high resolution and in three dimensions without the need for destructive sectioning techniques such as microtome cutting, where information can easily be lost due to the limited thickness of the sample. Additionally, it allows unbiased examination of the sample since the entire organism can be cleared without predetermination of specific organs or regions within organs. The optical tissue-clearing method has opened new avenues for neuroscience, immunology, and developmental biology research.

The basic principles of tissue clearing involve fixation, dehydration, and clearing of the tissue. The tissue is first fixed to preserve its structural integrity and prevent degradation. Fixation is typically followed by dehydration, which involves replacing water in the tissue with a series of organic solvents such as methanol, ethanol, xylene, and tetrahydrofuran. Finally, the tissue is submerged into a RI matching reagent such as BABB that renders the sample transparent in the BABB reagent and during the imaging process allowing maximum light penetration. Different clearing agents have different clearing properties, and the choice of clearing agent depends on the specific tissue and imaging technique used[2,16].

1.5.1 History of optical tissue clearing technology

The history of optical tissue-clearing technology dates back to the late 19th century when the first attempts were made to make biological tissues transparent. In 1914, Werner Spalteholz developed a tissue-clearing method that involved immersing tissues in a mixture of methyl salicylate and benzyl benzoate. This method, known as the Spalteholz technique, was widely used for decades and is still used today in some applications. However, the Spalteholz technique has several limitations, including the long clearing times and the toxicity of the clearing agents used[16].

In recent years, several new tissue-clearing methods have been developed that overcome some of the limitations of the Spalteholz technique. These include the Scale[80], CLARITY[81], iDISCO[82], and vDISCO[2,10] methods. Each method has strengths and weaknesses and is optimized for tissue types and imaging techniques. In addition to the limitation posed by the technique, the technology to take full advantage of cleared tissues was also limited. The combination of the wide use of transgenic animals that allowed fluorescent tagging of proteins of interest, antibody labeling, and the development of the first light sheet microscope in 2007 by Dodt et al.[13] allowed the wide use of tissue clearing technologies. Light sheet fluorescent microscope especially provided a big step forward in the field as it addressed several caveats with conventional imaging modalities such as confocal imaging[79]. For example, due to differences in imaging mechanism, LSFM illuminates the specimen with a thin light sheet instead of a focused laser beam, which illuminates the entire specimen plane, enabling rapid imaging with minimum photodamage. The entire plane illumination mechanism allows bigger samples to be imaged using an LSFM. However, the imaging modality and the clearing protocol must be decided based on the sample and the scientific question the sample bears to answer[16].

There have been numerous tissue-clearing protocols developed in the past decade which can be categorized as follows: hydrogel-based clearing, aqueous-based clearing, and solvent-based clearing.

Hydrogel-based tissue clearing protocols, such as CLARITY[81], PACT[83], and PARS[84], utilize acrylamide monomers to form a tissue-hydrogel hybrid, allowing for the immobilization of amino group-containing molecules by cross-linking. The hydrogel embedding thus keeps large tissues intact and decreases structural damage. However, hydrogel-based protocols require longer incubation times and specialized equipment[85].

Aqueous-based methods utilize water-soluble agents such as sugars, dextran, sucrose, urea, and amino alcohol to achieve transparency. These methods are less destructive to the tissue and display high levels of biocompatibility and biosafety[85]. The different subtypes of aqueous-based methods depend on the reagents used in the protocols for decolorization, delipidation, or RI-matching steps. Some examples include SeeDB[86], Scale[80], and CUBIC[87] protocols.

The solvent-based clearing is a category of tissue-clearing methods that is historically the oldest and relies on organic solvents to remove lipids and other light-scattering molecules from tissues. These solvents are chosen based on their ability to dissolve lipids and other molecules in tissues while minimizing tissue structure damage and preserving labeled molecules' fluorescence. The most commonly used solvents for solvent-based clearing are organic solvents such as benzyl alcohol, benzyl benzoate, dibenzyl ether, and THF[16]. Using these solvents can lead to significant tissue shrinkage, which can be beneficial for imaging thick samples[88]. However, solvent-induced tissue shrinkage can also cause deformation of the tissue structure, making it difficult to reconstruct the 3D architecture of the tissue accurately. Solvent-based clearing methods are relatively simple and more straightforward than other tissue-clearing methods[85]. Some examples of solvent-based clearing include 3DISCO[89], uDISCO[88], iDISCO[82], ECi[90], and vDISCO[2,10]. SHANEL[17] has been another solvent-based protocol recently devised, specifically improving tissue-clearing technologies in human tissues using molecules such as CHAPS to enhance penetration of antibodies[17].

The different approaches to tissue clearing expand the application of this technology by providing specialized protocols for a variety of purposes, such as investigating notoriously difficult bone tissue[91,92], using an endogenous fluorescent signal or antibody labeling, as well as for a variety of sizes, such as organoids, mouse embryos, whole mouse organs, whole mouse bodies, and whole human organs.

For this thesis, understanding the challenge bone tissue brings to clearing is crucial. Bone tissue is innately dense and mineralized compared to other body parts. The high mineral content of bone, primarily hydroxyapatite, scatters and absorbs light, making it difficult for light to penetrate deep into the tissue[93]. Light scattering and absorption result in reduced transparency and hinder optical imaging techniques. Additionally, bone tissue contains various distinct layers regarding tissue integrity: cortical bone (compact bone) and trabecular bone (spongy bone). These variations further contribute to light scattering and complicate the optical clearing process.

Moreover, collagen fibers within the bone matrix can also interfere with optical transparency. Collagen has a high refractive index, leading to light scattering and limiting the ability to achieve clear visualization[94] of structures within the bone. The presence of collagen fibers is also a significant challenge to note for meninges clearing. The dural layer of the meninges is specifically densely populated with collagen fibers[95].

Efforts to optically clear bone tissue involve techniques such as decalcification, which removes the mineral content, and various chemical treatments to reduce light scattering and increase tissue transparency. Some commonly used agents include Ethylenediaminetetraacetic acid (EDTA), a chelating agent that binds to calcium ions, aiding their removal from the tissue. It is often used in a buffered solution depending on the tissue and the required decalcification amount[96]. Formic acid is another agent that is widely used for decalcification. It is an organic acid that helps dissolve calcium salts and aid in the decalcification process. However, it is known to distort the tissue[96]. Hydrochloric acid (HCl) may dissolve calcium salts in diluted amounts. Overall, the choice of decalcification agent depends on many factors, such as the tissue type, desired decalcification rate, and, most importantly, downstream applications[97]. Different agents may be more effective for specific tissue types or experimental requirements.

A more detailed overview of clearing technologies can be found in our review[16].

1.5.2 Applications of tissue clearing

Tissue clearing has various applications in life sciences and biomedical research. These applications include the study of cancer biology, developmental biology, immunology, neuroscience, and neuroimmunology[16]. Tissue clearing can also be used to study the distribution and dynamics of cells and tissues [98] and investigate the interaction between cells,

drugs, and disease models[10]. Additionally, it can be used for drug screening[15] and regenerative medicine by allowing researchers to visualize and track the destination of cells[99].

In order to achieve an unbiased understanding and answer questions from the above fields, a whole mouse body approach is ideal. Some protocols have achieved whole-body clearing by removing the skin where they leverage the circulatory system of mice to perfuse clearing reagents[14,84,87]. However, subsequent imaging and analysis steps have been limiting (size, brightness of fluorophore) the wide use of these protocols. The development of the vDISCO protocol manuscript[2] was, therefore, essential. With this protocol paper, in addition to demonstrating the pipeline from immunolabeling and clearing to imaging and data processing steps, various biological applications were shared. These applications included: visualization of the entire mouse lymphatic system, virus tracing, a methodology to detect and quantify organ-specific metastases at single-cell level in the entire mouse body with cancer, evaluation of β-cell distribution in the pancreas of transgenic pigs, the visualization of sensory nerves and immune cells in the skin as well as their connectivity to the spinal cord, neuronal projection map of a transgenic mouse and the discovery of skull-meninges channels (SMCs) connecting the mouse skull bone marrow to the dura[2,10].

Among all, tissue clearing has helped to advance neuroscience and neuroimmunology. Tissue clearing provides a significant advantage as it enables the mapping of neuronal circuits and the visualization of the spatial organization of neurons and the brain and surrounding tissue within intact organs or organisms. Upon setting new standards for spatial data with the vDISCO protocol, the next important step was to combine spatial results with molecular data.

1.6 Omics technologies to understand cellular heterogeneity

The building blocks of life, cells, are defined by the genes it transcribes in RNA form, which is translated to protein. Hence, the information on which genes and proteins are present in the cell gives us important clues about a cell‘s functionality. Omics technologies have revolutionized our understanding of cellular heterogeneity on every cellular level, providing valuable insight into the complex landscape of various cell populations within tissues. Omics technologies exemplify the shift in biological experimentation towards systems biology, emphasizing the need for high-throughput screens of biological events or diseases. For instance, transcriptomics, a branch of omics technology, has been instrumental in identifying and characterizing different cell and tissue types based on their unique RNA expression profiles. By analyzing the transcriptomes of individual cells, researchers have classified cell populations, identified

specific cell types within tissues[100], and decipher how tissues distinctly react to specific injuries[101]. Identification of single cells has led to the discovery of previously unknown cell subtypes[102] and has provided a deeper understanding of cellular diversity.

Similarly, proteomics, another omics technology, has been employed to investigate the protein expression profiles of different cell populations[103]. Researchers can gain insights into specific cell types' functional roles and activities by studying the proteome, which represents the complete set of proteins in a cell or tissue. On the other hand, using technologies such as flow cytometry, which represents a targeted set of proteins in a cell or tissue, has been instrumental in classifying immune cells and immune responses[104]. Protein-level analysis has been used to identify differentially expressed proteins in various cell populations, helping elucidate their unique functions and contributions to tissue heterogeneity. Epigenomics and metabolomics are additional layers of further characterizing a cell population or a tissue, expanding our understanding of the molecular landscape of a given specimen[105].

Collectively, omics technologies have provided powerful tools for characterizing and understanding cellular heterogeneity at multiple levels. These technologies have revealed cell populations' complexity within tissues and paved the way for further investigations into their functional roles and contributions to biological processes.

1.6.1 RNA Technologies in cellular heterogeneity

RNA is a vital intermediary molecule in cells, facilitating the transfer of genetic information from DNA to the protein synthesis machinery. Messenger RNA (mRNA) has gained significant prominence in RNA sequencing technologies[106] among the various types of RNA present in cells. mRNA has gained significance because it carries the genetic code for protein synthesis, making it a valuable target for studying cellular function and categorizing cells of interest.

RNA sequencing can be performed in two main ways: bulk RNA sequencing and single-cell RNA sequencing (scRNA-Seq). Both methods rely on cDNA preparation from the RNA, preparation of a library from the cDNAs, and sequencing[106]. RNA is initially fragmented and then reverse-transcribed. Upon cDNA generation, adapters are ligated to the end of the cDNA molecules, enabling amplification of the molecules using PCR. The amplification step enables the enrichment of the cDNA fragments to be detectable for the sequencing reaction.

Bulk RNA sequencing involves analyzing RNA from a collection of cells or tissue as a whole. While collecting whole tissue provides collective information about gene expression within the

tissue, it may lose the ability to discern cell heterogeneity unless specific cell populations are pre-selected.[106] Conversely, scRNAseq enables gene expression analysis at the single-cell level using barcoding techniques. Single-cell level barcoding approach provides more detailed and cell-type-specific data, although it can be more costly and computationally demanding for data analysis.

Both bulk RNA sequencing and scRNAseq have advantages and applications depending on the research question. Bulk RNA sequencing is suitable for obtaining an overall view of gene expression within a tissue, whereas scRNAseq provides insights into cellular heterogeneity and allows for identifying rare cell populations.

1.6.2 Analysing RNA Technologies

Analyzing RNA-seq data involves several key steps to gain meaningful insights into gene expression and uncover biological patterns. RNA-seq analysis can be demanding in terms of computational power and the need for a bioinformatics background. The process typically begins with raw sequencing reads obtained from the sequencer, which is then subjected to quality control and preprocessing steps to remove low-quality reads and adaptors. After preprocessing, the reads are aligned or mapped to a reference genome or transcriptome to identify the origins of the sequenced fragments[107].

Following alignment, the expression levels of genes or transcripts are quantified, which involves counting the number of reads that align to each gene or transcript. Most core facilities that perform sequencing often provide alignment services, as these processes are often straightforward and repetitive. Next, normalization methods are applied to the data to adjust for differences in sequencing depth and other technical factors, ensuring fair sample comparisons. With normalized expression values, the downstream analysis starts.

Downstream analysis can vary depending on the question to be answered. Some standard visualization methods represent the results using a dimensionality reduction method such as Uniform Manifold Approximation and Projection or Principal Component Analysis. The resulting plot provides information on the similarity of expression patterns among samples. After investigating the differentially expressed genes, heatmaps and volcano plots may represent the results. Enrichment analyses are often used to provide an overview of the affected pathways[108].

Python[109] or R programming[110] language based packages perform the analyses mentioned above. Ultimately, applying and interpreting RNA-seq data requires computational and biological knowledge with context. Thus, the generation of the RNA-seq results from a collaboration between a bioinformatician and a biologist, which is also the case for the study presented (Section 2.1).

1.6.2 Protein-based technologies in cellular heterogeneity

Proteins are undoubtedly one of the most critical macromolecules in the functioning and survival of cells. They provide structural support, enzymatic activities, cellular signaling, gene expression regulation, immune defense, cell adhesion, and communication. Thus, understanding the proteomic state of a cell provides unprecedented information on the cell's functions. One of the most common ways to investigate the proteomic signature of a cell is mass spectrometry-based proteomics. Mass-spectrometry-based proteomics technology allows the identification, quantification, and characterization of a protein within a sample. The basic principle is that the mass spectrometer ionizes protein molecules which separates them based on their mass-to-charge ratio allowing the detection of resulting ions[103]. Based on the results, bioinformatics analysis provides information on the proteins detected and their relative abundance within a given sample. Targeted approaches exploring post-translational modifications and protein-protein interactions may provide further information on the proteomic signature. As single-cell barcoding technologies have not yet been employed for proteomics methods, proteomics datasets are often presented in bulk. Although bulk datasets defeat the idea of understanding cellular heterogeneity within a tissue, targeted approaches where enrichment of specific cell types may enable the identification of new cell types, cellular heterogeneity, or simply understanding the proteomic signature of a particular sample.

Flow cytometry, on the other hand, is somewhat limited yet widely used for high-throughput analysis based on a cell's physical and chemical properties. It is a targeted approach where fluorescently labeled antibodies are utilized to mark specific proteins within or on the surface of the cell[104]. Measuring fluorescent intensity and cell characteristics allows the characterization of distinct cell populations, cell cycle analysis, assessment of immune responses, and disease-related changes in cellular populations. Flow cytometry technology is often used to enrich a particular cell type population, followed by mass-spectrometry-based proteomics or RNA sequencing technologies.

1.6.2 Analysing protein-based technologies

Mass-spectrometry-based proteomics data analysis involves intricate serial steps to decipher the complex protein composition within biological samples. After acquiring raw mass spectra, the data undergoes preprocessing, including peak detection, noise filtering, and deisotoping, to generate clean and informative spectra. The next crucial phase is peptide identification, where the acquired spectra are compared against protein sequence databases using search algorithms like SEQUEST, Mascot, or MaxQuant[111]. This step aims to match observed peptides to their corresponding proteins and determine their abundance levels.

Following peptide identification, statistical methods are applied to evaluate the significance of peptide matches and control the false discovery rate. Subsequent data analysis often involves functional annotation, where identified proteins are categorized based on biological processes, molecular functions, and cellular components using tools like Gene Ontology (GO)[108,112] or pathway databases. The downstream analysis may be performed in platforms with graphical user interfaces such as Perseus[113]. However, these software are limited in changing parameters for your specific needs. Therefore python based packages that enable data handling and visualization, such as scanpy[109] can also be used to process mass-spectrometry-based proteomics data.

Interpreting mass-spectrometry-based proteomics data requires both computational expertise and biological knowledge to navigate the complexities of the data and derive meaningful biological conclusions. Thus, for the study in Section 1.2, I have collaborated with computational scientists to ensure our data's correct processing and interpretation. The integration of multiple analysis approaches and validation strategies ensures robust and reliable results, aiding in understanding the proteome's dynamic changes under various biological conditions.

2. AIM

The thesis objective was to investigate the role of the skull bone marrow in brain diseases and its potential implications and provide an optimized optical whole-body clearing and volumetric imaging protocol (vDISCO) with the following aims:

1) Examine the cellular heterogeneity in various bone marrow in mouse in physiological and pathological (after stroke) state using single cell and bulk RNAseq and mass-spectrometry-based proteomics
2) Investigate the cellular heterogeneity in various human bone marrow using scRNAseq and mass-spectrometry-based proteomics.
3) Provide in-depth spatial, cellular, and quantitative characterization of skull organization evidencing SMCs in humans.
4) Investigate the skull's *in vivo* response to various neurological disorders in mice and humans.
5) Provide an in-depth protocol for establishing and executing vDISCO tissue clearing protocol that can be adapted to various biological questions.

This study presents a novel approach to understanding brain health through the lens of systems biology, specifically focusing on the role and characteristics of skull bone marrow in both health and disease contexts.

3. STUDIES

The original numbering of tables, figures, and supplementary material within each article has been retained.

3.1 Study I: Distinct molecular profiles of skull bone marrow in health and neurological disorders

The following section includes the original research article "Distinct molecular profiles of skull bone marrow in health and neurological disorders," published in *Cell* (Kolabas, Kuemmerle, Perneczky, Forstera, et al., 2023).

Here, we aimed to elucidate the skull's molecular profile, structural connections to the meninges, and response to neurological disorders. To decipher these research topics, we employed cutting-edge technologies ranging from scRNAseq, mass-spectrometry-based proteomics, tissue clearing, LSFM, confocal, 2-photon, sEM, and TSPO-PET imaging in mice and humans.

We created comprehensive and numerous datasets of scRNAseq and mass-spectrometry-based proteomics that will be publicly available for further hypothesis generation and/or validation. The datasets include scRNAseq and proteomics of six bones, meninges, and brain in naïve, sham-operated, and stroke mice. In humans, we generated a scRNAseq dataset of one skull and a proteomics dataset of 20 skulls, vertebrae, and pelvis.

We showed skull dynamics using 2-photon live imaging of the mouse skull longitudinally from a naïve state up to 72 hours after stroke. We also suggested that skull immune cells end up in the brain 72h after stroke, validating previous literature.

We imaged and demonstrated more than 500 SMCs in humans, delivering an understanding of the connections' landscape in three distinct locations of the skull. Furthermore, we delivered images of the SMCs using various microscopes, shedding light on their structure.

Lastly, we analyzed TSPO-PET images of the skulls of patients with various neurological disorders and reported that skull inflammatory response is defined spatially and temporally, reflecting the brain inflammatory response.

This manuscript presents a wealth of data with numerous novel findings, expanding our understanding of the skull and its role in neurological conditions.

Cell

Distinct molecular profiles of skull bone marrow in health and neurological disorders

Graphical abstract

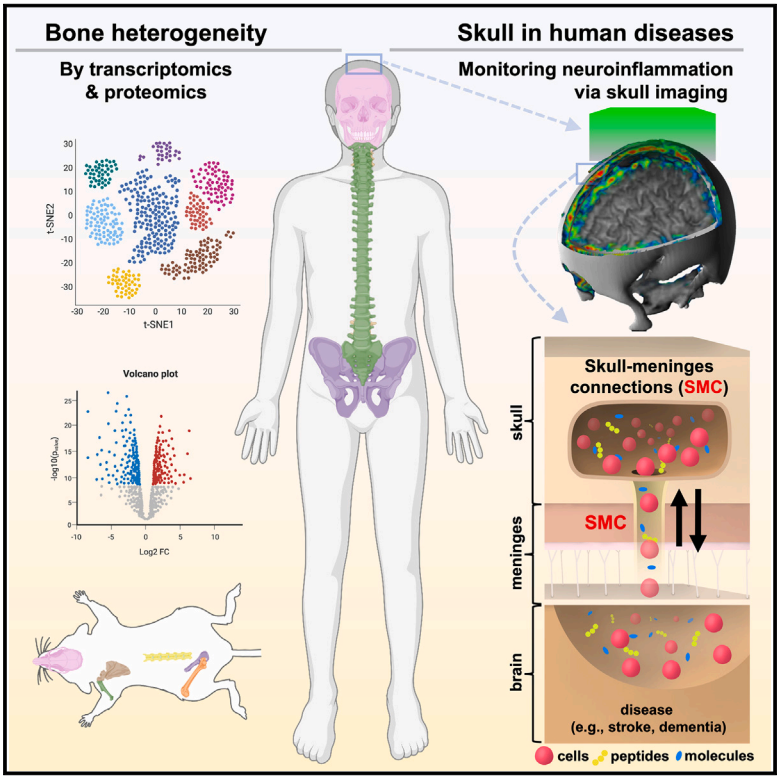

Highlights

- Bone marrow across the body display molecular heterogeneity in mice and humans
- Calvaria cells have a distinct profile that is relevant to brain pathologies
- Structural details of human skull-meninges connections are revealed
- TSPO-PET imaging of human skulls can be a proxy of neuroinflammation in the brain

Authors

Zeynep Ilgin Kolabas, Louis B. Kuemmerle, Robert Perneczky, ..., Matthias Brendel, Fabian J. Theis, Ali Erturk

Correspondence

ali.erturk@helmholtz-munich.de

In brief

The bone marrow of the skull has a unique molecular and functional composition, as well as disease-specific inflammatory responses that can be observed through human translocator protein positron emission tomography (TSPO-PET) imaging, suggesting that it has potential as a site for brain disease diagnosis, monitoring, and treatment.

Kolabas et al., 2023, Cell *186*, 3706–3725
August 17, 2023
https://doi.org/10.1016/j.cell.2023.07.009

CellPress

CellPress
OPEN ACCESS

Cell

Resource

Distinct molecular profiles of skull bone marrow in health and neurological disorders

Zeynep Ilgin Kolabas,[1,2,3,39] Louis B. Kuemmerle,[1,4,39] Robert Perneczky,[5,6,7,8,9,39] Benjamin Förstera,[1,2,39] Selin Ulukaya,[1] Mayar Ali,[1,3,4] Saketh Kapoor,[1] Laura M. Bartos,[10] Maren Büttner,[4] Ozum Sehnaz Caliskan,[11] Zhouyi Rong,[1,2,12] Hongcheng Mai,[1,2,12] Luciano Höher,[1] Denise Jeridi,[1] Muge Molbay,[1] Igor Khalin,[2] Ioannis K. Deligiannis,[13] Moritz Negwer,[1] Kenny Roberts,[14] Alba Simats,[2] Olga Carofiglio,[2] Mihail I. Todorov,[1,2] Izabela Horvath,[1,15] Furkan Ozturk,[1] Selina Hummel,[6,10] Gloria Biechele,[10] Artem Zatcepin,[6,10] Marcus Unterrainer,[10,16] Johannes Gnörich,[10] Jay Roodselaar,[17,18] Joshua Shrouder,[2] Pardis Khosravani,[19] Benjamin Tast,[19] Lisa Richter,[19] Laura Díaz-Marugán,[2] Doris Kaltenecker,[1,20] Laurin Lux,[1] Ying Chen,[2] Shan Zhao,[1,2] Boris-Stephan Rauchmann,[5,9,21] Michael Sterr,[22,23] Ines Kunze,[22,23] Karen Stanic,[1,2] Vanessa W.Y. Kan,[24] Simon Besson-Girard,[2,3] Sabrina Katzdobler,[6,25] Carla Palleis,[6,25] Julia Schädler,[26] Johannes C. Paetzold,[1,27] Sabine Liebscher,[8,24,32] Anja E. Hauser,[17,18] Ozgun Gokce,[2,8] Heiko Lickert,[22,23,30] Hanno Steinke,[28] Corinne Benakis,[2] Christian Braun,[29] Celia P. Martinez-Jimenez,[13,30] Katharina Buerger,[2,6] Nathalie L. Albert,[10] Günter Höglinger,[6,25] Johannes Levin,[6,8,25] Christian Haass,[6,8,31]

(Author list continued on next page)

[1]Institute for Tissue Engineering and Regenerative Medicine (iTERM), Helmholtz Center, Neuherberg, Munich, Germany
[2]Institute for Stroke and Dementia Research, LMU University Hospital, Ludwig-Maximilians University Munich, Munich, Germany
[3]Graduate School of Systemic Neurosciences (GSN), Munich, Germany
[4]Institute of Computational Biology, Helmholtz Zentrum München, German Research Center for Environmental Health, Neuherberg, Germany
[5]Division of Mental Health in Older Adults and Alzheimer Therapy and Research Center, Department of Psychiatry and Psychotherapy, University Hospital, Ludwig Maximilian University Munich, 80336 Munich, Germany
[6]German Center for Neurodegenerative Diseases (DZNE) Munich, Munich, Germany
[7]Ageing Epidemiology (AGE) Research Unit, School of Public Health, Imperial College London, London, UK
[8]Munich Cluster for Systems Neurology (SyNergy), Munich, Germany
[9]Sheffield Institute for Translational Neuroscience, University of Sheffield, Sheffield, UK
[10]Department of Nuclear Medicine, University Hospital, Ludwig-Maximilians-Universität München, Munich, Germany
[11]Institute for Diabetes and Obesity, Helmholtz Center Munich and German Center for Diabetes Research (DZD), 85764 Neuherberg, Germany
[12]Munich Medical Research School (MMRS), 80336 Munich, Germany
[13]Helmholtz Pioneer Campus (HPC), Helmholtz Munich, Neuherberg, Germany
[14]Wellcome Sanger Institute, Cambridge, UK

(Affiliations continued on next page)

SUMMARY

The bone marrow in the skull is important for shaping immune responses in the brain and meninges, but its molecular makeup among bones and relevance in human diseases remain unclear. Here, we show that the mouse skull has the most distinct transcriptomic profile compared with other bones in states of health and injury, characterized by a late-stage neutrophil phenotype. In humans, proteome analysis reveals that the skull marrow is the most distinct, with differentially expressed neutrophil-related pathways and a unique synaptic protein signature. 3D imaging demonstrates the structural and cellular details of human skull-meninges connections (SMCs) compared with veins. Last, using translocator protein positron emission tomography (TSPO-PET) imaging, we show that the skull bone marrow reflects inflammatory brain responses with a disease-specific spatial distribution in patients with various neurological disorders. The unique molecular profile and anatomical and functional connections of the skull show its potential as a site for diagnosing, monitoring, and treating brain diseases.

INTRODUCTION

The complex interplay between immune cells at the central nervous system (CNS) borders and the CNS resident immune system has become the subject of intensive research.[1] The dura mater of the meninges is directly connected to the adjacent skull bone marrow via skull-meninges connections (SMCs) that allow the trafficking of immune cells[2–5] and might facilitate the

CellPress
OPEN ACCESS

Anna Kopczak,[2] Martin Dichgans,[2,6,8] Joachim Havla,[24,32] Tania Kümpfel,[24,32] Martin Kerschensteiner,[8,24,32] Martina Schifferer,[6,8] Mikael Simons,[6,8] Arthur Liesz,[2,3,8] Natalie Krahmer,[11] Omer A. Bayraktar,[14] Nicolai Franzmeier,[2] Nikolaus Plesnila,[2,8] Suheda Erener,[1] Victor G. Puelles,[33,34,35,36] Claire Delbridge,[37] Harsharan Singh Bhatia,[1,2] Farida Hellal,[1,2,8] Markus Elsner,[1] Ingo Bechmann,[28] Benjamin Ondruschka,[26] Matthias Brendel,[6,8,10] Fabian J. Theis,[4,38] and Ali Erturk[1,2,3,8,40,*]

[15]School of Computation, Information and Technology (CIT), TUM, Boltzmannstr. 3, 85748 Garching, Germany
[16]Department of Radiology, University Hospital, LMU Munich, Munich, Germany
[17]Charité - Universitätsmedizin Berlin, Department of Rheumatology and Clinical Immunology, Berlin, Germany
[18]Immune Dynamics, Deutsches Rheuma-Forschungszentrum (DRFZ), a Leibniz Institute, Berlin, Germany
[19]Biomedical Center (BMC), Core Facility Flow Cytometry, Faculty of Medicine, LMU Munich, Munich, Germany
[20]Institute for Diabetes and Cancer, Helmholtz Munich, Munich, Germany
[21]Institute of Neuroradiology, University Hospital LMU, Munich, Germany
[22]Institute of Diabetes and Regeneration Research, Helmholtz Diabetes Center, Helmholtz Zentrum München, Neuherberg, Germany
[23]Institute of Stem Cell Research, Helmholtz Zentrum München, Neuherberg, Germany
[24]Institute of Clinical Neuroimmunology, University Hospital Munich, Ludwig-Maximilians University Munich, Munich, Germany
[25]Department of Neurology, Ludwig-Maximilians-Universität München, Munich, Germany
[26]Institute of Legal Medicine, University Medical Center Hamburg-Eppendorf, Hamburg, Germany
[27]Department of Computing, Imperial College London, London, UK
[28]Institute of Anatomy, University of Leipzig, 04109 Leipzig, Germany
[29]Institute of Legal Medicine, Faculty of Medicine, LMU Munich, Germany
[30]TUM School of Medicine, Technical University of Munich, Munich, Germany
[31]Metabolic Biochemistry, Biomedical Center (BMC), Faculty of Medicine, Ludwig-Maximilians-Universität München, Munich, Germany
[32]Biomedical Center (BMC), Medical Faculty, Ludwig-Maximilians Universität Munich, Munich, Germany
[33]III. Department of Medicine, University Medical Center Hamburg-Eppendorf, Hamburg, Germany
[34]Hamburg Center for Kidney Health (HCKH), University Medical Center Hamburg-Eppendorf, Hamburg, Germany
[35]Department of Clinical Medicine, Aarhus University, Aarhus, Denmark
[36]Department of Pathology, Aarhus University Hospital, Aarhus, Denmark
[37]Institute of Pathology, Department of Neuropathology, Technical University Munich, TUM School of Medicine, Munich, Germany
[38]Department of Mathematics, Technische Universität München, Garching bei München, Germany
[39]These authors contributed equally
[40]Lead contact
*Correspondence: ali.erturk@helmholtz-munich.de
https://doi.org/10.1016/j.cell.2023.07.009

preferential recruitment of immune cells to the meninges from the skull bone marrow.[5–7]

In mice, high-throughput, multidimensional techniques, such as flow and mass cytometry and single-cell RNA sequencing (scRNA-seq), have provided a detailed map of the cell-type composition and molecular profiles of meningeal immune cells.[8–12] CNS border-derived cells can be functionally distinct from blood-derived cells of the same type[5] and cells from different regions of the CNS borders.[12,13]

By contrast, little functional and multidimensional molecular data are available for the skull bone marrow and how it relates to other bones. For example, Herisson et al.[4] found a higher influx of monocytes and neutrophils from the skull than from the tibia after brain injury, and Cugurra et al.[5] showed that dural monocytes and neutrophils are mainly directly derived from the skull bone marrow. Basic scRNA-seq data of the unperturbed skull in comparison to the tibia marrow were obtained by Mazzitelli et al..[14] Proteome-wide characterization of the bone marrow in mice has focused on individual cell types and bones in homeostasis[15–18] or has used antibody-based methods.[19] For the skull bone marrow, profiling has been limited to small flow or mass cytometry panels.[6,9,10] Thus, it remains unclear whether the expression profiles of skull bone marrow cells are distinct from those of other bones and whether different types of bone marrows react differently to brain injury.

In humans, the functional roles and molecular makeups of the skull bone marrow, and other bone marrows are even less well characterized. A limited number of 'omics studies of the human bone marrow have been presented,[20–23] but a systematic characterization of potential differences among different bone marrows under different conditions is yet to be performed. Even on an anatomical level, although the presence of human SMCs has been suggested using microcomputed tomography (microCT),[4] their detailed conformation at the cellular level remains elusive.

Here, we performed a systematic and comprehensive molecular analysis of the RNA and protein expression profiles of diverse bone marrow cells in mice and humans. In mice, we performed bulk and scRNA-seq and bulk proteomics on cells from six different bones, the dura, and the brain in three conditions (naive, middle cerebral artery occlusion [MCAo], and sham-operated animals). Our data show that different bones have distinct molecular profiles, with the skull calvaria bone displaying the highest number of differentially expressed genes (DEGs) and ligand-receptor (LR) pairs, mainly related to migration and inflammation.

For studies in humans, we collected post-mortem samples from the skull, vertebra, and pelvis of 20 deceased individuals and performed proteomic analysis, again showing a unique molecular profile of the skull. Using optical clearing on human

skull + meninges + brain specimens, we characterized the anatomical details of SMCs at the cellular level. Using functional imaging in patients, we found disease-specific increases in 18 kDa translocator protein (TSPO) positron emission tomography (PET) signal in different parts of the skull in numerous neurological diseases and a strong correlation between changes in the brain and skull TSPO-PET signal in patients with Alzheimer's disease (AD) and stroke in longitudinal data. These data provide a critical link between the skull and neurological diseases in humans.

RESULTS

Skull is a dynamic site that responds to stroke

To test the skull marrow's involvement in the response to brain injury, we used MCAo as a model for stroke in mice.[24] In MCAo, the mice first undergo a neck incision to expose the carotid artery before the occlusion of the middle cerebral artery (Figure 1A). A sham-operation procedure without MCAo mimics a local injury without inducing stroke.[24–26]

Two-photon imaging on the skull after stroke (n = 3 for naive and sham, n = 5 for MCAo) at baseline and 2, 24, and 72 h post injury showed that both sham and MCAo groups had a significant decrease of $LysM^+$ cells (mostly myeloid cells) (Figure S1A, $p = 0.004$ in sham and $p \leq 0.0001$ in MCAo). Furthermore, there was a higher efflux of myeloid cells from the skull after stroke (Figure S1B), similar to what was observed for $Ly6C^{hi}$ monocytes and neutrophils.[4]

Next, we studied immune cells in the skull marrow and brain using KikGR mouse model.[5,27] We used ultraviolet laser illumination to convert a photoconvertible protein to RFP in the skull area above the ischemic brain region (Figures S1C–S1E). We detected RFP^+ B, T, and myeloid cells in the ipsilateral brain 1 and 6 h after photoconversion (Figure S1C), indicating that immune cells from the skull marrow are recruited to the brain after injury.[2,4–6]

Expression differences between cells of different bone marrows

Next, we assessed if/how skull cells might be different. To this end, we performed scRNA-seq analysis on three flat bones (calvaria, scapula, and pelvis [ilium]), two long bones (humerus and femur), and one irregular bone (vertebra from thoracic level T5 to lumbar L3), along with dura mater and brain samples in naive, sham-operated, and MCAo-operated animals (Figure 1A).

Single-cell transcriptomics of >100,000 cells across the bones and conditions revealed 17 coarse and 50 fine cell types (Figures 1B–1D). We found a bone-specific abundance of the coarse cell types, whereas meninges and brain-specific cells were separated (Figure 1B). We detected large numbers of neutrophils (~25%) and erythroid cells (~30%) along with other expected cell types (Figures 1E and S1F). Neutrophil populations were clearly separated between the conditions (Figure 1C). Standard cell-type proportions were homogeneously distributed among different bones (Figures 1E, 1F, S1G–S1J, and S2). Cell-type proportions were validated per mouse by deconvolving pooled samples with SNPs and flow cytometry, with an overall correlation of 0.88 (Figure 1F).

To investigate changes in absolute cell numbers, we imaged whole mouse bodies at cellular resolution using vDISCO tissue clearing[28] and found that the number of total cells (propidium iodide [PI]-labeled cells) increased in the calvaria marrow of mice after stroke compared with controls (Figures S3A–S3C; Video S1). The overall increase in cell number contrasts with the decrease in $LysM^+$ cells quantified by live imaging (Figure S1A), suggesting the mobilization of specific cell types out of the skull, whereas there is an overall increase in immune cell numbers as a response to injury.

Hierarchical clustering showed that the long bones, femur, and humerus clustered together with the pelvis. Likewise, the two flat bones, scapula and calvaria, clustered together. The irregular vertebral bone branched with the flat bones in naive condition and after MCAo surgery and with the long bones and pelvis in sham condition (Figure 1G). Calvaria clustered with scapula in naive and sham conditions. Notably, it formed its own branch in MCAo condition, indicating a skull-specific immune reaction to brain injury.

To assess how strongly the gene expression profiles of one bone's population diverge from the other bones' pooled population for each cell type, we used principal component regression analysis (Figure 2A). The calvaria's neutrophils diverged most from the neutrophils of the other bones in all three conditions.

On analyzing DEGs, we found the highest number in the calvaria for all conditions (Figure 2B; Table S1, tabs 5–13): in naive condition, 96; sham condition, 15; and MCAo condition, 62 genes were upregulated, whereas 138, 538, and 62 were downregulated, respectively. In all three conditions, most of the differentially downregulated genes in the calvaria were observed in progenitor cells such as pro-neutrophils, granulocyte-monocyte progenitors, and erythroid progenitors, whereas the upregulated genes were mostly in the myeloid lineage (Figure 2B).

In naive condition calvaria myeloid cell DEGs related to the regulation of apoptotic processes and programmed cell death pathways (Table S1, tabs 5–7), and calvaria-unique DEGs were mostly transcription factors, immediate early genes, and taxis-related genes (Figure 2C; Table S1, tabs 5–7). Transcription factors included *Nr4a1* and *Nr4a2* involved in cellular proliferation, apoptosis, metabolism, and T cell regulation,[29] with an anti-inflammatory and damage-limiting role after ischemic stroke.[30] Taxis-related DEGs include chemokines and chemokine receptors, e.g., *Cxcr4*, *Ccrl2*, *Ccl4*, and *Cxcl2*. Finally, the calvaria exhibited DE pro- and anti-inflammatory genes mostly in neutrophils, such as *Il1b*,[31] *Ptgs2*,[32] and *Thbs2*,[33] of which some are also involved in cell adhesion and migration. In sham-condition calvaria, some genes were common with naive differentially upregulated genes (DUGs) such as *Nr4a1* and *Egr1* in addition to some distinct ones such as *Btg2* (anti-proliferation factor).[34]

In MCAo-condition calvaria, neutrophils harbored most DUGs. Some DUGs were in common with other conditions such as *Nr4a1*, *Cxcl2*, *Ccrl2*, and *Egr1*, whereas others were unique to stroke, such as *Cd69* (T cell migration),[35] *Gpr35* (inflammation regulation),[36] and *Nr4a3* (T cell and progenitor proliferation)[29] (Figure 2C). We validated the upregulation of *Nr4a1* in the calvaria using tissue clearing and immunostaining (Figures 2D and 2E) and RNAscope[37] (Figure 2F).

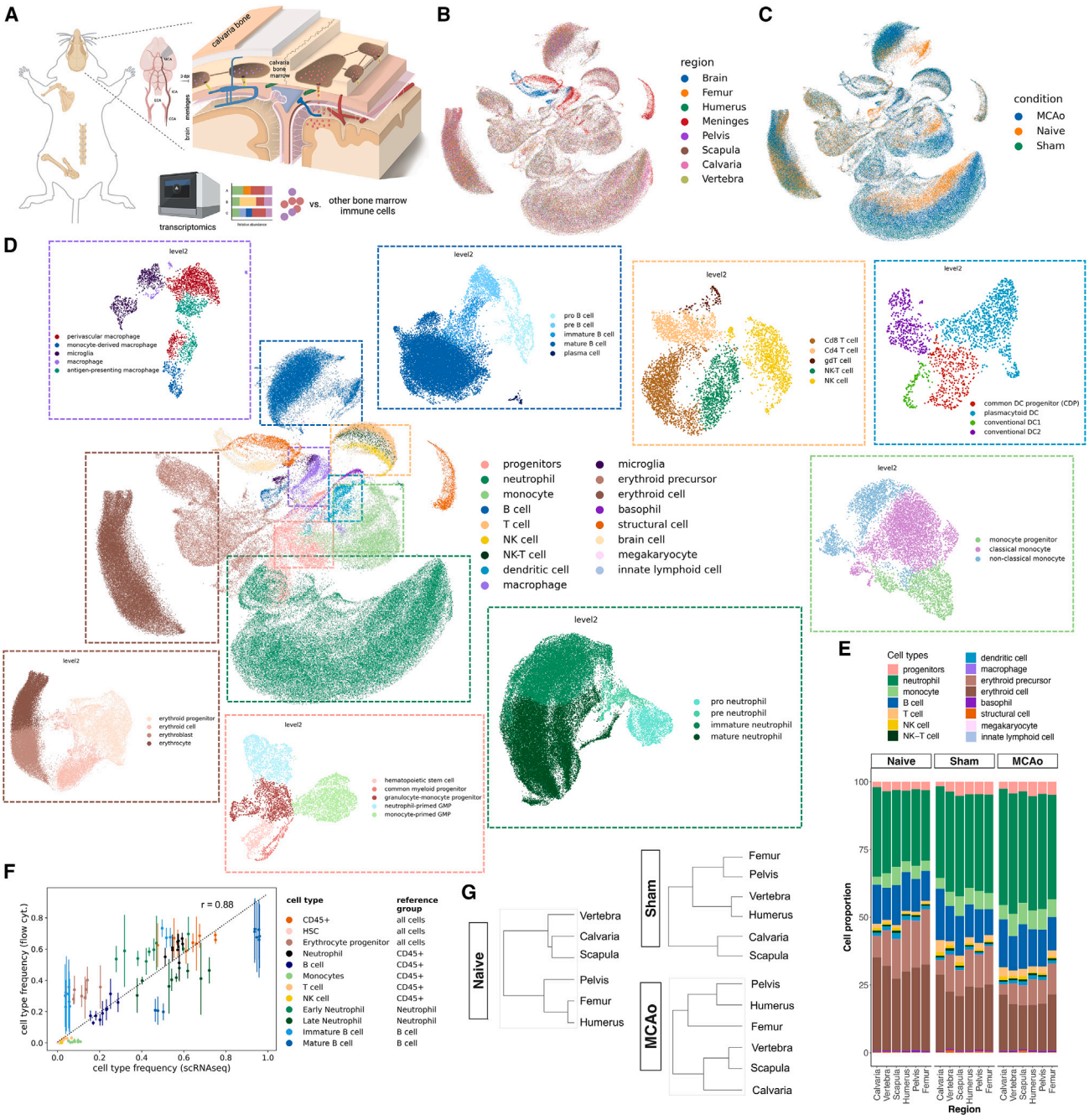

Figure 1. Bones diverge based on transcriptional signature of cell types

(A) Experimental design of single-cell RNA sequencing of bones, dura, and brain, and a schematic of the middle cerebral artery occlusion (MCAo) model of stroke.

(B–D) Uniform manifold approximation and projection (UMAP) distribution of scRNA-seq colored by (B) region, (C) condition: naive, sham-operated, and MCAo, and (D) cell type with fine annotated cell types in the surrounding with matching color.

(E) Relative proportions of the coarse cell types.

(F) Correlation between relative proportions of the cell types in scRNA-seq and independent animals measured by flow cytometry using 15 color panel. Mean Pearson correlation over conditions and bones is 0.875.

(G) Dendrograms for naive, sham, and MCAo conditions. (n = 3 pooled animals for sham and n = 6 pooled animals for MCAo.).

See also Figures S1 and S2.

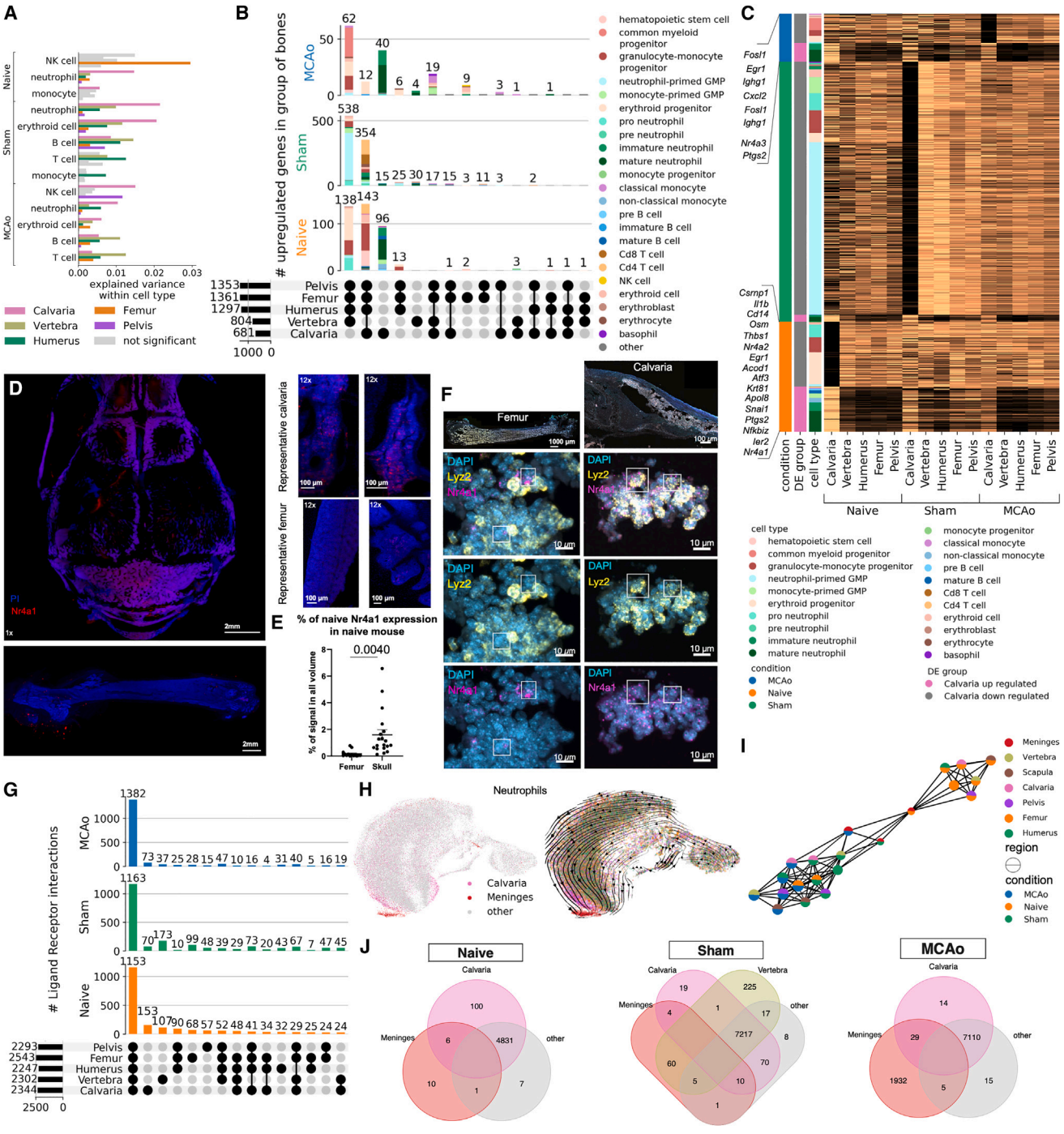

Figure 2. Different cell types show unique differentially expressed genes and ligand-receptor pairs between bones

(A) PC regression plot shows how strongly each bone's cell population diverges from the pooled population of other bones by variance explained for each coarse cell type. Only significant differences are shown for level 1 annotations. (permutation test, $p < 0.0001$)

(B) Differentially expressed genes in naive, sham, and MCAo conditions ($p < 0.05$, LFC > 1 threshold). Each bar represents the fine cell-type color the genes are upregulated in. Fine cell annotations are used.

(C) Calvaria-unique upregulated genes in the three conditions. ($p < 0.05$, LF change > 1)

(D) Representative images of *Nr4a1* labeling after clearing and light-sheet fluorescent microscopy, n = 3.

(E) Threshold based quantification of 12× scans of Nr4a1 ($p = 0.0040$). Nr4a1+ voxels as % of total volume. Data represented as ±SEM.

(F) *Nr4a1* transcript is shown to colocalize with *Lyz2* and *Mpo*, myeloid cell marker and progenitor marker, respectively, using RNAscope.

(G) Ligand-receptor interactions in three conditions on coarse cell-type annotations. (permutation test, 1000 permutations, $p = 0$)

(legend continued on next page)

Focusing on the damage-associated molecular patterns (DAMPs) in CD45+ immune cells, known to guide the immune response in trauma and infection,[38] we found calvaria-specific expressions of *Trem1*, *Trpm2*, *Nlrp3*, *Trem2*, and *Cgas* (Figure S3D). The skull was unique in downregulating *Trem1* and *Tlr2* in response to MCAo (Figure S3E).

On investigating the LR interactions using CellPhoneDB,[39] we identified bone-type unique interactions (Figure 2G; Table S1, tabs 14–28). In each of the three conditions, we found a core module of LR interactions common to all bones. The numbers of common LR pairs increased for MCAo (naive, 1,153; sham, 1,163; and MCAo, 1,382 pairs). Among the unique interactions, calvaria had the most for naive and MCAo (153 and 73, respectively), whereas vertebra had the most in sham (173).

Gene ontology (GO)-term analysis showed that common pairs to all bones in all conditions were mostly involved in cell migration, cytokine production, and immune regulation such as *Pecam1-Cd177*,[40] *Cd74-Mif*,[41] and *Lgals9-Cd47* (Table S1, tabs 18, 23, and 28). The calvaria-unique pairs included *Il1b-Adrb2* and *Ccl4-Ccr5* in naive, *Ccl4-Cnr2* in sham, and *Cxcl2-Dpp4* and *Cd28-Cd86* in MCAo conditions. Naive LR pairs had GO terms mostly related to taxis, cell motility, and cytokine production whereas sham had immune activity-related terms (Figure S3F; Table S1, tabs 18, 23, and 28). Skull-unique LR pairs in MCAo were mostly related to cell migration, chemotaxis, or immune cell activation (Figure S3F).

In conclusion, calvaria displayed the highest number of DUGs and LR pairs among the bones tested, suggesting a distinct molecular profile related to migration and inflammation, especially in the myeloid lineage. This unique signature might underly the differential cell recruitment from the skull bone marrow to the brain.[2,4–6]

Skull and meningeal neutrophils share unique similarities

As most of the calvaria-specific genes were in neutrophils (Figure 2B), we next examined their developmental trajectories using RNA velocity[42] in its scVelo[43] implementation and pseudotime,[44] which aligned well with the RNA velocity trajectory (Figures 2H and S3G). Our analysis revealed a subset of mature neutrophils from calvaria clustering next to a group of neutrophils found in the dura (Figure 2H). Along the trajectory, we observed a higher percentage of late neutrophils in the calvaria compared with other bones (Figure S3G). Upon injury, we observed a shift toward late neutrophils in the dura, most prominently in MCAo (Figure S2A). A representative phase portrait of a calcium-binding gene *S100a6* confirmed the validity of our scVelo trajectory analysis (Figure S3H).

To investigate the similarity of mature neutrophils in the calvaria and dura, we performed branching trajectory analysis using partition-based graph abstraction (PAGA).[45] We observed a clear distinction between the naive vs. injury groups with the dura positioned in the middle (Figure 2I). The meningeal neutrophils from the naive condition connected with almost all bones in the naive condition, whereas the sham and MCAo meningeal neutrophils connected to the calvaria's sham and MCAo, revealing a similarity between their late-stage neutrophil population profiles. The number of common DEGs between the dura and the calvaria also increased from 6 upregulated and 7 downregulated genes in naive (Figures 2J and S3I–S3K) to 29 upregulated to 15 downregulated genes in MCAo (Figure S3K).

The calvaria displayed the highest pro-inflammatory signature among bones in all conditions (Figure S3L) with neutrophils having the highest pro-inflammatory signature in the calvaria and B cells having the lowest (Figures S3L and S3M). Comparing the pro- and anti-inflammatory scores of the meningeal immune cells with those of the bones, we saw a stronger inflammatory response to injury and especially to MCAo in the meningeal cells, mainly in monocytes and neutrophils.

We validated our scRNA-seq results using bulk RNA-seq for the same bones. Uniform manifold approximation and projection (UMAP) showed similar trends as we saw in scRNA-seq data (Figure S4A). The overall mean correlation of gene expression values between the bulk dataset and a pseudo-bulk created from the scRNA-seq dataset was r = 0.81 (Figure S4B). 69 of the 98 genes in naive, 19 of the 78 genes in sham, and 48 of the 62 genes significantly upregulated in calvaria in the pseudo-bulk scRNA-seq data showed the same trend in both datasets (Figure S4C). 9, 4, and 21 of these genes showed the same trend and were also significant in both samples for naive, sham, and MCAo conditions, respectively (Figure S4C; Table S1, tabs 31–34).

We also sequenced CD45+ cells in 6-month-old 5xFAD AD model mice vs. littermates using smart-Seq2 (n = 3 per group) (Figures S4D and S4E). Comparing smart-Seq2 data from wild-type calvaria and femur with our scRNA-seq dataset, we found that 15 of the 23 upregulated genes showed the same trend in both (Figure S4F; Table S1, tab 35).

Overall, our data show that bones change their transcriptome in pathologies, and the calvaria holds a distinct profile mostly close to meninges.

Protein-level bone heterogeneity in mice

After transcriptomics, we also investigated proteome profiles in mouse bones, meninges, and brain using mass spectrometry proteomics (three biological replicates) (Figures 3A and S5). We quantified 9,597 proteins in total, 4,172 present in at least half of the samples (Figure S5A) and at least 5,000 proteins were present in at least one sample of each bone (Figures S5B–S5D).

(H) Left: in the neutrophil subpopulation, calvaria, and dura neutrophils are highlighted in region-based UMAP. Right: projected developmental trajectory of MCAo neutrophils subset using scVelo.

(I) PAGA analysis on the neutrophils subpopulation demonstrates separation of samples based on condition.

(J) DE genes (DEGs) among dura, calvaria, and other bones, in three conditions (n = 3 pooled animals for sham and n = 6 pooled animals for MCAo). ($p < 0.05$, LF change > 0.5)

See also Figures S3 and S4.

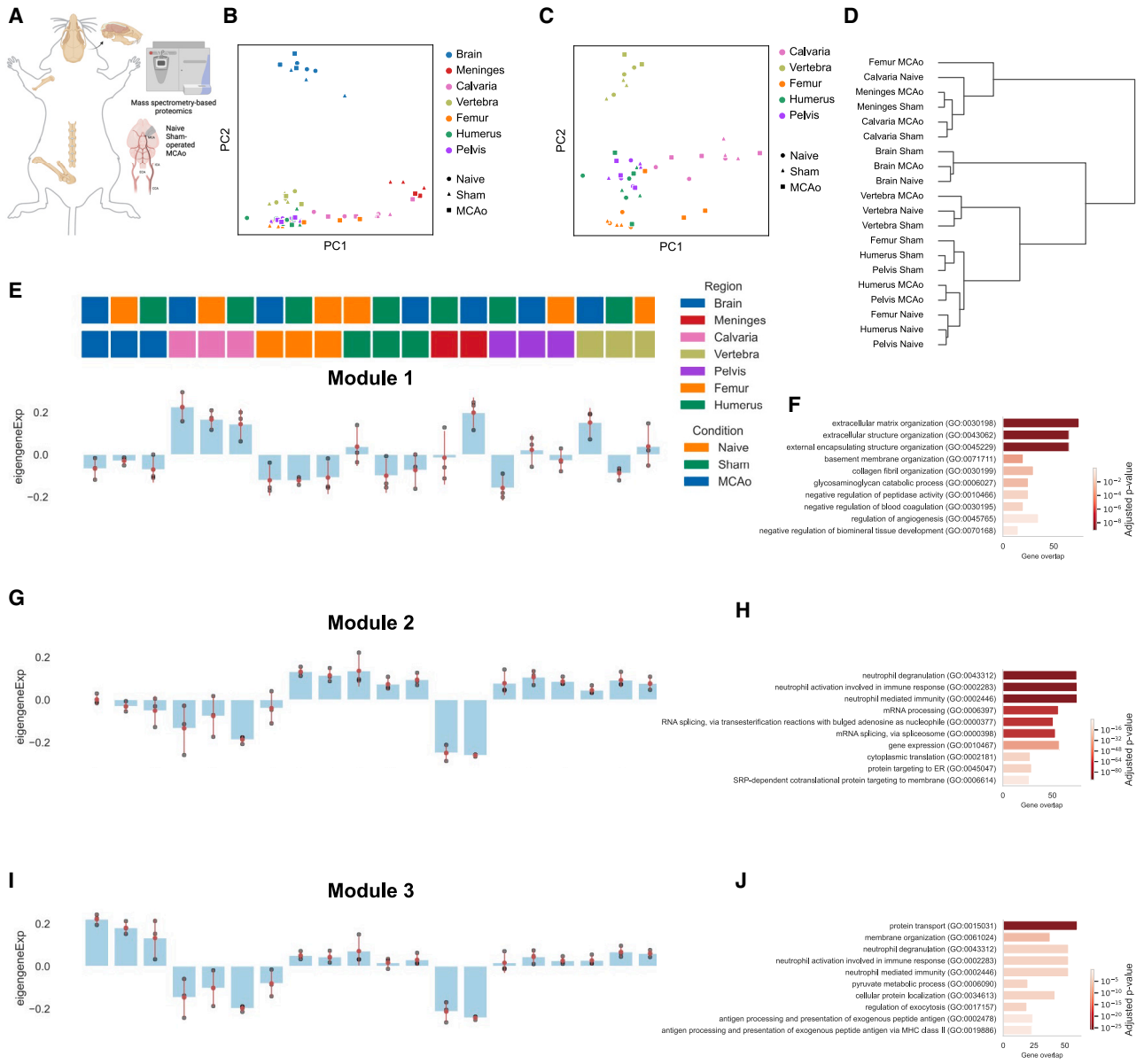

Figure 3. Proteomics identifies protein modules that characterize inter-bone expression differences

(A) Illustration of the experimental pipeline is shown: mouse calvaria, humerus, vertebra, pelvis, and femur from three animals were collected to perform mass spectrometry in three different conditions, that is, naive, sham-operated, and MCAo.

(B and C) Principal component analysis (PCA) of (B) six bones, dura, and brain and (C) six bones in naive, sham, and MCAo conditions.

(D) Dendrogram demonstrates the relation among bones and conditions.

(E–J) Protein expression modules identified by WGCNA among bones, brain, and meninges. Module distributions are shown in the left-hand panels the corresponding GO terms in the right-hand panels (n = 3 independent samples each for bones and brain for all conditions, n = 3 for meninges MCAo and sham conditions).

See also Figure S5.

Principal component analysis (PCA) showed segregation of the brain and meninges from bones. Calvaria samples were distributed over the PC1, clustering closest to the meninges (Figure 3B) and closer to femur in MCAo conditions (Figure 3C). We did not observe any clustering based on conditions (Figures 3B and 3C). On comparing the calvaria's proteomic signature in sham and MCAo, we found 28 upregulated and 6 downregulated proteins (Figure S5E; Table S2, tab 10). Prominent examples include complement proteins such as CFB, which regulates B cell differentiation[46] and cell adhesion factors including CD9[47] and NID2[48] (Table S2, tab 10).

A matrix plot and a dendrogram confirmed the segregation of calvaria, meninges, and femur MCAo samples from all other bones across all conditions (Figures 3D, S5C, and S5D). We

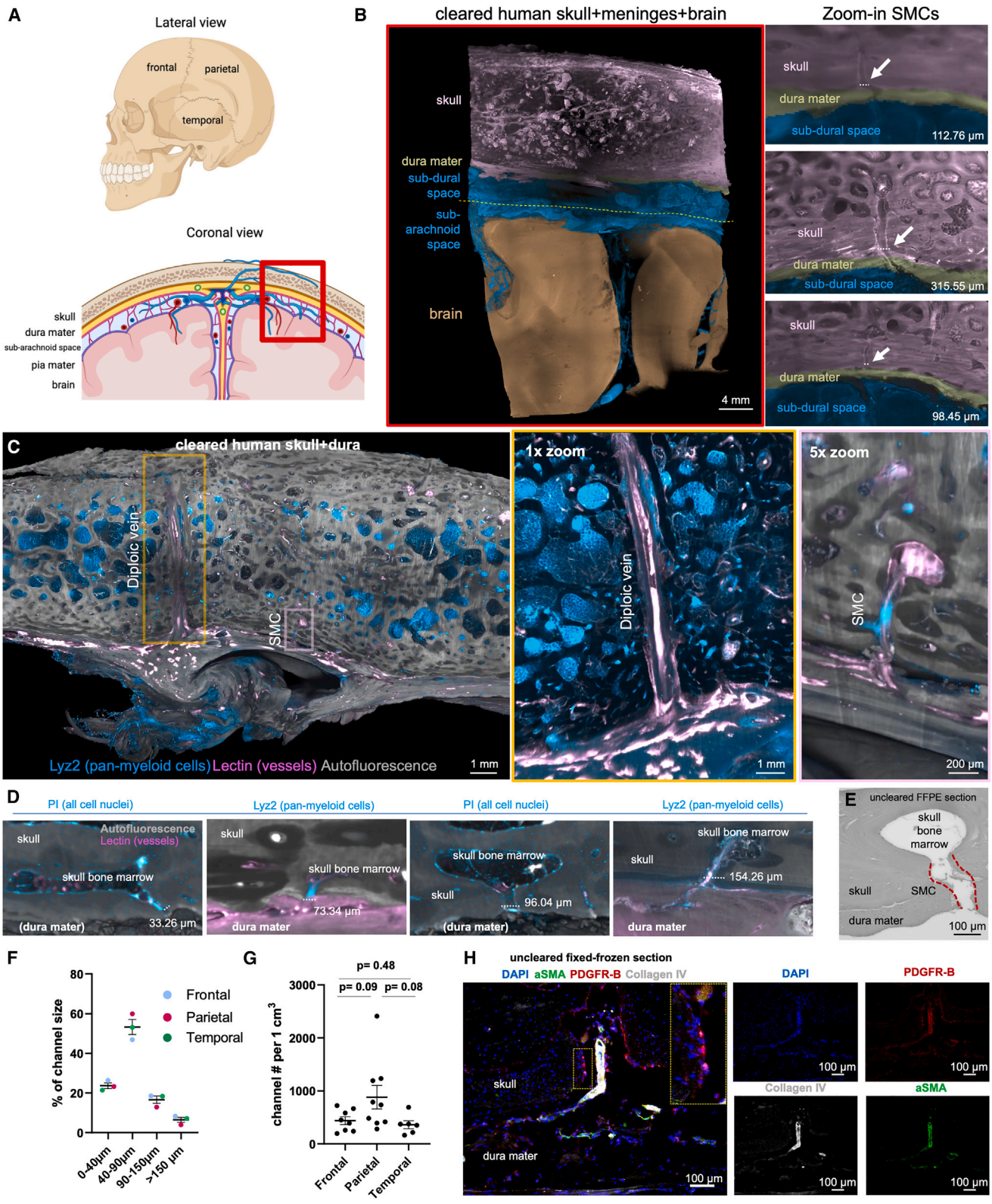

(legend on next page)

found 45 upregulated proteins in the calvaria in naive condition ($p < 0.005$, log fold change [LFC] > 1), 65 proteins in sham, and 67 proteins in MCAo compared with other bones, whereas we identified a higher number of downregulated proteins (Figures S5F–S5K; Table S2, tabs 1, 4, and 7).

Using weighted correlation network analysis (WGCNA), we identified three modules with calvaria-specific differences. Module 1 was (mostly related to extracellular matrix [ECM] organization) increased in calvaria samples for all three conditions as well as meninges MCAo and vertebra MCAo samples (Figures 3E and 3F). Module 2 (mainly involved in neutrophil degranulation and immunity, and mRNA processing) showed a decreased expression in brain, calvaria, and meninges (Figures 3G and 3H). Module 3 was also downregulated in calvaria and meninges (Figure 3I) with GO terms related to protein transport, neutrophil degranulation, and immune pathways (Figure 3J). Comparing the protein with scRNA-seq data for module 2, we found a Spearman correlation value of R = 0.42, suggesting that this phenomenon is recapitulated on the RNA level[49] (Figure S5L). Our proteomic analysis confirms neutrophils as a major source of the differences between calvaria and the other bones.

Characterization of SMCs in human samples

We next explored the relevance of our findings in humans. First, we characterized SMCs using tissue clearing and light-sheet fluorescent imaging in 23 skull + dura mater samples in frontal, parietal, and temporal regions coming from seven human skulls (Figures 4A and S5M). We used immunofluorescence to label myeloid cells (LYZ2) and macrophages (IBA1) (Figures S5N and S5O), PI to label cell nuclei, and lectin to label vasculature (Figures 4B–4D). Human SMCs most often transverse the dura mater, opening to the sub-dural space underneath to arachnoid granulations[50] (Figure 4B; Videos S2 and S3). We confirmed that SMCs transverse the dura using bright-field imaging of uncleared formalin-fixed paraffin-embedded (FFPE) sections of decalcified human skull (Figure 4E).

We quantified more than 500 SMCs and found that they are mostly 40–90 μm wide (Figures 4F and S5P) as suggested.[4] Some SMCs were >150 μm, which were often surrounding big blood vessels and occasionally diploic veins (Figure 4C; Video S3). Region-based analysis did not reveal significant differences (Figures 4G and S5Q). We next used graph analysis and found the average shortest path length from a bone marrow cavity to SMC as ~3,000 μm, and the average radius along the shortest path as ~37 μm (Figure S5R). Furthermore, using histology on skull + dura mater, we found that PDGFR-B signal was present both at the vessels and at the SMC lumen (Figure 4H). This suggests that the SMC lumen is lined with a layer of fibroblastic cells, known antigen-presenting cells,[51] that might potentiate cerebrospinal fluid (CSF) sampling already at the beginning of the SMCs.

Finally, we performed scanning electron microscopy on human skull + dura mater (Figures S5S–S5W). We found similar structures as we identified using tissue clearing, immunohistochemistry (IHC), and as previously shown using microCT[4] that were filled with fat/lipids. The SMC structure showed immune cells within, in addition to a fibroblastic cell layer (Figures S5S–S5W) as suggested by histology (Figure 4H). These findings suggest that human SMCs might be filled with fat, unlike those of mice,[4] allowing immune trafficking while serving as an energy source to hematopoietic stem cells.[52–54]

Human skull proteome is distinct from vertebra and pelvis

Next, we obtained 20 post-mortem human skull, vertebra, and pelvis samples from two independent autopsy centers for proteomic analysis (Figures 5A and S6A). We detected 8,526 protein groups before and 5,320 protein groups after filtering (Figure 5B).

The highest number of uniquely detected proteins was in the skull with 105 unique proteins (Figure 5C). GO analysis revealed 27 skull-specific synapse and synaptic signaling related terms. For example, the term "chemical synaptic transmission" was represented by proteins such as SYP, SYN3, SNAP25, and SLC17A7 (Figure 5D; Table S2, tabs 14–16). Mouse proteome also showed a positive trend in *Syp* and *Snap25* proteins in the calvaria (Figure S6B). This might suggest that skull is more involved in neuropeptide or neurotransmitter-based communication, compared with other bones.[55]

The PC1 of PCA plot depicts the distinct nature of the skull, whereas PC2 demonstrates that the skull samples have a larger variance (Figure 5E). Euclidian distance between pairs showed the differences between skull and pelvis to be the highest and that between vertebra and pelvis to be the lowest (Figure 5F). Bone proteome differences were not driven by age, post-mortem interval, sex, or cause of death (Figure S6C). On the global proteomic scale, we observed a strong downregulation of proteins in the skull compared with other bones, few DE proteins between the vertebra and the other bones, and a strong

Figure 4. Tissue clearing enables a comprehensive characterization of human skull-meninges connections

(A) Frontal, parietal, and temporal regions of the skull and coronal view depicting the meningeal layers and the brain.

(B) Representative light-sheet microscopy image of cleared tissue corresponding to the red box in (A). The right panels show skull-meninges channels connecting the skull bone marrow to the sub-dural space and to the dura mater.

(C) Representative skull piece cleared and imaged for SMC quantification in different regions of the human skull. Diploic vein and an exemplary SMC are shown.

(D) Representative skull-meninges-channels in different sizes: ~33, ~73, ~96, and ~154 μm. Autofluorescence in gray, lectin in magenta. Left panels are labeled with PI (cyan) and right panels with LYZ2 (cyan). Dura mater in some panels is not preserved in (D).

(E) Human SMC example from 1 μm thick FFPE embedded skull-dura section.

(F) Quantification for % of channel size in frontal, parietal, and temporal regions. Data represented as ± SEM.

(G) Quantification for annotated channel numbers, normalized to 1 cm^3 (22 region of interests (ROIs) in total, >500 channels, from seven post-mortem samples, frontal vs. parietal $p = 0.09$, parietal vs. temporal $p = 0.08$, and frontal vs. temporal $p = 0.48$). Data represented as ±SEM.

(H) Human SMC example with an artery passing to the skull from 8 μm thick fixed-frozen skull-dura section labeled with DAPI (blue), aSMA (green), PDGFR-B (red), and CollagenIV (gray).

See also Figure S5.

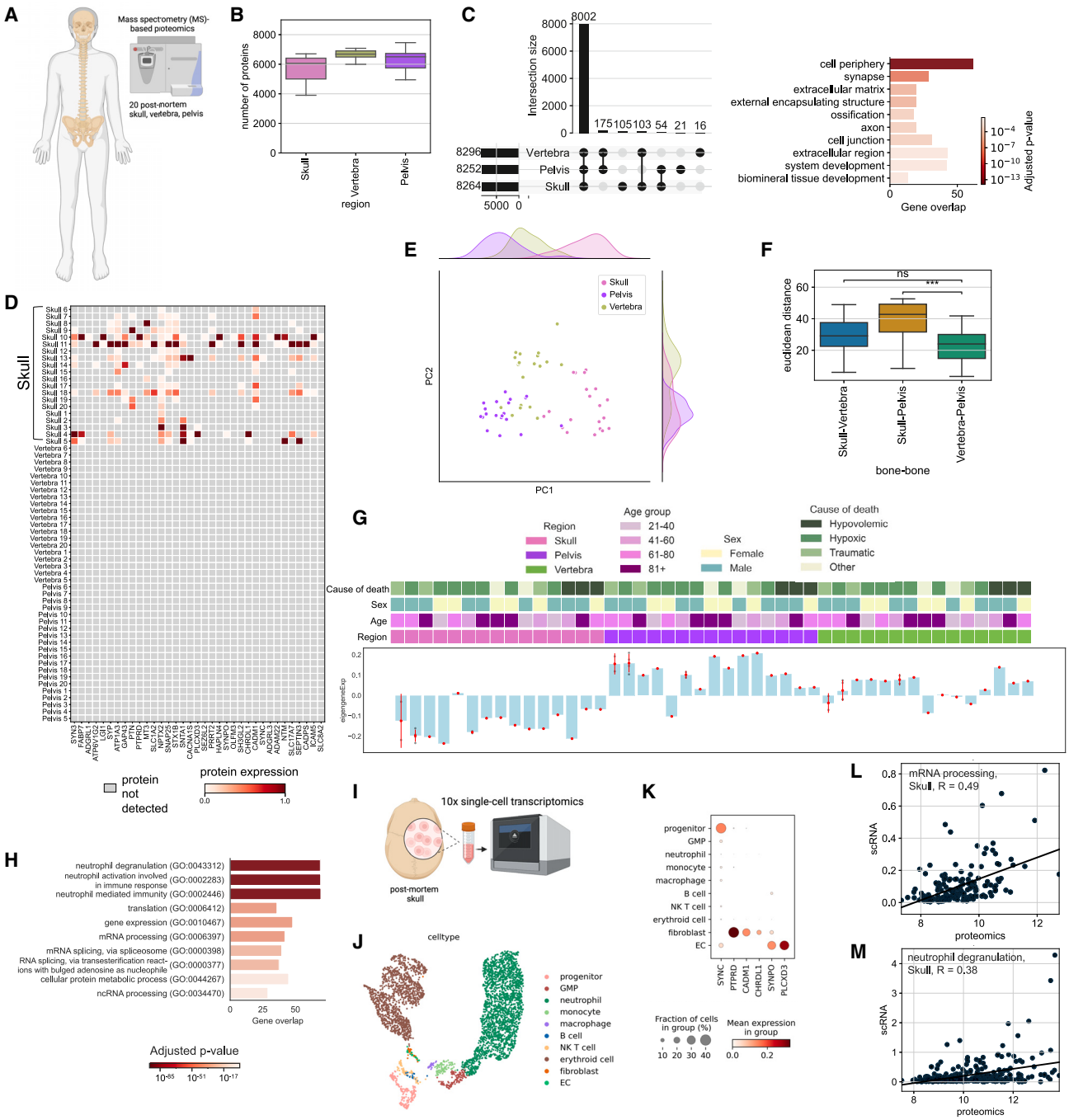

Figure 5. Human bones differentially express distinct protein modules

(A) Illustration of the experimental pipeline, 60 bones in total were collected to perform mass spectrometry-based proteomics on 20 skull, 20 vertebra, and 20 pelvis.

(B) The number of proteins detected from each bone is shown with a boxplot.

(C) The number of common proteins and unique proteins detected from different bones are shown with an upset plot. GO terms associated with unique skull proteins are shown at the bottom.

(D) Expression levels of a selection of proteins belonging to GO terms related to synapse term that were detected in more than half of the skull samples uniquely.

(E) Principal component analysis of the three bones analyzed.

(F) Boxplot depicts the Euclidean distances between pairs of bones using the first 2 principal components. (p = 2.862e-04 for skull-pelvis vs. vertebra-pelvis, p value =2.862e-04 for skull-pelvis vs. vertebra-pelvis)

(G) WGCNA among bones reveal one significant module where calvaria genes are downregulated compared with two other bones with some exceptions. Biggest source of variance is the bone type.

(legend continued on next page)

upregulation of proteins in the pelvis (Figures S6D–S6I; Table S2, tabs 19–27).

Cellular processes such as translation, metabolism of RNA, and leukocyte activation-related terms were downregulated in the calvaria, whereas ECM organization-related terms were upregulated (Figure S6E; Table S2, tab 20). These differences are in line with our mouse scRNA-seq dataset, e.g., in the collagens *Col1a1* and *Col1a2* in naive ($p = 0.0004$ and $p = 0.0016$, respectively) and MCAo ($p = 0.00005$ and $p = 0.0002$, respectively) conditions. In mice, *COL1A1* and *COL1A2* were also among the top DE proteins in the calvaria (Table S2, tabs 1, 4, and 7). ECM strongly influences immune cell functions,[56] suggesting that the functional role of ECM differences should be investigated further. Additionally, the most abundant protein in our human skull dataset was *COL1A1*, a structural protein encapsulating blood vessels in bone marrow,[57] suggesting differences in the vascular organization of the skull bone marrow.

Using WGCNA, we identified a module that was downregulated in the skull samples of the human proteomics dataset (Figure 5G), whose GO terms were very similar to mouse proteome modules: most prominently neutrophil degranulation and mRNA processing (Figure 5H).

Overall, two notable groups of proteins showed interesting expression profiles between the bones. First, we identified several proteins unique to the skull that relate to synapses, and second, a downregulation of neutrophil degranulation and mRNA processing in the skull. To test how these differences would translate into the RNA level, we performed scRNA-seq of one human post-mortem skull (Figure 5I). After annotating 10 cell types (Figures 5J and S6J), we assessed the presence and expression levels of unique skull proteins (Figure 5C). Six of the 256 unique synapse-relevant genes were detected in the dataset, mostly in fibroblasts (Figure 5K). This allowed us to rule out immune cell expression as a source of the synapse-related terms. We speculate that the difference in synaptic protein levels could either hint at a denser or more active innervation of the skull bone marrow or it might reflect the immune surveillance of the brain that leads to a transport of peptides from brain to the skull.

The human scRNA-seq data supported the presence of the mRNA processing and neutrophil degranulation modules. Proteomics data and scRNA-seq data correlated with R values of $R = 0.49$ and $R = 0.38$ for the genes in these GO terms, respectively (Figures 5L and 5M). This correlation from both mouse and human datasets suggests a consistently low neutrophil degranulation and lower mRNA processing, based on previously reported correlations between mRNA-protein levels.[58,59] Thus, we conclude that the human skull differs from other bones at both transcriptomic and proteomic levels.

TSPO signal in the skull is associated with inflammatory, ischemic, and neurodegenerative CNS diseases

Next, we examined the reaction of the skull to different neurological disorders in patients. TSPO is a protein markedly upregulated in the brain during neuroinflammation and is used as a PET biomarker.[60,61] We also found significantly higher *Tspo* RNA levels in the calvaria in injury compared with naive mice (Figure S7A), especially in neutrophils. To confirm the ability of PET imaging to measure skull-specific TSPO-PET signals, we performed imaging on three living mice and immediately isolated the skulls. The isolated skulls had a strong association with the skull signal in the live animals confirming the skull origin of the TSPO signal (Figure S7B).

Next, we assessed TSPO-PET signals in 50 patients belonging to the AD continuum, 43 patients with 4-repeat tauopathies (4RTs),[62] 10 patients in the post-acute phase of stroke, 15 patients with relapsing-remitting multiple sclerosis (RRMS),[63] and 14 patients with primary progressive multiple sclerosis (PPMS) (Table S3, tab 1). We used 3D surface projections on a CT template to show substantial relative TSPO-PET differences in patients belonging to the AD continuum compared with healthy controls (Figure 6A). We found a clear increase in TSPO-PET signals in calvaria regions adjacent to the frontal, parietal, and motor cortices of patients belonging to the AD continuum (Figures 6A–6F; Video S4). Similarly, elevated skull inflammation was observed in each cohort of patients with distinct patterns in different pathological conditions (Figures 6B–6F), e.g., a prominent temporal pole signal in stroke and multiple sclerosis patients (Figures 6B and 6E), in the skull base in RRMS and PPMS patients (Figure 6D), and in the skull adjacent to the prefrontal cortex and the motor area in 4RT patients (Figures 6C and 6D). In 5xFAD mouse model of AD, we observed a similar TSPO signal elevation in the fronto-parietal and temporal regions compared with controls (Figures S7C and S7D). These results indicate that TSPO-PET imaging of the skull can reveal distinct signal patterns in inflammatory, ischemic, and degenerative CNS conditions, at least at the cohort level.

In the AD continuum patients, the overall TSPO-PET signal was increased in females over males and was negatively associated with age in patients with AD (Figures S7E and S7F). We did not find statistically significant differences between male and female patients in the 4RT, stroke, and PPMS cohorts, although RRMS showed increased TSPO tracer uptake in males (Figure S7E). We did not find significant correlations with AD severity based on cognitive tests such as mini-mental-state examination (MMSE), the Consortium to Establish a Registry for AD (CERAD) neuropsychological test battery, and the clinical dementia rating (CDR) scale (Figure S7G). There were also no significant associations with specific clinical stages of AD such as in the

(H) GO terms from the module of skull downregulated proteins.
(I) Single-cell sequencing of post-mortem skull sample illustration.
(J) UMAP of single-cell sequencing of post-mortem skull sample (n = 1).
(K) Expression of unique skull detected proteins in the scRNA-seq data.
(L) Correlation plot of the module from (G), mRNA processing GO term. Protein expression vs. scRNA-seq. Spearman correlation, $R = 0.49$, $p < 0.0001$.
(M) Correlation plot of the module from (G), neutrophil degranulation GO term protein expression. Protein expression vs. scRNA-seq. Spearman correlation, $R = 0.38$, $p < 0.0001$.
See also Figure S6.

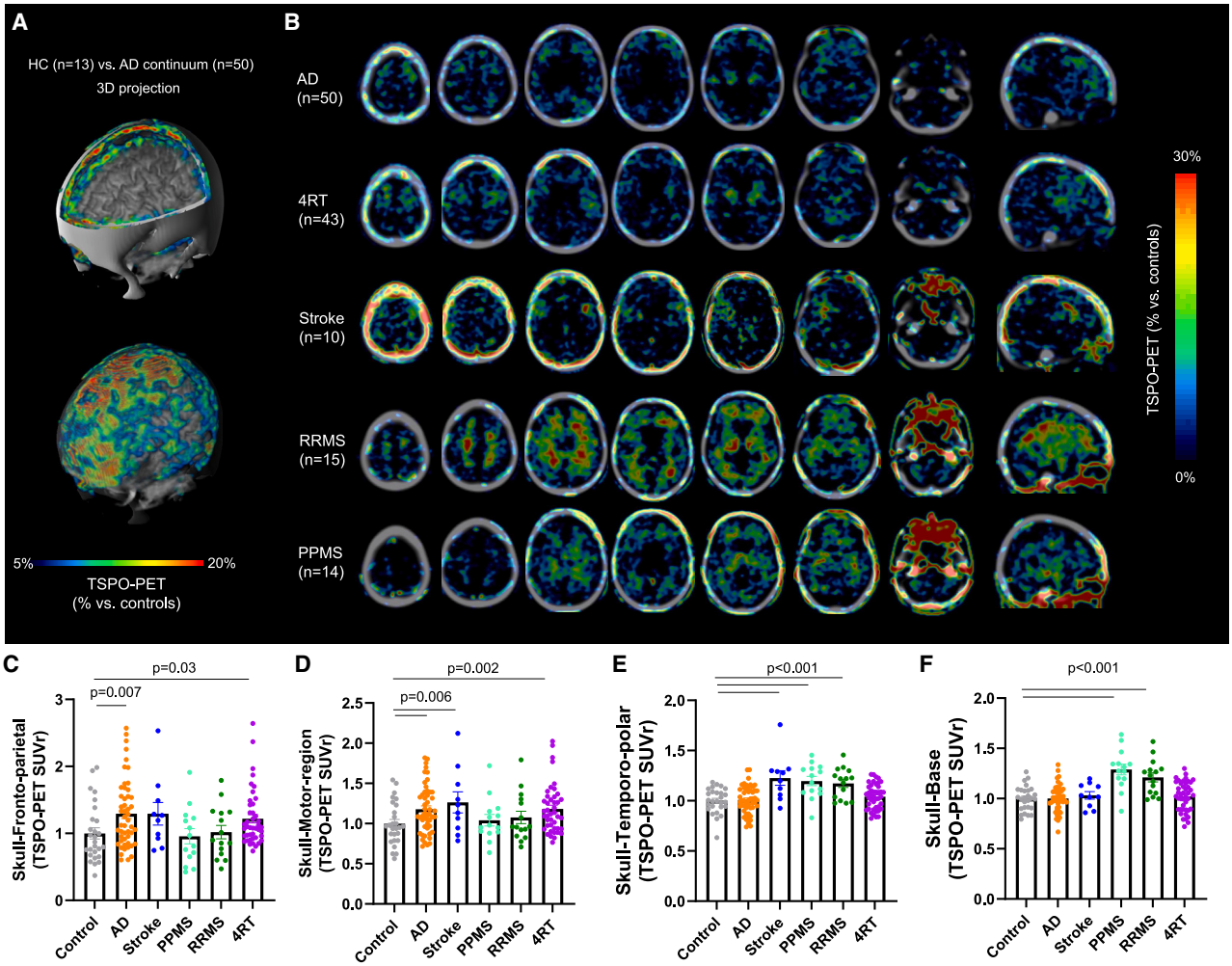

Figure 6. Distinct TSPO uptake patterns are observed in the skull of patients with inflammatory, ischemic, and degenerative CNS diseases

(A) 3D surface projection (triple fusion with CT and MRI templates; quadrant cut [top]; transparent CT [bottom] displaying increased activity within skull) shows %-TSPO-PET differences between patients with AD and healthy controls at the group level.

(B) Average TSPO-PET signal in Alzheimer's disease (AD), stroke, primary progressive multiple sclerosis (PPMS), relapsing-remitting multiple sclerosis (RRMS), and 4-repeat tauopathy (4RT) patients.

(C–F) TSPO-PET signal quantifications in skull regions adjacent to different brain regions: (C) fronto-parietal area ($p = 0.007$ for control vs. AD, and $p = 0.03$ for control vs. 4RT), (D) motor area ($p = 0.006$ for control vs. AD and stroke, and $p = 0.002$ for control vs. 4RT), (E) temporopolar area ($p < 0.001$ for control vs. stroke, PPMS, and RRMS), and (F) skull base ($p < 0.001$ for control vs. PPMS and RRMS). Data represented as ±SEM. One-way ANOVA with Bonferroni post hoc correction (see STAR Methods for details). Data were normalized as described in the STAR Methods. Significant differences of disease vs. controls are indicated. Pairwise comparisons of all groups can be found in Table S3.

See also Figure S7.

comparison of the prodromal stage characterized by subjective cognitive decline (SCD) or mild cognitive impairment (MCI) and the AD dementia stage (Figure S7H). Early and late clinical AD subgroups displayed a similar increase in the calvaria TSPO-PET signal (Figures S7G and S7H), suggesting that skull inflammation occurs during all stages of the AD continuum.

Notably, a significant correlation between the TSPO-PET signals in the calvaria and the brain was only observed in Braak stage VI regions, which can suggest an increasing skull inflammation with advanced tau spread (Figure S7I). TSPO-PET levels in the calvaria were associated with decreased β-amyloid$_{42}$ but not β-amyloid$_{40}$ concentration in CSF (Figures S7J and S7K). Lower β-amyloid$_{42}$ in CSF is associated with more fibrillar amyloid deposits in the brain,[64] suggesting that β-amyloid is also a trigger for increasing skull inflammation. By comparison, the C2 bone of the vertebra had no significant increase compared with controls in any of our cohorts (Figure S7L).

Next, we performed longitudinal analysis on patients with stroke and AD. Our stroke patients were scanned again 3 months after the stroke, whereas patients with AD were imaged 18 months after their baseline scan. Time points were chosen based on clinical necessity. On comparing 13 patients with AD

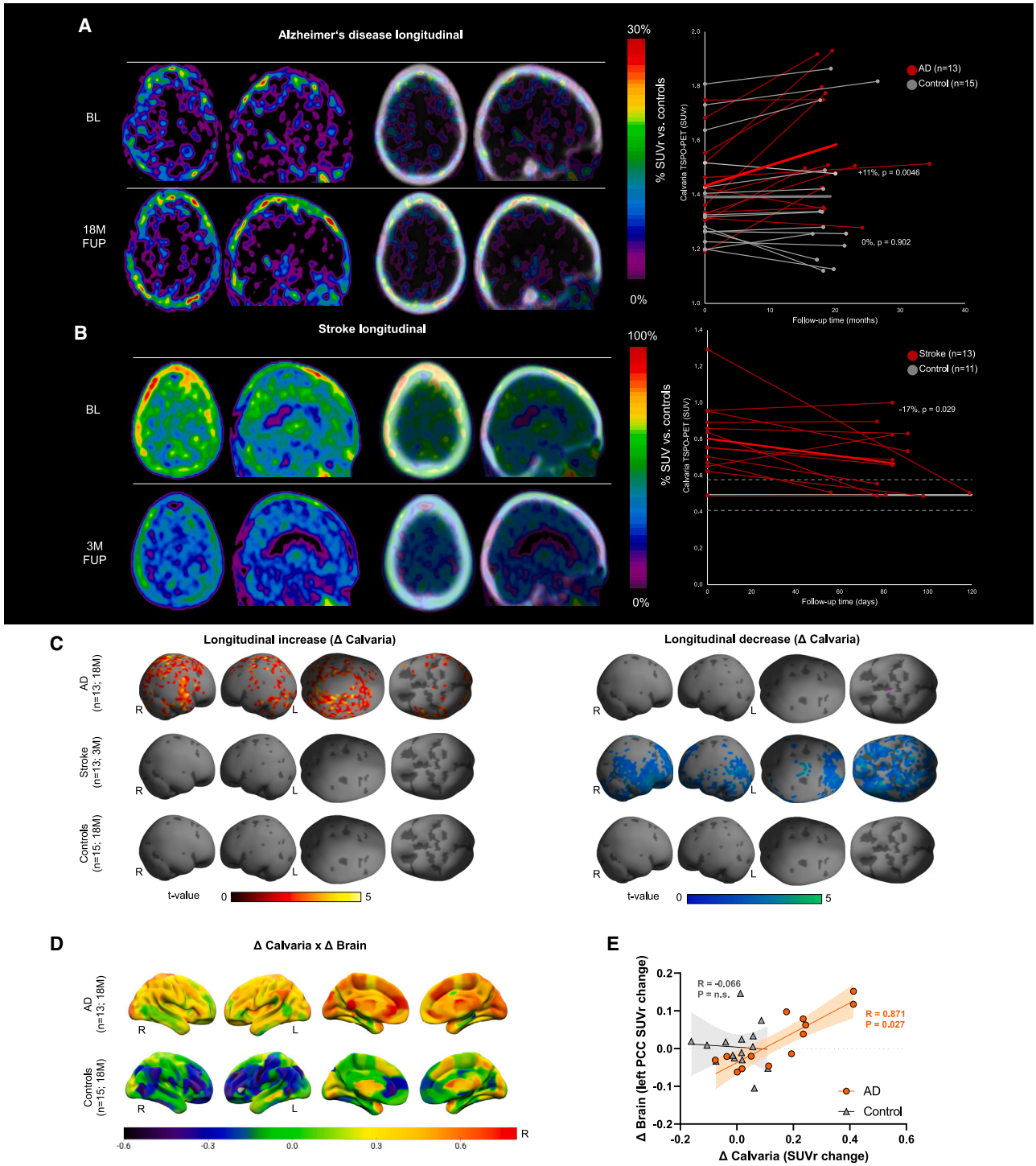

Figure 7. Serial calvaria TSPO-PET imaging of patients with Alzheimer's disease and stroke

(A and B) Axial and sagittal slices show %PET difference images of patients with Alzheimer's disease (AD, n = 13, A, +11%, p = 0.0046 in AD vs. 0%, p = 0.902 in controls) and stroke (n = 13, B, -17%, p = 0.029 in stroke) against age-matched healthy controls (normalized as described in the STAR Methods). Controls in (A) (n = 15) were imaged serially and controls in (B) (n = 11) were imaged at a single time point. %PET difference images are depicted with and without CT overlay. Right panels show individual time courses of calvaria TSPO-PET signals of (A) patients with Alzheimer's disease and healthy controls at a median follow-up

(legend continued on next page)

with 15 serially imaged age-matched healthy controls, we found, on average, an 11% increase in the skull TSPO-PET signal in patients with AD ($p = 0.0046$, paired t test), whereas healthy controls revealed no change ($p = 0.902$, paired t test, Figure 7A). By contrast, we observed a 17% decrease ($p = 0.029$, paired t test) in the skull TSPO-PET signal of stroke patients 3 months after the onset of their stroke (13 stroke patients, 11 controls) (Figure 7B).

After normalization (see STAR Methods), we generated surface projections to reflect the pattern of longitudinal TSPO-PET changes by statistical parametric mapping (SPM) (voxels with $p < 0.05$, uncorrected for multiple comparisons) (Figure 7C) on SPM12 skull surface template. We observed that signal increases in patients with AD were mainly observed in areas highly relevant to AD pathology such as the skull covering the temporal and parietal cortices[65] and were also in line with the regions we report as significantly higher in the baseline condition, i.e., motor area and fronto-parietal cortex (Figures 6C and 6D). In stroke patients, we observed a longitudinal decrease in the whole skull without specific regional preferences (Figure 7C).

We correlated TSPO-PET changes in 246 brain regions of the Brainnetome Atlas[66] with the overall skull TSPO-PET signal changes in patients with AD and found that regional increases of microglial activation in the brain are correlated with progressive overall skull inflammation (Figure 7D). This association was found for brain regions highly relevant to AD pathology, namely the posterior cingulate cortex (PCC), which remained statistically significant even after strict false discovery rate (FDR) correction for multiple comparisons (Figure 7E). Only weak correlations were found in controls (Figure 7D). These results suggest that skull responds to brain inflammation in AD and may serve as a proxy for monitoring neuroinflammation in humans.

DISCUSSION

Neuroinflammation is a significant factor in many CNS disorders. Recent findings suggest that studying the connections between the dura mater and neighboring calvaria marrow could provide insights into brain inflammation. Observing cells and molecules specifically associated with the calvaria-meninges-brain axis could be an effective way to monitor and understand this process.

Our study shows that there is a clear difference between the marrow cells suggesting localized functions for different bones. Our human proteomics analysis confirmed that human skull has a distinct molecular profile as in mice. As these proteomics data were obtained from post-mortem individuals with a wide range of ages and pathologies, it suggests that the skull bone marrow remains distinct across a wide range of conditions. Moreover, the increased levels of brain-related, especially synaptic proteins, in the human skull suggests that communication along the skull-meninges-brain axis might occur in both directions.[55]

Overall, our extensive data on human SMCs using tissue clearing of large samples of human skulls with attached dura mater suggest that they facilitate immune cell trafficking between the skull and meningeal surface of the brain similar to detailed observations provided in different studies in mice.[2,4–6] Although the disruption of the blood-brain barrier after pathological conditions such as stroke as well as the infiltrating immune cells through blood has been well-documented,[12,67,68] it is currently still unclear under which conditions and what fraction of immune cells reach the meninges or to the parenchyma from the calvaria compared with other routes.[6,12,69]

Several studies demonstrated the clinical utility of TSPO-PET imaging in neurological diseases such as AD, Huntington's disease (HD), amyotrophic lateral sclerosis, Parkinson's disease, multiple sclerosis, and migraine.[70,71] The correlations between brain and skull inflammation signal we observed with a third-generation TSPO-PET ligand [^{18}F]GE-180[72] suggest that the use of skull imaging for the early diagnosis and/or monitoring of brain pathologies should be further investigated. However, given the limited disease specificity of the TSPO signal, it is likely that different contrast agents and imaging modalities will be needed for clinical applications. Our data support the notion of chronic inflammation in patients with AD[73,74] vs. resolving inflammation in stroke patients after acute trauma.[75,76] As calvaria cells are localized very close to the surface, it could be easier and faster to image it by different modalities, for example, optoacoustic imaging technologies in the future, which are portable and less costly compared with MRI/PET imaging and could provide early point-of-care diagnosis.[77]

TSPO is strongly upregulated in microglia and astrocytes upon activation and is also expressed on infiltrating macrophages in the brain.[60] However, its sources outside the brain are less understood as many immune cell types including neutrophils express TSPO.[78,79] The increased cell numbers in the skull marrow in response to injury also suggest a mechanism for the increase in TSPO signals seen in mouse and human data for various diseases, although more detailed studies are needed to establish the sources of signal increase for each condition.[80,81]

Our data suggest that different bones in the body have distinct molecular profiles. Notably, the response of the calvaria to neurological pathologies is different from other bones, indicating

interval of 18 months and (B) patients with stroke at a median follow-up interval of 84 days. Mean (thick line) and standard deviation (dashed lines) of calvaria TSPO-PET.

(C) Surface projections show statistical parametric mapping (SPM) of longitudinal TSPO-PET changes (left: increases, hot/right: decreases, cold) of patients with AD, patients with stroke, and healthy controls. Voxels with $p < 0.05$ (t value threshold 1.78, uncorrected for multiple comparisons) are projected on the SPM12 skull surface template.

(D) Brain surface projections show regional correlations (Pearson's correlation coefficient, R) of longitudinal TSPO-PET changes in calvaria with longitudinal TSPO-PET changes in brain of patients with AD and healthy controls.

(E) Correlation between calvaria and brain TSPO-PET changes in the left posterior cingulate cortex that survived false discovery rate correction for multiple comparison of 246 brain regions ($R = 0.871$, $p = 0.027$ in AD vs. $R = -0.066$, p = n.s. in controls).

that the skull may be useful for monitoring and potentially controlling inflammation in various brain pathologies in the future.

Limitations of the study

Our data have limitations, despite the rich data on molecular analysis and imaging in mice and humans. We could not statistically compare transcriptomics differences in mice and humans due to the limited number of samples. We only focused on a selected number of bones in mice and humans. Also, for ethical reasons, we could not obtain bone samples from healthy humans for comparison with pathological states. Different causes of death might also be affecting the molecular profile of the samples.

Although our data provide leads for the molecules that might regulate the skull's response to disease, only future mechanistic studies can clarify their exact involvement. Future work must explore inter-individual differences and gene expression profile evolution over time in mice. Additional characterization of the specific contribution of skull immune cells compared with other bones and exact routes of trafficking is necessary to understand the neuroimmune axis. Although our study suggested B cell, T cell, and myeloid cell trafficking, it would be interesting to elucidate specific cell-type dynamics in certain disease cases. Finally, our detailed demonstration of skull inflammation in diverse diseases in humans suggests that it can be used for diagnosing or monitoring diseases in the future, but detailed clinical studies are needed to explore its clinical utility.

STAR★METHODS

Detailed methods are provided in the online version of this paper and include the following:

- KEY RESOURCES TABLE
- RESOURCE AVAILABILITY
  - Lead contact
  - Materials availability
  - Data and code availability
- EXPERIMENTAL MODEL AND STUDY PARTICIPANT DETAILS
  - Animals
  - Human samples and participants
- METHOD DETAILS
  - Middle cerebral artery occlusion (MCAo) model
  - Skull preparation for chronic imaging
  - Live Imaging
  - Behavioral experiments - Neuroscore
  - Perfusion, fixation and tissue preparation
  - vDISCO whole-body immunostaining, PI labeling and clearing
  - *Nr4a1* labeling and clearing of mice bones with SHANEL
  - Human skull labeling and clearing with SHANEL
  - Light sheet microscopy imaging
  - Reconstruction of whole-mouse body and mouse head scans
  - Fixed-formalin paraffin embedding, sectioning and H&E staining
  - Human fixed frozen sections, immunohistochemistry and imaging
  - Single-cell isolation for scRNAseq and proteomics
  - Cell sorting and plate-based bulk RNA-sequencing
  - Single-cell suspension isolation from the human bones for proteomics
  - Single-cell isolation from human skull for scRNAseq
  - scRNA sequencing – 10x Genomics
  - Sample preparation for bulk RNA isolation
  - Bulk RNA isolation, library preparation and sequencing
  - Flow cytometry
  - Multiplexed RNAscope smFISH
  - High-resolution imaging
  - Image stitching
  - Scanning electron microscopy
  - Proteomics Sample Preparation
  - Liquid chromatography and mass spectrometry (LC-MS/MS)
  - Proteomics data processing
  - Small animal PET/MRI acquisition
  - Human TSPO-PET imaging acquisition
- QUANTIFICATION AND STATISTICAL ANALYSIS
  - Single-cell RNA data analysis
  - Bulk RNA data analysis for 5xFAD dataset
  - Bulk RNA data analysis for MCAo dataset
  - Statistical analysis of KikGR animals
  - Image Analysis
  - Proteomics data analysis
  - Small animal PET/MRI analysis
  - Human TSPO-PET imaging analysis
  - Statistics for human TSPO-PET imaging
- ADDITIONAL RESOURCES

SUPPLEMENTAL INFORMATION

Supplemental information can be found online at https://doi.org/10.1016/j.cell.2023.07.009.

ACKNOWLEDGMENTS

This project has received funding from the European Research Council (ERC) under the European Union's Horizon 2020 research and innovation program (ERC CoG no. 865323 to A.E. and ERC-StG 802305 to A.L.) and Nomis Foundation (A.E.). This work was further supported by Vascular Dementia Research Foundation, Deutsche Forschungsgemeinschaft (DFG, German Research Foundation) under Germany's Excellence Strategy within the framework of the Munich Cluster for Systems Neurology (EXC 2145 SyNergy, ID 390857198 and ID 390857198 [C.P.]), grant DI-722/16-1 (project ID: 428668490) and a dedicated grant to M. Brendel. (BR4580/1-1), to I. Khalin (457586042), ICARUS study (FOR 2879, ID 405358801), procurement of the MRI scanner (DFG, INST 409/193-1 FUGG), to N.K. and O.S.C. through Emmy Noether Programme (KR5166/1-1), and to A.E.H. (DFG SFB1444, Project 14, DFG HA5354/12-1). Additionally, C.P. supported by Friedrich-Baur-Stiftung, C.P. and S. Katzdobler. by Lüneburg Heritage Foundation, A.E.H. by the Einstein Foundation Berlin, project A 2019-559, V.G.P. by Novo Nordisk Foundation (Young Investigator Award; NNF21OC0066381), R.P. by the National Institute for Health and Care Research (NIHR) Sheffield Biomedical Research Centre (NIHR203321), and M. Brendel, B.-S.R., and R.P. by the Hirnliga e.V. (Manfred-Strohscheer-Stiftung) and the Alzheimer Forschung Initiative e.V. (project ID 19063p). GE Healthcare made GE-180 cassettes available through an early-access model. The BMBF has supported the work of J.L. by (FKZ: FKZ161L0214B, ClinspectM), J. Schädler and B.O. within the NATON

collaboration of the Network University Medicine (01KX2121) and V.G.P. by eMed Consortia "Fibromap." A.L., Z.I.K., and M.A. are members of the GSN at the University of Munich. We acknowledge SFB-Project CCR1052-A9, the technical support of Core Facilities of Genomics at Helmholtz Munich and Flow cytometry at Biomedical Center Munich. We thank Uta Mamrak for performing MCAo surgeries; Alex Nazlidis for contribution to Figure 1A; Cornelia Niemann, Lucia Rodriguez, and Georg Kislinger for technical assistance for SEM experiments; and Giovanna Palumbo during PET imaging. The graphical abstract and experimental pipeline in Figures 1, 3, 4, and 5 were created with BioRender.com.

AUTHOR CONTRIBUTIONS

Conceptualization and management of whole project, A.E.; methodology, Z.I.K., L.B.K., B.F., B.T., L.R., I.H., and M.N.; software, L.B.K., M.A., M. Büttner, I.H., M.N., M.I.T., and J.C.P.; validation, Z.I.K., L.B.K., S.U., I.H., K.R., and O.A.B.; formal analysis, Z.I.K., L.B.K., M.A., M. Büttner, M. Brendel, N.F., L.M.B., G.B., S.H., J.G., M. Schifferer, A.S., L.H., I.H., M.N., M.I.T., L.L., J.C.P., S.U., S. Kapoor, O.S.C., and N.K.; investigation, Z.I.K., S.U., M. Sterr, I. Kunze, H.L., I.K.D., C.P.M.-J., M. Schifferer, A.S., O.C., L.D.-M., C. Benakis, A.L., P.K., K.R., O.A.B., D.J., M.M., F.O., J. Shrouder, J.R., A.E.H., S.Z., D.K., I. Khalin, N.P., B.F., H.S.B., Z.R., H.M., M.M., K.S., F.H., S.B.-G., O.G., S. Kapoor, O.S.C., N.K., V.W.Y.K., and S.L.; writing – original draft, Z.I.K., S.E., and A.E.; writing – review & editing, Z.I.K., M.E., and A.E.; funding acquisition, A.E.; visualization, Z.I.K., L.B.K., M.A., S.U., L.H., and A.Z.; resources, R.P., M. Brendel, H.S., I.B., C. Braun, C.D., J. Schädler, B.O., V.G.P., N.L.A., M.U., J.G., S. Katzdobler, C.P., A.K., K.B., J.L., C.H., M. Simons, M.D., G.H., J.H., T.K., and M.K.; project administration, Z.I.K.; supervision, F.H., S.E., H.S.B., F.J.T., M.E., and A.E.

DECLARATION OF INTERESTS

M. Brendel received speaker honoraria from GE healthcare, Roche, and Life Molecular Imaging and is an advisor of Life Molecular Imaging. J.H. reports personal fees, research grants, and non-financial support from Merck, Bayer, Novartis, Roche, Biogen, and Celgene and non-financial support of the Guthy-Jackson Charitable Foundation—none in relation to this study. C.P. is inventor in a patent "Oral Phenylbutyrate for Treatment of Human 4-Repeat Tauopathies" (EP 23 156 122.6) filed by LMU Munich. T.K. has received speaker honoraria and/or personal fees for advisory boards from Bayer Healthcare, Teva Pharma, Merck, Novartis, Sanofi/Genzyme, Roche, and Biogen as well as grant support from Novartis and Chugai Pharma—none in relation to this study. M.K. has been on advisory boards for Biogen, medDay Pharmaceuticals, Novartis, and Sanofi; has received grant support from Sanofi and Biogen; and has received speaker fees from Abbvie, Almirall, Biogen, medDay Pharmaceuticals, Merck Serono, Novartis, Roche, Sanofi, and Teva—none in relation to this study. R.P. has received speaker honoraria, research support, and consultancy fees from Janssen, Eli Lilly, Biogen, Wilmar Schwabe, Takeda, Novo Nordisk, and Bayer Healthcare. N.K. has received speaker honoraria from Novartis and Regeneron and research grants from Regeneron—none in relationship to this study. M.I.T., H.S.B., M.N., and A.E. received speaker honoraria from Miltenyi Biotec—none in relation to this study. A.E. is co-founder of Deep Piction and 1X1 Biotech.

INCLUSION AND DIVERSITY

We support inclusive, diverse, and equitable conduct of research. We worked to ensure sex balance in the selection of non-human subjects. We worked to ensure diversity in experimental samples through the selection of the genomic datasets. One or more of the authors of this paper self-identifies as an underrepresented ethnic minority in their field of research or within their geographical location. One or more of the authors of this paper self-identifies as a gender minority in their field of research. One or more of the authors of this paper self-identifies as a member of the LGBTQIA+ community. We avoided "helicopter science" practices by including the participating local contributors from the region where we conducted the research as authors on the paper.

Received: December 6, 2021
Revised: April 24, 2023
Accepted: July 7, 2023
Published: August 9, 2023

REFERENCES

1. Rustenhoven, J., and Kipnis, J. (2022). Brain borders at the central stage of neuroimmunology. Nature *612*, 417–429. https://doi.org/10.1038/s41586-022-05474-7.
2. Cai, R., Pan, C., Ghasemigharagoz, A., Todorov, M.I., Förstera, B., Zhao, S., Bhatia, H.S., Parra-Damas, A., Mrowka, L., Theodorou, D., et al. (2019). Panoptic imaging of transparent mice reveals whole-body neuronal projections and skull–meninges connections. Nat. Neurosci. *22*, 317–327. https://doi.org/10.1038/s41593-018-0301-3.
3. Cai, R., Pan, C., Ghasemigharagoz, A., Todorov, M.I., Förstera, B., Zhao, S., Bhatia, H.S., Mrowka, L., Theodorou, D., Rempfler, M., et al. (2019). Panoptic vDISCO imaging reveals neuronal connectivity, remote trauma effects and meningeal vessels in intact transparent mice. Preprint at bioRxiv. https://doi.org/10.1101/374785v1.
4. Herisson, F., Frodermann, V., Courties, G., Rohde, D., Sun, Y., Vandoorne, K., Wojtkiewicz, G.R., Masson, G.S., Vinegoni, C., Kim, J., et al. (2018). Direct vascular channels connect skull bone marrow and the brain surface enabling myeloid cell migration. Nat. Neurosci. *21*, 1209–1217. https://doi.org/10.1038/s41593-018-0213-2.
5. Cugurra, A., Mamuladze, T., Rustenhoven, J., Dykstra, T., Beroshvili, G., Greenberg, Z.J., Baker, W., Papadopoulos, Z., Drieu, A., Blackburn, S., et al. (2021). Skull and vertebral bone marrow are myeloid cell reservoirs for the meninges and CNS parenchyma. Science *373*, eabf7844. https://doi.org/10.1126/science.abf7844.
6. Brioschi, S., Wang, W.-L., Peng, V., Wang, M., Shchukina, I., Greenberg, Z.J., Bando, J.K., Jaeger, N., Czepielewski, R.S., Swain, A., et al. (2021). Heterogeneity of meningeal B cells reveals a lymphopoietic niche at the CNS borders. Science *373*, eabf9277. https://doi.org/10.1126/science.abf9277.
7. Wang, Y., Chen, D., Xu, D., Huang, C., Xing, R., He, D., and Xu, H. (2021). Early developing B cells undergo negative selection by central nervous system-specific antigens in the meninges. Immunity *54*, 2784–2794.e6. https://doi.org/10.1016/j.immuni.2021.09.016.
8. Rustenhoven, J., Drieu, A., Mamuladze, T., de Lima, K.A., Dykstra, T., Wall, M., Papadopoulos, Z., Kanamori, M., Salvador, A.F., Baker, W., et al. (2021). Functional characterization of the dural sinuses as a neuroimmune interface. Cell *184*, 1000–1016.e27. https://doi.org/10.1016/j.cell.2020.12.040.
9. Van Hove, H., Martens, L., Scheyltjens, I., De Vlaminck, K., Pombo Antunes, A.R., De Prijck, S., Vandamme, N., De Schepper, S., Van Isterdael, G., Scott, C.L., et al. (2019). A single-cell atlas of mouse brain macrophages reveals unique transcriptional identities shaped by ontogeny and tissue environment. Nat. Neurosci. *22*, 1021–1035. https://doi.org/10.1038/s41593-019-0393-4.
10. Mrdjen, D., Pavlovic, A., Hartmann, F.J., Schreiner, B., Utz, S.G., Leung, B.P., Lelios, I., Heppner, F.L., Kipnis, J., Merkler, D., et al. (2018). High-dimensional single-cell mapping of central nervous system immune cells reveals distinct myeloid subsets in health, aging, and disease. Immunity *48*, 380–395.e6. https://doi.org/10.1016/j.immuni.2018.01.011.
11. Jordão, M.J.C., Sankowski, R., Brendecke, S.M., Sagar, A., Locatelli, G., Tai, Y.-H., Tay, T.L., Schramm, E., Armbruster, S., Hagemeyer, N., et al. (2019). Single-cell profiling identifies myeloid cell subsets with distinct fates during neuroinflammation. Science *363*, eaat7554. https://doi.org/10.1126/science.aat7554.
12. Schafflick, D., Wolbert, J., Heming, M., Thomas, C., Hartlehnert, M., Börsch, A.-L., Ricci, A., Martín-Salamanca, S., Li, X., Lu, I.-N., et al. (2021). Single-cell profiling of CNS border compartment leukocytes reveals that B cells and their progenitors reside in non-diseased meninges.

Nat. Neurosci. *24*, 1225–1234. https://doi.org/10.1038/s41593-021-00880-y.

13. Beuker, C., Schafflick, D., Strecker, J.-K., Heming, M., Li, X., Wolbert, J., Schmidt-Pogoda, A., Thomas, C., Kuhlmann, T., Aranda-Pardos, I., et al. (2022). Stroke induces disease-specific myeloid cells in the brain parenchyma and pia. Nat. Commun. *13*, 945. https://doi.org/10.1038/s41467-022-28593-1.
14. Mazzitelli, J.A., Smyth, L.C.D., Cross, K.A., Dykstra, T., Sun, J., Du, S., Mamuladze, T., Smirnov, I., Rustenhoven, J., and Kipnis, J. (2022). Cerebrospinal fluid regulates skull bone marrow niches via direct access through dural channels. Nat. Neurosci. *25*, 555–560. https://doi.org/10.1038/s41593-022-01029-1.
15. Zaro, B.W., Noh, J.J., Mascetti, V.L., Demeter, J., George, B., Zukowska, M., Gulati, G.S., Sinha, R., Flynn, R.A., Banuelos, A., et al. (2020). Proteomic analysis of young and old mouse hematopoietic stem cells and their progenitors reveals post-transcriptional regulation in stem cells. eLife *9*, e62210. https://doi.org/10.7554/eLife.62210.
16. Ryan, D.G., Knatko, E.V., Casey, A.M., Hukelmann, J.L., Dayalan Naidu, S., Brenes, A.J., Ekkunagul, T., Baker, C., Higgins, M., Tronci, L., et al. (2022). Nrf2 activation reprograms macrophage intermediary metabolism and suppresses the type I interferon response. iScience *25*, 103827. https://doi.org/10.1016/j.isci.2022.103827.
17. Chumak, V., Sielatycka, K., Ciechanowicz, A., Bujko, K., Ratajczak, M.Z., and Kucia, M. (2023). Proteomic analysis of murine bone marrow very small embryonic-like stem cells at steady-state conditions and after in vivo stimulation by nicotinamide and follicle-stimulating factor reflects their germ-lineage origin and multi germ layer differentiation potential. Stem Cell Rev. Rep. *19*, 120–132. https://doi.org/10.1007/s12015-022-10445-6.
18. Guérit, D., Marie, P., Morel, A., Maurin, J., Verollet, C., Raynaud-Messina, B., Urbach, S., and Blangy, A. (2020). Primary myeloid cell proteomics and transcriptomics: importance of β-tubulin isotypes for osteoclast function. J. Cell Sci. *133*, jcs239772. https://doi.org/10.1242/jcs.239772.
19. Andersson, S., Nilsson, K., Fagerberg, L., Hallström, B.M., Sundström, C., Danielsson, A., Edlund, K., Uhlen, M., and Asplund, A. (2014). The transcriptomic and proteomic landscapes of bone marrow and secondary lymphoid tissues. PLoS One *9*, e115911. https://doi.org/10.1371/journal.pone.0115911.
20. Wang, D., Eraslan, B., Wieland, T., Hallström, B., Hopf, T., Zolg, D.P., Zecha, J., Asplund, A., Li, L.H., Meng, C., et al. (2019). A deep proteome and transcriptome abundance atlas of 29 healthy human tissues. Mol. Syst. Biol. *15*, e8503. https://doi.org/10.15252/msb.20188503.
21. Hennrich, M.L., Romanov, N., Horn, P., Jaeger, S., Eckstein, V., Steeples, V., Ye, F., Ding, X., Poisa-Beiro, L., Lai, M.C., et al. (2018). Cell-specific proteome analyses of human bone marrow reveal molecular features of age-dependent functional decline. Nat. Commun. *9*, 4004. https://doi.org/10.1038/s41467-018-06353-4.
22. Tonglin, H., Yanna, Z., Xiaoling, Y., Ruilan, G., and Liming, Y. (2021). Single-cell RNA-seq of bone marrow cells in aplastic anemia. Front. Genet. *12*, 745483.
23. Ho, A.D., Horn, P., Hennrich, M., Jaeger, S., Romanov, N., Ding, X., Bork, P., Aloy, P., and Gavin, A.-C. (2016). Proteomics analysis of cellular network in human bone marrow reveals lineage skewing towards megakaryocytes and decrease in lymphoid development upon aging. Blood *128*, 2658. https://doi.org/10.1182/blood.V128.22.2658.2658.
24. Lourbopoulos, A., Mamrak, U., Roth, S., Balbi, M., Shrouder, J., Liesz, A., Hellal, F., and Plesnila, N. (2017). Inadequate food and water intake determine mortality following stroke in mice. J. Cereb. Blood Flow Metab. *37*, 2084–2097. https://doi.org/10.1177/0271678X16660986.
25. Liesz, A., Dalpke, A., Mracsko, E., Antoine, D.J., Roth, S., Zhou, W., Yang, H., Na, S.Y., Akhisaroglu, M., Fleming, T., et al. (2015). DAMP signaling is a key pathway inducing immune modulation after brain injury. J. Neurosci. *35*, 583–598. https://doi.org/10.1523/JNEUROSCI.2439-14.2015.
26. Roth, S., Yang, J., Cramer, J.V., Malik, R., and Liesz, A. (2021). Detection of cytokine-induced sickness behavior after ischemic stroke by an optimized behavioral assessment battery. Brain Behav. Immun. *91*, 668–672. https://doi.org/10.1016/j.bbi.2020.11.016.
27. Nowotschin, S., and Hadjantonakis, A.-K. (2009). Use of KikGR a photoconvertible green-to-red fluorescent protein for cell labeling and lineage analysis in ES cells and mouse embryos. BMC Dev. Biol. *9*, 49. https://doi.org/10.1186/1471-213X-9-49.
28. Pan, C., Schoppe, O., Parra-Damas, A., Cai, R., Todorov, M.I., Gondi, G., von Neubeck, B., Böğürcü-Seidel, N., Seidel, S., Sleiman, K., et al. (2019). Deep learning reveals cancer metastasis and therapeutic antibody targeting in the entire body. Cell *179*, 1661–1676.e19. https://doi.org/10.1016/j.cell.2019.11.013.
29. Herring, J.A., Elison, W.S., and Tessem, J.S. (2019). Function of Nr4a orphan nuclear receptors in proliferation, apoptosis and fuel utilization across tissues. Cells *8*, 1373. https://doi.org/10.3390/cells8111373.
30. Strecker, J.-K., Liebmann, M., Revenstorff, J., Beuker, C., Schmidt-Pogoda, A., Hucke, S., Vogl, T., Roth, J., Thomas, C., Kuhlmann, T., et al. (2022). The nuclear receptor NR4A1 restrains neutrophil granulocyte mediated brain damage in cerebral ischemia. Preprint at bioRxiv. https://doi.org/10.1101/2022.02.27.482146.
31. Hewett, S.J., Jackman, N.A., and Claycomb, R.J. (2012). Interleukin-1β in central nervous system injury and repair. Eur. J. Neurodegener. Dis. *1*, 195–211.
32. Hellmann, J., Tang, Y., Zhang, M.J., Hai, T., Bhatnagar, A., Srivastava, S., and Spite, M. (2015). Atf3 negatively regulates Ptgs2/Cox2 expression during acute inflammation. Prostaglandins Other Lipid Mediat. *116–117*, 49–56. https://doi.org/10.1016/j.prostaglandins.2015.01.001.
33. Papageorgiou, A.-P., Swinnen, M., Vanhoutte, D., VandenDriessche, T., Chuah, M., Lindner, D., Verhesen, W., de Vries, B., D'hooge, J., Lutgens, E., et al. (2012). Thrombospondin-2 prevents cardiac injury and dysfunction in viral myocarditis through the activation of regulatory T-cells. Cardiovasc. Res. *94*, 115–124. https://doi.org/10.1093/cvr/cvs077.
34. Kim, S.H., Jung, I.R., and Hwang, S.S. (2022). Emerging role of anti-proliferative protein BTG1 and BTG2. BMB Rep. *55*, 380–388. https://doi.org/10.5483/BMBRep.2022.55.8.092.
35. Cibrián, D., and Sánchez-Madrid, F. (2017). CD69: from activation marker to metabolic gatekeeper. Eur. J. Immunol. *47*, 946–953. https://doi.org/10.1002/eji.201646837.
36. MacKenzie, A.E., Lappin, J.E., Taylor, D.L., Nicklin, S.A., and Milligan, G. (2011). GPR35 as a novel therapeutic target. Front. Endocrinol. *2*, 68.
37. Wang, F., Flanagan, J., Su, N., Wang, L.-C., Bui, S., Nielson, A., Wu, X., Vo, H.-T., Ma, X.-J., and Luo, Y. (2012). RNAscope: a novel in situ RNA analysis platform for formalin-fixed, paraffin-embedded tissues. J. Mol. Diagn. *14*, 22–29. https://doi.org/10.1016/j.jmoldx.2011.08.002.
38. Gong, T., Liu, L., Jiang, W., and Zhou, R. (2020). DAMP-sensing receptors in sterile inflammation and inflammatory diseases. Nat. Rev. Immunol. *20*, 95–112. https://doi.org/10.1038/s41577-019-0215-7.
39. Efremova, M., Vento-Tormo, M., Teichmann, S.A., and Vento-Tormo, R. (2020). CellPhoneDB: inferring cell–cell communication from combined expression of multi-subunit ligand–receptor complexes. Nat. Protoc. *15*, 1484–1506. https://doi.org/10.1038/s41596-020-0292-x.
40. Deng, H., Hu, N., Wang, C., Chen, M., and Zhao, M.-H. (2018). Interaction between CD177 and platelet endothelial cell adhesion molecule-1 downregulates membrane-bound proteinase-3 (PR3) expression on neutrophils and attenuates neutrophil activation induced by PR3-ANCA. Arthritis Res. Ther. *20*, 213. https://doi.org/10.1186/s13075-018-1710-0.
41. Farr, L., Ghosh, S., and Moonah, S. (2020). Role of MIF cytokine/CD74 receptor pathway in protecting against injury and promoting repair. Front. Immunol. *11*, 1273. https://doi.org/10.3389/fimmu.2020.01273.
42. La Manno, G., Soldatov, R., Zeisel, A., Braun, E., Hochgerner, H., Petukhov, V., Lidschreiber, K., Kastriti, M.E., Lönnerberg, P., Furlan, A., et al.

(2018). RNA velocity of single cells. Nature *560*, 494–498. https://doi.org/10.1038/s41586-018-0414-6.

43. Bergen, V., Lange, M., Peidli, S., Wolf, F.A., and Theis, F.J. (2020). Generalizing RNA velocity to transient cell states through dynamical modeling. Nat. Biotechnol. *38*, 1408–1414. https://doi.org/10.1038/s41587-020-0591-3.
44. Haghverdi, L., Büttner, M., Wolf, F.A., Buettner, F., and Theis, F.J. (2016). Diffusion pseudotime robustly reconstructs lineage branching. Nat. Methods *13*, 845–848. https://doi.org/10.1038/nmeth.3971.
45. Saelens, W., Cannoodt, R., Todorov, H., and Saeys, Y. (2019). A comparison of single-cell trajectory inference methods. Nat. Biotechnol. *37*, 547–554. https://doi.org/10.1038/s41587-019-0071-9.
46. CFB protein expression summary - The Human Protein Atlas. https://www.proteinatlas.org/ENSG00000243649-CFB.
47. Reyes, R., Cardeñes, B., Machado-Pineda, Y., and Cabañas, C. (2018). Tetraspanin CD9: A key regulator of cell adhesion in the immune system. Front. Immunol. *9*, 863.
48. Nid nidogen 2 [Mus musculus (house mouse)] - Gene - NCBI. https://www.ncbi.nlm.nih.gov/gene?Db=gene&Cmd=DetailsSearch&Term=18074.
49. Liu, Y., Beyer, A., and Aebersold, R. (2016). On the dependency of cellular protein levels on mRNA abundance. Cell *165*, 535–550. https://doi.org/10.1016/j.cell.2016.03.014.
50. Shah, T., Leurgans, S.E., Mehta, R.I., Yang, J., Galloway, C.A., de Mesy Bentley, K.L., Schneider, J.A., and Mehta, R.I. (2023). Arachnoid granulations are lymphatic conduits that communicate with bone marrow and dura-arachnoid stroma. J. Exp. Med. *220*, e20220618. https://doi.org/10.1084/jem.20220618.
51. Kündig, T.M., Bachmann, M.F., DiPaolo, C., Simard, J.J.L., Battegay, M., Lother, H., Gessner, A., Kühlcke, K., Ohashi, P.S., Hengartner, H., et al. (1995). Fibroblasts as efficient antigen-presenting cells in lymphoid organs. Science *268*, 1343–1347. https://doi.org/10.1126/science.7761853.
52. Wang, H., Leng, Y., and Gong, Y. (2018). Bone marrow fat and hematopoiesis. Front. Endocrinol. *9*, 694.
53. Robles, H., Park, S., Joens, M.S., Fitzpatrick, J.A.J., Craft, C.S., and Scheller, E.L. (2019). Characterization of the bone marrow adipocyte niche with three-dimensional electron microscopy. Bone *118*, 89–98. https://doi.org/10.1016/j.bone.2018.01.020.
54. Tratwal, J., Rojas-Sutterlin, S., Bataclan, C., Blum, S., and Naveiras, O. (2021). Bone marrow adiposity and the hematopoietic niche: A historical perspective of reciprocity, heterogeneity, and lineage commitment. Best Pract. Res. Clin. Endocrinol. Metab. *35*, 101564. https://doi.org/10.1016/j.beem.2021.101564.
55. Shi, S.X., Shi, K., and Liu, Q. (2021). Brain injury instructs bone marrow cellular lineage destination to reduce neuroinflammation. Sci. Transl. Med. *13*, eabc7029. https://doi.org/10.1126/scitranslmed.abc7029.
56. Sutherland, T.E., Dyer, D.P., and Allen, J.E. (2023). The extracellular matrix and the immune system: A mutually dependent relationship. Science *379*, eabp8964. https://doi.org/10.1126/science.abp8964.
57. Ben Shoham, A., Rot, C., Stern, T., Krief, S., Akiva, A., Dadosh, T., Sabany, H., Lu, Y., Kadler, K.E., and Zelzer, E. (2016). Deposition of collagen type I onto skeletal endothelium reveals a new role for blood vessels in regulating bone morphology. Development *143*, 3933–3943. https://doi.org/10.1242/dev.139253.
58. Maier, T., Güell, M., and Serrano, L. (2009). Correlation of mRNA and protein in complex biological samples. FEBS Lett. *583*, 3966–3973. https://doi.org/10.1016/j.febslet.2009.10.036.
59. de Sousa Abreu, R., Penalva, L.O., Marcotte, E.M., and Vogel, C. (2009). Global signatures of protein and mRNA expression levels. Mol. Biosyst. *5*, 1512–1526. https://doi.org/10.1039/b908315d.
60. Guilarte, T.R., Rodichkin, A.N., McGlothan, J.L., Acanda De La Rocha, A.M., and Azzam, D.J. (2022). Imaging neuroinflammation with TSPO: A new perspective on the cellular sources and subcellular localization. Pharmacol. Ther. *234*, 108048. https://doi.org/10.1016/j.pharmthera.2021.108048.
61. Werry, E.L., Bright, F.M., Piguet, O., Ittner, L.M., Halliday, G.M., Hodges, J.R., Kiernan, M.C., Loy, C.T., Kril, J.J., and Kassiou, M. (2019). Recent developments in TSPO PET imaging as A biomarker of neuroinflammation in neurodegenerative disorders. Int. J. Mol. Sci. *20*, 3161. https://doi.org/10.3390/ijms20133161.
62. Palleis, C., Sauerbeck, J., Beyer, L., Harris, S., Schmitt, J., Morenas-Rodriguez, E., Finze, A., Nitschmann, A., Ruch-Rubinstein, F., Eckenweber, F., et al. (2021). In vivo assessment of neuroinflammation in 4-repeat tauopathies. Mov. Disord. *36*, 883–894. https://doi.org/10.1002/mds.28395.
63. Unterrainer, M., Mahler, C., Vomacka, L., Lindner, S., Havla, J., Brendel, M., Böning, G., Ertl-Wagner, B., Kümpfel, T., Milenkovic, V.M., et al. (2018). TSPO PET with [18F]GE-180 sensitively detects focal neuroinflammation in patients with relapsing-remitting multiple sclerosis. Eur. J. Nucl. Med. Mol. Imaging *45*, 1423–1431. https://doi.org/10.1007/s00259-018-3974-7.
64. Hansson, O., Lehmann, S., Otto, M., Zetterberg, H., and Lewczuk, P. (2019). Advantages and disadvantages of the use of the CSF Amyloid β (Aβ) 42/40 ratio in the diagnosis of Alzheimer's disease. Alzheimers Res. Ther. *11*, 34. https://doi.org/10.1186/s13195-019-0485-0.
65. Braak, H., and Braak, E. (1991). Neuropathological stageing of Alzheimer-related changes. Acta Neuropathol. *82*, 239–259. https://doi.org/10.1007/BF00308809.
66. Fan, L., Li, H., Zhuo, J., Zhang, Y., Wang, J., Chen, L., Yang, Z., Chu, C., Xie, S., Laird, A.R., et al. (2016). The human Brainnetome atlas: A new brain atlas based on connectional architecture. Cereb. Cortex N. Y. NY: 1991 *26*, 3508–3526. https://doi.org/10.1093/cercor/bhw157.
67. Yang, C., Hawkins, K.E., Doré, S., and Candelario-Jalil, E. (2019). Neuroinflammatory mechanisms of blood-brain barrier damage in ischemic stroke. Am. J. Physiol. Cell Physiol. *316*, C135–C153. https://doi.org/10.1152/ajpcell.00136.2018.
68. Jickling, G.C., Liu, D., Ander, B.P., Stamova, B., Zhan, X., and Sharp, F.R. (2015). Targeting neutrophils in ischemic stroke: translational insights from experimental studies. J. Cereb. Blood Flow Metab. *35*, 888–901. https://doi.org/10.1038/jcbfm.2015.45.
69. Pulous, F.E., Cruz-Hernández, J.C., Yang, C., Kaya, Z., Wojtkiewicz, G., Capen, D., Brown, D., Wu, J.W., Vinegoni, C., Yamazoe, M., et al. (2021). Cerebrospinal fluid outflow through skull channels instructs cranial hematopoiesis. https://doi.org/10.1101/2021.08.27.457954.
70. Barc, K., and Kuźma-Kozakiewicz, M. (2019). Positron emission tomography neuroimaging in neurodegenerative diseases: Alzheimer's disease, Parkinson's disease, and amyotrophic lateral sclerosis. Neurol. Neurochir. Pol. *53*, 99–112. https://doi.org/10.5603/PJNNS.a2019.0013.
71. Hadjikhani, N., Albrecht, D.S., Mainero, C., Ichijo, E., Ward, N., Granziera, C., Zürcher, N.R., Akeju, O., Bonnier, G., Price, J., et al. (2020). Extra-axial inflammatory signal in parameninges in migraine with visual aura. Ann. Neurol. *87*, 939–949. https://doi.org/10.1002/ana.25731.
72. Wadsworth, H., Jones, P.A., Chau, W.-F., Durrant, C., Fouladi, N., Passmore, J., O'Shea, D., Wynn, D., Morisson-Iveson, V., Ewan, A., et al. (2012). [18F]. GE-180: A novel fluorine-18 labelled PET tracer for imaging translocator protein 18kDa (TSPO). Bioorg. Med. Chem. Lett. *22*, 1308–1313. https://doi.org/10.1016/j.bmcl.2011.12.084.
73. Rejc, L., Gómez-Vallejo, V., Joya, A., Arsequell, G., Egimendia, A., Castellnou, P., Ríos-Anglada, X., Cossío, U., Baz, Z., Iglesias, L., et al. (2022). Longitudinal evaluation of neuroinflammation and oxidative stress in a mouse model of Alzheimer disease using positron emission tomography. Alzheimers Res. Ther. *14*, 80. https://doi.org/10.1186/s13195-022-01016-5.
74. Fan, Z., Okello, A.A., Brooks, D.J., and Edison, P. (2015). Longitudinal influence of microglial activation and amyloid on neuronal function in

Alzheimer's disease. Brain *138*, 3685–3698. https://doi.org/10.1093/brain/awv288.

75. Thiel, A., Radlinska, B.A., Paquette, C., Sidel, M., Soucy, J.-P., Schirrmacher, R., and Minuk, J. (2010). The temporal dynamics of poststroke neuroinflammation: A longitudinal diffusion tensor imaging–guided PET study with 11C-PK11195 in acute subcortical stroke. J. Nucl. Med. *51*, 1404–1412. https://doi.org/10.2967/jnumed.110.076612.

76. Shi, K., Tian, D.-C., Li, Z.-G., Ducruet, A.F., Lawton, M.T., and Shi, F.-D. (2019). Global brain inflammation in stroke. Lancet Neurol. *18*, 1058–1066. https://doi.org/10.1016/S1474-4422(19)30078-X.

77. Beziere, N., von Schacky, C., Kosanke, Y., Kimm, M., Nunes, A., Licha, K., Aichler, M., Walch, A., Rummeny, E.J., Ntziachristos, V., et al. (2014). Optoacoustic imaging and staging of inflammation in a murine model of arthritis. Arthritis Rheumatol. *66*, 2071–2078. https://doi.org/10.1002/art.38642.

78. Largeau, B., Dupont, A.-C., Guilloteau, D., Santiago-Ribeiro, M.-J., and Arlicot, N. (2017). TSPO PET imaging: from microglial activation to peripheral sterile inflammatory diseases? Contrast Media Mol. Imaging *2017*, 6592139. https://doi.org/10.1155/2017/6592139.

79. Shah, S., Sinharay, S., Patel, R., Solomon, J., Lee, J.H., Schreiber-Stainthorp, W., Basuli, F., Zhang, X., Hagen, K.R., Reeder, R., et al. (2022). PET imaging of TSPO expression in immune cells can assess organ-level pathophysiology in high-consequence viral infections. Proc. Natl. Acad. Sci. USA *119*, e2110846119. https://doi.org/10.1073/pnas.2110846119.

80. Bartos, L.M., Kirchleitner, S.V., Kolabas, Z.I., Quach, S., Blobner, J., Mueller, S.A., Ulukaya, S., Hoeher, L., Horvath, I., Wind-Mark, K., et al. (2023). Deciphering sources of PET signals in the tumor microenvironment of glioblastoma at cellular resolution. Preprint at bioRxiv. https://doi.org/10.1101/2023.01.26.522174.

81. Bartos, L.M., Kunte, S.T., Beumers, P., Xiang, X., Wind, K., Ziegler, S., Bartenstein, P., Choi, H., Lee, D.S., Haass, C., et al. (2022). Single-cell radiotracer allocation via immunomagnetic sorting to disentangle PET signals at cellular resolution. J. Nucl. Med. *63*, 1459–1462. https://doi.org/10.2967/jnumed.122.264171.

82. Schindelin, J., Arganda-Carreras, I., Frise, E., Kaynig, V., Longair, M., Pietzsch, T., Preibisch, S., Rueden, C., Saalfeld, S., Schmid, B., et al. (2012). Fiji: an open-source platform for biological-image analysis. Nat. Methods *9*, 676–682. https://doi.org/10.1038/Nmeth.2019.

83. Wolf, F.A., Angerer, P., and Theis, F.J. (2018). SCANPY: large-scale single-cell gene expression data analysis. Genome Biol. *19*, 15. https://doi.org/10.1186/s13059-017-1382-0.

84. Percie du Sert, N.P., Hurst, V., Ahluwalia, A., Alam, S., Avey, M.T., Baker, M., Browne, W.J., Clark, A., Cuthill, I.C., Dirnagl, U., et al. (2020). The ARRIVE guidelines 2.0. The ARRIVE guidelines 2.0: Updated guidelines for reporting animal research. PLoS Biol. *18*, e3000410. https://doi.org/10.1371/journal.pbio.3000410.

85. Xiang, X., Wind, K., Wiedemann, T., Blume, T., Shi, Y., Briel, N., Beyer, L., Biechele, G., Eckenweber, F., Zatcepin, A., et al. (2021). Microglial activation states drive glucose uptake and FDG-PET alterations in neurodegenerative diseases. Sci. Transl. Med. *13*, eabe5640.

86. Schmitt, J., Palleis, C., Sauerbeck, J., Unterrainer, M., Harris, S., Prix, C., Weidinger, E., Katzdobler, S., Wagemann, O., Danek, A., et al. (2021). Dual-phase β-amyloid PET captures neuronal injury and amyloidosis in corticobasal syndrome. Front. Aging Neurosci. *13*, 661284. https://doi.org/10.3389/fnagi.2021.661284.

87. Wang, T., Ouzounov, D.G., Wu, C., Horton, N.G., Zhang, B., Wu, C.-H., Zhang, Y., Schnitzer, M.J., and Xu, C. (2018). Three-photon imaging of mouse brain structure and function through the intact skull. Nat. Methods *15*, 789–792. https://doi.org/10.1038/s41592-018-0115-y.

88. Khalin, I., Heimburger, D., Melnychuk, N., Collot, M., Groschup, B., Hellal, F., Reisch, A., Plesnila, N., and Klymchenko, A.S. (2020). Ultrabright fluorescent polymeric nanoparticles with a stealth pluronic shell for live tracking in the mouse brain. ACS Nano *14*, 9755–9770. https://doi.org/10.1021/acsnano.0c01505.

89. Cai, R., Kolabas, Z.I., Pan, C., Mai, H., Zhao, S., Kaltenecker, D., Voigt, F.F., Molbay, M., Ohn, T.L., Vincke, C., et al. (2023). Whole-mouse clearing and imaging at the cellular level with vDISCO. Nat. Protoc. *18*, 1197–1242. https://doi.org/10.1038/s41596-022-00788-2.

90. Susaki, E.A., Tainaka, K., Perrin, D., Kishino, F., Tawara, T., Watanabe, T.M., Yokoyama, C., Onoe, H., Eguchi, M., Yamaguchi, S., et al. (2014). Whole-brain imaging with single-cell resolution using chemical cocktails and computational analysis. Cell *157*, 726–739. https://doi.org/10.1016/j.cell.2014.03.042.

91. Zhao, S., Todorov, M.I., Cai, R., Maskari, R.A., Steinke, H., Kemter, E., Mai, H., Rong, Z., Warmer, M., Stanic, K., et al. (2020). Cellular and molecular probing of intact human organs. Cell *180*, 796–812.e19. https://doi.org/10.1016/j.cell.2020.01.030.

92. Holzwarth, K., Köhler, R., Philipsen, L., Tokoyoda, K., Ladyhina, V., Wählby, C., Niesner, R.A., and Hauser, A.E. (2018). Multiplexed fluorescence microscopy reveals heterogeneity among stromal cells in mouse bone marrow sections. Cytometry A *93*, 876–888. https://doi.org/10.1002/cyto.a.23526.

93. Safaiyan, S., Besson-Girard, S., Kaya, T., Cantuti-Castelvetri, L., Liu, L., Ji, H., Schifferer, M., Gouna, G., Usifo, F., Kannaiyan, N., et al. (2021). White matter aging drives microglial diversity. Neuron *109*, 1100–1117.e10. https://doi.org/10.1016/j.neuron.2021.01.027.

94. Picelli, S., Björklund, A.K., Reinius, B., Sagasser, S., Winberg, G., and Sandberg, R. (2014). Tn5 transposase and tagmentation procedures for massively scaled sequencing projects. Genome Res. *24*, 2033–2040. https://doi.org/10.1101/gr.177881.114.

95. Pedersen, K.B., Williams, A., Watt, J., and Ronis, M.J. (2019). Improved method for isolating high-quality RNA from mouse bone with RNAlater at room temperature. Bone Rep. *11*, 100211. https://doi.org/10.1016/j.bonr.2019.100211.

96. Bayraktar, O.A., Bartels, T., Holmqvist, S., Kleshchevnikov, V., Martirosyan, A., Polioudakis, D., Ben Haim, L., Young, A.M.H., Batiuk, M.Y., Prakash, K., et al. (2020). Astrocyte layers in the mammalian cerebral cortex revealed by a single-cell in situ transcriptomic map. Nat. Neurosci. *23*, 500–509. https://doi.org/10.1038/s41593-020-0602-1.

97. Kislinger, G., Gnägi, H., Kerschensteiner, M., Simons, M., Misgeld, T., and Schifferer, M. (2020). ATUM-FIB microscopy for targeting and multiscale imaging of rare events in mouse cortex. STAR Protoc. *1*, 100232. https://doi.org/10.1016/j.xpro.2020.100232.

98. Bhatia, H.S., Brunner, A.-D., Öztürk, F., Kapoor, S., Rong, Z., Mai, H., Thielert, M., Ali, M., Al-Maskari, R., Paetzold, J.C., et al. (2022). Spatial proteomics in three-dimensional intact specimens. Cell *185*, 5040–5058.e19. https://doi.org/10.1016/j.cell.2022.11.021.

99. Demichev, V., Messner, C.B., Vernardis, S.I., Lilley, K.S., and Ralser, M. (2020). DIA-NN: neural networks and interference correction enable deep proteome coverage in high throughput. Nat. Methods *17*, 41–44. https://doi.org/10.1038/s41592-019-0638-x.

100. Overhoff, F., Brendel, M., Jaworska, A., Korzhova, V., Delker, A., Probst, F., Focke, C., Gildehaus, F.-J., Carlsen, J., Baumann, K., et al. (2016). Automated spatial brain normalization and hindbrain white matter reference tissue give improved [18F]-florbetaben PET quantitation in Alzheimer's model mice. Front. Neurosci. *10*, 45. https://doi.org/10.3389/fnins.2016.00045.

101. Brendel, M., Probst, F., Jaworska, A., Overhoff, F., Korzhova, V., Albert, N.L., Beck, R., Lindner, S., Gildehaus, F.-J., Baumann, K., et al. (2016). Glial activation and glucose metabolism in a transgenic amyloid mouse model: A triple-tracer PET study. J. Nucl. Med. *57*, 954–960. https://doi.org/10.2967/jnumed.115.167858.

102. Reifschneider, A., Robinson, S., van Lengerich, B., Gnörich, J., Logan, T., Heindl, S., Vogt, M.A., Weidinger, E., Riedl, L., Wind, K., et al. (2021). Loss of TREM2 reduces hyperactivation of progranulin deficient microglia but not lysosomal pathology. https://doi.org/10.1101/2021.07.08.451574.

103. Albert, N.L., Unterrainer, M., Fleischmann, D.F., Lindner, S., Vettermann, F., Brunegraf, A., Vomacka, L., Brendel, M., Wenter, V., Wetzel, C., et al. (2017). TSPO PET for glioma imaging using the novel ligand 18F-GE-180: first results in patients with glioblastoma. Eur. J. Nucl. Med. Mol. Imaging *44*, 2230–2238. https://doi.org/10.1007/s00259-017-3799-9.

104. Luecken, M.D., and Theis, F.J. (2019). Current best practices in single-cell RNA-seq analysis: a tutorial. Mol. Syst. Biol. *15*, e8746. https://doi.org/10.15252/msb.20188746.

105. Lun, A.T., Bach, K., and Marioni, J.C. (2016). Pooling across cells to normalize single-cell RNA sequencing data with many zero counts. Genome Biol. *17*, 75. https://doi.org/10.1186/s13059-016-0947-7.

106. Wolf, F.A., Hamey, F.K., Plass, M., Solana, J., Dahlin, J.S., Göttgens, B., Rajewsky, N., Simon, L., and Theis, F.J. (2019). PAGA: graph abstraction reconciles clustering with trajectory inference through a topology preserving map of single cells. Genome Biol. *20*, 59. https://doi.org/10.1186/s13059-019-1663-x.

107. Gulati, G.S., Sikandar, S.S., Wesche, D.J., Manjunath, A., Bharadwaj, A., Berger, M.J., Ilagan, F., Kuo, A.H., Hsieh, R.W., Cai, S., et al. (2020). Single-cell transcriptional diversity is a hallmark of developmental potential. Science *367*, 405–411. https://doi.org/10.1126/science.aax0249.

108. Hie, B., Cho, H., DeMeo, B., Bryson, B., and Berger, B. (2019). Geometric sketching compactly summarizes the single-cell transcriptomic landscape. Cell Syst. *8*, 483–493.e7. https://doi.org/10.1016/j.cels.2019.05.003.

109. Raudvere, U., Kolberg, L., Kuzmin, I., Arak, T., Adler, P., Peterson, H., and Vilo, J. (2019). g:profiler: a web server for functional enrichment analysis and conversions of gene lists (2019 update). Nucleic Acids Res. *47*, W191–W198. https://doi.org/10.1093/nar/gkz369.

110. Huang, X., and Huang, Y. (2021). Cellsnp-lite: an efficient tool for genotyping single cells. Bioinformatics *37*, 4569–4571. https://doi.org/10.1093/bioinformatics/btab358.

111. Huang, Y., McCarthy, D.J., and Stegle, O. (2019). Vireo: bayesian demultiplexing of pooled single-cell RNA-seq data without genotype reference. Genome Biol. *20*, 273. https://doi.org/10.1186/s13059-019-1865-2.

112. Patro, R., Duggal, G., Love, M.I., Irizarry, R.A., and Kingsford, C. (2017). Salmon provides fast and bias-aware quantification of transcript expression. Nat. Methods *14*, 417–419. https://doi.org/10.1038/nmeth.4197.

113. Patel, H., Ewels, P., Peltzer, A., Botvinnik, O., Sturm, G., Moreno, D., Vemuri, P., Silviamorins, A., Garcia, M.U., Pantano, L., et al. (2023). nf-core/rnaseq: nf-core/rnaseq v3.11.1—Plastered Radium Rhino. https://doi.org/10.5281/zenodo.7789554.

114. Love, M.I., Huber, W., and Anders, S. (2014). Moderated estimation of fold change and dispersion for RNA-seq data with DESeq2. Genome Biol. *15*, 550. https://doi.org/10.1186/s13059-014-0550-8.

115. Berg, S., Kutra, D., Kroeger, T., Straehle, C.N., Kausler, B.X., Haubold, C., Schiegg, M., Ales, J., Beier, T., Rudy, M., et al. (2019). ilastik: interactive machine learning for (bio)image analysis. Nat. Methods *16*, 1226–1232. https://doi.org/10.1038/s41592-019-0582-9.

116. Kuleshov, M.V., Jones, M.R., Rouillard, A.D., Fernandez, N.F., Duan, Q., Wang, Z., Koplev, S., Jenkins, S.L., Jagodnik, K.M., Lachmann, A., et al. (2016). Enrichr: a comprehensive gene set enrichment analysis web server 2016 update. Nucleic Acids Res. *44*, W90–W97. https://doi.org/10.1093/nar/gkw377.

117. Rezaie, N., Reese, F., and Mortazavi, A. (2022). PyWGCNA: A Python package for weighted gene co-expression network analysis. https://doi.org/10.1101/2022.08.22.504852.

118. Rominger, A., Brendel, M., Burgold, S., Keppler, K., Baumann, K., Xiong, G., Mille, E., Gildehaus, F.-J., Carlsen, J., Schlichtiger, J., et al. (2013). Longitudinal assessment of cerebral β-amyloid deposition in mice overexpressing Swedish mutant β-amyloid precursor protein using 18F-florbetaben PET. J. Nucl. Med. *54*, 1127–1134. https://doi.org/10.2967/jnumed.112.114660.

119. Hammers, A., Allom, R., Koepp, M.J., Free, S.L., Myers, R., Lemieux, L., Mitchell, T.N., Brooks, D.J., and Duncan, J.S. (2003). Three-dimensional maximum probability atlas of the human brain, with particular reference to the temporal lobe. Hum. Brain Mapp. *19*, 224–247. https://doi.org/10.1002/hbm.10123.

120. Finze, A., Biechele, G., Rauchmann, B.-S., Franzmeier, N., Palleis, C., Katzdobler, S., Weidinger, E., Guersel, S., Schuster, S., Harris, S., et al. (2022). Individual regional associations between Aβ-, tau- and neurodegeneration (ATN) with microglial activation in patients with primary and secondary tauopathies. Preprint at medRxiv. https://doi.org/10.1101/2022.11.12.22282082.

STAR★METHODS

KEY RESOURCES TABLE

REAGENT or RESOURCE	SOURCE	IDENTIFIER
Antibodies		
Atto647NconjugatedantiGFP nanobooster	Chromotek	Cat.#gba647n-100;RRID:AB_2629215
Anti-NUR77 antibody	Abcam	Cat# ab153914
anti-Lysozyme antibody	Abcam	Cat#ab108508; RRID:AB_10861277
Goat anti-Rabbit IgG (H+L) Highly Cross-Adsorbed Secondary Antibody, Alexa Fluor 647	Abcam	Cat#A-21245; RRID:AB_141775
APC/Cyanine7 anti-mouse Ly-6G/Ly-6C (Gr-1) Antibody	Biolegend	Cat#108423; RRID:AB_2137486
APC anti-mouse CD11c Antibody	Biolegend	Cat# 117309; RRID:AB_313778
BD Horizon™ BUV395 Rat Anti-Mouse CD45	BD Biosciences	Cat#565967; RRID:AB_2739420
BD Horizon™ BV421 Rat Anti-Mouse CD117	BD Biosciences	Cat# 562609; RRID:AB_11154585
BD Pharmingen™ PerCP-Cy5.5 Rat Anti-Mouse F4/80	BD Biosciences	Cat# 567202; RRID:AB_2916500
Brilliant Violet 510™ anti-mouse I-A/I-E Antibody	Biolegend	Cat# 107635; RRID:AB_2561397
Brilliant Violet 650™ anti-mouse TER-119/Erythroid Cells Antibody	Biolegend	Cat# 116235; RRID:AB_11204244
Brilliant Violet 711™ anti-mouse NK-1.1 Antibody	Biolegend	Cat# 108745; RRID:AB_2563286
Brilliant Violet 785™ anti-mouse/human CD11b Antibody	Biolegend	Cat# 101243; RRID:AB_2561373
PE anti-mouse CD179a (VpreB) Antibody	Biolegend	Cat# 143603; RRID:AB_11147372
PE/Dazzle™ 594 anti-mouse CD182 (CXCR2) Antibody	Biolegend	Cat# 149317; RRID:AB_2750072
BD Pharmingen™ PE-Cy™7 Rat Anti-Mouse Ly-6A/E	BD Biosciences	Cat# 561021; RRID:AB_2034021
BD Pharmingen™ Alexa Fluor® 700 Rat Anti-Mouse CD3 Molecular Complex	BD Biosciences	Cat# 561388; RRID:AB_10642588
Brilliant Violet 605™ anti-mouse Ly-6C Antibody	Biolegend	Cat# 128035; RRID:AB_2562352
BD Pharmingen™ PE-Cy™5 Rat Anti-Mouse CD45R/B220	BD Biosciences	Cat#553091; RRID:AB_394621
Donkey anti-Rabbit IgG (H+L) Highly Cross-Adsorbed Secondary Antibody, Alexa Fluor 647	Invitrogen	Cat#A-31573; RRID:AB_2536183
Alexa Fluor 594 Anti-alpha smooth muscle Actin antibody [1A4]	Abcam	Cat#ab202368;RRID:AB_2924381
Anti-PDGFRB antibody produced in rabbit	Merck	Cat# HPA028499; RRID:AB_10602018
Mouse Anti-Human Type IV Collagen-FITC (2F11)	SouthernBiotech	Cat#1460-02; RRID:AB_2794763
Chemicals, peptides, and recombinant proteins		
Methyl-beta-cyclodextrin	Sigma	Cat#332615
Hydroxy-L-proline	Sigma	Cat#441562
4%paraformaldehyde(PFA)	Morphisto	Cat.#11762.05000
Tetrahydrofuran	Sigma	Cat#186562
Benzyl alcohol	Sigma	Cat#24122
Benzyl benzoate	Sigma	Cat#W213802
Ethylenediamine tetra acetic acid	Carl Roth	Cat#1702922685
CHAPS	Roth	Cat# 1479.4
Guanidine hydrochloride	Roth	Cat# 6069.3
Acetic acid	Roth	Cat# T179.1
TritonX-100	PanReac Applichem	Cat.#A4975,1000
N-Methyldiethanolamine	Sigma	Cat.#471828
Dichloromethane	Roth	Cat.#KK47.1
RPE buffer	Qiagen	Cat#1018013

(*Continued on next page*)

Continued

REAGENT or RESOURCE	SOURCE	IDENTIFIER
Propidium iodide	ThermoFisher	Cat.#P3566
Lycopersicon Esculentum (Tomato) Lectin	Invitrogen	Cat.# L32470
Critical commercial assays		
10x Chromium Single Cell 3′ Library & Gel Bead Kit v3 for mouse and v3.1 for human	10x Genomics	https://www.10xgenomics.com/support/single-cell-gene-expression
RNAscope Multiplex Fluorescent Reagent Kit v2 Assay	Advanced cell Diagnostics, Bio-Techne	https://acdbio.com/rnascope-multiplex-fluorescent-v2-assay
Deposited data		
Mass spectrometry raw data	This paper	PRIDE accession code: PXD041665
All code used in this study	This paper	https://github.com/erturklab/skull_immune
Patient source file	This paper	Table S3
Single-cell sequencing raw counts matrices and annotation and bulk RNA-sequencing data	This paper	NCBI's GEO: GSE192616
Experimental models: Organisms/strains		
LySM-GFP (Lyz2tm1.1^{Graf}, MGI: 2654931)	MMRC	Strain#012039-MU;RRID: MMRRC_012039-MU
5xFAD (B6SJL-Tg(APPSwFlLon,PSEN1*M146L *L286V)6799Vas/Mmjax MGI:3693208)	Jackson Laboratory	Strain#034848-JAX;RRID: MMRRC_034848-JAX
KikGR33 (Tg(CAG-KikGR)33Hadj/J)	Jackson Laboratory	Strain#013753:RRID:IMSR_JAX:013753
C57BL/6J mouseline	Jackson Laboratory	Strain#:000,664;RRID:IMSR_JAX:000,664
C57BL/6NJ mouseline	Jackson Laboratory	Strain#:005304:RRID:IMSR_JAX:005304
Software and algorithms		
ImSpector	MiltenyiBiotec	https://www.miltenyibiotec.com/DE-en/products/ultramicroscope-blaze.html
Imaris	Bitplane AG	https://imaris.oxinst.com/
Vision4D	Arivis	https://www.arivis.com/de/
Fiji	Schindelin et al.[82]	https://ImageJ.net/software/fiji/
syGlass VR	syGlass	https://www.syglass.io
Scanpy v. 1. 6	Wolf et al.[83]	https://scanpy.readthedocs.io/en/stable/
GraphPadPrism (8.2.1)	GraphPad software	https://www.graphpad.com
PMOD	Digilent	https://www.pmod.com/web/
IBM SPSS Statistics version 22.0	IBM	https://www.ibm.com/spss
Image analysis algorithm	This paper	https://github.com/erturklab/skull_immune
Other		
0.22 μm syringe filter	Sartorius	Cat#16532
SCEM medium	Sectionlab	SCEM
70 μm Falcon™ Cell Strainers	Falcon	Cat#08-771-2
35° ultra-diamond knife	Diatome	https://www.scienceservices.eu/tools-supplies/diamond-knifes/ultra
EconoSpin(TM) All-in-1 Mini Spin Clumns for DNA/RNA extraction	Epoch life sciences	Cat#1920-250

RESOURCE AVAILABILITY

Lead contact

Further information and requests for resources should be directed to and will be fulfilled by the lead contact, Ali Erturk (ali.erturk@helmholtz-munich.de).

Materials availability

This study did not generate new unique reagents.

Data and code availability

- Single-cell RNA sequencing data raw counts, matrices and annotation and bulk RNA datasets are available via NCBI's GEO (GSE192616), proteomic data is available on PRIDE, accession code: PXD041665 and patient source file human TSPO-PET imaging study can be found under supplemental information. Imaging data is available upon request from the corresponding author.
- All code used in this study can be found as jupyter notebooks in the project github repository: https://github.com/erturklab/skull_immune.
- Any additional information required to reanalyze the data reported in this paper is available from the lead contact upon request.

EXPERIMENTAL MODEL AND STUDY PARTICIPANT DETAILS

Animals

Animal housing and experiments in this work were conducted in agreement with the institutional guidelines (Klinikum der Universität München/Ludwig Maximilian University of Munich, Technische Universitaet Muenchen, Regierung von Oberbayern and UK Home Office), after approval of the ethical review board of the government of Upper Bavaria (Regierung von Oberbayern, Munich, Germany), and in accordance with the European directive 2010/63/EU for animal research. The transgenic lines used in this study are C57BL/6, LySM-GFP (Lyz2tm1.1Graf, MGI: 2654931) and 5xFAD (B6SJL-Tg(APPSwFILon,PSEN1*M146L*L286V)6799Vas/Mmjax MGI:3693208) acquired from Charles River and Jackson Laboratory. KikGR33 (Tg(CAG-KikGR)33Hadj/J) mice were kindly given to C.B. by Dr. Josef Anrather, Weill Cornell Medical College, New York. KikGR33 mice were bred and housed at the animal core facility of the Center for Stroke and Dementia Research (Munich, Germany), and for which male mice were used. 3-month-old male mice were used in study with the exception of bulk AD and 5xFAD TSPO-PET dataset, where the sex of the animals were female and the age were 6-months-old for bulk AD and 4.5-months-old for TSPO-PET dataset. In all in vivo experiments in this study, littermates of the same sex were randomly assigned to experimental groups, the animals were housed under a 12/12 h light/dark cycle, all animals were healthy in the beginning of the experiment, no drugs were given to animals during the time of data acquisition, no specific food, temperature and cage conditions were kept. All data are reported according to the ARRIVE.[84]

Human samples and participants

All anatomy donors or next-of-kin gave their informed and written consent to explore the cadavers for research and educational purposes. The signed consents are kept at the institutes involved. Institutional approval was obtained in accordance to the Saxonian Death and Funeral Act of 1994, of the independent ethics committee of the Hamburg Chamber of Physicians (protocol 2020-10353-BO-ff) and the Ethics committee of Technical University of Munich (67/22S). The skull samples in this study are coming from the following sources: University Medical Center Hamburg-Eppendorf, Institute of Legal Medicine; Institut für Allgemeine Pathologie und Pathologische Anatomie, Technische Universität München and Anatomy Institute, University of Leipzig, Institut für Rechtsmedizin der Universität München. A detailed list of post-mortem samples used for light sheet imaging and proteomics samples are given in Figures S5O and S7A.

Regarding human participants: ten patients with stroke, 29 patients with multiple sclerosis (15 with relapsing remitting multiple sclerosis and 14 with primary progressive multiple sclerosis), 43 patients with 4R tauopathies, 50 patients with AD and 27 age- and sex-matched individuals without objective cognitive impairment and with intact motor function were available for calvaria analysis of TSPO-PET. Sample sizes were determined in the specific study protocols, based on comparisons of TSPO-PET signals in brain between disease and controls. Power was set to 0.8 and alpha was set to 0.05 with the goal to achieve effect sizes of 1.0, also graded sufficient to test for differences in skull TSPO-PET signals. Allocation into study groups was determined by the clinical diagnosis. Severe neurological disorders other than the investigated diagnosis were excluded in the study protocols, assuming immunocompetence in all participants. All participants were naïve to TSPO-PET at study inclusion. In one set of analyses stroke, MS and 4R tauopathy patients were compared with controls, while the AD cohort, for which additional biomarkers were available, was analyzed separately. All patients with multiple sclerosis were investigated during observational studies. We included all baseline scans of therapy naïve patients with primary progressive multiple sclerosis (n=14) and patients with relapsing remitting multiple sclerosis (n=15; previously published in Unterrainer et al.[63]) regardless of therapy regimes. However, patients who received steroid therapy < 4 weeks prior to PET as well as patients with additional CNS pathologies were excluded a priori. PET acquisition and PET data analyses of the multiple sclerosis cohort (ethics-application: 601–16) were approved by the local institutional ethics committee (LMU Munich) and the German radiation protection (BfS-application: Z 5 – 22463/2 – 2015 - 006) authorities. The 4R-tauopathy cohort[62] was composed of patients with possible or probable β-amyloid negative corticobasal syndrome (n=29) and patients with possible or probable progressive supranuclear palsy Richardson syndrome (n=14) according to Armstrong Clinical Research and Movement Disorders Society criteria respectively. Detailed inclusion and exclusion criteria were published elsewhere.[62] One case was excluded due to cropped skull. PET acquisition and PET data analyses of the 4R-tauopathy cohort (ethics-applications: 17–569 & 17–755) were approved by the local institutional ethics committee (LMU Munich) and the German radiation protection (BfS-application: Z 5 - 22464/2017-047-K-G) authorities. A total of 27 healthy controls deriving from the different cohorts were included to cover the whole age range of patients. PET acquisition and PET data analyses of the stroke cohort

(ethics-application: 19–428) were approved by the local institutional ethics committee of the LMU Munich (ethics-application: 19–428) and the German radiation protection authority (BfS-application: Z 5 - 22464/2019-163-G). To compare different patient cohorts, we used harmonized data from different PET imaging studies: All patients with acute ischemic stroke (n=10) were recruited from the ongoing ICARUS study which included a TSPO-PET up to 10 days after stroke onset. Inclusion criteria were an age ≥50 years, acute ischemic stroke as defined by an acute focal neurological deficit in combination with a corresponding infarct as documented by diffusion-weighted imaging (DWI)-positive lesion on brain MRI, presence of an infarct involving the cortex or a strictly subcortical infarct, written informed consent; and willingness to participate in study assessments including follow-up. Exclusion criteria were among others multiple infarcts, infratentorial infarcts affecting the brain stem or cerebellum, immunomodulatory therapies within the last 3 months, chronic inflammatory disease, and infectious diseases (< 7 days prior to stroke). The AD cohort was composed of nine cases with subjective cognitive decline due to AD, 13 cases with mild cognitive impairment due to AD, 18 cases with AD dementia, and 12 cases with corticobasal syndrome, dementia and underlying AD. Initial results of brain TSPO labeling in this cohort are published elsewhere.[85] Two patients with AD were excluded from the cross-sectional TSPO-PET group comparison due to limited field of view. Participants were enrolled in the interdisciplinary AD study "Activity of Cerebral Networks, Amyloid and Microglia in Aging and AD (ActiGliA)". In the AD cohort and its controls, Aβ-PET was performed in all participants using [^{18}F]flutemetamol.[86] PET acquisition and PET data analyses of the AD cohort (ethics-applications: 17-569 & 17-755) were approved by the local institutional ethics committee (LMU Munich) and the German radiation protection (BfS-application: Z 5 - 22464/2017-047-K-G) authorities. Longitudinal follow-up imaging within the ActiGliA cohort was available for 13 patients of the AD continuum and 15 controls at a median interval of 18 months. Additionally, 3 months follow-up imaging was available for 13 patients with stroke. Age, gender, SNP coding and medication status of participants are provided in Table S3.

METHOD DETAILS

Middle cerebral artery occlusion (MCAo) model

The MCAo model was used to generate transient cerebral ischemic strokes by introducing an intraluminal filament through the carotid artery of mice anesthetized with isoflurane mixed with 30% O_2 and 70% N_2O. To initiate the occlusion the left common carotid artery and interna of the animal were permanently ligated and a silicon capped nylon suture (6/0) was introduced through a cut in the common carotid artery and advanced through the external carotid artery until it reached and obstructed the MCA for 30 minutes. Regional cerebral blood flow was monitored, in the bregma coordinates 2-mm posterior, 5-mm lateral, via transcranial laser Doppler flowmeter from the induction of stroke until 10 minutes after retraction of the filament and reperfusion took place. After the procedure, mice were left for recovery in temperature-controlled cages for two hours in order to minimize the risk of hypothermia. Sham-operated animals were subjected to the same procedure without the insertion of the filament. Body temperatures were kept constant throughout all surgeries with a feedback-controlled heating pad at 37.0 ± 0.5 °C. Animals were then kept in their home cages with facilitated access to water and food whilst being subjected to behavioral tests for three days. Mice were excluded in case of insufficient MCA occlusion (a reduction in blood flow to 15% of the baseline value) or blood flow recovery >80% within 10 min of reperfusion.

Skull preparation for chronic imaging

Experiments were carried out on 8-12 weeks old male LysM-GFP -/+ mice. Induction of anesthesia with buprenorphine (0.1 mg/kg Bw) and isoflurane (5%, 30s), was followed by maintenance anesthesia with 1.5-2.5% isoflurane in room air with 30% oxygen/70% air under continuous monitoring of body temperature 37.5 C° with a feedback-controlled heating pad. Glass window preparation was adapted from described method.[87] Mouse was placed on a stereotactic frame (RWD Life Science Co.,LTD, Shenzhen, China) where head was fixed by ear bars and the eyes were covered with Bepanthen ointment (AG Bayer, Leverkusen, Germany). The left parietal bone was exposed after resection of the mouse scalp. Sterile saline was applied to the skull and the periosteum were gently removed with forceps. Then, Ultraviolet-curable glue Loctite 4305 (Henkel, Düsseldorf, Germany) was applied onto the parietal bone surface. A sterile round glass window of 3-mm diameter was placed on the skull followed by two by 1s exposures every 3s of ultraviolet light source UV301D UV 365NM Light Flashlight (LIGHTFE Lighting Co., Ltd., Shenzhen, China) to cure the glue. Then, skull surrounding the window was prepared for the dental cement application by putting for 1 min onto the surface of iBond Self Etch (Kulzer GmbH., Hanau, Germany) solution with subsequent curing by UV source for 5 s using Demi™ Ultra Dental Curing Lights (Kerr Corporation, Brea, CA, USA). Then on top of the etching solution the dental cement Tetric EvoFlow® (Ivoclar Vivadent, Schaan, Liechtenstein) was applied. Before UV curing, the titanium ring was placed on the skull to have the window in its center and then cement was cured with the same UV source (Demi™ Ultra Dental Curing Lights) for not more than 5 s including every side around the ring. Finally, a thin stripe of dental cement was applied onto the inner edge of the ring, with subsequent 5 s UV exposing, to fix the ring to the skull. Carprofen (4mg/kg every 24h) was administered i.p. for the following 72 hours.

Live Imaging

For multiphoton imaging, we used an upright Zeiss LSM710 confocal microscope equipped with a Ti:Sa laser (Chameleon Vision II) from Coherent (Glasgow, Scotland) and 2 external photomultiplier detectors for red and green fluorescence.[88] Anesthetized animals (1.5 % of isoflurane) were placed on a heating pad under the microscope. For visualization of the vasculature, 5 min prior to the

imaging, the fluorescent tracer Tetramethylrhodaminisothiocyanat-Dextran (TMR-Dextran), 3000 Da MW (Sigma-Aldrich, St.Luis, MI, UA) was injected subcutaneously. The scanning was performed with Z-stack, 50-100 μm depth, laser (900 nm) power from 6-8% till 12-16% depending on the region of interest (ROI) depth. GAASP detector with LP<570 nm filter for the GFP channel, LP>570 nm for the TMR channel, and NDD detector SP<485 nm for the bone visualization, all with master gain 600. Image size 1024x1024, 8 bit. Objective: W Plan-Apochromat 20x/1.0 DIC M27 75mm. For the series scanning, the laser power was 8-10%, 5 frames every 1 s. For each animal, 2-3 ROI was chosen which were imaged at baseline, 2, 24, and 72 hours post-stroke, or at the respective time point for naïve and sham-operated animals.

Behavioral experiments - Neuroscore

Neuroscore[24] was performed to assess each animal's general and focal deficits every day. The scoring was composed of general deficits (scores): fur (0 to 2), ears (0 to 2), eyes (0 to 4), posture (0 to 4), spontaneous activity (0 to 4), and epileptic behavior (0 to 12); and focal deficits: body asymmetry (0 to 4), gait (0 to 4), climbing on a surface inclined at 45° (0 to 4), circling behavior (0 to 4), forelimb asymmetry (0 to 4), compulsory circling behavior (0 to 4), and whisker response to touch (0 to 4). This resulted in a score of 0 to 56 in total; up to 28 from general and up to 28 from focal deficits.

Perfusion, fixation and tissue preparation

After the mice were anesthetized with a mixture of midazolam, medetomidine and fentanyl (MMF) (1ml/100g of body mass for mice; i.p.), and showed no pedal reflex, they were intracardially perfused with 0.1 M PBS (combined with heparin, 10 U/ml, Ratiopharm). 100-125 mmHg pressure with a Leica 13 Perfusion One system was used for perfusion. PBS ran for 3-4 minutes for single-cell isolation experiment, 5-10 minutes for tissue clearing experiments to let the blood wash out at room temperature. For single-cell isolation experiments, bones were dissected as detailed in the Single cell isolation method section. For the tissue clearing experiments, PBS perfusion was followed by the administration of 4% paraformaldehyde (PFA) in 0.1 M PBS (pH 7.4) (Morphisto, 11762.01000) for 10-20 minutes. After removal of the skin and a washing step with PBS to clean the animal as much as possible, the animals were post-fixed by 4% PFA for the first 24 hours at 4°C and washed three times with 0.1M PBS before processing with the clearing protocol.

vDISCO whole-body immunostaining, PI labeling and clearing

The detailed protocol of vDISCO was described previously.[2,89] The mouse bodies were placed inside a 300 ml glass chamber (Omnilab, 5163279), to be filled with the appropriate solution regarding the protocol to cover the entire body of the animal (~250-300ml). A transcardial-circulator system was established in order to allow peristaltic pumping of the solutions (ISMATEC, REGLO Digital MS-4/8 ISM 834; reference tubing, SC0266), with the pressure being set at 180-230 mmHg (50-60 rpm). The tubing was set to allow pumping of the solutions through the heart (attached to a perfusion needle (Leica, 39471024)) into the vasculature with the same entry point used for PBS and PFA perfusion steps described above. The other end of the tube was immersed into the chamber with a loose end to allow suction of the solution into the body. The samples were initially perfused with a decolorization solution (25% of CUBIC reagent 1[90] which is composed of 25 wt% urea (Carl Roth, 3941.3), 25 wt% N,N,N',N'-tetrakis (2-hydroxypropyl)ethylenediamine (Sigma, 122262) and 15 wt% Triton X-100 (AppliChem, A4975,1000) in 0.1 M PBS)) for 2 days, refreshing the solutions every 12h. Samples were washed with PBS for 3x2h. Then, decalcification solution (10 wt/vol% EDTA in 0.01 PBS, pH~8-9, Carl Roth, 1702922685) was perfused for 2 days followed by half a day with permeabilization solution composed of 0.5% Triton X-100, 1.5% goat serum (GIBCO, 16210072), 0.5 mM of Methyl-beta-cyclodextrin (Sigma, 332615), 0.2% trans-1-Acetyl-4-hydroxy-L-proline (Sigma, 441562), 0.05% sodium azide (Sigma, 71290) in 0.01 M PBS. To initiate the PI labeling and boosting, the setup was adjusted. The free end of the perfusion tube was connected to a 0.22 μm syringe filter (Sartorius, 16532) and an infrared lamp (Beuer, IL21) was aimed at the chamber to enable the solution's temperature to be around 26-28 °C. This setup was then left running for 6 days after the addition of 35 μl of nanobooster (stock concentration 0.5 – 1 mg/ml) and 290 μl of propidium iodide (stock concentration 1 mg/ml) which was added directly into the refreshed permeabilization solution. Next, the body was placed into a 50 ml tube (Falcon, 352070), with the same permeabilization and labeling solution, and an extra 5 μl of nanobooster was added. The tube was then put on a shaker at RT for 2 additional days for labeling. Atto647N conjugated anti GFP nanobooster (Chromotek, gba647n-100) and Propidium iodide (PI, Sigma, P4864), was used to boost the signal from the LysM animals and stain cell nuclei respectively in the study. Then, the animals were placed back into the initial perfusion setup, where the washing solution was perfused for 2x12h, which was composed of; 1.5% goat serum, 0.5% Triton X-100, 0.05% of sodium azide in 0.1 M PBS. 0.1 M PBS was used to wash the sample 3x2h. 3DISCO protocol was applied for whole body clearing. The animals were freed from the perfusion system, but kept in glass chambers and placed on top of shakers (IKA, 2D digital) at room temperature inside a fume hood. Glass chambers were sealed with parafilm and covered with aluminum foil along with the 3DISCO application. For dehydration, sequential immersion of tetrahydrofuran (THF) (Sigma, 186562) (50 Vol% THF, 70 Vol% THF, 80 Vol% THF, 100 Vol% THF and again 100 Vol% THF) was applied every 12 hours. Then three hours of dichloromethane (DCM) (Sigma, 270997) immersion for delipidation was followed by indefinite immersion in BABB (benzyl alcohol + benzyl benzoate 1:2, Sigma, 24122 and W213802) solution for refractive index matching.

Nr4a1 labeling and clearing of mice bones with SHANEL

Mouse heads and left femurs were collected from three-month-old, male, wild-type C57Bl6/J mice (n=3). After dissection to remove surrounding tissue, bones were decalcified in 20% (wt/vol) ethylenediamine tetraacetic acid (EDTA, pH=8.0, prepared in dH2O) for two

days at 37°C. EDTA was removed by washing in 0.1 M PBS for 3x2 hours. Bones were stained and cleared using the SHANEL protocol.[91] Samples were dehydrated in 50–70–100% ethanol/dH2O for 1 hour each, delipidated in dichloromethane/methanol (2:1) for 6 hours and rehydrated in sequence with the same dilutions backward. Next, they were incubated in acetic acid/dH2O (30 mL/L) 2 hours for extracellular matrix hydrolyzation and washed with dH2O for 3x15 minutes. Then, samples were incubated in extracellular matrix proteoglycan extraction solutions consist of 4 M guanidine hydrochloride, 0.05 M sodium acetate, and 2% Triton X-100 in 0.1 M PBS for 2 hours, washed first with dH2O and then PBS for 3x15 minutes each, followed by incubation in 10% 3-[(3-Cholamidopropyl)-dimethylammonio]-1-propansulfonat (CHAPS) + 25% N-Methyldiethanolamine (NMDEA) in dH2O at 37°C for further permeabilization and washed with dH2O for 3x15 minutes. Blocking was performed with 0.2% TritonX-100, 10% DMSO, 10% goat serum in 0.1 M PBS (blocking solution) for 6 h at 37°C. Anti-NUR77 antibody (1:200, Abcam, ab153914) were added with 0.2% Tween-20, 5% dimethyl sulphoxide (DMSO), 5% goat serum, 0.001% heparin in 0.1 M PBS (primary antibody solution) and incubated for 2 days at 37°C. After washing with 0.2% Tween-20, 0.001% heparin in 0.1 M PBS (washing solution) 4x20 minutes, bones were incubated with Goat anti-Rabbit IgG (H+L) Highly Cross-Adsorbed Secondary Antibody, Alexa Fluor 647 (1:200, Abcam, A-21245) and propidium iodide (1:1000) in 0.2% Tween-20, 5% goat serum, 0.001% heparin in 0.1 M PBS (secondary antibody solution) for 2 days at 37°C, washed with washing solution. Clearing was performed by dehydrating the bones in dilutions of 50-70-100-100% ethanol/dH2O for 12 h each, followed by delipidation of the samples in 100% dichloromethane (DCM) for 15 minutes. Finally, samples were kept in refractive index matching solution BABB (benzyl alcohol + benzyl benzoate 1:2, Sigma, 24122 and W213802). If not stated otherwise, steps were performed with constant shaking at room temperature inside a fume hood.

Human skull labeling and clearing with SHANEL

SHANEL protocol with extended incubation periods were performed on human post-mortem skull pieces. Bones were decalcified in 20% (EDTA, pH=8.0) for 1.5-2 months (until the bone becomes cuttable) at 37°C EDTA was removed by washing in 0.1 M PBS for 3x2 hours. Bones were incubated in 10% CHAPS + 25% NMDEA solution for 4 days at 37°C and washed with dH2O for 3x20 minutes. Bones were dehydrated in 50-70-100% ethanol/dH2O, each with overnight incubation, delipidated overnight in DCM/MeOH (2:1) and rehydrated. Then, samples were incubated in acetic acid for 4 hours, followed by incubation with 4 M guanidine hydrochloride, 0.05 M sodium acetate, and 2% Triton X-100 in 0.1 M PBS for 2 days and washed first with dH2O and then PBS for 3x20 minutes. Samples were incubated in a blocking solution overnight at 37°C. Staining was performed in two groups: some samples were incubated with recombinant anti-Lysozyme antibody (1:250, Abcam, ab108508) in primary antibody solution for 10 days at 37°C, washed with washing solution 4x20 minutes, then stained with Lycopersicon Esculentum (Tomato) Lectin (LEL, TL), DyLight 649 (1:500, Invitrogen, L32470) for 7 days at 37°C, washed with washing solution 4x20 minutes, incubated with Goat anti-Rabbit IgG (H+L) Highly Cross-Adsorbed Secondary Antibody, Alexa Fluor 568 (1:200, A-11036, Thermo Fisher) and washed. The remaining samples were stained with Lycopersicon Esculentum (Tomato) Lectin and Propidium Iodide (1:1000, Sigma, P4864) in primary antibody solution, washed and proceeded with clearing. Clearing was performed by dehydrating the bones in dilutions of 50-70-100-100% ethanol/dH2O for 12 h each, delipidated in 100% DCM for 15 minutes and incubated indefinitely in BABB (benzyl alcohol + benzyl benzoate 1:2, Sigma, 24122 and W213802). If not stated otherwise, steps were performed with constant shaking at room temperature inside a fume hood.

Light sheet microscopy imaging

Single plane illumination (light sheet) image stacks were acquired using an Ultramicroscope II and Ultramicroscope Blaze (Miltenyi BioTec). The available filter sets were ex 470/40 nm, em 535/50 nm; ex 545/25 nm, em 605/70 nm; ex 560/30 nm, em 609/54 nm; ex 580/25 nm, em 625/30 nm; ex 640/40 nm, em 690/50 nm. The filter sets used to capture the LysM signal and the PI labeling were 640/40 nm and 545/25 nm filter sets, respectively. Low magnification whole-body imaging of the LysM mice was performed with Ultramicroscope Blaze, with a 1.1x objective, 3x8 tiling with 35% overlap and 6 μm z-step. Exposure time was 120 ms, and laser power was 25% and 12% for LysM (647nm) and PI (594nm) channels, respectively. The depth of the scans was approximately 13 mm from dorsal and ventral surfaces, which were then reconstructed. The whole head images were taken with an Olympus MVX10 zoom body, which offered zoom-out and -in ranging from 0.63x up to 6.3x. The depth of the scans was approximately 4 mm and the z-step used was 6 μm combined with an exposure time of 200 ms. Human bone pieces were imaged with 1.1x magnification using LaVision BioTec MI PLAN 1.1x/0.1 NA (WD = 17 mm), with 1.66X zoom, as stacks, tiles were adjusted to cover all the bone surface with 25-35% overlap. The depth of scans was 1-1.5 cm. Higher magnification imaging of ROIs from mice bones were obtained with 12x magnification using PLAN 12x/0.53 NA (WD = 10 mm), LaVision 470 BioTec MI) objective as 1 tile, step size of 6 μm. Depth of scans was 0.5-1 mm. Following settings were kept the same for all samples: Exposure time: 120 ms; light sheet width: 100%; and light sheet thickness: 7 μm (NA 0.31). Multiple tile scans were stitched with Fiji's stitching plugin (http://discotechnologies.org/SHANEL/manual_stitching.py) and visualized in 3D using Imaris (v.9.6 × 64, Imaris).

Reconstruction of whole-mouse body and mouse head scans

The image stacks were acquired and saved by ImSpector (Miltenyi BioTec) as 16-bit grayscale TIFF images for each channel separately. The whole-body tiled stacks were initially stitched utilizing Fiji/ImageJ to obtain stitching on the xy-axis (http://discotechnologies.org/SHANEL/manual_stitching.py). Next, Vision 4d (Arivis AG) was used to fuse the stacks in the z-axis. For heads, one tile stacks were acquired, hence stitching was not necessary. Imaris (Bitplane AG) was used to visualize both whole body and intact mouse heads.

Fixed-formalin paraffin embedding, sectioning and H&E staining

Fixed formalin paraffin-embedded samples were acquired from decalcified human skulls initially by using the Sakura Tissue-Tek VIP 6 AI machine. The samples were placed in holders and were sectioned as 1 μm thick slices using Microm HM 355S microtome. Sections were then placed in the Sakura Tissue-Tek Prisma machine for H&E staining. The images were then acquired by a bright field microscope using 40x magnification.

Human fixed frozen sections, immunohistochemistry and imaging

Fixed samples were placed in 15% sucrose in PBS until they sunk and then in 30% sucrose overnight. Samples were frozen in SCEM medium (Sectionlab, Japan). 7 μm cryosections were cut using Kawamoto's film method[92] on a cryostat, which were then stored at −80°C until further use. For immunofluorescence, sections were thawed, rehydrated in PBS, blocked with 10% serum, and stained with antibodies in 1% serum in PBS containing DAPI for 1–2 h. Antibodies used were; anti-SMA-Alexa Fluor A594, 1A4, Abcam; Collagen-IV-FITC, 2F11, Southern Biotec; anti-PDGFRB, HPA028499, Merck; Donkey anti-Rabbit IgG (H+L) Highly Cross-Adsorbed Secondary Antibody, Alexa Fluor 647. Stained sections were washed and mounted with aqueous mounting medium (Fluoromount, Thermo Fisher, MA, US).

Sections were imaged with at a Zeiss LSM880 using a 20x objective.

Single-cell isolation for scRNAseq and proteomics

Single-cell isolation from the calvaria, brain, meninges, humerus, scapula, vertebra, femur and pelvis was done for one animal at a time. Three naïve, six MCAo-operated and three sham operated animals were pooled in threes for single-cell RNA sequencing. Another cohort of three animals for naïve, three animals for sham-operated and three MCAo-operated animals were not pooled and were treated separately for proteomic analysis. These experiments were performed on sham and MCAo animals that had the procedure three days prior to the single-cell isolation experiment. Separate equipment was utilized during the isolation to ensure high viability of cells free of contamination. The animals were anesthetized with Isoflurane and then with a Ketamine/Xylazine mixture (0.6 ml Ketamine + 0.3 ml Xylazine + 5.1 ml Saline, 0.2 ml for 20 gr animals). Then animals were transcardially perfused with 10 ml of ice-cold 0.1 M PBS. After the blood was rinsed, the calvaria bone, humerus, scapula, vertebra, femur, brain, meninges, and pelvis were dissected and processed by separate people to minimize the time required in order to keep the cell viability to a maximum and conditions comparable for all locations. The isolated cells were processed with 37°C pre-warmed DMEM (Thermo Fischer, 21013024) with 10% heat inactivated fetal bovine serum (FBS) (Sigma Aldrich, F7524-100ML). For brain cell isolation; the brain was isolated from the calvaria and the rest of the body, then, the cortex was separated and the leptomeninges was removed from the surface, the final sample consisted of the injured region. The sample was placed in 5 ml of trypsin enzyme with 0.05% concentration and incubated in a pre-heated 37°C water bath for 2 minutes. Following this, the reaction was stopped with 10 ml of 37°C pre-warmed DMEM with 10% heat inactivated FBS, the cells were dissociated by gentle tritration with a 1000μl and 200μl pipette and filtered through 70 μm Falcon™ Cell Strainers (08-771-2). For meningeal cell isolation; after the brain was removed, the meningeal dura layer that was attached to the calvaria bone, was plucked carefully using fine tipped dissection pincers (Dumont #55 Forceps, Dumostar, 11295-51, FST) under a dissection microscope. Leptomeninges was not isolated and therefore is not included in this study. The dissected meninges was placed in 37°C pre-warmed DMEM with 10% heat-inactivated FBS solution, shredded with a fine scalpel, gently titrated with a 200 μl pipette and filtered through a 70 μm Falcon™ Cell Strainers (08-771-2). For humerus, vertebrae and femur cell isolation; the bone was dissected from the body and the muscles and connective tissue were meticulously cleared off. The bone marrow inside was flushed out to the collection tube with the help of a syringe (Braun, Injekt - F Solo 2-piece Fine Dosage Syringe 1 ml x 100), and further dissection of the bone was performed by fine pincers (Dumont #55 Forceps, Dumostar, 11295-51, FST). The remaining bone was cut into small pieces and added to the cell mix. This mixture was shortly vortexed with 37 °C warmed DMEM with 10% heat-inactivated FBS and filtered with 70 μm (Falcon™ Cell Strainers, 08- 771-2). Lastly, for the flat bones, calvaria, scapula and pelvis, after carefully clearing the non-bone parts in the sample i.e., muscles and connective tissue, they were cut into small pieces (Extra Fine Bonn Scissors, 14084-08, FST), and shortly vortexed and filtered through 70 μm Falcon™ Cell Strainers (08-771-2). After all the samples were ready, they were centrifuged at 4 °C, with 1000 rpm, for 5 minutes. The supernatant of all samples was then discarded and the remaining precipitate was put into small 1.5 ml Eppendorf tubes (Eppendorf Safe-Lock Tubes, 1.5 mL, Eppendorf Quality™, 0030120086) after resuspension with DMEM. Cell viabilities and numbers were checked with trypan blue by an automated cell counter (TC20™ Automated Cell Counter) and controlled by manual counting (Neubauer Cytometry Chamber, MARI0640031).

Cell sorting and plate-based bulk RNA-sequencing

6-month-old mice were used for this study (3 5XFAD, 3 wildtype littermates). Cell sorting for CD45 and CD11b positive cells, cDNA generation and library construction was performed as described previously.[93] Briefly, after cells were passed through a 70 μm cell strainer, staining was performed for 15 min using 7AAD (Thermo Fisher, A1310, 25 ug/ml) and the antibodies against CD45 (eFluor 450,30-F11, eBioscience,Cat.:48-0451-82, 1:200) and CD11b (PE/Cy7,M1/70, eBioscience, Cat:25-0112-82,1:200). Cells were then washed with PBS (Sigma, D8537). Viable (7AAD negative) immune cells (CD45 and CD11b positive cells) were sorted by flow cytometry (SH800; Sony) into the 96-well plates by groups of 50 cells per well (we acquired 69 samples). The 96-well plates were filled with 4 μl lysis buffer containing 0.05% Triton X-100 (Sigma), ERCC (External RNA Controls Consortium) RNA spike-in Mix (Ambion,Life

Technologies) (1:24000000 dilution), 2.5 μM oligo-dT, 2.5 mM dNTP and 2 U/μl of recombinant RNase inhibitor (Clontech). The plate was spun down and frozen at -80 C.

cDNA and cDNA libraries were generated using an improved version of the Smart-seq2 protocol. The plates with the sorted pools were first thawed and then incubated for 3 min at 72°C and immediately placed on ice. To perform reverse transcription (RT), we added to each well a mix of 0.59 μl H2O, 0.5 μL SMARTScribe™ Reverse Transcriptase (Clontech), 2 μL 5x First Strand buffer, 0.25 μl Recombinant RNase Inhibitor (Clontech), 2 μl Betaine (5 M Sigma), 0.5 μl DTT (100 mM), 0.06 μl MgCl2 (1 M Sigma), and 0.1 μl Template-switching oligos (TSO) (100 μM AAGCAGTGGTATCAACGCAGAGTACrGrG+G). Next, RT reaction mixes were incubated at 42°C for 90 min followed by 70°C for 5 min and 10 cycles of 50°C 2 min, 42°C 2 min; finally ending with 70°C for 5 min for enzyme inactivation. Pre-amplification of cDNA was performed by adding 12.5 μl KAPA HiFi Hotstart 2x (KAPA Biosystems), 2.138 μl H2O, 0.25 μl ISPCR primers (10 μM, 5′ AAGCAGTGGTATCAACGCAGAGT-3), 0.1125 μl Lambda Exonuclease under the following conditions: 37°C for 30 min, 95°C for 3 min, 20 cycles of (98°C for 20 sec, 67°C for 15 sec, 72°C for 4 min), and a final extension at 72°C for 5 min. Libraries were then cleaned using AMPure bead (Beckman-Coulter) cleanup at a 0.7:1 ratio of beads to PCR product. Library was assessed by Bioanalyzer (Agilent 2100), using the High Sensitivity DNA analysis kit, and also fluorometrically using Qubit's DNA HS assay kits and a Qubit 4.0 Fluorometer (Invitrogen, LifeTechnologies) to measure the concentrations. Samples were normalized to 160 pg/μL. Sequencing libraries were constructed by using an in-house produced Tn5 transposase.[94] Libraries were barcoded with the Illumina Nextera XT (FC-131-1096, Illumina) and pooled, then went through three rounds of AMPure bead (Beckman-Coulter) cleanup at a 0.8:1 ratio of beads to library. Libraries were sequenced 2x100 reads base-pairs (bp) paired-end on Illumina HiSeq4000.

Single-cell suspension isolation from the human bones for proteomics

Bone samples were collected into formalin and were washed with PBS within 24 hours of fixation. Then, samples were placed in 20% EDTA (pH∼8) in 37°C. EDTA was changed every second day. When all bones reached a cuttable softness with scissors and a scalpel, the samples were washed with PBS overnight. 20 skull, vertebra and pelvis were dissected by carefully clearing the non-bone parts in the sample i.e., muscles and connective tissue. The same sizes of bones were cut into small pieces on a glass petri-dish with PBS. The resulting cell suspension was filtered through 40 μm Falcon™ Cell Strainers into a 50 ml Falcon tube. The samples were centrifuged for 5 minutes in 12000g. The supernatant was discarded. The pellet was resuspended in 1 ml pbs and transferred to 1.5 ml Eppendorf tube (Eppendorf Safe-Lock Tubes, 1.5 mL, Eppendorf Quality™, 0030120086). The tubes were centrifuged for another 5 minutes in 12000g. PBS was discarded and samples were stored in -80 until all samples were acquired.

Single-cell isolation from human skull for scRNAseq

Sample was sectioned in the clinic with an electric saw to generate thinner, smaller pieces and was collected in DMEM + 10% FCS. The sample was brought to lab from the clinic on ice. Using a needle and a syringe, the bone marrow cells were flushed DMEM + 10% FCS (Gluc + /Glut +) into a 50 ml tube. Bone was further crushed using a mortar on ice in order to release more marrow cells into the cell suspension. Each sample was filtered through a 70 μm strainer and centrifuged at 500 rcf for 5 mins at 4°C. Supernatant was discarded. The pellet was resuspended in 10 ml chilled PBS / 2%BSA. Then, the cells were visually counted using trypan blue to assess the high viability. Next, the samples were washed again as above and resuspended for loading to the 10X Chromium.

scRNA sequencing – 10x Genomics

Samples were used for scRNA-seq if the fraction of dead cells determined by trypan blue staining was below 20%. Cell suspensions were diluted with PBS/2% FCS for mouse experiments and PBS/2% BSA for the human experiment, to a final concentration of 1000 cell/μl and 17.000 cells per sample were loaded onto 10x Chromium Single Cell RNA-seq chips to recover a target cell number of 10.000 cells per sample. Libraries were generated in three replicates for the mouse experiment. The 10x Chromium Single Cell 3′ Library & Gel Bead Kit v3 for mouse and v3.1 for human was used following the manufacturer's protocol. Libraries were sequenced on an Illumina HiSeq 4000 (150 bp, paired end) for mouse experiment and NovaSeq6000 for human experiment.

Sample preparation for bulk RNA isolation

Mice were deeply anaesthetized with ketamine (120mg/kg) and xylazine (16mg/kg) and transcardiacally perfused with cold PBS. The necessary samples were quickly harvested and placed in ice-cold RNAlater solution in 1.5 ml tubes.[95] The samples were left in RNAlater solution for 24h in 4 °C. Next, the solution was discarded and samples were placed in -80 for storage until RNA isolation.

Bulk RNA isolation, library preparation and sequencing

The samples were processed 12 at a time. Samples were in a 2 ml Eppendorf tube. 1 ml of Trizol and a metal bead was added to each sample. Samples were then lysed in Tissue Lyser with 30 Hz frequency for 3 minutes. 200 μl of Chloroform was added to each sample. After rigorous vortexing, samples were incubated at room temperature for 15 minutes. Next, samples were centrifuged at 10,000 g for 10 minutes at 4°C. The upper phase of the sample was transferred into a new tube. 240 μl, 100% seq-grade EtOH was added and samples were briefly vortexed. The samples were loaded into Econospin columns and were centrifuged at 13000 g for 30 seconds at room temperature. Flow-through was discarded. The samples were washed 3x with RPE buffer (Qiagen #1018013) and centrifuged at 13000 g for 30 seconds each time. After the last wash, sample was centrifuged dry. Next, columns were

transferred into new 1.5 ml tubes with open lids for 10 minutes. RNAse free water was used to elute the sample in 30 μl. Final centrifuge was performed at 9000 g for 2 minutes at room temperature. All samples were subjected to Nanodrop, Qubit and Bioanalyzer assays in order to determine quality and quantity of each sample. Samples were stored at -80 until all samples were processed. Only samples with RIN>8 were used. Illumina ligation stranded mRNA prep kit was used for library preparation and the sequencing of 95 samples were performed on a PE 2x100 flow cell.

Flow cytometry

Cell isolation and labeling

Cell isolations were prepared as previously described in "Single cell isolation for scRNAseq and proteomics" section. The suspended cells were centrifuged at 500g for 7 minutes at 4°C. The supernatant was discarded, and samples were resuspended in 1 ml FACS buffer. The 1 ml buffer with cells was transferred to a FACS tube. Tubes were spun down at 500 g 7 minutes at 4°C. The supernatant was discarded and each sample was resuspended in 50μl FACS buffer with 0.5 μl FC blocker. The samples were incubated for 10 minutes, in dark on ice. Then 50 μl of antibody mix was added to each sample: (1 μl each from Ly-6G/Ly-6C (APC/Cyanine7, Biolegend, #108423), Cd11c (APC, Biolegend #117309), F4/80 (PerCP-Cy5, BD, #567202), CD45 (BUV395, BD. #565967), CD117(BV421, BD, #566290), I-A/I-E (Brilliant Violet 510, Biolegend, #107635), Ter-119 (BV650, Biolegend, #128035), NK-1.1 (Brilliant Violet 711, Biolegend, #108745), CD11b (Brilliant Violet, Biolegend, #101243), CD179a (PE, Biolegend, #143603), CD45R/B220 (PE-Cy5, BD, #553091), CD182 (CXCR2) (PE/Dazzle 594, Biolegend, 149317), Ly-6A/E (PE Cy 7, BD, #561021) and 1.5 μl each from CD3 Alexa Fluor 700, BD, #561388), Ly-6C (Brilliant Violet 605, Biolegend, 128035), 34 μl FACS buffer). Samples were incubated for 15 minutes on ice in dark. After the staining 3 ml of FACS buffer was added to each sample. The samples were centrifuged at 500 g 7 minutes at 4°C. After discarding the supernatant, samples were resuspended in 200 μl of FACS buffer to be measured by the machine.

Proportions

Sample were recorded on a LSRFortessa (BD) and data were analyzed with FLowJo software (Tree Star). Cell numbers were calculated as percentage of an appropriate gate. After gating out doublets, dead cells (SytoxGreen+) and red blood cells (Ter119+), white blood cell (CD45+) subpopulations were defined as follows: T-cells (CD3+), immature B-cells (B220dim I-A/I-Evar), mature B-cells (B220+ I-A/I-E+), NK-cells (NK1.1+), monocytes (F4/80+), eosinophils (Ly6G-, SSChigh), early neutrophils (Ly6G+, CXCR2-), late neutrophils (Ly6G+, CXCR2+) and hematopoetic stem-/progenitor cells (LSK cells, Lineage-, Sca-1+, c-Kit+).

Photoconversion KikGR

Mice were anesthetized with 1.5–2% isoflurane (vol/vol), delivered in medicine air, and maintained at 37 °C throughout the procedure. Briefly, a skin midline incision was made on the head of the mouse, and the skull was exposed. Photoconversion was performed with a defocused (5-mm beam diameter) violet laser source (405 nm, peak power 4.5 mW, ThorLabs) placed 5 cm above the skull of the brain ischemic region (ipsilateral) for 3 min. Mouse skin was then sutured and allowed to recover on a heating pad until responsive. One hour or six hours after photonconversion, mice were anesthetized with isofluorane and transcardially perfused with 20 ml cold PBS containing Heparin (2U/ml). Cell suspensions from brain and skull (ipsilateral and contralateral), spleen and femur were isolated as indicated below for flow cytometric analysis and the percentage of photoconverted red cells (KikGR+) was analyzed in the appropriate cell populations.

Cell isolation

Mice were deeply anaesthetized with ketamine (120mg/kg) and xylazine (16mg/kg) and transcardiacally perfused with cold PBS. The skull, femur, spleen and brain were immediately harvested and kept on ice. The olfactory bulb and cerebellum were discarded, and the brain was mechanically dissociated in RPMI media with a douncer homogenizer, followed by a Percoll gradient centrifugation. For the isolation of skull bone marrow, meninges were peeled from the skull cup under the microscope and not included in this study. The isolated calvarium was cut into small pieces and mechanically dissociated on top of a 40 μm cell strainer with the end of a 1-mL syringe plunger. After centrifugation at 500g for 7 minutes, cell suspensions were washed with PBS or FACS buffer.

Flow cytometry of KikGR animals

For differentiation of live and dead cells we stained cells with the Zombie NIR (BioLegend). For surface marker analysis, nonspecific binding was blocked by incubation for 10 min at 4 °C with anti-CD16/CD32 antibody (Biolegend, 5 ng/μL) antibody and stained with the appropriate antibodies for 15 min at 4 °C. The following antibodies were used for extracellular staining: CD45 (clone 30-F11, eFluor450, Invitrogen # 48-0451-82), CD11b (clone M1/70, PE/Cy7, Invitrogen # 25-0112-82), Ly6C (clone HK1.4, PerCP/Cy5.5, BioLegend #128012), Ly6G (clone 1A8-Ly6g, PE-eFluor610, Invitrogen #61-9668-82), CD3 (Clone 17A2, APC, Invitrogen # 17-0032-82) and CD19 (eBio1D3, APC/eFluor780, Invitrogen # 47-0193-82).

Cells were washed with FACS buffer, resuspended in 200 μl of FACS buffer and acquired using a Cytek® Northern Lights (Cytek® Biosciences, US) and analyzed using FlowJo software (Treestar, US). Isotype controls were used to establish compensation and gating parameters.

Multiplexed RNAscope smFISH

Large tissue section staining and fluorescent imaging were conducted largely as described previously.[96] Sections were cut from fixed frozen samples embedded in OCT at a thickness of 10 μm using a cryostat, placed onto Hydrophilic Plus slides (BioSB) and stored at -80°C until stained.

Fixed frozen tissue sections were processed using a Leica BOND RX to automate staining with the RNAscope Multiplex Fluorescent Reagent Kit v2 Assay (Advanced Cell Diagnostics, Bio-Techne), according to the manufacturers' instructions. Probes may be found in Table S1, tab 37. Prior to staining, sections were post-fixed in 4% paraformaldehyde in PBS at 4°C for 15 minutes, then dehydrated through a series of 50%, 70%, 100%, and 100% ethanol, for 5 minutes each. To maximize adhesion of sections, slides were then baked at 37°C for 30 minutes. Following manual pre-treatment, automated processing included digestion with Protease III for 10 minutes prior to probe hybridisation. Tyramide signal amplification with TSA Vivid 520, TSA Vivid 570, and TSA Vivid 650 (Tocris Bioscience) and TSA-biotin (TSA Plus Biotin Kit, Perkin Elmer) and streptavidin-conjugated Atto 425 (Sigma Aldrich) was used to develop RNAscope probe channels.

To reduce autofluorescence, slides were treated immediately post-staining with TrueBlack® Plus Lipofuscin Autofluorescence Quencher (Biotium) for 5 minutes, then washed several times with PBS before mounting with ProLong Gold Antifade Mountant (Thermo).

High-resolution imaging

Stained sections were imaged with a Perkin Elmer Opera Phenix Plus High-Content Screening System, in confocal mode with 2 μm z-step size, using a 40X (NA 1.1, 0.149 μm/pixel) water-immersion objective. Channels: DAPI (excitation 375 nm, emission 435-480 nm), Atto 425 (ex. 425 nm, em. 463-501 nm), TSA Vivid 520 (ex. 488 nm, em. 500-550 nm), TSA Vivid 570 (ex. 561 nm, em. 570-630 nm), TSA Vivid 650 (ex. 640 nm, em. 650-760 nm).

Image stitching

Confocal image stacks were stitched as two-dimensional maximum intensity projections using proprietary Acapella scripts provided by Perkin Elmer. Resulting images were viewed as OME-TIFFs using OMERO Plus (Glencoe Software).

Scanning electron microscopy

Human skull samples were freshly prepared, dissected and immersed into fixative (4% PFA and 2.5% glutaraldehyde in 0.1 M sodium cacodylate buffer, pH 7.4; Science Services). After decalcification in EDTA for 1 month at 4°C and 1 month at room temperature, skull samples were washed, further dissected into 1x2 mm slabs bearing dura and bone layers and immersion fixed for 24h in fixative. We applied a standard rOTO en bloc staining protocol including postfixation in 2% osmium tetroxide (EMS), 1.5% potassium ferricyanide (Sigma) in 0.1 M sodium cacodylate (Science Services) buffer (pH 7.4).[97] Staining was enhanced by reaction with 1% thiocarbohydrazide (Sigma) for 45 min at 40°C. The tissue was washed in water and incubated in 2% aqueous osmium tetroxide, washed and further contrasted by overnight incubation in 1% aqueous uranyl acetate at 4°C and 2 h at 50°C. Samples were dehydrated in an ascending ethanol series and infiltration with LX112 (LADD). Blocks were screened for tunnel structures transversing from the bone to the dura on cross sections using sequential trimming (TRIM2, Leica) and light microscopy of semithin sections. Serial sections were taken with a 35° ultra-diamond knife (Diatome) on an ATUMtome (Powertome, RMC) at a nominal cutting thickness of 200 nm and collected on freshly plasma-treated (custom-built, based on Pelco easiGlow, adopted from M. Terasaki, U. Connecticut, CT), carbon coated Kapton tape (kindly provided by Jeff Lichtman and Richard Schalek). Tape stripes were assembled onto adhesive carbon tape (Science Services) attached to 4-inch silicon wafers (Siegert Wafer) and grounded by adhesive carbon tape strips (Science Services). EM micrographs were acquired on a Crossbeam Gemini 340 SEM (Zeiss) with a four-quadrant backscatter detector at 8 kV using ATLAS5 Array Tomography (Fibics). We acquired medium resolution (40-100 nm) images of the entire section and the region of interest and processed in Fiji.[82]

Proteomics Sample Preparation

Sample preparation for proteomics analysis was performed as described previously with slight modifications.[98] Briefly, for mouse samples, SDC lysis buffer (2% SDC, 100 mM Tris-HCl pH 8.5) was used to lyse the cell pellets at 95°C for 45 min at 600 rpm in a thermoshaker. For human samples which were fixed in PFA, prior to the SDC lysis buffer step, the samples were first resuspended in 6% SDS buffer, heat denatured, sonicated and then precipitated using 80% acetone overnight in -20°C. Next day, these samples were centrifuged and the pellet was resuspended in SDC lysis buffer. After this, the procedure remains the same for both mouse and human samples. Naïve meninges samples from mice were lost during sample preparation. The samples in SDC buffer were sonicated in high mode for 15 cycles (30 sec OFF, 30 sec ON) (Bioruptor® Plus; Diagenode). The samples were again heated at 95°C for 45 min at 600 rpm in a thermoshaker. The extracted and solubilized protein concentration was estimated by BCA method and 25 μg of protein was further reduced and alkylated using a final concentrations of 10 mM TCEP and 40 mM CAA in dark, at 45°C for 10 min with 600 rpm in a thermoshaker. The protein samples were digested overnight with Trypsin and LysC (1:50, protease:protein ratio) at 37°C, 1,000 rpm shake. Resulting peptides were acidified with 1% TFA 99% isopropanol with 1:1 volume-to-volume ratio, vortexed and centrifuged to pellet residual particles. The supernatant was transferred to fresh tubes and subjected to in-house built StageTip clean-up consisted of three layers of styrene divinylbenzene reversed-phase sulfonate (SDB-RPS; 3 M Empore) membranes. Peptides were loaded on the activated (100% ACN, 1% TFA in 30% Methanol, 0.2% TFA, respectively) StageTips, run through the SDB-RPS membranes, and washed by EtOAc including 1% TFA, isopropanol including 1% TFA, and 0.2% TFA, respectively. Peptides were then eluted from the membranes via 60 μL elution buffer (80% ACN, 1.25% NH4OH) and dried using vacuum centrifuge

(40 min at 45°C). Finally, peptides were reconstituted in 10 μL of loading buffer (2% ACN, 0.1% TFA) and peptide concentration was estimated using PierceTM Quantitative Colorimetric Peptide Assay.

Liquid chromatography and mass spectrometry (LC-MS/MS)

The mass spectrometry data was acquired in data independent acquisition (DIA) mode. The LC-MS/MS analysis was carried out using EASY nanoLC 1200 (Thermo Fisher Scientific) coupled with trapped ion mobility spectrometry quadrupole time-of-flight single cell proteomics mass spectrometer (timsTOF SCP, Bruker Daltonik GmbH, Germany) via a CaptiveSpray nano-electrospray ion source. Peptides (50 ng) were loaded onto a 25 cm Aurora Series UHPLC column with CaptiveSpray insert (75 μm ID, 1.6 μm C18) at 50°C and separated using a 50 min gradient (5-20% buffer B in 30 min, 20-29% buffer B in 9 min, 29-45% in 6 min, 45-95% in 5 min, wash with 95% buffer B for 5 min, 95-5% buffer B in 5 min) at a flow rate of 300 nL/min. Buffer A and B were water with 0.1 vol% formic acid and 80:20:0.1 vol% ACN:water:formic acid, respectively. MS data were acquired in single-shot library-free DIA mode and the timsTOF SCP was operated in DIA/parallel accumulation serial fragmentation (PASEF) using the high sensitivity detection-low sample amount mode. The ion accumulation and ramp time was set to 100 ms each to achieve nearly 100% duty cycle. The collision energy was ramped linearly as a function of the mobility from 59 eV at 1/K0 = 1.6 Vs cm−2 to 20 eV at 1/K0 = 0.6 Vs cm−2. The isolation windows were defined as 24 X 25 Th from m/z 400 to 1000.

Proteomics data processing

diaPASEF raw files were searched against the human uniport database using DIA-NN.[99] Peptides length range from seven amino acids were considered for the search including N-terminal acetylation. Oxidation of methionine was set as a variable modification and cysteine carbamidomethylation as fixed modification. Enzyme specificity was set to Trypsin/P with 2 missed cleavages. The FASTA digest for library-free search was enabled for predicting the library generation. The FDR was set to 1% at precursor and global protein level. Match-between-runs (MBR) feature was enabled and quantification mode was set to "Robust LC (high precision)". The Protein Group column in DIA-NN's report was used to identify the protein group and PG.MaxLFQ was used to calculate the differential expression.

Small animal PET/MRI acquisition

All rodent PET procedures followed an established standardized protocol for radiochemistry, acquisition times and post-processing,[100,101] which was transferred to a novel PET/MRI system.[102] All mice were scanned with a 3T Mediso nanoScan PET/MR scanner (Mediso Ltd, Hungary) with a triple-mouse imaging chamber. A 15-minute anatomical T1 MR scan was performed at 45 min after [18F]-GE180 injection (head receive coil, matrix size 96 × 96 × 22, voxel size 0.24 × 0.24 × 0.80 mm^3, repetition time 677 ms, echo time 28.56 ms, flip angle 90°). Injected dose was 13 ± 2 MBq delivered in 200 μl saline via venous injection. PET emission was recorded at 60-90 min p.i. PET list-mode data within 400–600 keV energy window were reconstructed using a 3D iterative algorithm (Tera-Tomo 3D, Mediso Ltd, Hungary) with the following parameters: matrix size 55 × 62 × 187 mm^3, voxel size 0.3 × 0.3 × 0.3 mm^3, 8 iterations, 6 subsets. Decay, random, and attenuation correction were applied. The T1 image was used to create a body-air material map for the attenuation correction.

Human TSPO-PET imaging acquisition

All participants were scanned at the Department of Nuclear Medicine, LMU Munich, using a Biograph 64 PET/CT scanner (Siemens, Erlangen, Germany). Before each PET acquisition, a low-dose CT scan was performed for attenuation correction. Emission data of TSPO-PET were acquired from 60 to 80 minutes[62,103] after the injection of 187 ± 11 MBq [^{18}F]GE-180 as an intravenous bolus, with some patients receiving dynamic PET imaging over 90 minutes. The specific activity was >1500 GBq/μmol at the end of radiosynthesis, and the injected mass was 0.13 ± 0.05 nmol. All participants provided written informed consent before the PET scans. Images were consistently reconstructed using a 3-dimensional ordered subsets expectation maximization algorithm (16 iterations, 4 subsets, 4 mm gaussian filter) with a matrix size of 336 × 336 × 109, and a voxel size of 1.018 × 1.018 × 2.027 mm. Standard corrections for attenuation, scatter, decay, and random counts were applied. For the AD cohort, emission data of Aβ-PET were acquired from 90 to 110 minutes after injection of 188 ± 10 MBq [^{18}F]flutemetamol. Aβ-PET was assessed by a visual read (one expert reader), and the decision of Aβ-positivity/negativity was supported by a software-driven approach implemented in HERMES Gold (V4.17, HERMES Medical Solutions AB, Stockholm, Sweden). One positive evaluated target region (frontal, temporal, parietal, posterior cingulate) defined the scan as positive.

QUANTIFICATION AND STATISTICAL ANALYSIS

Single-cell RNA data analysis

Count matrix generation

Count matrices were created using CellRanger (v. 3.0.2) aligning reads to the mouse genome mm10 (ensrel97). Spliced and unspliced matrices for RNA-velocity[43] analysis were computed using the velocyto (0.17.17) pipeline. (n=3 pooled animals for sham and n=6 pooled animals for MCAo).

Quality control

Samples were jointly analyzed using scanpy[83] (v. 1.6) and anndata (v. 0.7.5) in Python 3.7. Different quality control filters[104] were used to account for the characteristics of the different samples: In bone samples, all cells with a mitochondrial read fraction higher than 0.2 were removed. In meninges and brain samples, thresholds were 0.3 and 0.6, respectively. Further, cells with less than 1000 UMI counts (bone samples) and 500 UMI counts (meninges, brain), and more than 50,000 UMI counts were removed. We did not apply a minimum gene filter per cell to retain erythroblasts. All genes expressed in less than 10 cells were removed. To estimate doublets, we used the tool scrublet with a doublet score threshold of 0.1 and removed cells with a higher doublet score. Additionally, we filtered out two small clusters that showed dendritic cell markers as well as markers from other cell types as they might also be doublets, and a sub cluster of early monocytes that showed an increased mitochondrial fraction. Finally, our filtered dataset contained 147,082 cells expressing 17,040 genes coming from 32 samples.

Data preprocessing

To normalize the data with scran,[105] size factors were determined as follows: data were first temporarily normalized by total with a target sum of 10,000 per cell followed by log+1-scaling. Then, for each cell, 30 nearest neighbors were computed and data were clustered with Leiden clustering at default resolution 1. Small clusters with less than 100 cells were merged with closely related clusters based on the PAGA graph. For PAGA graph calculations we used scanpy's implementation with default parameters.[106] Then, size factors were computed on these clusters and the UMI count data were divided by scran size factors for each cell and log+1-scaled. Then, mitochondrial reads were removed and 4,000 highly variable genes per sample were computed (highly_variable_genes with flavor "cell_ranger" in scanpy). Further, cell cycle scores were computed (score_genes_cell_cycle in scanpy). To evaluate batch effects, PC regression scores for the variance explained by cell cycle, anatomic region and condition were computed for the full dataset and the MCAo replicates, respectively. PC regression scores were lowest in the condition and replicate covariate, respectively, and therefore no batch effect correction was performed.

Dendrograms

With scanpy's dendrogram function SciPy's hierarchical linkage clustering was calculated on a Pearson correlation matrix over regions which was calculated for 50 averaged principal components.

Cell type annotations

Cell types were annotated according to a two-step procedure. In a first step a Leiden clustering was calculated on the log-normalized data. The Leiden clusters were annotated with coarse cell type labels according differentially expressed known markers. In the second step leiden clustering with multiple resolutions were calculated for each coarse cell type. Based on differently expressed known markers, as well as additional information like number of genes[107] and scVelo[43] implementation of RNA velocity[42] the clusters were annotated with fine cell types, and coarse annotations were refined.

Variance explained by covariates and PC regression

To quantify how strong cell type populations of each region diverge from the other regions the explained variance was calculated by linear regression in PCA space. For each bone the cell type populations were grouped into the given bone vs the other bones. Scores were only calculated if there were at least 20 cells in each of both groups. 50 principal components were calculated for each cell type. A linear regression on the group variable was calculated for each PC component. R2 scores of the linear regression were multiplied by the eigenvalues of the pc components and normalized by the eigenvalue sum, and finally summed up to the variance explained. The significance of each obtained variance explained score was measured via a permutation test. The region annotations were permuted 1000 times. Scores with a p-value below 0.0001 were considered as significant. We decided to exclude scapula in further downstream analysis because we detected an overall decrease in log counts in this sample.

Combinatorial DE tests

For each gene, two t-tests were calculated to identify if the gene is upregulated in a group of bones. To define the two bone groups for a given gene, bones were ordered by the gene's mean expression and split in two groups at the highest mean expression gap. The first t-test was conducted on the two groups and the second on the two bones closest to the expression gap. The second test ensures that the expressions of the two closest bones of the two groups are significantly different. The maximal p-value and minimal log fold change of both tests were used to identify DEGs. The chosen thresholds are $p < 0.05$ and LF change > 1 (> 0.5 for neutrophils analysis).

Other differential expression tests

Differences of DAMP expressions and pro- and anti-inflammatory genes were measured with t-tests ($p < 0.05$, Benjamini-Hochberg correction). The distributions of each DAMP's expression over CD45+ cells of each bone in the scRNA-seq data were tested for significance differences between conditions. The pro- and anti-inflammatory genes were tested individually as well as the mean expression of pro- and anti-inflammatory gene sets respectively between groups of bones and conditions.

Ligand receptor (LR) interactions

For each bone ligand receptor interaction pairs between cell types were calculated with CellPhoneDB's[39] statistical analysis. An interaction is defined by four variables: ligand, receptor, ligand cell type and receptor cell type. For a fair comparison between bones, pairs were only calculated on cell types that had at least 10 cells in each bone. The statistical analysis was applied on log normalized counts. 400 cells per cell type were sampled to generate a uniform background distribution of the permutation test which otherwise would be skewed towards highly abundant cell types. Cell types with more than 400 cells were down sampled using geometric sketching[108] (geosketch v 1.2), while the other cell types were up sampled. Strict thresholds based on the CellPhoneDB p-values

were applied to reduce the number of false positives: Interactions were considered as significant for p-values equal to 0 (1000 permutations). Interactions were only considered unique to a bone group if the p-value difference between that group and the non-significant group was above 0.95.

Gene ontology enrichment

Enrichment of Gene ontology (GO) terms for biological processes were calculated using GProfiler.[109]

RNA velocity

RNA velocity[42] in its scVelo[43] (v 0.2.3) implementation was used as follows: the dataset with spliced and unspliced raw counts was reduced to the given cell type and condition. Then genes were filtered to 2000 genes with at least 20 counts each, and cells were normalized (filter_and_normalize function in scVelo). First and second order moments for velocity estimation with the scVelo's dynamical model were calculated with default parameters.

Pseudotime analysis

Diffusion pseudotime[44] was calculated to order cells along the neutrophil maturation trajectory. For naive, sham and MCAo a PCA and neighbors' graph were recalculated on the neutrophils population. The default parameters of scanpy's tl.dpt function was used. As root point we selected the most extreme pro-neutrophil cell from the umap. For cell density visualization along pseudotime[44] the cell count was smoothed with a Gaussian kernel according to the default parameters of seaborn's (v 0.11.1) kdeplot function. Densities were normalized for each region separately.

Donor Deconvolution based on SNPs

To enable statistical tests between different groups in the scRNA-seq data and validate the obtained cell type proportions we deconvolved the samples of pooled animals based on obtained SNPs profiles of the measured transcripts. For SNPs calling we used cellsnp-lite[110] (v. 1.2.2). Based on the obtained SNPs of each cell vireo[111] (v. 0.2.3) was used to demultiplex the 3 animals in each pooled sample. Erythrocytes were removed from the analysis as they only express the hemoglobin genes which leads the deconvolution algorithm to identify Erythrocytes as one donor.

Correlation of proportions with flow cytometry data

Pearson-correlation between cell type proportions of scRNA-seq and flow cytometry was measured over all cell types obtained in flow cytometry. Since flow cytometry measurements are relative to gated subgroups, we transformed the proportions of scRNA-seq cell types relative to comparable coarse subgroups as well. The significance of proportion differences between bones or conditions were obtained by t-tests over flow cytometry samples and over SNPs based deconvolved animals of the pooled scRNA-seq samples. A few cell type proportion differences were observed consistently with statistical significance ($p < 0.05$) in both methods. E.g., we observed a significantly higher number of mature B-cells in sham-operated and MCAo operated compared to naïve animals (Table S1, tab 3). Other cell type differences were observed with either one of the methods, but did not always reach statistical significance in both (Table S1, tabs 3 and 4). Upon injury, B-cell progenitors were depleted in both the flow cytometry and the scRNAseq data. Moreover, mature neutrophils in the calvaria had a strong trend for an increased cell proportion that, however, did not reach significance (Table S1, tabs 1–4).

Other differential expression tests

Differences of DAMP expressions and pro- and anti-inflammatory genes were measured with t-tests ($p < 0.05$, Benjamini-Hochberg correction). The distributions of each DAMP's expression over CD45+ cells of each bone in the scRNA-seq data were tested for significance differences between conditions. The pro- and anti-inflammatory genes were tested individually as well as the mean expression of pro- and anti-inflammatory gene sets respectively between groups of bones and conditions.

Bulk RNA data analysis for 5xFAD dataset

BCL files were demultiplexed with the bcl2fastq software from Illumina. After quality control with FastQC, reads were aligned using rnaSTAR65 to the GRCm38 (mm10) genome with ERCC synthetic RNA added. Read counts were collected using the parameter "quantMode GeneCounts" of rnaSTAR and using the unstranded values. We filtered out data points with less than 6000 genes or a mitochondrial fraction above 0.0015. Data points were log-normalized by total counts. The significance of the *Tspo* difference between WT and 5xFAD was calculated with a t-test. Differentially expressed genes between bones were obtained from t-tests with Benjamini-Hochberg correction and a p-value threshold of 0.05. The PCA was calculated on log normalized counts. (n=3 5xFAD, 5 wildtype animals, 50 cells per sample, 69 samples in total: 37 wildtype, 32 5xFAD).

Bulk RNA data analysis for MCAo dataset

For the count matrix generation reads were aligned to the GRCm39 genome with Salmon[112] using the nf-core/rnaseq pipeline[113] (v. 3.9). No sample was excluded after quality control. Differentially expressed genes between bones were obtained using the DESeq2 model.[114] The UMAP was calculated based on a PCA on log-normalized counts (normalization by total counts). For the comparison with scRNA-seq mouse data the pearson-correlation between mean log raw counts over genes of single cell and bulk data of each bone was calculated. (n=5 naïve, 5 sham, 6 MCAo animals).

Statistical analysis of KikGR animals

Due to high penetration of UV laser, some Cd11b+ cells, that could be microglia were illuminated as well. To control for this offset, the percentage of microglia illuminated was subtracted from myeloid cells. Acquired data was analyzed and visualized using GraphPad

Prism (version 8.0) using two-tailed t-test. (Each dot represents a biological replicate, n=5 for 1h and n=4 animals for 6h, data represented as ± SEM).

Image Analysis

2-Photon analysis

We analyzed the 2-photon image stacks as maximum intensity projected time-series (3 frames per batch). We trained a random forest pixel classifier (Ilastik[115] with default settings) on 3 images of the green channel (LysM-eGFP) and used that for subsequent classification of the LysM-eGFP channel of each image stack. This gave 8-bit probabilities for each frame, which we then thresholded and watershed-segmented using ImageJ.[82] We performed this procedure with the pixel count (=area) occupied by GFP+ cells. We normalized $LysM^{+}$ cell density at each time point to the cell density at baseline for each ROI. To account for other influences such as laser skull exposure, laser illumination, and anesthesia we further normalized the fold changes in sham and MCAo to those observed in naïve animals at the same time point. The quantification graph was analyzed and visualized using GraphPad Prism (version 8.0) using two-tailed t-test and simple linear regression. (n=3 for naïve and sham and n=5 animals for MCAo, data represented as ± SEM.)

Tissue cleared mouse head analysis

For quantification of the mouse heads, manual ROIs were drawn on the frontal and parietal skull bones. C57BL6/J mice has been used for naïve condition quantification. The areas above manually selected threshold based on bone marrow coverage were recorded. The quantification graph was analyzed and visualized using GraphPad Prism (version 8.0) (Ordinary one-way ANOVA with multiple comparisons). (n=3 per group, data represented as ± SEM).

Nr4a1 *analysis*

Three naïve mice heads and femurs were labeled with *Nr4a1* antibody and propidium iodide (for nuclei staining) and high-resolution images were obtained for 20 ROIs from the mouse skulls and 14 ROIs from the femurs (Figure 2D). We then quantified the number of voxels with a signal above threshold and found that a significantly higher percentage of *Nr4a1* positive voxels in the mouse head (Figure 2E). For the quantification of *Nr4a1*, same-sized regions of interest (ROIs) of 12x scans of the Nr4a1 channel was used. For each of these, an expert manually selected the signal activation threshold after visual inspection in an image analysis software (e.g., Fiji). These thresholds were then used in Python to obtain binary masks of active expression of the same size as the ROI. Pixels that have higher intensity than the threshold in the Nr4a1 channel are assigned the value of 1 (positive pixels), and the rest, 0. The total amount of pixels above threshold in each ROI is the number of positive pixels in the binary mask, whereas the percentage of signal in the volume is calculated as the number of positive pixels divided by the number of total pixels in the ROI. The quantification was analyzed and visualized using GraphPad Prism (version 8.0) using two tailed t-test. (n=3 per group, data represented as ± SEM).

Human skull segmentation and channel measurement

Segmentation of the skull channels network and measurement of skull meninges channels were performed by using syGlass (https://www.syglass.io/). This software allows to visualize the microscopic data of the light sheet microscopes in 3D in Virtual Reality (VR). To segment and measure the data, smaller ROIs were cut out in VR. In these ROIs the openings in the meninges connected to the skull meninges channels were segmented up to the channel network that connects to the first bone marrow chambers in the skull. Then the Virtual reality software was used to change visual settings in order to measure, segment and to generate videos in 3D. The quantification was analyzed and visualized using GraphPad Prism (version 8.0) using two tailed t-test. (n=7 post-mortem samples, 23 ROI in total, 522 channels, data represented as ± SEM).

Graph Representation of the Skull Channels

In order to achieve an additional compact representation of the skull channels we extracted a graph representation from the human skull segmentation described above using VR. We used the *voreen* open-source software to generate a centerline representation and second a graph representation with edges and nodes. In total, the skull channel graph consists of 399 nodes, and 440 edges with an average node degree of 2.21. The images are rendered using the Syglass software (Figure S6R).

Proteomics data analysis

Both human and mouse samples were jointly analyzed using scanpy (v. 1.9.1) and anndata (v. 0.7.6) in Python 3.8 and follows similar analysis pipeline. (n=3 independent samples each for bones and brain for all conditions, n=3 for meninges MCAo and sham conditions.)

Quality control

All proteins expressed in less than half of the bone samples were filtered out. For mice, the meninges were excluded from the filtration criterion since we identify the least number of proteins.

Data preprocessing

The data was further log-transformed and normalised per sample. KNN imputation was our method of choice using KNNImputer (n_neighbors=5) from the sklearn package (v. 0.22).

Gene set enrichment analysis (GSEA)

Enrichment of Gene ontology (GO) terms for biological processes were analysed using GProfiler[109] and Enrichr.[116]

Weighted correlation network analysis (WGCNA)

To identify the different modules of correlated genes in our datasets, WGCNA were used [python version: PyWGCNA[117]]. This method is an unsupervised algorithms for finding clusters (modules) of highly correlated genes based on a graph where nodes represents genes/proteins and the adjacency matrix is calculated based on the co-expression similarity between the nodes. Modules are then identified as clustered of interconnected nodes (genes/proteins) using hierarchical clustering. Gene ontology enrichment is further applied for genes/proteins identified from each module are to determine the biological processes pathways related to these modules.

Dendrograms

With scanpy's dendrogram function scipy's hierarchical linkage clustering was calculated on a Pearson correlation matrix over regions which was calculated for 50 averaged principal components.

Differential expression tests

To identify differentially regulated genes across two conditions (e.g. one bone vs the rest), scanpy's method that ranks genes group using t-tests was used. The maximal p-value and minimal log fold change were used to identify differentially expressed proteins/genes (DEPs). The chosen thresholds are $p < 0.05$ and LF change > 1. These DEPs were further used to plot the volcano plots.

Small animal PET/MRI analysis

To capture skull specific PET signal from the skull in three wildtype mice, immediately after in vivo TSPO-PET imaging of mice, the brain, blood (perfusion via PBS) and all tissue surrounding the skull bone was removed. The skull bone of each mouse was imaged via a second TSPO-PET session. The signal attributable to the skull in the in vivo TSPO-PET images were compared to the signal in the respective skull-only TSPO-PET as standard of truth. For this purpose, an in-house CT template to delineate the skull bone in PET was used and a cluster-based analysis (k-means clustering) was performed, dividing the skull into 50 regions of increasing PET signal intensity. We studied TSPO-PET images of 5xFAD mice (n=6) and wild-type mice (n=6), all female at an age of 4.5 months. Normalization of injected activity was performed by cerebellar scaling[118] to ensure consistency with human data. TSPO labeling in the skull was obtained in each mouse from a fronto-parietal volume-of-interest (comprising 24 mm^3) and from a temporal volume-of-interest (comprising 16 mm^3), which were semi-automatically delineated using an in-house CT template. Fronto-polar skull was spared to avoid signal spill-over from regions with strong amyloidosis and microglial activation inside the brain. TSPO labeling of the skull was compared 5xFAD and wild-type mice. Voxel-wise differences were calculated to allow a volume-of-interest independent validation of elevated skull tracer binding in 5xFAD mice. The quantification and visualization was done using GraphPad Prism (version 8.0) using two-tailed t-test (data represented as ± SEM) and correlation analysis.

Human TSPO-PET imaging analysis

All TSPO-PET data were analyzed using PMOD. Spatial normalization was performed to a tracer specific templates in the Montreal Neurology Institute (MNI) space which was acquired via MRI-based spatial normalization. All images were normalized by cerebellar grey matter scaling (defined by the Hammers atlas[119]) prior to analysis and a standardized-uptake-value (SUV) analysis served for pseudo-reference tissue independent validation.

For stroke, multiple sclerosis and 4R tauopathy patients we defined three target regions based on a voxel-wise exploratory analysis: temporopolar skull (comprising 18 cm^3), skull base (comprising 97 cm^3), and prefrontal skull (comprising 7 cm^3). All regions were semi-automatically delineated using the human CT template available in PMOD. Region-based PET values were normalized to a composition of values of exactly age-matched ($\leq$ 1 year difference) controls at the group level. Voxel-wise differences (% vs. age-matched controls) were calculated to allow a volume-of-interest independent validation of elevated skull tracer binding in all patient groups. Following the region-based approach, we used compositions of exactly age-matched controls for this calculation.

For the AD cohort, TSPO labeling in the calvaria was obtained in each participant from a large fronto-parietal volume-of-interest (comprising 66 cm^3), which was semi-automatically delineated using the human CT template available in PMOD. Posterior and frontal calvaria was spared to avoid signal spill-over from sinuses and extracranial structures. Furthermore, we used a Brainnetome[66] atlas-based classification of cortical brain regions and corresponding calvaria regions to test for regional calvaria-brain associations. To this end, we increased the dimension of the atlas by a factor of 1.2 and we delineated all volumes-of-interest that were represented in the calvaria as defined by the CT template ($\geq$50% of voxels included). This approach resulted in 64 individual calvaria-brain region pairs. TSPO labeling of the calvaria was compared between AD patients with β-amyloid pathophysiology (AD) and β-amyloid negative controls. Voxel-wise differences were calculated to allow a volume-of-interest independent validation of elevated calvaria tracer binding in patients with AD. TSPO labeling of the calvaria was correlated with age, sex, and cognitive testing (MMSE, CERAD, CDR) as well as with β-amyloid levels in CSF. Calvaria-brain associations of TSPO-PET were tested for the global calvaria volume-of interest with Braak stage and β-amyloid related composite brain regions. Furthermore, calvaria-brain associations were tested by a correlation matrix of the predefined 64 volume-of-interest pairs. Single region increases in patients with AD vs. healthy controls were correlated between calvaria and brain regions.

As a validation of specificity, we performed an additional analysis of TSPO tracer uptake in the corpus vertebrae of C2. This bone was chosen as a negative control region since it was captured in nearly all acquisitions as the most remote bone structure relative to skull. The analysis was performed manually using HERMES Full Flex (V4.17, HERMES Medical Solutions AB, Stockholm, Sweden). A 1.0 mm3 sphere was placed in the center of C2 and SUV was extracted and normalized to cerebellar uptake (i.e. SUVr).

For longitudinal imaging, individual follow-up TSPO-PET SUVr of the fronto-parietal region were compared to baseline by a paired t-test for both patients of the AD continuum and controls. For patients with stroke, we used SUV normalization since distinct changes of tracer uptake in whole brain did not allow reference tissue normalization for the longitudinal analysis. Here, individual follow-up TSPO-PET SUV of the infarct region were compared to baseline by a paired t-test, as no 3 month follow-up scans were available for healthy controls. As a region independent analysis we used the skull template implemented in SPM (V12, University College of London, London, UK) running in Matlab version R2016 (MathWorks Inc., Natick, MA) and performed a voxel wise paired t-test analysis between baseline and follow-up images of patients of the AD continuum and controls (SUVr) as well as patients with stroke (SUV). A p value threshold of 0.05, incorrectly for multiple comparisons, was considered significant to obtain a pattern of changes rather than only peak clusters with the highest changes. Significant changes were displayed as a skull surface projection. The ActiGliA cohort also allowed to correlate changes of TSPO tracer uptake in brain with changes of TSPO tracer uptake in skull for patients of the AD continuum and controls (not feasible in stroke due to the individual locations of the lesion). Skull was treated as one region of interest as described for the longitudinal analysis above. Brain was parcellated into 246 regions of the brainnetome atlas.[120] Chances of all 246 brain regions were correlated with changes in skull separately for patients of the AD continuum and controls. An FDR correction for multiple comparisons was applied to the respective p values.

Statistics for human TSPO-PET imaging

Group comparisons of VOI-based PET results between patient groups with mixed neurological disorders and controls (n=5 groups) were assessed by 1-way ANOVA and Bonferroni post hoc correction for multiple comparisons using IBM SPSS Statistics (version 22.0; SPSS). All data were controlled for age, sex and the TSPO single nucleotide polymorphism at the individual subject level.

Group comparison of Human TSPO-PET results between controls and AD patients were assessed by a two-tailed t-test in SPSS Statistics (version 22.0; SPSS), controlled for age, sex and the TSPO single nucleotide polymorphism. For correlation analyses, Pearson coefficients of correlation (R) were calculated. A threshold of P less than 0.05 was considered to be significant for the rejection of the null hypothesis. The visualization of the data was done using GraphPad Prism (version 8.0), (data represented as ± SEM).

ADDITIONAL RESOURCES

Videos related to this work: https://www.discotechnologies.org/Calvaria/.

CellPress
OPEN ACCESS

Supplemental figures

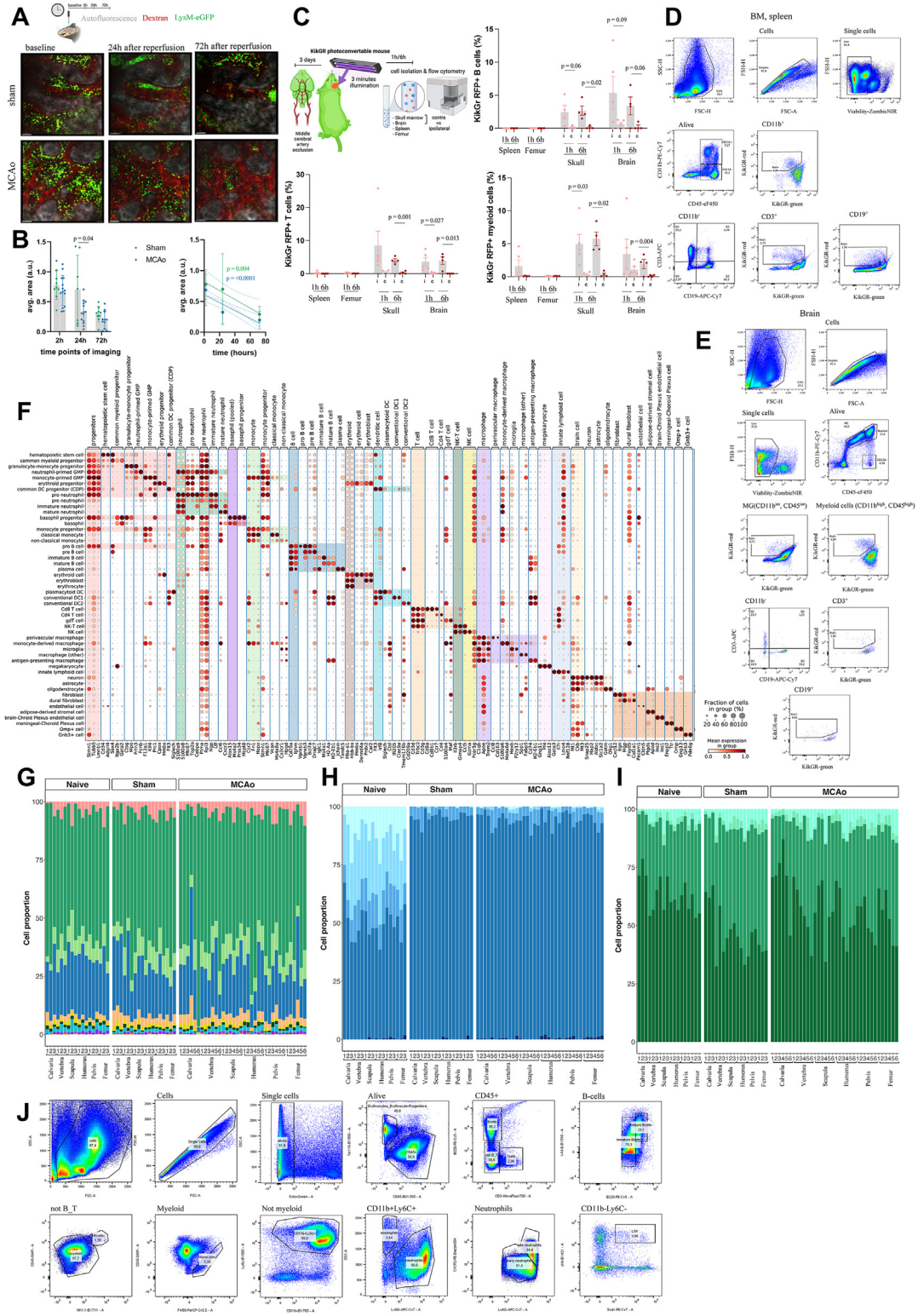

(legend on next page)

Figure S1. Assessment of skull cell dynamics and details of cell-type annotations, related to Figure 1

(A) Overview of the two-photon experiment and representative images from sham and MCAo groups. 2, 24, and 72 h after surgeries same ROIs were imaged. Per each imaging session, animals were given dextran for vessel labeling (n = 3 for naive and sham and n = 5 animals for MCAo). Scale bars, 50 μm.

(B) Quantification of changes in area between sham and MCAo conditions. LysM was quantified based on maximum intensity projected time series of 3 frames per batch. Average area of LysM cells in MCAo is less than sham in 24 h ($p = 0.04$) and both conditions have significant decrease of LysM cells over time ($p = 0.004$ for sham and $p < 0.0001$ in MCAo)Data represented as ±SEM.(see STAR Methods for details).

(C) Photoconversion in KikGR mouse model to track cell trafficking from skull to brain 3 days after stroke. B cell (1 h, ipsi vs. contra skull, $p = 0.06$, brain, $p = 0.09$. 6 h ipsi vs. contra skull, $p = 0.02$, brain, $p = 0.06$), T cells (1 h, ipsi vs. contra brain, $p = 0.027$. 6 h ipsi vs. contra skull, $p = 0.001$, brain, $p = 0.013$), and myeloid cells (1 h, ipsi vs. contra skull, $p = 0.03$. 6 h ipsi vs. contra skull, $p = 0.02$, brain, $p = 0.004$) were analyzed within the skull and brain compartment at indicated time points. Data represented as ±SEM.

(D and E) Gating strategy for B cells, T cells, myeloid cells in bone marrow and spleen (D) and in brain (E).

(F) Coarse and fine annotated cell types and their marker genes.

(G–I) Deconvolved pooled data using SNPs showing (G) coarse annotations, (H) B cell fine cell annotation, and (I) neutrophils fine cell annotations.

(J) Gating strategy for proportions: B cells, T cells, monocytes, neutrophils, eosinophils, erythroid cells, progenitors, NK cells, late neutrophils, B cell progenitors for flow cytometry experiment demonstrating proportions.

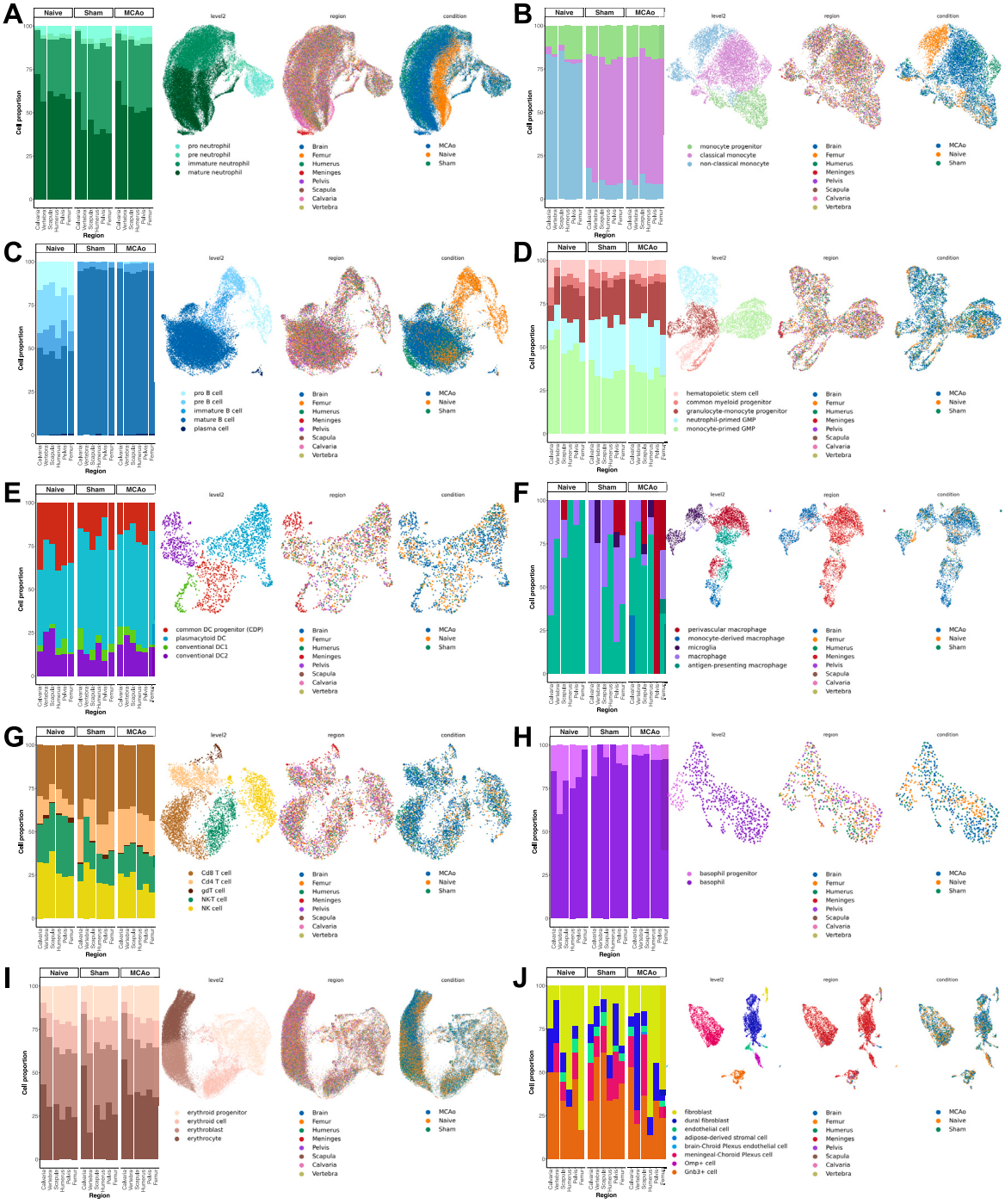

Figure S2. Proportions and UMAP of fine cell types over all conditions, related to Figure 1

Coarse cell types are shown separately with their fine cell-type proportion over three conditions, and their UMAP distribution for the cell-type, condition and region: (A) neutrophils, (B) monocytes, (C) B cells, (D) progenitors, (E) dendritic cells, (F) macrophages, (G) T and NK cells, (H) basophils, (I) erythroid cells, and (J) structural cells.

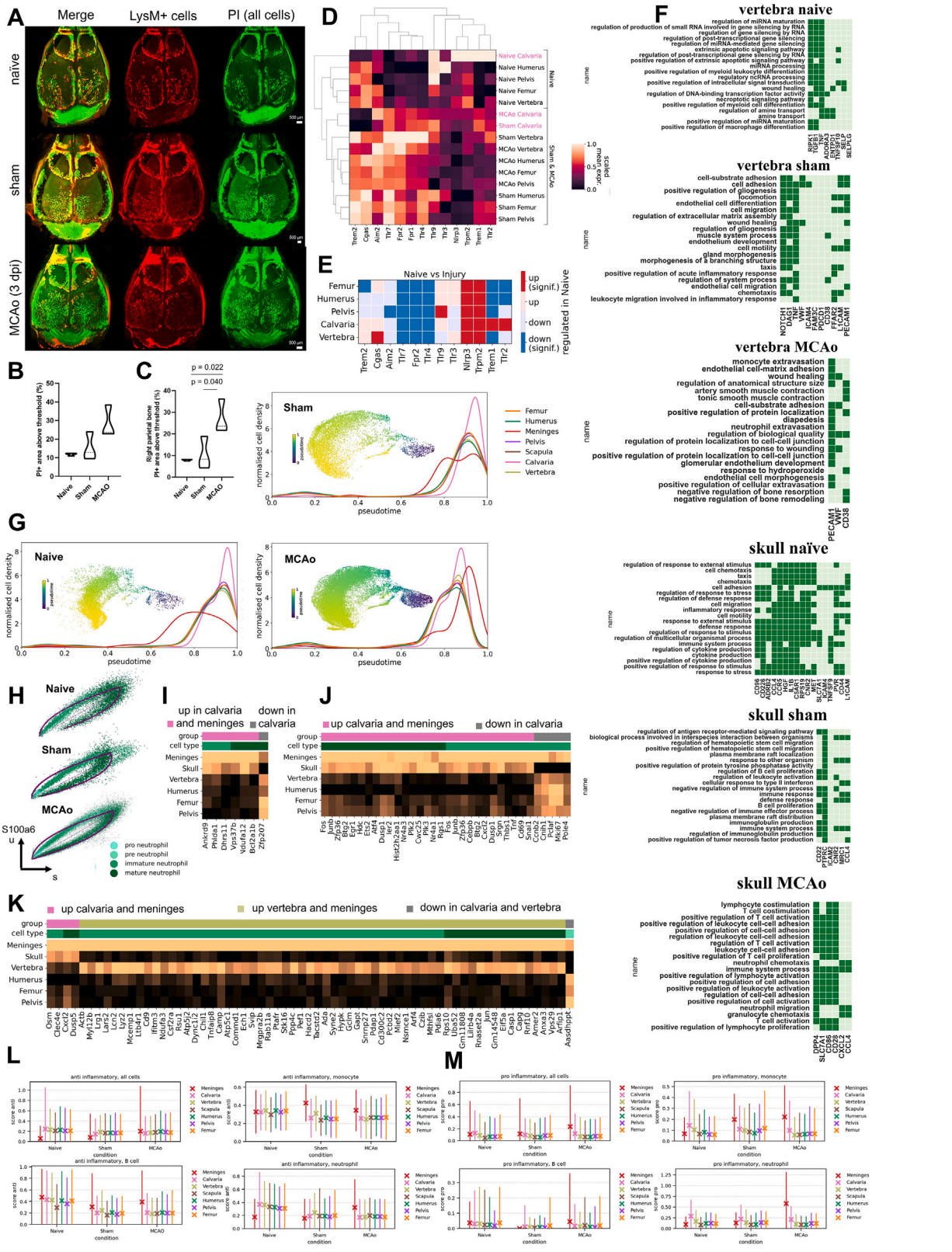

(legend on next page)

Figure S3. Analysis of skull cell numbers, neutrophil development, and inflammatory responses in different bones and the meninges, related to Figure 2

(A) Whole head clearing of LysM mice in naive, sham, and MCAo (stroke on left side) condition.

(B) Quantification of PI signal in the frontal and parietal bones show a strong trend ($F(2,6) = 5.027$, $p = 0.522$) for increased PI signal in MCAo condition compared to sham ($p = 0.124$) and naive conditions ($p = 0.053$).

(C) Quantification of PI signal in the contralateral parietal skull bone of show increase ($F(2,6) = 8.323$, $p = 0.019$) in PI signal in MCAo condition compared to sham ($p = 0.040$) and naive ($p = 0.022$) conditions (n = 3 per group); dpi, days post injury.

(D) Expression of DAMP relevant genes in three conditions with their relative hierarchical clustering.

(E) Comparison of naive vs. injury response of specific DAMP genes. Color code indicates significance ($p < 0.05$).

(F) The unique LR pairs in the skull and vertebra in three different conditions. LR pairs that occur in at least 5 different cell-type pairs in a given bone group are shown. (permutation test, 1000 permutations, $p = 0$)

(G) Pseudo-time analysis of naive, sham, and MCAo with normalized cell density in each condition for each region.

(H) Phase portrait showing unspliced and spliced counts in neutrophils of gene *S100a6* for naive, sham and MCAo respectively.

(I–K) Mean expressions of upregulated genes in meninges and in a single other group in (I) naive, (J) sham, and (K) MCAo.

(L and M) Mean and standard deviation of (L) anti-inflammatory and (M) pro-inflammatory score over cells of all cell types, B cells, neutrophils, and monocytes in naive, sham, and MCAo (significance and LFC in Table S1, tabs 29 and 30). Inflammatory score is based on the expression of *Il6*, *Il1a*, *Il1b*, Ifng, Il11, Il7d, Il7f, Il18 and *Tnf* (pro-inflammatory) and *Il1rn*, *Tgfb1*, *Il4*, *Il10*, *Il12a*, and *Il13* (anti-inflammatory).

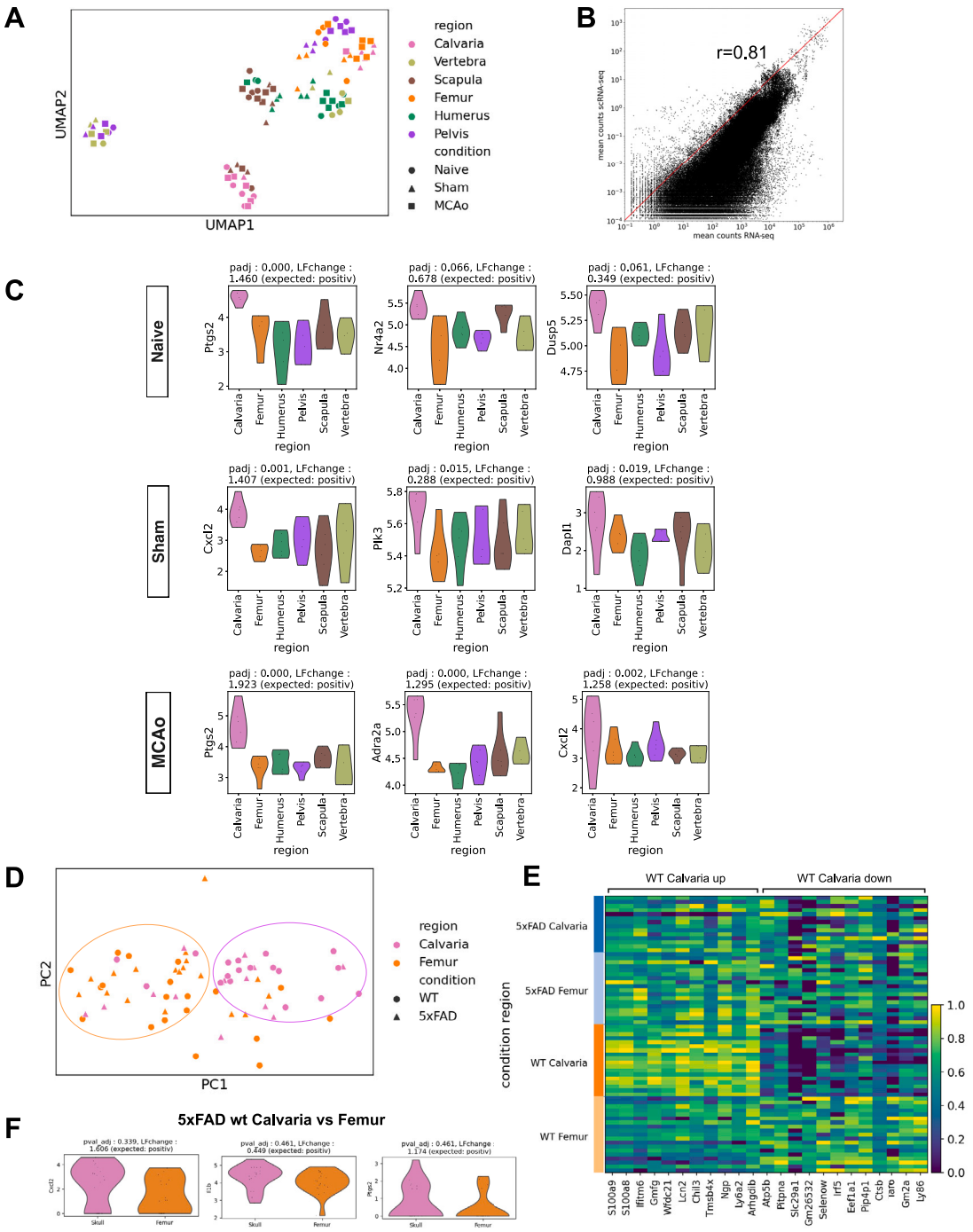

Figure S4. Analysis of bulk RNA-seq data of bone marrow cells, related to Figure 2

(A) PCA of calvaria, scapula, humerus, vertebra, pelvis, and femur from 5 naive, 5 sham, 6 MCAo animals. Color represents region and shape represents condition.

(B) Correlation between bulk RNA gene expression and scRNA-seq pseudobulked dataset. r = 0.81.

(C) Representative genes that show the same trend with scRNA-seq data for each condition. p values and log-fold changes are given on top of each violin plot ($p < 0.001$ for Ptgs2, $p = 0.066$ for Nr4a2, and $p = 0.061$ for Dusp5 in naive, $p = 0.001$ for Cxcl2, $p = 0.015$ for Plk3 and $p = 0.019$ for Dapl1 in sham, $p < 0.001$ for Ptgs2, $p < 0.001$ for Adra2a, and $p = 0.002$ for Cxcl2 in MCAo). Single-cell expression of these genes are given with "expected," positive means scRNA-seq data showed an increased trend of the given gene.

(legend continued on next page)

(D) PCA of femur and calvaria in 5xFAD model of Alzheimer's disease. 5xFAD animals are compared with their littermate controls. Colors represent different bones whereas shapes represent condition.

(E) Calvaria upregulated and downregulated genes in control case. There are no differentially expressed genes in AD case. The expression of the differentially expressed genes are shown in all groups for comparison. ($p < 0.05$)

(F) Selected upregulated genes that show the same trend in 5xFAD dataset. p values and log-fold change are given on top of each violin plot ($p < 0.339$ for Cxcl2, $p = 0.461$ for Il1b, and $p = 0.461$ for Ptgs2 . Single-cell expression of these genes are given with expected, positive means scRNA-seq data showed an increased trend of the given gene.

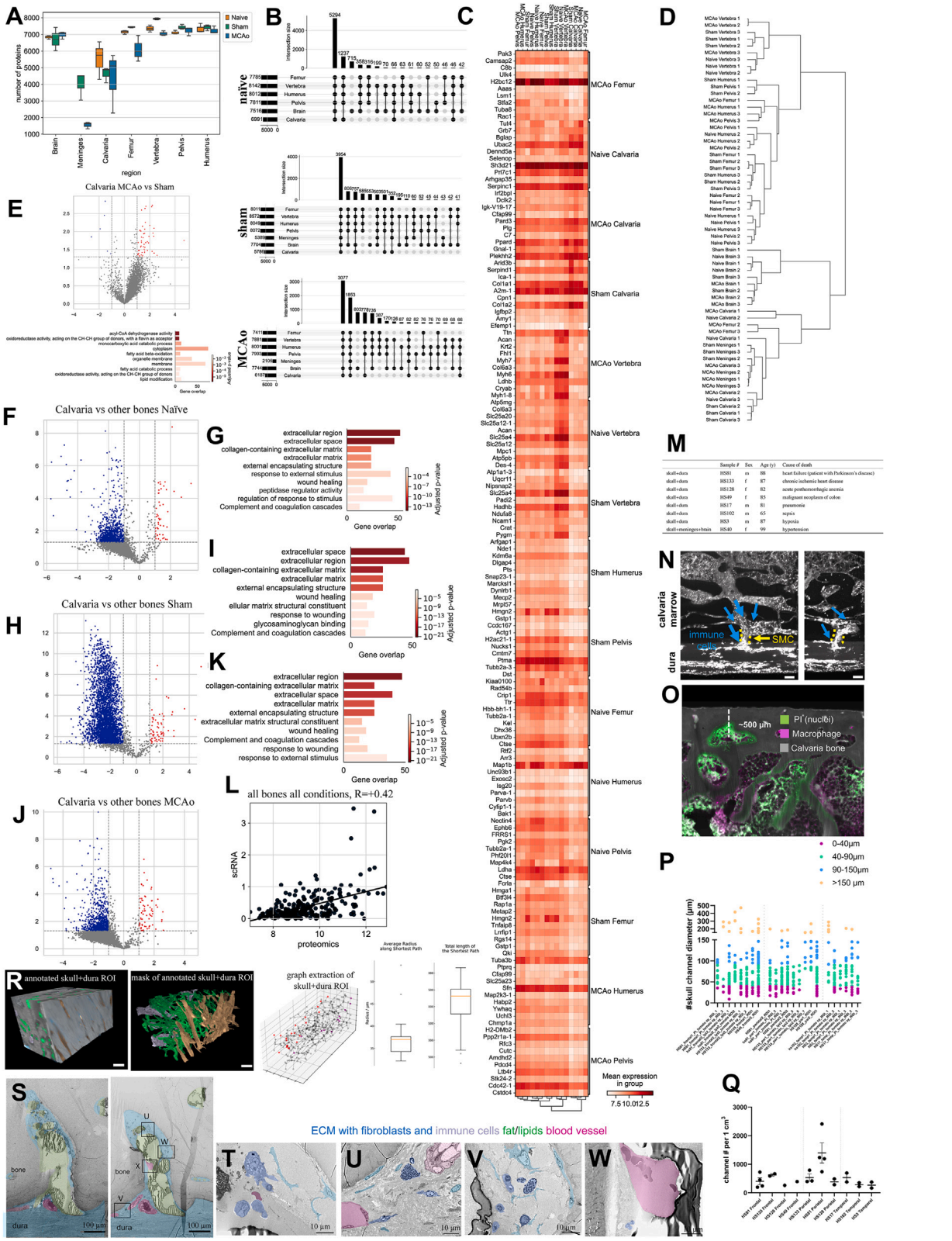

(legend on next page)

Figure S5. Details of the analysis of mouse proteome data and human skull-meninges channels, related to Figures 3 and 4

(A) Number of proteins detected from each bone.

(B) Number of common proteins and unique proteins detected from different bones for different conditions. Top: naive, middle: sham, and bottom: MCAo.

(C) 10 top upregulated proteins for each region in each condition (LFC > 1, $p < 0.05$).

(D) Dendrogram for each sample and condition is shown.

(E) Volcano plot shows the difference between calvaria MCAo vs. sham. (LFC > 1, $p < 0.05$) Related GO terms are shown below.

(F–K) Volcano plots are showing (F) naive calvaria vs. other bones, (H) sham calvaria vs. other bones and (J) MCAo calvaria vs. other bones, respectively. (LFC > 1, $p < 0.05$) (G–K) GO terms of upregulated calvaria proteins in (G) naive, (I) sham, and (K) MCAo conditions are provided below each volcano plot.

(L) Correlation plot of module 2 of WGCNA neutrophil degranulation GO term proteins with scRNA-seq expression levels. Spearman correlation, $R = +0.42$, $p < 0.0001$.

(M) Details for post-mortem tissue clearing and light-sheet fluorescent imaging experiments.

(N) Channels connecting calvaria's bone marrow to the meninges with Iba1+ cells. Scale bars, 150 μm.

(O) Human bone marrow labeled for cell nuclei (PI, in green), macrophage (Iba1, in magenta) is shown with calvaria bone (autofluorescence).

(P) Skull channel diameter distribution based on each ROI quantified.

(Q) Channel number per 1 cm^3 distribution over all ROIs and samples.

(R) Annotated skull + dura ROI, bottom part shows dura with brown annotation, skull channels are annotated in green and bone marrow is annotated in gray. Annotated dura, skull and bone marrow mask. Graph extraction of human skull architecture, total length, and radius of the shortest path from skull marrow to the dural meninges in μm, respectively. Scale bars, 500 μm.

(S–W) 200 nm thick scanning electron microscopy images of a SMC with zoom-ins. (S) shows different axial depths of the same channel.

A

Sample #	Sex	Age (y)	PMI (h)	Category of death
1	m	23	36	hypoxic
2	m	56	36	hypovolemic
3	m	56	18	hypoxic
4	m	86	36	hypovolemic
5	f	77	26	hypovolemic
6	m	70	28	traumatic
7	m	69	17	hypoxic
8	m	92	27	traumatic
9	f	39	29	hypoxic
10	f	73	325	hypoxic
11	m	54	280	hypoxic
12	m	85	255	hypoxic
13	m	75	142	hypoxic
14	m	71	466	hypoxic
15	f	95	180	other
16	f	91	300	hypoxic
17	m	72	217	hypoxic
18	m	25	134	other
19	m	63	258	traumatic
20	f	46	220	traumatic

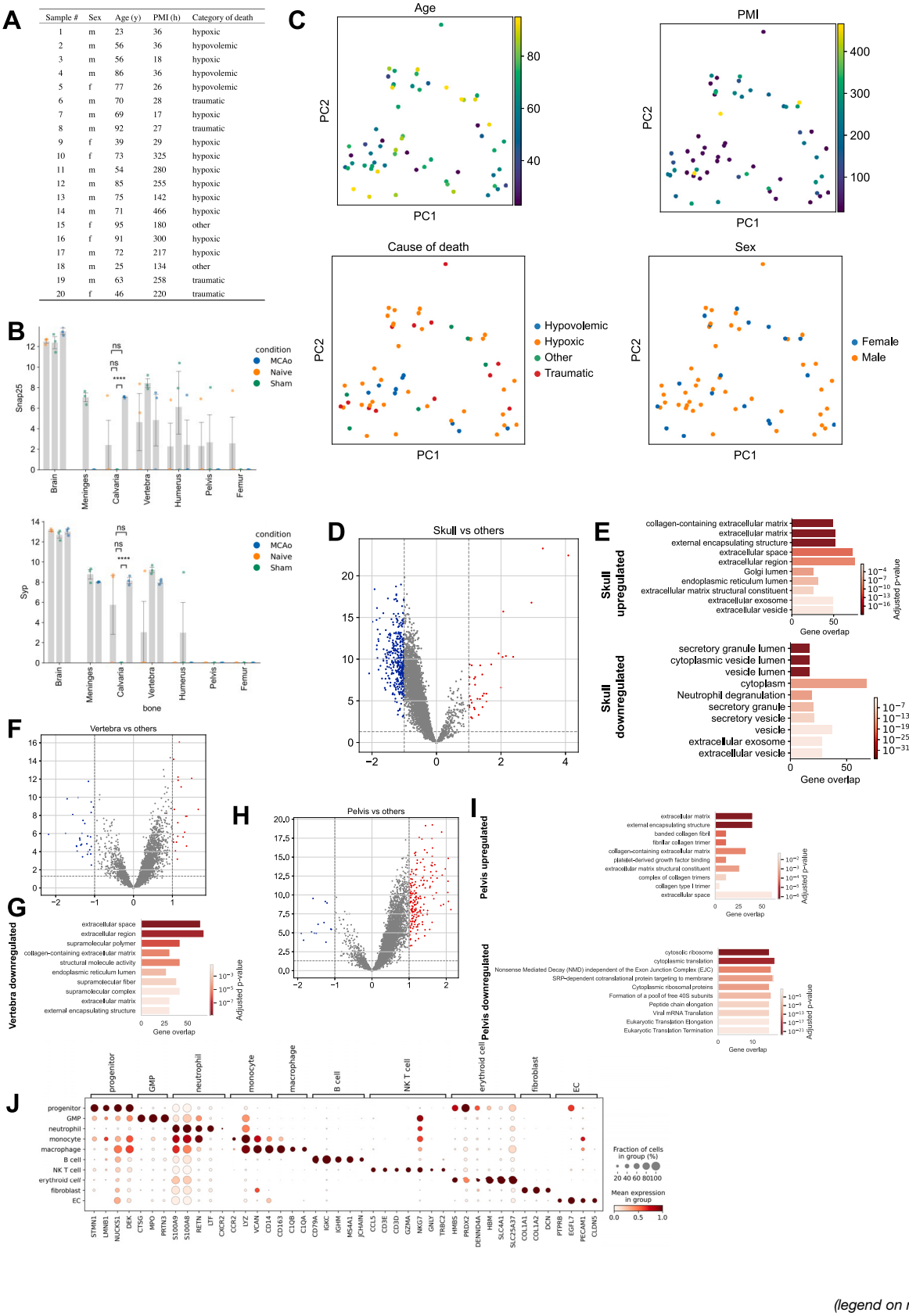

(legend on next page)

Figure S6. Details of the analysis of the human proteome data, related to Figure 5

(A) Post-mortem sample information, category of death is based on how death affects the brain.

(B) Two proteins found uniquely in the human skull that show a similar trend in the mouse dataset. Snap25 and Syp expression in calvaria MCAo is higher than in sham ($p = 5.786e-08$ and $p = 2.000e-05$, respectively).

(C) PCA of bones based on age, cause of death group, PMI, and sex, respectively; PMI, post-mortem interval.

(D–I) Volcano plots among different bones: calvaria vs. others (D), vertebra vs. others (F), and pelvis vs. others (H) suggest there is a global downregulation in the skull compared to pelvis. (LFC > 1, $p < 0.05$) with GO terms for upregulated and downregulated for each bone (E), (G), and (I).

(J) Cell-type annotation marker genes for scRNA-seq of human skull.

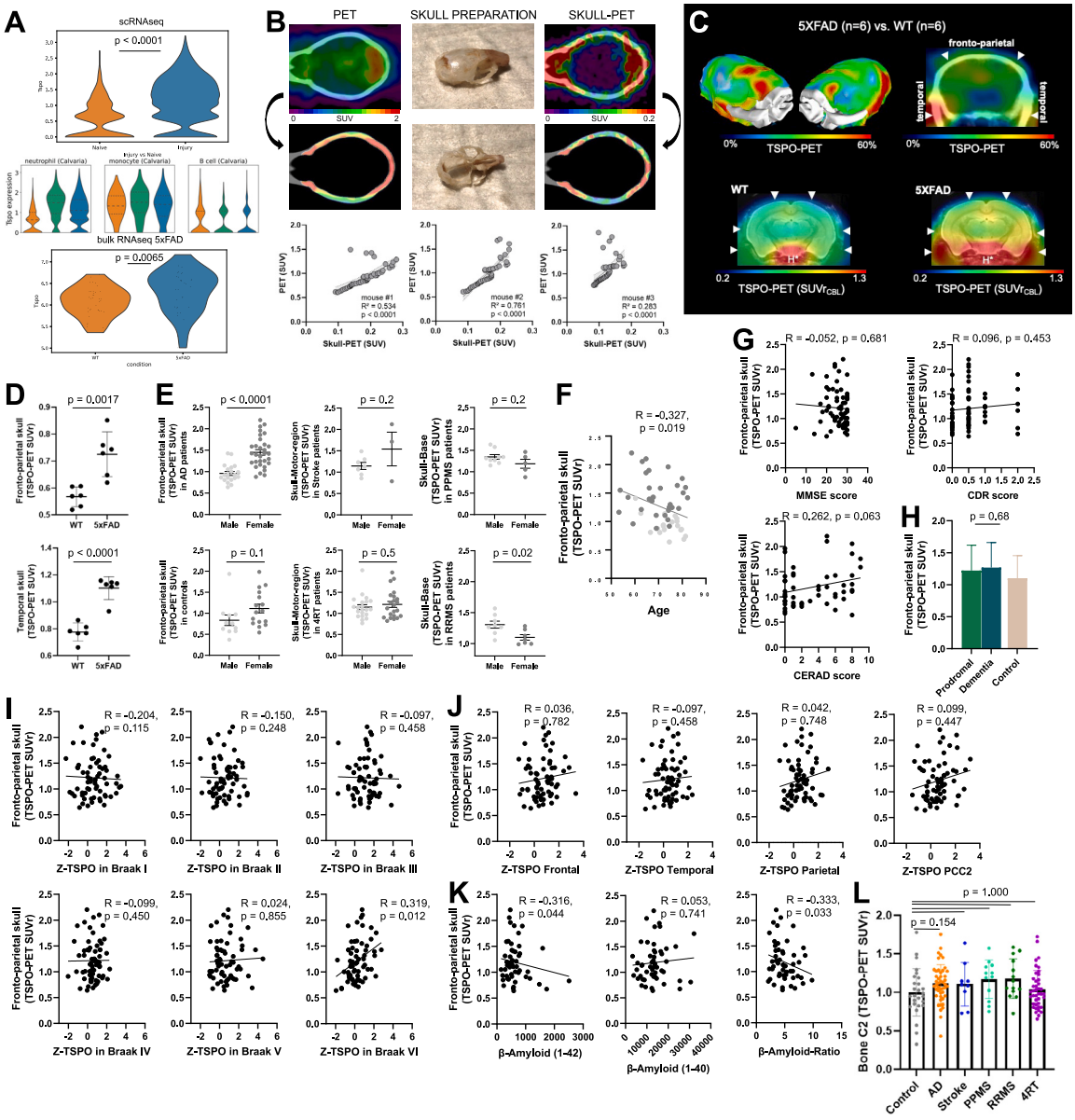

Figure S7. Influence of imaging method, and various covariates on TSPO-PET data, related to Figure 6

(A) TSPO RNA levels in naive vs. injury (MCAo + sham) ($p < 0.0001$) conditions in the skull from the scRNA-seq data. TSPO RNA levels in 5xFAD vs. wild type in the calvaria ($p = 0.0065$).

(B) *In vivo* TSPO-PET imaging of three wild-type mice, followed by a second scan after immediate removal of the brain, blood, and all tissue surrounding the skull bone. Signal attributable to the skull in the *in vivo* TSPO-PET images was compared to the signal in the respective skull-only TSPO-PET to delineate skull signal in mice (three replicates, $R^2 = 0.534, 0.761, 0.283$, $p < 0.0001$).

(C) Coronal slice upon a CT template shows %-TSPO-PET differences between 5xFAD and wild-type mice at the group level. Images indicate increased TSPO labeling in the fronto-parietal and temporal skull of 5xFAD mice in contrast against age-matched wild-type mice. White arrows indicate spots with higher increases of skull TSPO labeling when compared to adjacent increases of brain TSPO labeling in 5xFAD. Axial slices upon an MRI template show TSPO-PET in an individual 5xFAD and an individual wild-type mouse. Elevated TSPO labeling in fronto-parietal and temporal skull is present (white arrows) in the 5xFAD mouse when compared to the wild-type mouse. H* = hypophysis with known strong TSPO-PET signal.

(D) Fronto-patietal skull, $p = 0.0017$, temporal skull, $p < 0.0001$ (two-tailed t test). Data represented as ±SEM.

(E) Quantification of relevant skull signal sex differences for AD ($p < 0.0001$; controlled for age and TSPO-binding single nucleotide polymorphism), stroke ($p = 0.2$), PPMS ($p = 0.2$), RRMS ($p = 0.02$), 4RT ($p = 0.5$) patients and controls ($p = 0.1$). Data represented as ±SEM.

(F) Quantification of fronto-parietal skull signal age associated patterns ($p = 0.019$, two-tailed t test, controlled for gender and TSPO-binding single nucleotide polymorphism) among 50 AD continuum patients. Data are means ± SD. SUVr, standardized uptake value ratio.

(G) Fronto-parietal skull TSPO signal from patients with AD show no significant correlation with clinical severity in MMSE ($p = 0.681$), CERAD ($p = 0.063$), and CDR ($p = 0.453$) scorings.

(legend continued on next page)

(H) Fronto-parietal skull TSPO signal in Alzheimer's disease compared to control patients (prodromal vs. dementia: p = 0.63, data represented as ±SEM.).
(I) Fronto-parietal skull TSPO signal shows a positive association only with brain TSPO signal in the Braak VI stage region (p = 0.115 for Braak I, p = 0.248 for Braak II, p = 0.458 for Braak III, p = 0.450 for Braak IV, p = 0.855 for Braak V, and p = 0.012 for Braak VI).
(J) Fronto-parietal skull TSPO signal is not significantly associated with brain TSPO signal in any β-amyloid related regions: frontal (p = 0.782), temporal (p = 0.458), parietal (p = 0.748), and posterior cingulate cortex/precuneus (p = 0.447).
(K) Fronto-parietal skull TSPO signal is correlated with β-amyloid$_{42}$ (p = 0.044) but not β-amyloid$_{40}$ (p = 0.741) in cerebrospinal fluid, also reflected by the significant negative correlation of the β-amyloid ratio (p = 0.033).
(L) TSPO-PET signal quantifications in C2 bone of vertebra. One-way ANOVA with Bonferroni post hoc correction. See STAR Methods for details of normalization and statistical analysis. Significant differences of disease vs. controls are indicated (p = 1.0 for control vs. stroke, PPMS, RRMS, and 4RT, p = 0.154 for control vs. AD). Data represented as ±SEM. Pairwise comparison of all groups can be found in Table S3.

3.2 Study II: Whole-mouse clearing and imaging at the cellular level with vDISCO

The following section includes the original research article "Whole-mouse clearing and imaging at the cellular level with vDISCO," published in *Nature Protocols* (Cai, Kolabas, et al., 2023).

The ability to transparently clear and analyze entire rodent bodies presents an opportunity for a holistic approach to studying physiological and pathological events. While recent literature, including the uDISCO[88], the original vDISCO[10], DeepMACT[15], and wildDISCO[114], have introduced whole organism clearing and imaging, effectively detecting fluorescence signals in thick tissues has been challenging for several reasons.

Firstly, most tissue-clearing applications rely on detecting endogenous fluorescent proteins, which often experience significant signal reduction during the clearing process. These proteins are generally less bright than synthetic fluorescent dyes, such as those conjugated to secondary antibodies. Secondly, these proteins emit light in the visible spectrum, which overlaps with the obstructive autofluorescence of muscles and tissues.

To address these limitations, vDISCO has been previously developed as a novel method, pioneering whole-body immunolabeling and clearing by utilizing the small size of nanobodies (variable domain of heavy chain antibodies) instead of conventional antibodies[10]. As a result, the fluorescent signal is boosted and maintained for extended periods.

With the presented protocol paper of vDISCO, we demonstrate and expand the applications of vDISCO, facilitating the visualization of entire transparent bodies through tissues, bones, skin, and individual organs. By utilizing this method, we show the reconstructed map of the lymphatic system embedded in the muscles and bones of an adult mouse, visualization of pericytes of the whole mouse brain, and application of virus tracing in the mouse brain. We showcase different microscopes that could be used when utilizing vDISCO, underlining the versatility of our protocol.

In summary, with this paper, we present vDISCO: a groundbreaking approach to studying biological phenomena in an unbiased and comprehensive manner, offering new insights into physiological and pathological processes within transparent rodent bodies.

nature protocols

PROTOCOL

https://doi.org/10.1038/s41596-022-00788-2

Check for updates

Whole-mouse clearing and imaging at the cellular level with vDISCO

Ruiyao Cai[1,2,10], Zeynep Ilgin Kolabas[1,2,3,10], Chenchen Pan[1,2], Hongcheng Mai[1,2], Shan Zhao[1,2], Doris Kaltenecker[1,2,4], Fabian F. Voigt[5,6], Muge Molbay[1,2], Tzu-lun Ohn[1,2], Cécile Vincke[7,8], Mihail I. Todorov[1,2], Fritjof Helmchen[5,6], Jo A. Van Ginderachter[7,8] and Ali Ertürk[1,2,9]✉

Homeostatic and pathological phenomena often affect multiple organs across the whole organism. Tissue clearing methods, together with recent advances in microscopy, have made holistic examinations of biological samples feasible. Here, we report the detailed protocol for nanobody(V_HH)-boosted 3D imaging of solvent-cleared organs (vDISCO), a pressure-driven, nanobody-based whole-body immunolabeling and clearing method that renders whole mice transparent in 3 weeks, consistently enhancing the signal of fluorescent proteins, stabilizing them for years. This allows the reliable detection and quantification of fluorescent signal in intact rodents enabling the analysis of an entire body at cellular resolution. Here, we show the high versatility of vDISCO applied to boost the fluorescence signal of genetically expressed reporters and clear multiple dissected organs and tissues, as well as how to image processed samples using multiple fluorescence microscopy systems. The entire protocol is accessible to laboratories with limited expertise in tissue clearing. In addition to its applications in obtaining a whole-mouse neuronal projection map, detecting single-cell metastases in whole mice and identifying previously undescribed anatomical structures, we further show the visualization of the entire mouse lymphatic system, the application for virus tracing and the visualization of all pericytes in the brain. Taken together, our vDISCO pipeline allows systematic and comprehensive studies of cellular phenomena and connectivity in whole bodies.

Introduction

An unbiased way to analyze an entire organism would help improve the comparative study of pathologies that affect the whole body or individual organs[1]. If we consider histology and microscopy imaging, the sectioning of a small mammal such as a rodent into 5–100-µm-thick slices for the analysis of the entire body would be practically unfeasible, while other whole-body imaging techniques such as positron emission tomography or magnetic resonance imaging do not achieve sufficient resolution to detect morphological changes at cellular level[2–4]. The development of tissue clearing[5–10] methods that make histological samples optically transparent, deep-tissue immunolabeling techniques[11–14] and the maturation of light-sheet microscopy[15] have, over the past 15 years, allowed the adoption of a more holistic histological approach to study the structures of tissues and organs. Tissue clearing has even been applied to whole-body adult mice, paving the way to the concept of whole-body 3D histology via the detection of endogenously expressed fluorescent proteins; however, that approach relied on the removal of the skin[16–22]. Although fluorescent proteins are commonly used in microscopy, they are often not sufficiently bright to overcome the strong autofluorescence in a whole body originating from tissues such as skin, muscle and calcified bone. In addition, fluorescent proteins are quenched by the clearing reagents[16] and tend to bleach quickly during an imaging session, thus rendering multiple imaging sessions on the same sample often impossible. Cumulatively, these factors lead to signal detection of fluorescent structures being unreliable and, consequently, difficult or impossible to quantify. To address these issues, we developed a pipeline termed vDISCO (nanobody(V_HH)-boosted 3D imaging of solvent-cleared organs)[23]

[1]Institute for Tissue Engineering and Regenerative Medicine (iTERM), Helmholtz Munich, Munich, Germany. [2]Institute for Stroke and Dementia Research, Klinikum der Universität München, Ludwig Maximilian University of Munich, Munich, Germany. [3]Graduate School of Systemic Neurosciences (GSN), Munich, Germany. [4]Institute for Diabetes and Cancer, Helmholtz Munich, Munich, Germany. [5]Brain Research Institute, University of Zurich, Zurich, Switzerland. [6]Neuroscience Center Zurich, University of Zurich, Zurich, Switzerland. [7]Laboratory of Cellular and Molecular Immunology, Vrije Universiteit Brussel, Brussels, Belgium. [8]Myeloid Cell Immunology Lab, VIB Center for Inflammation Research, Brussels, Belgium. [9]Munich Cluster for Systems Neurology (SyNergy), Munich, Germany. [10]These authors contributed equally: Ruiyao Cai, Zeynep Ilgin Kolabas. ✉e-mail: erturk@helmholtz-muenchen.de

(Fig. 1) that allows easy head-to-toe imaging and the reliable analysis of an entire organism, at cellular resolution.

Development of vDISCO

In standard histology, the use of antibodies targeting the fluorescent proteins and conjugated to bright synthetic fluorophores (such as the ones from the Alexa and Atto family) represent a solution to increase the brightness and visibility of the proteins. Therefore, we reasoned that this strategy could be used to increase the signal of fluorescent proteins in an entire body.

Antibodies, however, are relatively big proteins (~150 kDa) and thus cannot penetrate in histological preparations for more than a few hundred micrometers (unless with the use of harsh chemical pretreatments such as with methanol[11]). We therefore decided to employ nanobodies to achieve whole-body immunolabeling (Fig. 2). In fact, nanobodies, being ten times smaller than antibodies (12–15 kDa) (refs. [24,25]), represent the smallest entities derived from immunoglobulins that are able to bind an antigen and can be conjugated to synthetic fluorophores[26].

Previously, we validated in dissected brains from CX3CR1-GFP[27] mice (expressing green fluorescent protein (GFP) in microglia) that the passive staining with nanobodies was more efficient in penetrating the tissue[23] compared with antibodies. However, we realized that passive incubation of whole mice with nanobodies alone was still not sufficient to achieve the level of extensive labeling we sought for targeting the entire body[23]. We therefore decided to exploit the cardiovascular network of the fixed animals to homogeneously inject the nanobodies in all body districts by using a high-pressure perfusion system (160–230 mmHg compared with 70–110 mmHg of standard perfusion protocols[28]) (Figs. 2, 3 and 4 and Extended Data Fig. 1). Additionally, we decreased sources of autofluorescence and light-scattering at two different timepoints by adding a decolorization and a decalcification step before immunolabeling and a clearing step after immunolabeling.

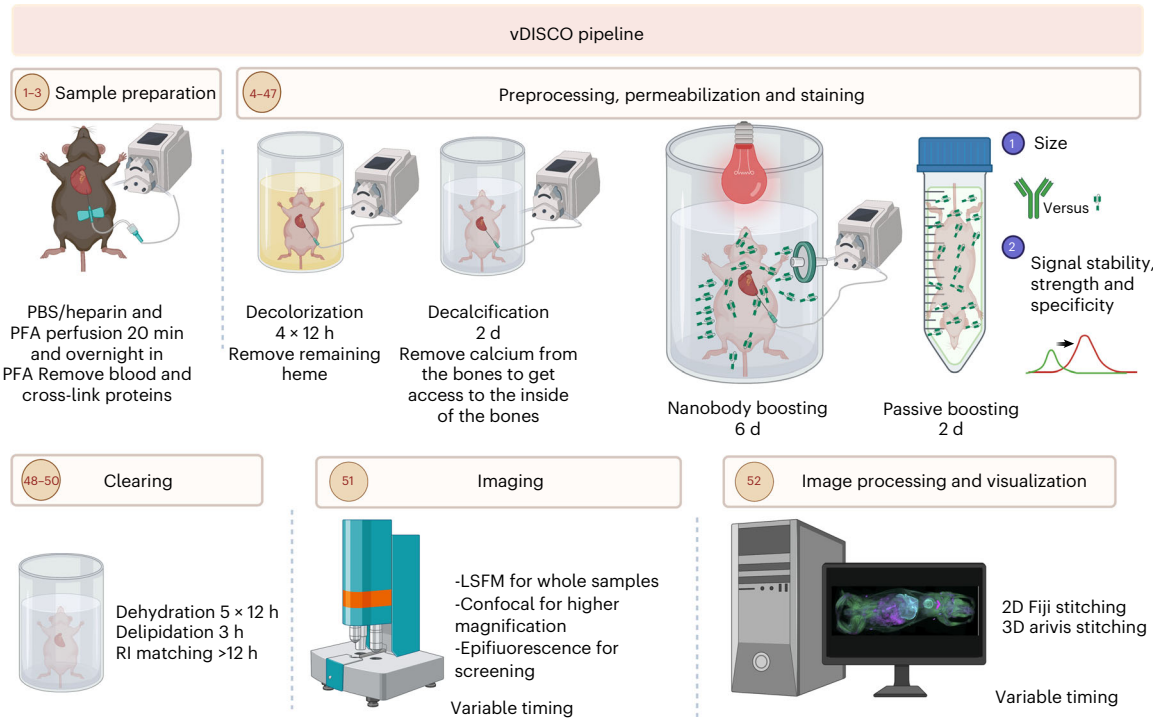

Fig. 1 | Overview of the vDISCO pipeline. Whole-body vDISCO has five main parts. After the sample is perfused with PBS and PFA (Steps 1–3), preprocessing steps such as decolorization and decalcification take ~4 d in total. Following this step, labeling and boosting take place, in which samples are incubated with nanobodies at higher temperatures for 6 d with active perfusion and 2 d in passive incubation. The use of nanobodies allows better penetration owing to their small size, and better signal-over-background ratio in cleared tissues compared with uncleared tissue owing to signal preservation and long-wavelength spectra. Additional dyes such as PI can also be incorporated here (Steps 4–47). Next, the 3DISCO clearing is performed (Steps 48–50). As a result, the cleared sample can be imaged with different microscopes: light-sheet, confocal or epifluorescence depending on the research focus (Step 51). After imaging, the data can be stitched if a tiling scan was utilized, and further analysis can take place (Step 52). The whole procedure takes ~3 weeks, and multiple samples can be processed at the same time. Figure created with BioRender.com.

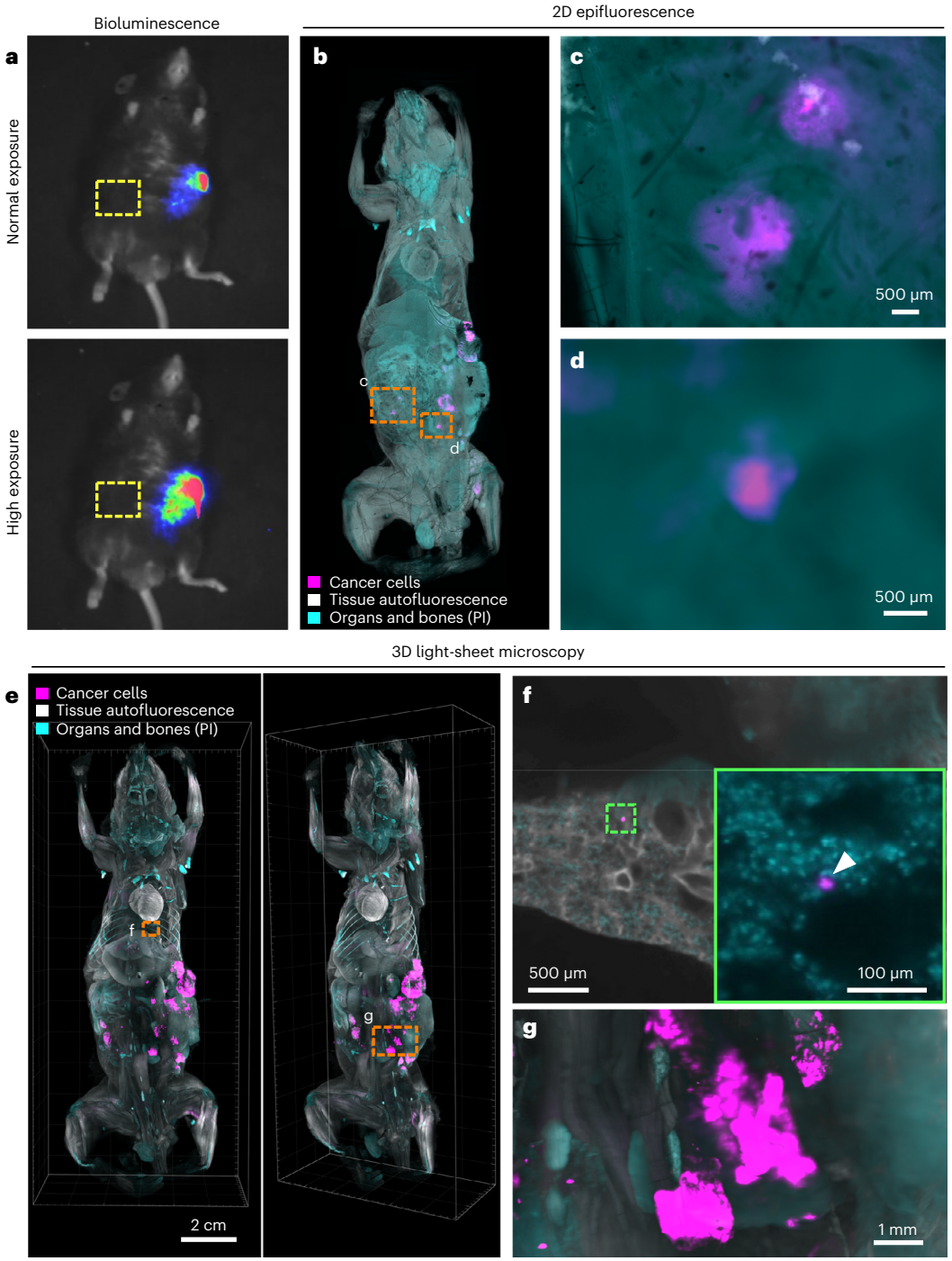

Fig. 2 | vDISCO imaging of a mouse with syngeneic pancreatic cancer. a, Normal and high exposure of bioluminescence imaging of the mouse with pancreatic cancer expressing eGFP at the end point of 38 d. **b**–**d**, 2D epifluorescence microscope imaging (**b**) of the same mouse after vDISCO labeling and clearing. The eGFP was boosted with nanobodies conjugated with Atto647N. Zoomed-in views (**c** and **d**) of the boxed regions in **b** indicate that the vDISCO pipeline provides more details of metastases (magenta) formation in the peritoneum that are not available from standard bioluminescence imaging (see **b**–**d** versus **a**). **e**, Ventral and 30° rotated views of the 3D reconstruction from light-sheet microscopy scanning of the mouse. **f**,**g**, Cellular-level-resolution light-sheet microscopy reveals individual metastases with various sizes and shapes, including a single disseminated cancer cell detected in the lungs (**f**, white arrowhead). In **b**–**g**, pancreatic cancer cells are shown in magenta, organs and bones labeled by PI are shown in cyan, and tissue autofluorescence is in white. Note that **f** was obtained by imaging the animal 2 years after vDISCO processing. Animal experiments followed European directive 2010/63/EU for animal research, reported according to the Animal Research: Reporting of In Vivo Experiments (ARRIVE) criteria, complied with the '3Rs' measure and were approved by the ethical review board of the government of Upper Bavaria (Regierung von Oberbayern, Munich, Germany) and conformed to institutional guidelines of Klinikum der Universität München/Ludwig Maximilian University of Munich). The severity of the procedure was medium.

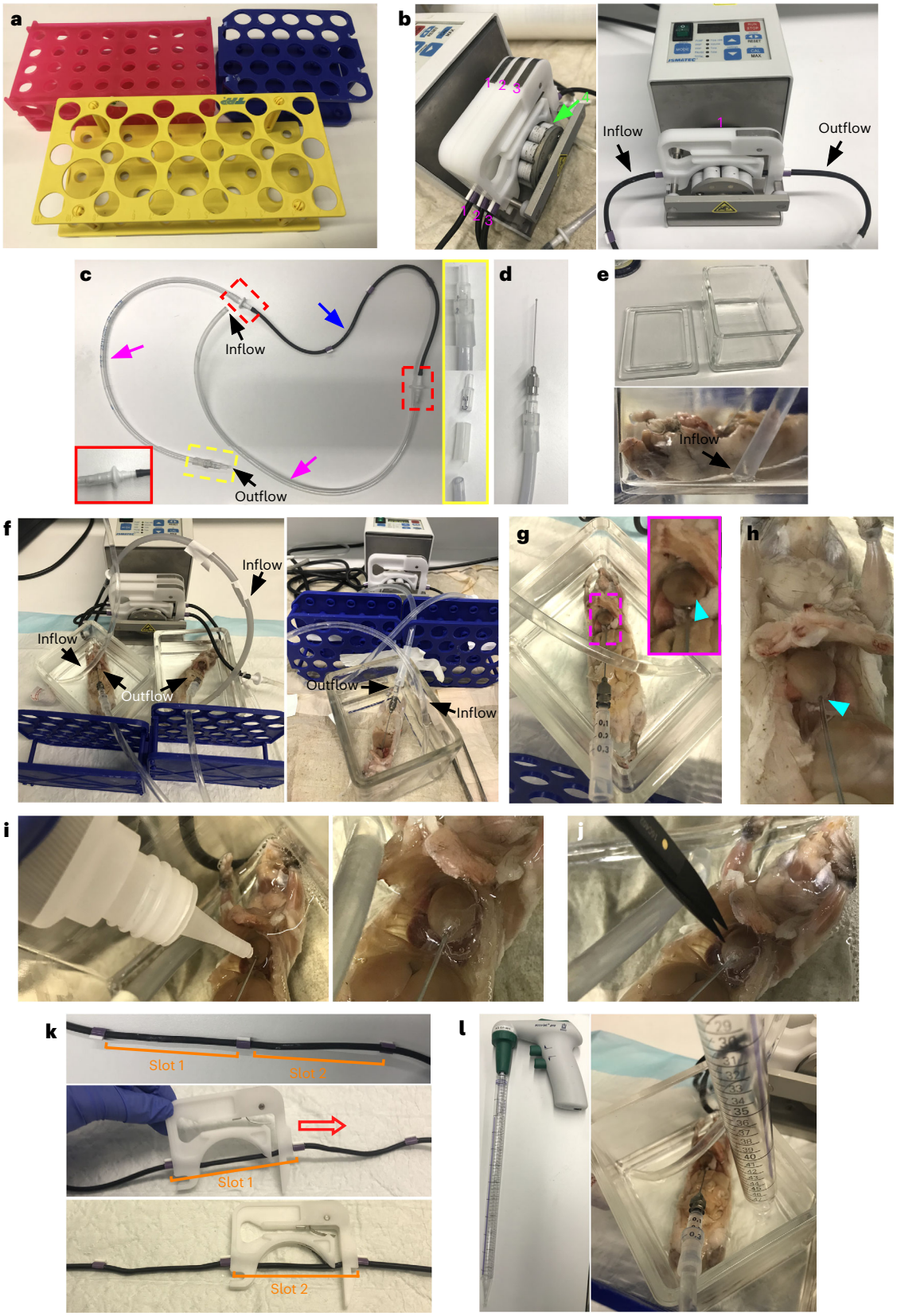
a
b
1 2 3
1 2 3
Inflow
1
Outflow
c
Inflow
Outflow
d
e
Inflow
f
Inflow
Inflow
Outflow
Outflow
Inflow
g
h
i
j
k
Slot 1
Slot 2
Slot 1
Slot 2
l

◀ **Fig. 3 | Whole-body active-vDISCO setup. a**, Sample holders used in whole-body active-vDISCO to hold the perfusion needle. **b**, The peristaltic pump that can hold four pumping channels; therefore, it can process four bodies at the same time. Left: three channels are indicated by magenta numbers; the green arrow indicates the slot for the fourth channel. Right: only one channel shown for the sake of simplicity; the inflow (sucking) end and the outflow (pumping) end are indicated by black arrows. **c**, Components of the tubing for a single channel: one reference tube (blue arrow), two PVC tubes to extend the reference tubing (magenta arrows), two hose tubing connectors (red boxes), and an outflow end made from the tip of 1 ml Braun syringe (yellow boxes). **d**, Perfusion needle. **e**, Top: glass chamber used for the perfusion and the whole-body clearing steps. Bottom: position of the sucking end of the pumping tube inside the glass chamber with the tip that reaches the bottom of the chamber. **f**, Different ways to position the pump in relation to the samples and to the sample holders. The inflow and outflow tubes are indicated by black arrows. **g**,**h**, The perfusion needle (**g**) inserted inside the entry point hole (cyan arrow) on the left ventricle. **i**, Super glue is applied to seal the hole. **j**, Cutting of the right ventricle. **k**, Pumping slots of a single reference tube. **l**, Strategy to change the perfusion solution. Animal experiments followed European directive 2010/63/EU for animal research, reported according to the Animal Research: Reporting of In Vivo Experiments (ARRIVE) criteria, complied with the '3Rs' measure and were approved by the ethical review board of the government of Upper Bavaria (Regierung von Oberbayern, Munich, Germany) and conformed to institutional guidelines of Klinikum der Universität München/Ludwig Maximilian University of Munich). The severity of the procedure was low.

Advantages and applications of vDISCO and comparison with other methods

In contrast to previous whole-body clearing protocols, vDISCO improves the signal-over-background ratio by synergistically combining different treatments.

First, the decalcification step reduces light scattering enabling the clearing of bones. Thus, the brain becomes optically accessible while still enclosed in the skull, with no need for dissection. vDISCO was able to confirm the presence of brain lymphatic vessels in the intact meningeal compartment[23,29,30], which would normally be damaged during the removal of the brain from the skull.

Previously we showed that, with nanobodies conjugated to far-red dyes such as Alexa647 or Atto647N, the fluorescent signal can be shifted to the far-red range. This range has the benefit of increasing the light penetration into the tissue and improving the signal-over-background ratio by reducing the autofluorescence[31]. As a result, fluorescent structures will appear in improved contrast and smaller cellular details such as neurites of neurons can be detected for image analysis in boosted samples compared with nonboosted samples. For example, neurons in scans from brains processed with vDISCO and obtained by light-sheet microscopy could be reliably traced[23] with algorithms that were implemented for higher resolution microscopy systems such as confocal[32].

The signal from the synthetic fluorophores is highly stable after clearing, and is retained for many months[23] and even years (Figs. 2 and 5). This allows the repeated imaging of the same samples for a long period of time.

Besides boosting fluorescent proteins expressed by transgenic lines, vDISCO is also compatible with virus tracing and transplanted fluorescent cells[1].

vDISCO does not require specialist and expensive equipment and could be implemented by researchers from any field. In fact, it simply consists of a series of steps where the samples are incubated or perfused with different solutions. Apart from the time needed to set up the pumping system, the actual work to change the solution takes a few minutes, allowing multiple samples to be started at the same time. Whole bodies can be processed in 2–3 weeks, while other whole-body clearing methods take 11–21 d only for the clearing step[18,21,22]. In our hands, we could run the staining and clearing of up to 18 animals at the same time by using six pumps simultaneously (three channels per each pump). This is sufficient to run an experiment with three conditions and with at least five animals per condition. It is possible to run more animals by increasing the number of the pumps. We could image 15 animals in ~2–3 months[1].

Imaging and analyzing samples in 3D is also convenient: whole organs can be imaged with the light-sheet microscope within a few hours, whole bodies within 3–14 d (depending on the imaging system), while data analysis can be concluded in 3–4 d or 1–2 weeks, again depending on the size of the data and the type of analysis. These timings are substantially shorter than the ones required in standard histology where the whole process from sectioning and reconstructing whole bodies would take several months and would require constant handling by the operator. Automated sectioning and imaging systems such as tomographic systems exist, but they are very time consuming, difficult to implement and therefore not routinely adopted by laboratories[33–35]. Moreover, the resulting data from sectioning might present artifacts or loss of molecular and tissue architectural features due to mechanical distortions during the slicing. These problems can lead to image alignment issues and misevaluation of the data, for example, in terms of connectivity, density and topography of the objects of interest.

Samples processed with vDISCO are compatible not only with light-sheet microscopes from different manufacturers and sources (Figs. 2e–g and 5 and Extended Data Fig. 2), but also with other fluorescence imaging systems such as epifluorescence (Fig. 2b–d), confocal (Figs. 6a) and two-photon

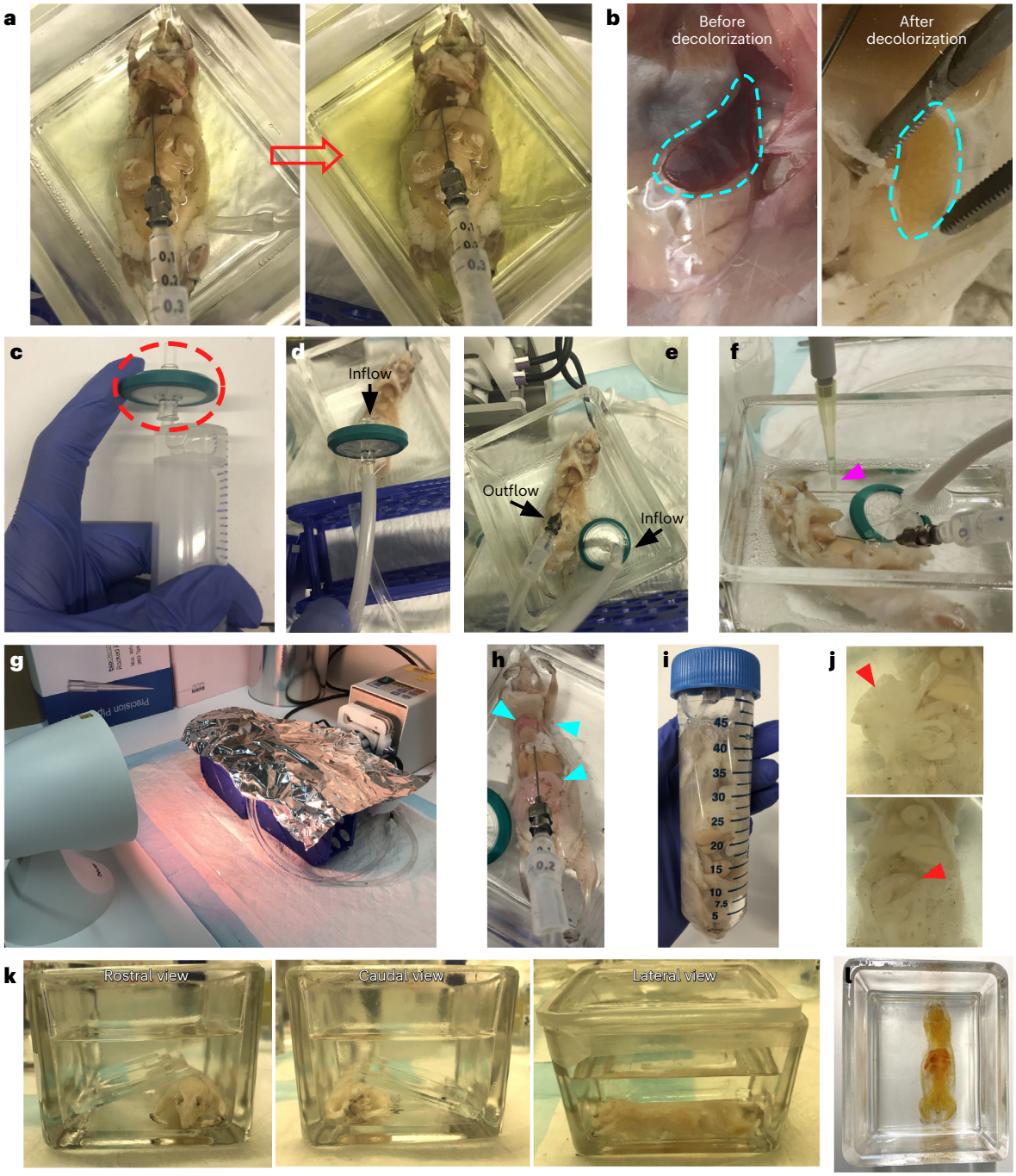

Fig. 4 | Whole-body active-vDISCO procedure. a,**b**, Pictures showing the successful elution of the heme from the body, indicated by the change of color of the decolorization solution, which turns from colorless into yellow (**a**), and the change of color of some organs such as the spleen, which turn from red into beige (**b**). **c**, The 0.22 µm filter (red dashed circle) used to prevent the formation of dye aggregates, must be wet by using a syringe before connecting it to the tube. **d**, Mounting of the filter onto the inflow (sucking) end of the perfusion channel. **e**, The inflow end with the filter is positioned inside the glass chamber. **f**, Picture showing the adding of the dye into the staining solution (magenta arrowhead) using a pipette. **g**, The chamber is covered with aluminum foil and heated up with an infrared lamp. **h**, Picture showing some organs turning pink after PI staining (cyan arrowheads). **i**, Final passive staining of the whole body inside a tube. **j**, Intestine is pushed into the abdomen before clearing. **k**, Different views of the animal inside the glass chamber during the clearing step. **l**, Dorsal view of the cleared animal inside the glass chamber. Animal experiments followed European directive 2010/63/EU for animal research, reported according to the Animal Research: Reporting of In Vivo Experiments (ARRIVE) criteria, complied with the '3Rs' measure and were approved by the ethical review board of the government of Upper Bavaria (Regierung von Oberbayern, Munich, Germany) and conformed to institutional guidelines of Klinikum der Universität München/Ludwig Maximilian University of Munich). The severity of the procedure was low.

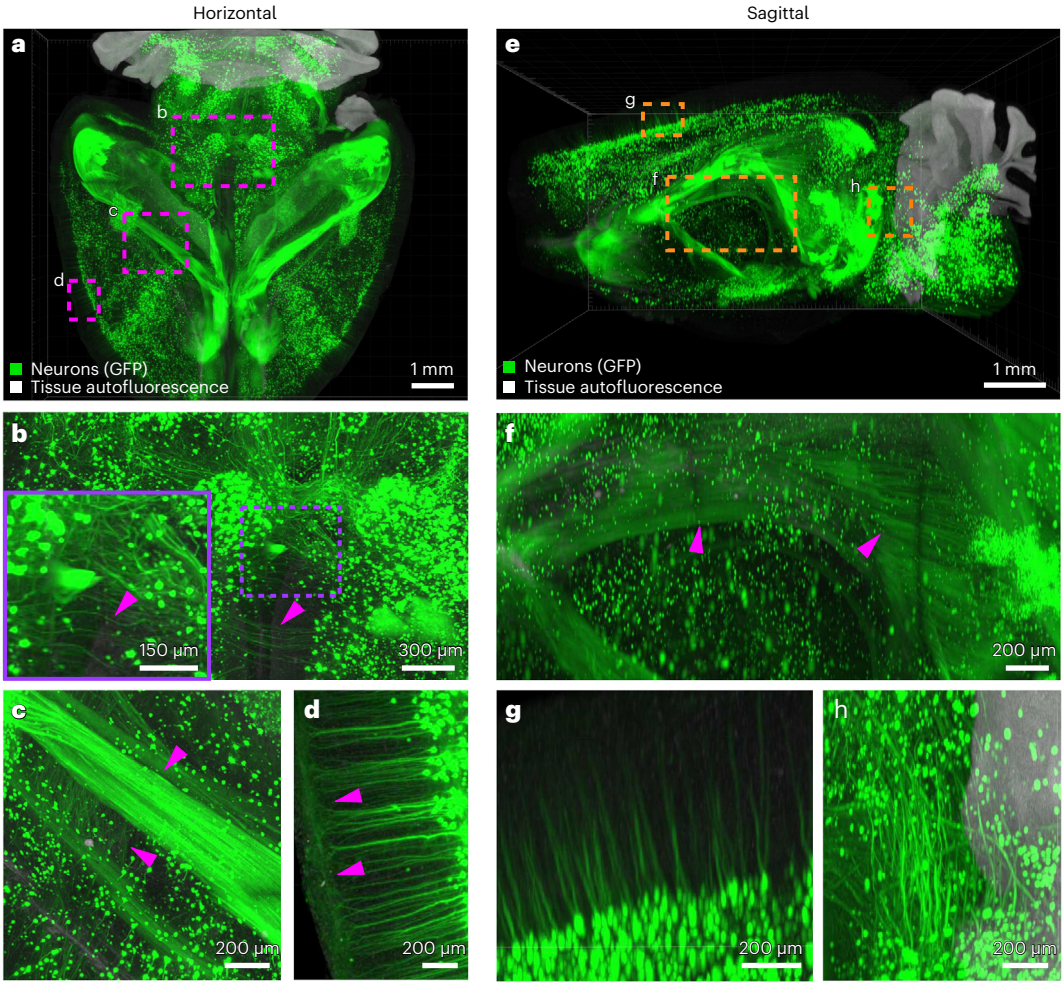

Fig. 5 | vDISCO processed Thy1-GFPM brain imaged with Z.1 light-sheet microscope. Imaris 3D reconstruction of a Thy1-GFPM mouse brain imaged by the Lightsheet Z.1 microscope 2 years after vDISCO processing. **a**–**h**, The brain was imaged horizontally and it is shown in horizontal view (**a**–**d**) and, after rotation of the 3D reconstruction volume, in sagittal view (**e**–**h**). **b**–**d**, Zoom-in images of the areas indicated by the boxed regions in **a**, showing commissural axons (**b**, arrowheads) crossing the two brain hemispheres, bundles of corpus callosum axons (**c**, arrowheads) and details of neurites of pyramidal cortical neurons projecting onto the surface of the brain (**d**, arrowheads). **f**–**h**, Zoom-in of the areas indicated by the boxed regions in **e**, showing neuronal details after rotating the brain to sagittal view: bundles of corpus callosum axons (**f**, arrowheads), pyramidal cortical neurons (**g**) and commissural axons (**h**) are visible with continuity even in sagittal view because of the isotropic resolution of the microscope. Similar results were achieved at least in two different samples. Animal experiments followed European directive 2010/63/EU for animal research, reported according to the Animal Research: Reporting of In Vivo Experiments (ARRIVE) criteria, complied with the '3Rs' measure and were approved by the ethical review board of the government of Upper Bavaria (Regierung von Oberbayern, Munich, Germany) and conformed to institutional guidelines of Klinikum der Universität München/Ludwig Maximilian University of Munich). The severity of the procedure was low.

microscopes (unpublished observations; R.C.). This versatility is useful because each imaging system has specific advantages such as higher resolution for confocal or speed for epifluorescence.

With the above-mentioned features, vDISCO can pave the way for a new histological approach capable of addressing the complexity of entire biological systems. This prevents potential bias when examining only a particular region of interest and the risk of overlooking important events in other regions. For example, vDISCO was used to reconstruct the neuronal projection map[23] of a Thy1-GFPM mouse where a subset of neurons expresses GFP[36]. This achievement led to the discovery of peripheral neuronal degeneration after traumatic brain injury[23]. vDISCO was also applied to holistically evaluate the extent of inflammation in different body parts after spinal cord injury[23] and, in combination with a deep-learning algorithm, to detect and quantify multi-organ metastases at single-cell level in mice with cancer[1].

With the clearing of entire heads, vDISCO was applied to comprehensively study the infiltration of peripheral monocytes/macrophages into the brain after stroke. This contributed to the elucidation and discovery of new routes called short skull–meninges connections that peripheral immune cells take to invade the cerebral tissue[23]. vDISCO can further clear whole mice with intact skin (Extended

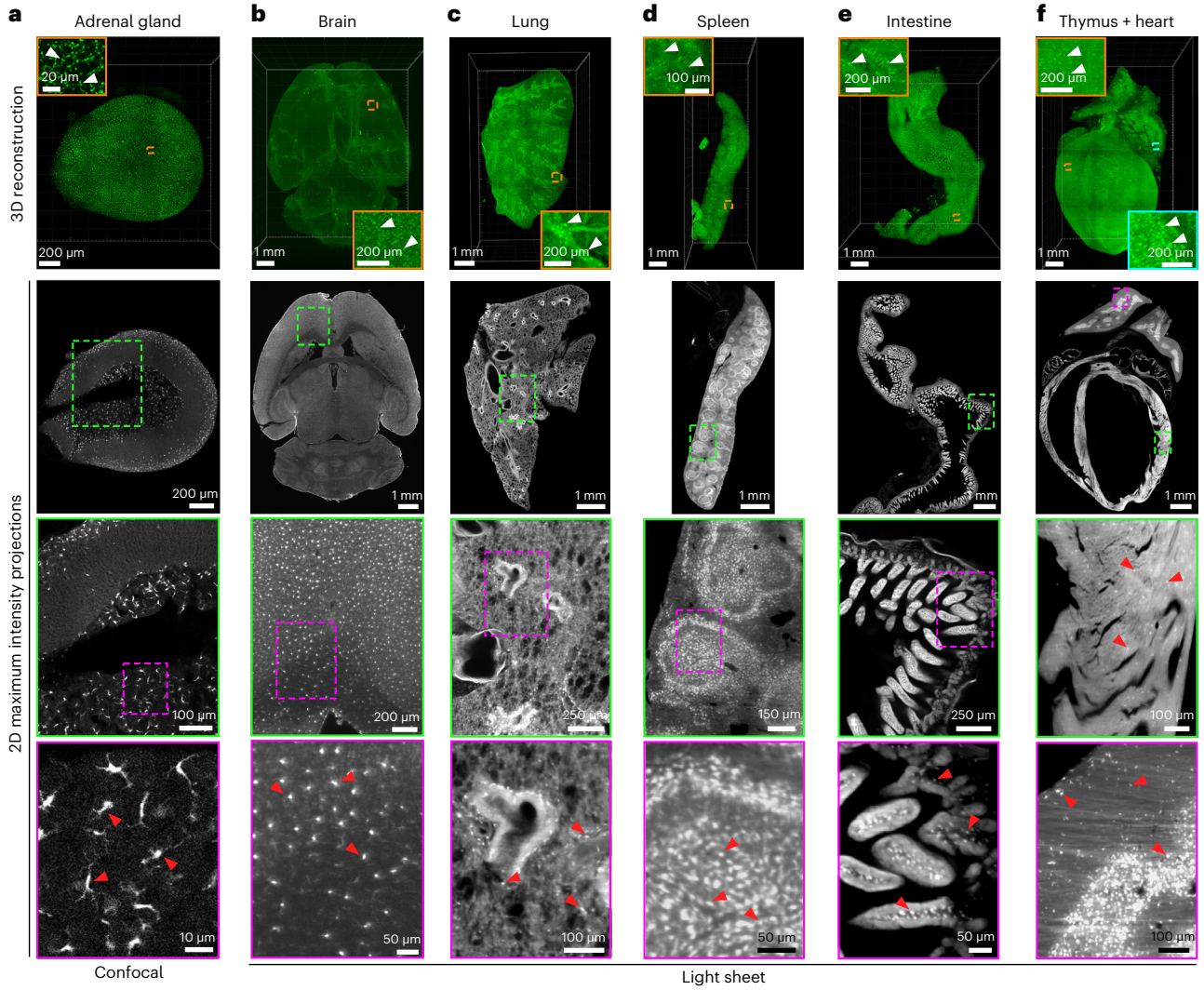

Fig. 6 | Passive-vDISCO on dissected organs imaged with confocal and light-sheet microscopy. a–f, 3D reconstructions and 2D maximum intensity projections of an adrenal gland (**a**), dissected brain (**b**), lung lobe (**c**), spleen (**d**), intestine segment (**e**) and thymus + heart (**f**) from the CX3CR1-GFP mouse line after passive-vDISCO. Zoom-in images from the dashed regions show individual CX3CR1 GFP+ immune cells (red arrowheads). To remove residual blood, the organs in **c** and **d** were initially decolorized for 2 d in the decolorization solution (25% dilution of the stock), while the ones in **e** and **f** were decolorized for 1 d in the decolorization solution (20% dilution of the stock). Similar results were observed in two independent animals. Animal experiments followed European directive 2010/63/EU for animal research, reported according to the Animal Research: Reporting of In Vivo Experiments (ARRIVE) criteria, complied with the '3Rs' measure and were approved by the ethical review board of the government of Upper Bavaria (Regierung von Oberbayern, Munich, Germany) and conformed to institutional guidelines of Klinikum der Universität München/Ludwig Maximilian University of Munich). The severity of the procedure was low.

Data Fig. 2), while all other previous methods required the removal of this organ[16–22] enabling the visualization of immune cells and sensory nerves in the skin and their connectivity with the spinal cord[23].

vDISCO was further used to boost the fluorescence signal in intact organs of large animal models; for instance, it was used to quantify and evaluate the distribution of β-cell islets in the pancreas of transgenic pigs expressing GFP[37].

Limitations

The use of organic solvents in the clearing step of vDISCO can decrease the retention of the proteins in the tissue, compared with hydrogel embedding methods[38]. As a result, low-expressed proteins can be difficult to detect. As the decolorization and clearing also delipidate the tissues, the retention of lipids and lipid-associated proteins might be affected by the approach[16,39]. For the same reason, lipophilic dyes such as DiI and myelin staining, previously shown as incompatible with organic-solvent-based methods[5], might not be detectable after vDISCO. Similarly, the success of vDISCO on

transgenic lines expressing fluorescent proteins related to lipid-associated proteins should be carefully evaluated, although a proper and extensive fixation of the tissue might help. In addition, samples deprived of lipids might not be compatible with electron microscopy[10].

With nanobodies binding to fluorescent proteins, vDISCO can theoretically boost up to 21 types of fluorescent protein, including mCherry and Venus. Validated fluorophores and fluorescent proteins are presented in Table 1. vDISCO is in principle compatible with nanobodies targeting endogenously expressed proteins as well[23]. However, the use of vDISCO as a primary staining approach is limited by the lack of nanobodies developed for histology. Nanobodies were in fact mostly optimized for in vivo applications such as therapeutic agents or as labels for intracellular markers in living cells[40]. The potential future development of nanobodies suitable for deep tissue immunolabeling of fixed thick specimens, as well as that of near-infrared fluorophores conjugable to the nanobodies, may expand the vDISCO applications and further the possible imaging depth[31].

A dedicated microscope is also required to scan the samples that are much larger than traditional slides. Typical organic-solvent-based clearing methods in fact shrink the samples up to 65% of their original volume[16,23], resulting in cleared mice (10 cm in length after shrinkage, 13–15 cm if the limbs are stretched) that could be imaged from head to toe but were still substantially bigger than the travel range of a light-sheet microscope developed for entire organs, in which case imaging of a whole animal could not be concluded in one session; rather, the sample was continuously displaced or flipped in order to image all the body parts. The resulting 20–24 individual scans acquired over 2–3 weeks were then stitched together[16,23]. The recent availability of light-sheet microscopes with bigger imaging chambers and larger sample holder stages[1,37] has importantly reduced the time and the amount of work spent during the data acquisition. Currently, in these systems, the image acquisition only takes 3–4 d for an adult mouse, although such systems must be coupled with very-long-distance objectives (minimum 20 mm) with the trade-off of reducing the resolution. We note that the rate of shrinkage must be carefully evaluated in different organs and tissues.

Lastly, the amount of raw data generated can be difficult to handle: the scans of a single animal can occupy 2–3 terabytes[23], to be analyzed with at least 256–512 gigabytes of computer random-access memory (RAM), which is not always available. Moreover, data sizes of hundreds or thousands of gigabytes are too complex or not feasible to be analyzed by a human operator. Algorithms that can automatically analyze the collected information are discussed later in the 'Data analysis and processing' section.

Experimental design: overview of the vDISCO pipeline

The vDISCO pipeline consists of sequential steps: sample preparation (Steps 1–3), decolorization, decalcification, permeabilization and staining (Steps 4–47), and tissue clearing (Steps 48–50). Following these steps, samples are ready to be imaged (Step 51) and be subjected to subsequent image processing, visualization and analysis pipelines (Step 52) (Fig. 1). If performed by a relatively experienced user, after validating the protocol in a pilot experiment with one animal, vDISCO would show a success rate of nine out of ten samples.

Choice of the sample and sample preparation

vDISCO is a robust method that has been extensively tested and reproduced in different experiments (Figs. 2, 5–9 and Extended Data Figs. 2 and 3). We recommend starting with samples bearing GFP, YFP, mCherry or RFP. For transgenic animals, genotyping should be performed to confirm the expression of the fluorescent protein. In addition, preliminary tests to assess the performance of staining must be performed if the chosen transgenic line is a reporter for lipid- or membrane-associated proteins (e.g., myelin basic protein).

A simpler version of vDISCO called 'passive-vDISCO'[23] (Tables 1–3, Figs. 6, 7 and 9, Extended Data Fig. 3 and 'Procedure' section) that has optional decolorization and decalcification steps and requires passive incubation can be applied on dissected organs and small samples such as embryos, half (Fig. 7 and Extended Data Fig. 3) or whole brains with spinal cord (Extended Data Fig. 4), lungs, gut, adrenal glands from mice (Fig. 6) and whole small pig organs such as pancreas[37]. Passive-vDISCO can also be used in sections to collect experimental data or quickly test and assess the performance of new nanobodies (Box 1). Both slices and dissected organs can be imaged with a broad variety of microscope systems, including confocal, epifluorescence and light-sheet microscopes (Figs. 6–9 and Extended Data Fig. 3). The decision to choose between whole-body vDISCO or

Table 1 | Nanobodies tested with vDISCO

Nanobody	Known target	Tested compatibility[a]	Company	Cat. no.	Lot/batch	Suggested concentration[b]	Protocol used	Tested samples	Performance	Note
GFP-Booster Atto647N (AB_2629215)	Anti-GFP	YFP, eYFP, eGFP	Chromotek	gba647n-100	60920001SAT2	Stock = 0.5–1 mg/ml Mouse brain: 1:500–1:700 (1.1–1.8 µg/ml) Whole mouse: 1:7,000 (0.08–0.14 µg/ml)	Standard passive and active vDISCO	Mouse organs and mouse whole body	Very bright, good penetration	14 d incubation for a whole brain
GFP-Booster Atto647N (AB_2629215)	Anti-GFP	YFP, eYFP, eGFP	Chromotek	gba647n-100	70213001SAT2	Stock = 0.5–1 mg/ml Mouse brain: 1:500–1:700 (1.1–1.8 µg/ml) Whole mouse: 1:7,000 (0.08–0.14 µg/ml)	Standard passive and active vDISCO	Mouse organs and mouse whole body	Very bright, good penetration	14 d incubation for a whole brain
GFP-Booster Atto647N (AB_2629215)	Anti-GFP	YFP, eYFP, eGFP	Chromotek	gba647n-100	71017011AT2	Stock = 0.5–1 mg/ml Mouse brain: 1:500–1:700 (1.1–1.8 µg/ml) Whole mouse: 1:7,000 (0.08–0.14 µg/ml)	Mild-vDISCO for passive staining	Mouse brain	Good signal and penetration	No signal using standard passive-vDISCO
GFP-Booster Atto647N (AB_2629215)	Anti-GFP	–	Chromotek	gba647n-100	80515001AT2	–		Mouse brain	Very weak signal	Withdrawn from the market by the company
GFP-Booster Atto647N (AB_2629215)	Anti-GFP	YFP, eYFP, eGFP	Chromotek	gba647n-100	90107001SAT2	Stock = 0.5–1 mg/ml Mouse brain: 1:500–1:700 (1.1–1.8 µg/ml) Whole mouse: 1:7,000 (0.08–0.14 µg/ml)	Mild-vDISCO for passive staining Standard vDISCO for active staining	Mouse organs and mouse whole body	In passive-vDISCO signal not so bright but visible, good penetration. In active-vDISCO good performance	14 d incubation for a whole brain
GFP-Booster 2AlexaFluor647 (AB_2827575)	Anti-GFP	YFP, eYFP, eGFP	Chromotek	gb2AF647-50	02TEC77	Stock = 0.5–1 mg/ml Mouse brain: 1:400–1:800 (0.6–2.5 µg/ml)	Mild-vDISCO for passive staining	Mouse brain	Bright, good penetration	14 d incubation for a whole brain
GFP-Booster 2AlexaFluor647 (AB_2827575)	Anti-GFP	YFP, eYFP, eGFP	Chromotek	gb2AF647-50	90212037AX2	Stock = 0.5–1 mg/ml Mouse brain: 1:400–1:800 (0.6–2.5 µg/ml	Mild-vDISCO for passive staining	Mouse brain	Bright, good penetration	14 d incubation for a whole brain
GFP-Booster 2AlexaFluor647 (AB_2827575)	Anti-GFP	–	Chromotek	gb2AF647-50	90524037AX2	–	Standard passive-vDISCO	1 mm mouse brain slices	Very weak signal	–

Table continued

Table 1 (continued)

Nanobody	Known target	Tested compatibility[a]	Company	Cat. no.	Lot/batch	Suggested concentration[b]	Protocol used	Tested samples	Performance	Note
GFP-Booster Atto488 (AB_2631386)	Anti-GFP	YFP, eYFP, eGFP	Chromotek	gba488-100	90305001AT1	Stock = 0.5–1 mg/ml Mouse brain: 1:500–1:700 (1.1–1.8 µg/ml)	-	Mouse brain	Very weak signal	-
GFP-Booster Atto594 (AB_2631387)	Anti-GFP	YFP, eYFP, eGFP	Chromotek	gba594-100	81212001AT3	Stock = 0.5–1 mg/ml Mouse brain: 1:500–1:700 (1.1–1.8 µg/ml)	Mild-vDISCO for passive staining	Mouse brain	Bright, good penetration	-
RFP-Booster Atto647N (AB_2631391)	Anti-RFP	mCherry	Chromotek	rba647n-100	81106002SAT2	Stock = 0.5–1 mg/ml Mouse brain: 1:500–1:700 (1.1–1.8 µg/ml) Whole mouse: 1:7,000 (0.08–0.14 µg/ml)	Standard active-vDISCO	Mouse whole body[1]	Bright, good penetration	-
RFP-Booster Atto594 (AB_2631390)	Anti-RFP	mCherry	Chromotek	rba594-100	71115002AT3	Stock = 0.5–1 mg/ml Mouse brain: 1:500–1:700 (1.1–1.8 µg/ml) Whole mouse: 1:7,000 (0.08–0.14 µg/ml)	Standard active-vDISCO	Mouse whole body[1,23]	Bright, good penetration	-
Fluotag-X4 anti-GFP AF647 (AB_2905517)	Anti-GFP	eGFP	NanoTag Biotechnologies	N0304-AF647	03190302	Stock = 1.25 µM Mouse brain: 1:300–1:500	Standard passive-vDISCO	Mouse brain and 50 µm slices	Very bright, penetration ok for half brain of mice	Increase the incubation time more than 30% with respect to the Chromotek nanobodies
Fluotag-X4 anti-GFP Atto647N (AB_2905516)	Anti-GFP	eGFP	NanoTag Biotechnologies	N0304-At647N	03190101	Stock = 1.25 µM Mouse brain: 1:300–1:500	Standard passive-vDISCO	1 mm mouse brain slices	Bright signal, very poor penetration	-
Fluotag-Q anti-GFP AF647 (AB_2905515)	Anti-GFP	eGFP	NanoTag Biotechnologies	N0301-AF647	03190101	Stock = 5 µM Mouse brain: 1:400–1:800	Standard passive-vDISCO	Mouse brain 50 µm slices	Very bright, good penetration	Increase the incubation time more than 30% with respect to the Chromotek nanobodies. Good results for microglia and pericytes in the brain
Fluotag-X4 anti-RFP AF565 (AB_2905518)	Anti-RFP	dsRed	NanoTag Biotechnologies	N0404-AF565	-	Stock = 1.25 µM Mouse half brain: 1:300–1:500	Standard passive-vDISCO	Mouse brain	Bright	8 d incubation for half brain

Table continued

Table 1 (continued)

Nanobody	Known target	Tested compatibility[a]	Company	Cat. no.	Lot/batch	Suggested concentration[b]	Protocol used	Tested samples	Performance	Note
Fluotag-X4 anti-RFP AF647 (AB_2905526)	Anti-RFP	tdTomato, mcherry	NanoTag Biotechnologies	N0404-AF647		Stock = 1.25 μM 1:500	Standard passive-vDISCO	Mouse half brain and 50 μm slices	Bright, moderate penetration	Increase the incubation time more than 30% with respect to the Chromotek nanobodies
Fluotag-X2 anti-mScarlet-i AF647 (AB_2905527)	Anti-mScarlet-i	tdTomato, mcherry	NanoTag Biotechnologies	N1302-AF565		Stock = 1.25 μM 1:350–1:500	Standard passive-vDISCO	Mouse half brain	Moderate penetration	Increase the incubation time more than 30% with respect to the Chromotek nanobodies
Fluotag-Q anti-RFP AF647 (AB_2905529)	Anti-RFP	tdTomato, mcherry	NanoTag Biotechnologies	N0401-AF647		Stock = 1.25 μM 1:350–1:500	Standard passive-vDISCO	Mouse half brain and 50 μm slices	Good penetration	Increase the incubation time more than 30% with respect to the Chromotek nanobodies
Custom-made anti-GFP AlexaFluo647; AB_2905530	Anti-GFP	eGFP	-	-	-	Stock = 0.46 mg/ml Mouse brain: 1:300–1:400 (1.38–1.5 μg/ml)	Standard passive-vDISCO	Mouse brain	Bright, good penetration	Increase the incubation time more than 20% with respect to the Chromotek nanobodies. Good results for staining neuronal lines

[a]According to the companies´ website: Chromotek anti-GFP nanobodies should be also compatible with CFP, wtGFP, GFP S65T, AcGFP, TagGFP, tagGFP2, mClover (Clover A206K), sfGFP, pHluorin, Venus and Citrine; Chromotek anti-RFP nanobodies should be also compatible with mRFP, mRFPruby and mPlum; Nanotag anti-GFP nanobodies should be also compatible with mEGFP, superfolder GFP and most common CFP and YFP variants; the clone 2B12 of the Nanotag anti-RFP/mScarlet-i nanobody should be also compatible with mOrange2, dsRed1, dsRed2, mRFP and mCherry. [b]Concentrations should be adjusted on the basis of sample size, expression of the fluorescent proteins and preliminary tests.

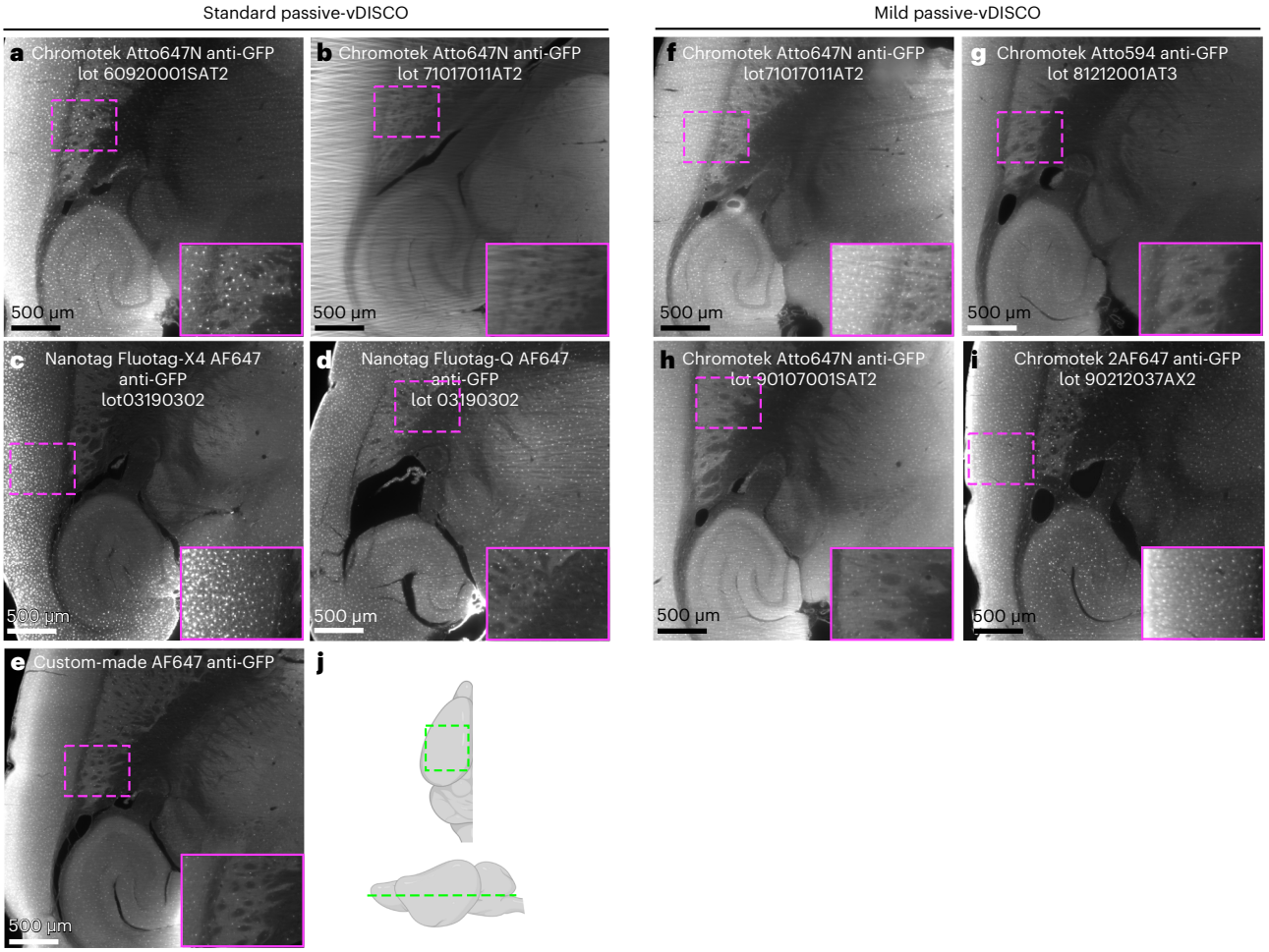

Fig. 7 | Performances of different kinds of nanobodies in passive-vDISCO. a–i, Light-sheet microscopy images of half mouse brains from CX3CR1-GFP line showing the performance of different batches of nanobodies from different sources and companies using standard passive-vDISCO (**a–e**) and mild passive-vDISCO (**f–i**). The nanobody that was used is indicated in each panel title. **j**, Illustration indicating the anatomic region of the brain (green dashed) that is displayed in **a–i**. Note that the imaging was taken either on the right or on the left hemisphere; the right hemisphere images were flipped to ease the comparison between the different nanobodies. All the results in this figure were similarly observed in at least two independent experiments for each kind of nanobody. Animal experiments followed European directive 2010/63/EU for animal research, reported according to the Animal Research: Reporting of In Vivo Experiments (ARRIVE) criteria, complied with the '3Rs' measure and were approved by the ethical review board of the government of Upper Bavaria (Regierung von Oberbayern, Munich, Germany) and conformed to institutional guidelines in Klinikum der Universität München/Ludwig Maximilian University of Munich). The severity of the procedure was low.

Box 1 | Nanobody validation in sections

Procedure

1 Cut a post-fixed organ of interest (e.g., brain) in 400–1,000 µm sections and place them into the wells of a 24-multiwell plate filled with 1× PBS, 0.5–1 ml each well. Cutting can be performed, for example, with a vibratome or a brain matrix.
2 Before staining, image the sections with a fluorescence microscope (e.g., confocal or epifluorescence) to verify that the sample bears fluorescence signal.
3 Incubate the sections completely immersed in the permeabilization solution for 3 h at 37 °C in the dark and with gentle shaking.
4 To test whether the nanobody is more suitable for passive-vDISCO or mild-vDISCO, allocate some sections to be incubated with the passive-vDISCO staining solution and some sections to be incubated with the mild-vDISCO staining solution. Exchange the permeabilization solution with the staining solutions (500 µl to 1 ml final volume each well) containing the nanobody and incubate overnight to 1 d at 37 °C in the dark and with gentle shaking. For the nanobody concentration, follow the information in Table 1 or the manufacturer datasheet.
▲ **CRITICAL STEP** Keep some sections that are not incubated with the nanobody as negative controls. Seal the 24-multiwell plate with tape or parafilm to prevent evaporation of the solutions.
5 Wash with the washing solution at RT three to four times for 10–20 min in the dark with gentle shaking.
6 Wash with 1× PBS at RT three to four times for 10–20 min in the dark with gentle shaking.
7 Image the stained slices with a confocal or epifluorescence microscope.

passive-vDISCO should be made before starting the whole pipeline, since passive-vDISCO requires the removal of the specimens of interest from the body.

Decolorization and decalcification

In whole-body vDISCO, the subsequent step after fixation is the perfusion with a decolorization solution, which has the purpose of removing the pigment heme contained in the blood. In the standard procedures to prepare the samples, perfusing with PBS before fixation does not completely wash the blood from organs rich of blood such as spleen and bone marrow; consequently, they will still appear dark red[16]. Heme in the blood is known to absorb light in the visible spectrum[31,41,42] and cause autofluorescence[31,43].

The decolorization solution is made by diluting ¼ CUBIC reagent #1 (CUBIC#1) solution[8,18] in PBS. The resulting solution contains Quadrol, which is the chemical with the strongest decolorization activity in CUBIC#1. In fact, Quadrol belongs to the chemical family of aminoalcohols, compounds that have previously been shown to efficiently elute heme from the blood[8,17–19,44]. Since CUBIC#1 is a very viscous reagent, in vDISCO whole-body perfusion system, only a less viscous 20–30% dilution of the reagent can be pumped. The dilution that retains a good decolorization ability is 25%, but this value should still be adjusted on the basis of the pumping system and the amount of blood present in the body. Other strategies for decolorization have been published before such as the use of H_2O_2 and peroxides or acid-acetone and strong bases to bleach or to dissociate the heme, respectively. However, we strongly discourage their application here, because these chemicals are known to detrimentally affect the antigenicity of the tissue[45–47].

In passive-vDISCO, the decolorization step is performed by passively incubating the samples with the decolorization solution. Since in this circumstance the reagents can only react with the sample via diffusion (substantially slower than via the active transport system), an incubation at 37 °C would help speed up the process (Table 2 and 'Procedure' section).

The decolorization step is followed by the decalcification of the bones. Bones, owing to their calcified nature and poor content of lipids, can interfere with imaging and impede light penetration[16,48]. We decided to exploit the calcium-chelating properties of ethylenediaminetetraacetic acid (EDTA), which has been successfully used in other bone-clearing protocols[21,22,49], to remove Ca^{2+} ion from the bones[21,22,49]. The vDISCO decalcification solution consists of 10% (wt/vol) EDTA dissolved in PBS and is pumped into the body of the animal via intracardial perfusion at room temperature for 2 d. We do not recommend acids including nitric acid or hydrochloric acid previously reported as decalcifying reagents[50], because they can disrupt the antigens in the tissue.

Although the decolorization and decalcification steps can be skipped when using passive-vDISCO, organs rich of blood (e.g. spleen) or dissected bones would still benefit by the two treatments after the sample preparation and before staining (Table 2).

Staining and choice of the dyes/nanobodies

In whole-body vDISCO, the staining step can start after the animal is decalcified and washed with PBS, while in passive-vDISCO, the staining can be performed straight after washing the post-fixed samples with PBS. The staining consists of two parts: permeabilization, which also has the aim to loosen the extracellular matrix, and the actual staining. In whole-body vDISCO, both parts are performed with active perfusion with the perfusion setting heated up to 28–30 °C with an infrared lamp (Fig. 4c–h), while in passive-vDISCO both parts are performed with passive incubation at 37 °C. The warm temperature is fundamental to increase the penetration of the dyes[11,51]. In the permeabilization part, the samples are perfused/incubated for 1 d with a permeabilization solution containing serum, Triton X-100, methyl-β-cyclodextrin, *N*-acetyl-L-hydroxyproline and sodium azide in PBS. Methyl-β-cyclodextrin has the purpose to destabilize the tissue collagen[10], while *N*-acetyl-L-hydroxyproline to extract the cholesterol[10]. Then the samples are stained by perfusing/incubating with this same solution containing the dye: 6 d of perfusion are sufficient for a whole body, while the timing for passive-vDISCO can vary depending on the size of the sample (e.g., 1–2 d for 1 mm sections, 14 d for whole mouse brains, Table 2). For some batches of nanobody that show poor stability in this staining solution (Table 1), dyes should be diluted in another solution with the same concentrations of serum, Triton and sodium azide in PBS, but without methyl-β-cyclodextrin and *N*-acetyl-L-hydroxyproline. We called this version of vDISCO 'mild-vDISCO' (Table 3). However, the absence of these two permeabilization reagents during the staining step can result in less dye penetration.

The staining part is particularly critical especially in whole-body vDISCO: the perfusion must run flawlessly to ensure that the nanobody can reach all body districts of the animal.

Table 2 | Tested experimental timings and solution volumes for passive-vDISCO

Sample	Decolorization time (optional, depending on the blood content)	Decalcification time	Final incubation volume	Permeabilization (37 °C) time	Staining (37 °C) time[a]	Washing (RT) time	50%–70%–80%–100% THF dilutions (RT) time	Final 100% THF (RT) time	DCM (RT) time	BABB (RT) time
500-µm-thick mouse brain slices (for nanobody validation)	–	–	500–700 µl	20 min	3 h	10 min each wash	20 min	30 min	10 min	At least 20 min
1-mm-thick mouse brain slices	–	–	1 ml	4–5 h	2–3 d	20–30 min each wash	45 min	45 min + 3 h	15 min	At least 2 h
Mouse small organs such as lymph nodes or adrenal glands	–	–	1.5 ml	12 h	4 d	20–30 min each wash	1 h	1 h + 2h	30 min	At least 3 h
Half mouse brain	–	–	3–4 ml	0.5–1 d	7–9 d	30–60 min each wash	1 h	1 h + overnight	30–60 min	At least 6 h
Whole mouse brain	–	–	4–4.5 ml	1–2 d	13–15 d	1–2 h each wash	2 h	2 h + overnight	1–2 h	At least 12 h
Mouse brain + spinal cord	–	–	10–13 ml	1–2 d	13–15 d	1–2 h each wash	2 h	2 h + overnight	1–2 h	At least 12 h
Mouse spinal cord	–	–	3–4 ml	5–7 h	4–5 d	20–30 min each wash	45 min	45 min + 8 h (or overnight)	30–45 min	At least 4 h
Mouse lung lobes	If blood content is high: 2 d in decol. solution (20% (vol/vol) of stock in PBS)	–	1 ml	12 h to 1 d	3–4 d	45 min to 1 h each wash	2 h	2 h + 8 h (or overnight)	1–2 h	At least 5 h
Mouse gut tracts	If blood content is high: 1 d in decol. solution (20% (vol/vol) of stock in PBS)	–	2–2.5 ml	1 d	5–6 d	45 min to 1 h each wash	1.5 h	1.5 h + 6 h (or overnight)	1 h	At least 4 h
Mouse whole spleen	If blood content is high: 2 d in decol. solution (25% (vol/vol) of stock in PBS)	–	1 ml	1 d	7–8 d	1–1.5 h each wash	2 h	2 h + overnight	1–2 h	At least 12 h
Mouse whole thymus + whole heart	If blood content is high: 1 d in decol. solution (20% (vol/vol) of stock in PBS)	–	1.5 ml	1 d	8–9 d	2 h each wash	2 h	2 h + overnight	1–2 h	At least 12 h
Mouse pups (P0)	–	–	4.5 ml	1 d	4 d	2 h each wash	2 h	2 h + overnight	1 h	At least 3–4 h
Mouse whole head	If blood content is high: 1 d in decol. solution (20% (vol/vol) of stock in PBS)	2 d	50 ml	2 d	6 d	6 h each wash	12 h	12 h	1 h	At least 5–6 h
2-mm-thick pig pancreas slices	–	–	4.5 ml	1–2 d	7–10 d	2 h each wash	2 h	2 h + overnight	1 h	At least 3–4 h

[a]Timings are given for Chromotek nanobodies; increase the staining time as indicated in Table 1 for other nanobodies

Table 3 | Experimental pipeline of standard vDISCO versus mild-vDISCO for passive staining

Step	Standard passive-vDISCO solutions	Mild-vDISCO solutions	Temperature
Decolorization (optional)	Decolorization solution	Decolorization solution	RT or up to 37 °C
Washing	1× PBS	1× PBS	RT
Decalcification (optional)	Decalcification solution	Decalcification solution	RT
Washing	1× PBS	1× PBS	RT
Permeabilization	Permeabilization solution	Permeabilization solution	37°C
Staining	Staining solution with methyl-β-cyclodextrin and *trans*-1-acetyl-4-hydroxy-l-proline, + dye	Mild staining solution without methyl-β-cyclodextrin and without *trans*-1-acetyl-4-hydroxy-l-proline, + dye	37°C
Washing	Washing solution	Washing solution	RT
Washing	1× PBS	1× PBS	RT
Clearing	THF series, DCM, BABB (Table 2)	THF series, DCM, BABB (Table 2)	RT

Dyes with small size are ideal for vDISCO owing to their better tissue penetration ability. We found that the small nuclear dye propidium iodide (PI) efficiently labels all the nuclei of the cells of our samples with both passive-vDISCO and whole-body vDISCO[23]. Interestingly, PI tends to accumulate in tissues dense of cells from organs such as thymus, lungs and especially bone and its marrow, in this way being a good stain to highlight the internal organs and bones of the animal. Owing to this property and its red spectrum (excitation (Ex)/emission (Em) = 535/617) the PI can be used in multichannel imaging with nanobodies conjugated with far-red fluorophores: for example, in the neuronal reporter line Thy1-GFPM, PI was used as counterstain for organs and bones, while the nanobody was used to follow the trajectories of the nerves through the bones[23]. The TO-PRO-3 far-red (Ex/Em = 642/661) nucleus dye can be used instead of PI, but it shows a strong batch-to-batch variability in terms of staining performance: some batches provide very low signal. We do not recommend DAPI (Ex/Em = 350/470) as counterstain of big tissues, because its UV spectrum allows only superficial penetration of the light[52]. However, DAPI can still be an option for staining slices.

For whole-body and passive immunolabeling of the samples, we exploited the small size of the nanobodies. Nanobodies show cross-compatibility with fluorescent proteins with a similar structure: for example, the anti-GFP can also bind (e)YFP, Venus, CFP and other GFP derivates, including eGFP, sfGFP etc., or the anti-RFP can also bind its derivates such as mRFP, mCherry, DsRed, etc. Further compatibility information can be found in the vendors datasheet: for example, the anti-RFP nanobody from the Chromotek company does not recognize tdTomato, while some clones from Nanotag do (R.C., unpublished observations), as also reported in Table 1.

We observed that fluorophores from the Atto and Alexa family give good performance with vDISCO (Table 1, Figs. 2 and 5–9 and Extended Data Figs. 2 and 3). If performing custom conjugation of the nanobody with a desired fluorophore (Fig. 7e and Extended Data Fig. 3c), different chemistries for the conjugation reaction might need to be tried (NHS, maleimide, enzymatic, etc.), depending on the sequence of the nanobody and the chosen dye: for example, it is known that Atto647N is a sticky dye that can cause unspecific staining of the tissue. Moreover, when lysine residues are present in the complementarity-determining regions of the nanobodies, site-directed chemistry should be favored to avoid the labeling affecting the binding capacity of the nanobody.

To exploit the deeper penetration of long-wavelength light, we preferred to use nanobodies conjugated to far-red fluorophores such as Alexa647 or Atto647N[1,23], except when we needed to multiplex different colors. Nanobodies show high performance variability as well: in our experience, diverse success in staining could be observed depending on the nanobody clone, the supplier, the conjugation strategy and even the batch of the same product (Fig. 7 and Extended Data Fig. 3). For instance, whole-body vDISCO was mostly performed with nanobodies from Chromotek[1,23]. These nanobodies are characterized by a high brightness and a good penetration capability in whole bodies[1,23], but in the standard passive-vDISCO protocol (Fig. 7a–e and Extended Data Fig. 3a–c) they showed variable results (e.g., Fig. 7a versus Fig. 7b), indicating a possible issue in the chemical bond between the nanobody and the fluorophore in our application. Therefore, some batches from

Chromotek require the use of mild–vDISCO (Tables 1 and 3, Fig. 7f–i, Extended Data Fig. 3d,e and 'Procedure' section). Nanobodies from Nanotag company were tested for vDISCO passive staining. We tested: FluoTag-X4 made by two clones that recognize two distinct epitopes of the same protein and each clone is coupled with two fluorophores (Table 1, Fig. 7c and Extended Data Fig. 3a), and FluoTag-Q (Table 1, Figs. 7d and 9d–h and Extended Data Fig. 3b) made by a clone coupled exactly 1 to 1 with the fluorophore molecules. Fluotag-X4 provided high brightness but penetrated less (e.g., Figure 7c versus Fig. 7i and Extended Data Fig. 3a versus Extended Data Fig. 3e); on the other hand, FluoTag-Q gave excellent results for passive staining of microglia and pericytes expressing GFP (Figs. 7d and 9d–h), although it also showed less penetration power than the Chromotek nanobodies in the Thy1-GFPM line (Extended Data Fig. 3b versus Extended Data Fig. 3e). In general, Nanotag nanobodies demonstrated very high stability, without the need to use mild-vDISCO (Tables 1 and 3 and Fig. 7). Since the nanobody clones are different from company to company, we hypothesize that the different penetration ability might be due to the surface charges of the clones. Nanotag nanobodies possess more negative charges on the surface that might interact with the tissue, slowing the penetration, while Chromotek nanobodies tend to have an almost neutral charge on the surface (personal communication). Other intrinsic properties of nanobodies can affect the overall penetration capability too, such as: distribution of charges in the amino-acid sequence, their complementarity-determining regions, the affinity and the epitope recognized. Nevertheless, the penetration performance can be increased by extending the incubation times for passive staining (e.g., 20–30% longer) and/or increasing the temperature up to 40 °C. We did not observe detrimental consequences of long incubations (up to 22 d). We also tested a custom-made nanobody conjugated to Alexa 647 with passive-vDISCO, which provided good staining in terms of signal stability, penetration and brightness in Thy1-GFPM brains (Extended Data Fig. 3c). Regarding the concentration, 0.08–0.14 μg ml^{-1} of nanobody is sufficient to stain a whole mouse, while 10× more concentrated nanobody was used for whole mouse brains processed with passive-vDISCO (Table 1). However, in both protocols the concentration can be adjusted on the basis of the expression of the fluorescent protein and the size of the sample.

Last, nanobodies must be validated before commencing the experiment to verify that the nanobody is able to sustain the staining and clearing conditions (Box 1). In general, nanobodies that do not normally give a good performance in standard immunohistochemistry and immunofluorescence should not be used with vDISCO. For more information about the tested samples, compatible fluorescent proteins, suggested concentrations, batch/lot numbers, suggested protocol, performances of staining and other information, see Table 1.

Tissue clearing

The clearing process starts after staining, and it is carried with a slightly modified version of 3DISCO[5,39], a straightforward and fast clearing protocol that can achieve high transparency. For both whole bodies and dissected samples, the clearing procedure consists of passive incubations of the samples with organic solvents. These solvents must not be perfused, since they can damage the pump components. In fact, organic solvents can often melt plastic; thus, plastic containers used for clearing must be checked for their resistance to these chemicals. In our experience, polypropylene from specific manufacturers stands organic solvents well (see 'Materials' section). Whole mice or big organs such as pig pancreas[37] can be placed in glass containers that can hold at least 350 ml, while slices or small mouse organs can be placed in plastic tubes or glass jars.

Then, samples are incubated with an ascending series of dilutions of tetrahydrofuran (THF) to dehydrate, dichloromethane (DCM) to delipidate and a mixture of benzyl alcohol and benzyl benzoate (BABB, which replaces dibenzyl ether (DBE) of the original 3DISCO) to match the refractive index (RI) and reach transparency. The duration of each dehydrating incubation is highly flexible and depends on the size of the sample and its lipid content (for THF timings, see Table 2). The delipidation with DCM is optional but recommended with lipid-rich organs or whole bodies (for DCM timings, see Tables 2 and 4). All procedure timings (Tables 2 and 4) can be adjusted and extended on the basis of preliminary tests. With overweight animals, prolonging all the steps of clearing will improve the transparency.

Since synthetic fluorophores are highly stable in the clearing reagents[23], over-incubating the samples for multiple days in the clearing solutions (if, for example, left by accident) did not result in dramatic bleaching of the fluorescence signal. The level of transparency will probably increase over time with a longer incubation in the RI matching solution as more solution penetrates the sample. BABB can be replaced with DBE with comparable results, although we chose to use BABB because it

Table 4 | vDISCO active staining pipeline

		Adult mouse			Mouse pups		
Step	**Solution**	**Modality**	**Time**	**Temperature**	**Modality**	**Time**	**Temperature**
Boosting							
Washing	1× PBS	Active	2–3 h × 2 times	RT	Active	4–5 h	RT
Decolorization	Decolorization solution	Active	2 d (refresh when solution turns yellow)	RT	Active	3 d (refresh when solution turns yellow)	RT
Washing	1× PBS	Active	2–3 h × 3 times	RT	Active	4–5 h	RT
Decalcification	Decalcification solution	Active	2 d	RT	Active	2 d	RT
Washing	1× PBS	Active	2–3 h × 3 times	RT	Active	4–5 h	RT
Permeabilization	Permeabilization solution	Active	12 h	RT	Active	12 h	RT
Staining	Staining solution (permeabilization solution + dye)	Active	6 d	With infrared lamp (26–28 °C)	Active	4–6 d	With infrared lamp (26–28 °C)
Staining	Staining solution (permeabilization solution + dye)	Passive	2 d	37 °C or RT for nanobodies with stability issues (Table 1)	–	–	–
Washing	Washing solution	Active	2–3 h × 3 times	RT	Active	4–5 h × 2 times	RT
Washing	1× PBS	Active	2–3 h × 3 times	RT	Active	4–5 h	RT
Clearing							
Dehydration	50%, 70%, 80% THF in distilled water	Passive	12 h each dilution of THF	RT	Passive	12 h each dilution of THF	RT
Dehydration	100% THF	Passive	12 h × 2 times	RT	Passive	12 h × 2 times	RT
Delipidation	100% DCM	Passive	3 h	RT	Passive	3 h	RT
Refractive index matching	BABB	Passive	>12 h	RT	Passive	>12 h	RT

is slightly denser than DBE and therefore samples are less subjected to moving during imaging. BABB represents the storing solution as well, where samples can be left for months and years, and if at room temperature and protected from light, they still retain fluorescence signal[23] (Figs. 2 and 5). Nevertheless, we did not experience fading of the signal if stored at 4 °C.

Last, samples stained with vDISCO can be cleared with other clearing protocols such as iDISCO+, which is based on methanol dehydration. This finding is interesting if the advantages of other clearing methods are desired: for example, iDISCO+ clearing is known to shrink the sample less compared with 3DISCO[53].

Imaging

The samples will stay transparent as long as they are completely submerged in the RI matching solution; thus, this solution must constitute the sample mounting medium for imaging as well.

Ideally the microscope's objectives should provide decent resolution with the highest possible numerical aperture (NA) and with the longest possible working distance (WD), to cover the whole thickness of the sample. The objectives can be air lenses or immersion lenses; the latter should be optimized for the RI of the RI matching solution or of the immersion medium, to reduce optical aberrations and increase the resolution.

An epifluorescence microscope such as the Zeiss AxioZoom EMS3/SyCoP3 (Extended Data Fig. 5a–d), which can support a long WD 1× air objective[1,23] ideal to quickly assess the success of the staining (e.g., while testing slices) or to obtain whole-body 2D images in 10–15 min.

On the other hand, light-sheet microscopes[15] (Extended Data Figs. 6, 7 and 8) are ideal to achieve 3D high-resolution imaging of cleared samples, because in these systems the light-sheet illuminated focal plane is simultaneously captured with a scientific complementary metal oxide semiconductor (sCMOS) camera, allowing very fast imaging and low photobleaching.

In particular, we used LaVision-Miltenyi Biotec Ultramicroscope II, LaVision-Miltenyi Biotec Blaze microscope for large samples, Zeiss Lightsheet Z.1 and mesoSPIM.

The Ultramicroscope II has an imaging chamber of 8 × 8 × 3.5 cm with a standard sample holder travel range of 1 ×1 × 1 cm (in the *XYZ* axes), which we increased to 1.1 cm in *z* by a custom-made stage (available from the manufacturer). This microscope was used to create the whole-body neuronal projection map of a Thy1-GFPM mouse[23], by using a 1× air objective coupled with a zoom body kept at 0.63×. With these settings the field of view (FOV) was 2 × 2.5 cm, which was able to cover the entire width of a mouse body. However, since the travel range of the sample holder was smaller than the size of the entire body volume, multiple scans of different body parts were first taken by displacing the body after each scan, and then the scans were stitched together. For labs owning the Ultramicroscope II, we suggest this strategy to image whole mice or samples bigger than the travel range, although the process of mounting the sample can be quite complicated and the entire imaging step can take 1–2 weeks (Extended Data Fig. 6a–j).

Therefore, we suggest using light-sheet microscopes with bigger sample holders and imaging chambers such as the LaVision-Miltenyi Biotec Blaze light-sheet microscope, which is also optimized for large samples, including whole mouse bodies[1] and intact human kidneys[37]. Our Blaze system possesses an elongated customized sample holder that can travel 4 × 9 × 5 cm in the *XYZ* axes and a large imaging chamber of 25 × 7 × 9 cm (both available from the manufacturer). Moreover, it works with a dipping 1.1× objective that has a FOV of 1.2 × 1.2 cm. With this microscope, an entire mouse can be imaged with one tiling scan in just 2–3 d, although we recommend imaging the body in two tiling scans with an overlap: the first scan covering one side and the other scan after flipping the animal. The two scans will be fused together in the end. This strategy will allow achieving the best resolution for both sides, overcome the limited WD of the objective and the possible incomplete transparency of the samples.

The Zeiss Lightsheet Z.1 is a light-sheet microscope with a closed chamber optimized for single organ or small organism imaging (Extended Data Fig. 8). It has an imaging chamber of 1 × 1 × 2 cm, a sample holder travel range of 1 × 5 × 1 cm and a rotation stage for multi-angle scans to achieve isotropic resolution in 3D (Fig. 5).

We used the Lightsheet Z.1 and the Ultramicroscope II to capture scans of whole mouse organs (e.g., lungs, heart and brain) with higher magnification and NA objectives such as a 5× objective for the Z.1 (Fig. 5), a 4× objective (Figs. 6b–f, 7 and 9d–h and Extended Data Fig. 3) or a 12× objective[23] (Fig. 9a–c) for the Ultramicroscope II. We recommend selecting the thinnest sheet available and setting the *Z*-step interval according to the size of the structures of interest (e.g., 2–10 μm for single-cell resolution).

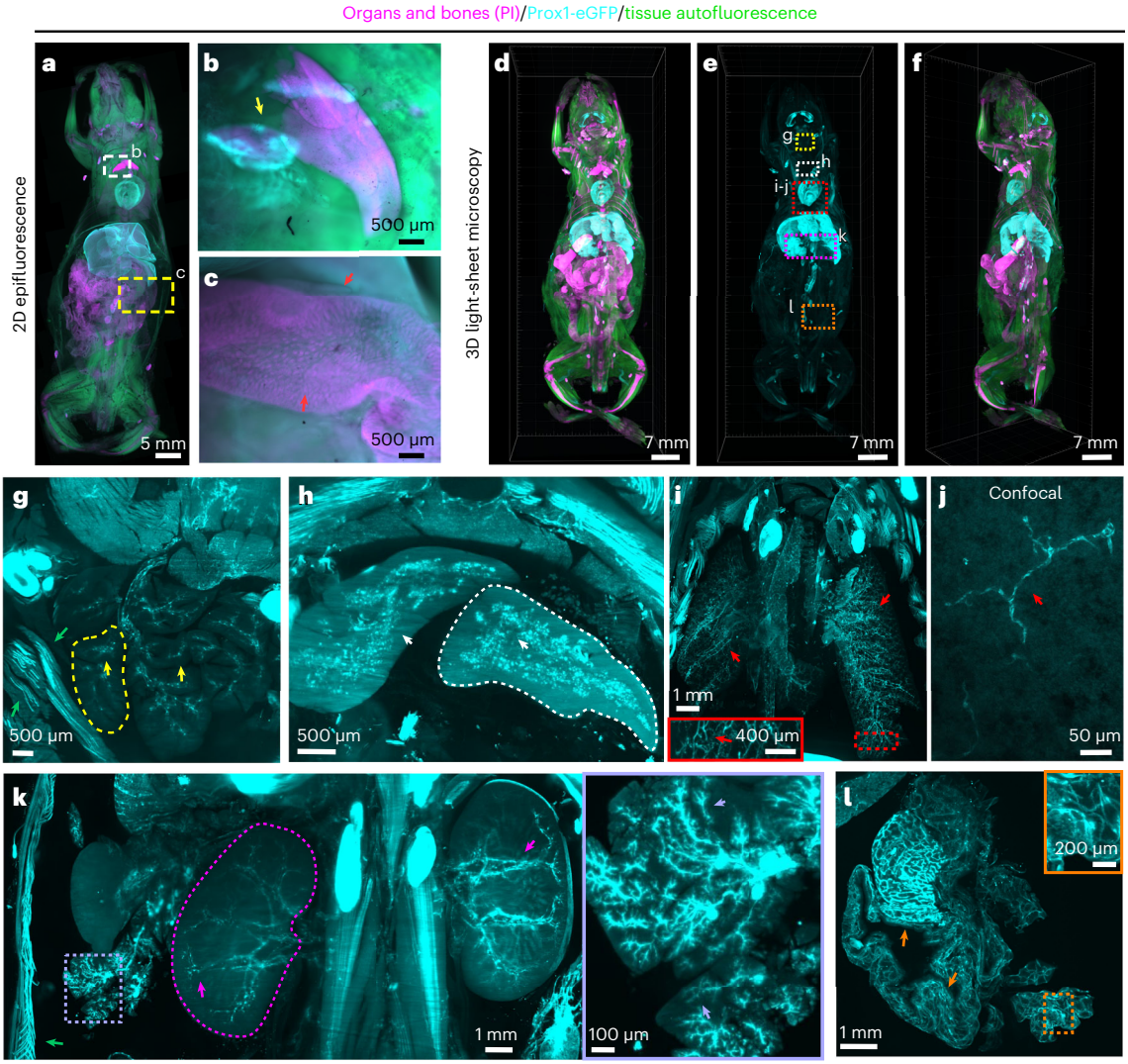

Fig. 8 | Prox1-EGFP whole-body scan taken with epifluorescence, light-sheet and confocal microscopy. a–**c**, 2D epifluorescence microscope imaging of a Prox1-EGFP mouse after vDISCO pipeline (**a**). Zoomed-in views (**b** and **c**) of the dashed regions in **a** showing the thymus (yellow arrow) and the intestine, respectively. Red arrows in **c** indicate intestine villi. **d**–**f**, 3D reconstruction of the same mouse imaged with light-sheet microscopy in dorsal (**d** and **e**) and 30° rotated view (**f**). **g**–**i** and **k**,**l**, High-magnification images of the different body regions indicated by the dashed boxes in **e** from the same whole-body light-sheet imaging scan in **d**. **j**, Confocal imaging of the lungs in **i**. In **g** and **h**, Prox1-EGFP+ signal is visible as cells in the region including the salivary glands (**g**, yellow arrows) and thymus (**h**, white arrows). The dashed yellow and white lines in **g** and **h** delimit a salivary gland and a thymus lobe, respectively. In **g** and **i**–**l**, Prox1-EGFP+ signal is visible as elongated structures in the body regions including some muscles (**g** and **k**, green arrows), in the body region showing the lungs (**i** and **j**, red arrows), in the body region including the pancreas (dashed violet box in **k**, violet arrows), in the kidneys (**k**, magenta arrows, right kidney is delimited by the dashed magenta line) and in the intestine (**l**, orange arrows). **g**–**i** and **l** are shown in ventral view, while **k** is shown in dorsal view. Note that some details of the Prox1-EGFP+ signal that are not visible in 2D epifluorescence imaging are now visible in light-sheet imaging, for example in the thymus (**b** versus **h**) and in the intestine (**c** versus **l**). Prox1-EGFP+ signal is shown in cyan in all the panels. In **a**–**c**, **d** and **f**, organs and bones are labeled by PI and shown in magenta while tissue autofluorescence is shown in green. Animal experiments followed European directive 2010/63/EU for animal research, reported according to the Animal Research: Reporting of In Vivo Experiments (ARRIVE) criteria, complied with the '3Rs' measure and were approved by the ethical review board of the government of Upper Bavaria (Regierung von Oberbayern, Munich, Germany) and conformed to institutional guidelines of Klinikum der Universität München/Ludwig Maximilian University of Munich). The severity of the procedure was low.

Cleared samples can subsequently be dissected from the vDISCO processed body in order to be imaged with higher-resolution but slower microscopes, including confocal[1,23] microscopes (Extended Data Fig. 5e–g), being aware that the commercial systems of these microscopes are normally coupled with high-NA objectives with therefore limited WD. Here, samples processed with vDISCO were imaged with the laser scanning confocal microscope Zeiss LSM 880 by using a Leica long WD 25× objective mounted on a custom mounting thread (external M27x0.75 to internal M25x0.75 adapter ring, which has no optics and does not modify any optical parameter; available from the manufacturer)[23] (Figs. 6a, 8j and 9h). However, the use of objectives from a different manufacturer can

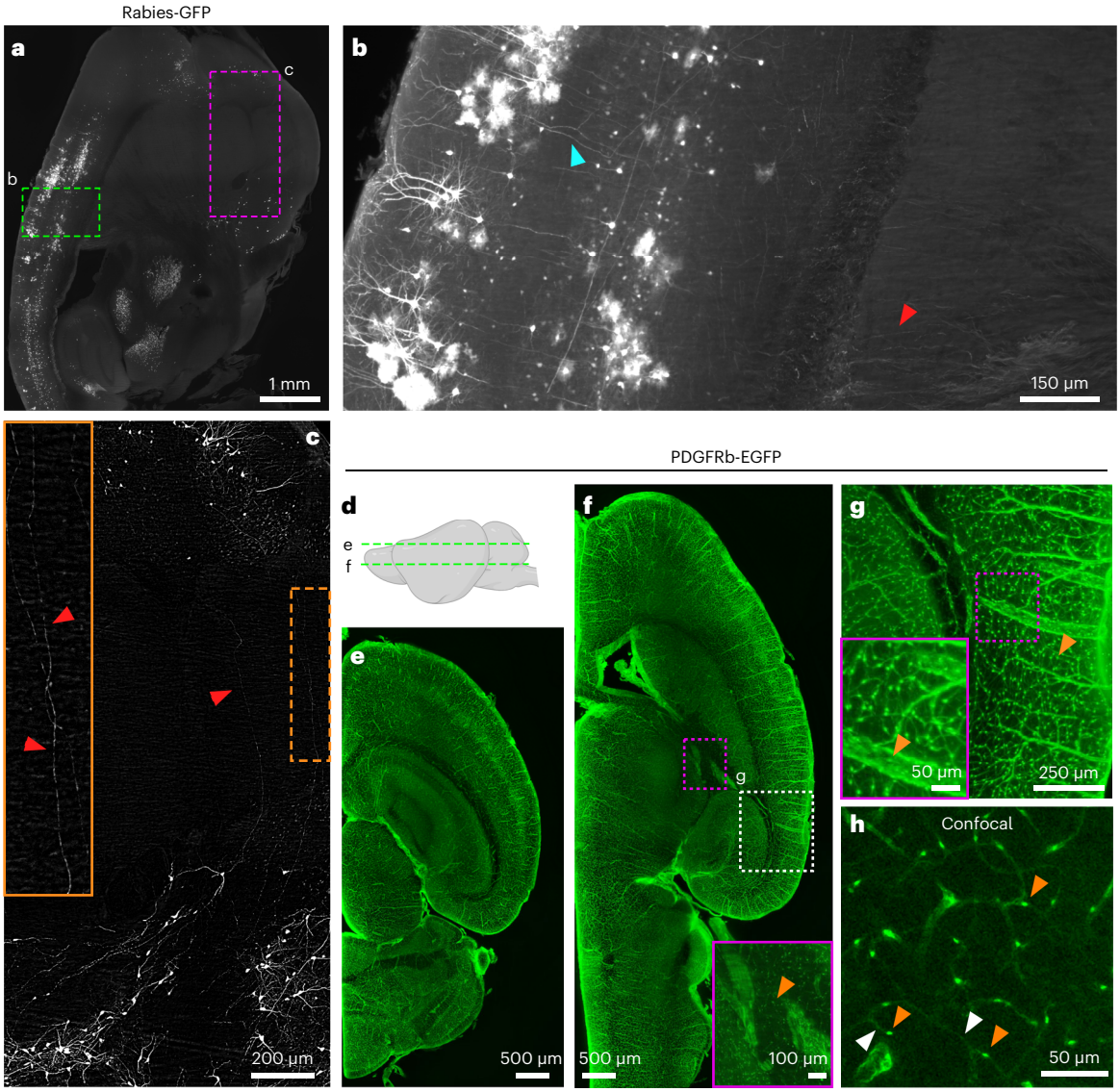

Fig. 9 | Virus tracing and pericytes in the brain processed by vDISCO. a–c, Light-sheet microscope 2D images of a brain from an adult Emx1-Cre × RΦGT mouse injected with EnvA-pseudotyped G-deleted rabies virus expressing GFP (SADB1969) into the neocortex and processed with vDISCO. The images show the virus traced neurons with single axons visible in the cortex (**b**, cyan arrowhead) and in the striatum (**b**, red arrowhead) in the raw data and in the postprocessed image (**c**, red arrow-heads). The postprocessing was performed with sharpening of the signal, noise filtering and background equalization and removal. **d–h**, Half brain of a PDGFRb-EGFP mouse processed with vDISCO and imaged with light-sheet microscopy (**e–g**) and confocal microscopy (**h**): two images (**e** and **f**) corresponding to optical slices indicated in **d** are shown. Single EGFP^{+} pericytes are visible throughout the brain and wrapping blood vessels (**f** and **g**, orange arrowheads). In **h**, in confocal imaging the pericyte somas (orange arrowheads) and their fine processes (white arrows) are visible. For both virus traced and pericyte samples, similar results were obtained in at least three independent brains. Animal experiments followed European directive 2010/63/EU for animal research, reported according to the Animal Research: Reporting of In Vivo Experiments (ARRIVE) criteria, complied with the '3Rs' measure and were approved by the ethical review board of the government of Upper Bavaria (Regierung von Oberbayern, Munich, Germany) and conformed to institutional guidelines of Klinikum der Universität München/Ludwig Maximilian University of Munich). The severity of the procedure was moderate for virus tracing and low for pericyte labeling.

have several drawbacks such as chromatic, spherical aberration and axial distortions, due to the mismatch in focal lengths and RI. We recommend the users choose the objective on the basis of their applications and, if possible, ask the microscope manufacturer about eventual drawbacks and customizations.

Last, the mesoSPIM[54] light-sheet microscope is a promising option for imaging large transparent samples. This microscope is characterized by an isotropic resolution and can achieve very high scanning speeds (15 min per mouse brain at 5 µm sampling versus 3 h of the Ultramicroscope II, thus 12× faster), owing to the FOV of 2–20 mm, the travel range of 52 × 52 × 102 mm and the 360° rotating sample holder for multiview imaging[54]. With its large travel range, the mesoSPIM is capable

of imaging the whole mouse central nervous system[54] without remounting the sample. Since the mesoSPIM is fully customizable, a version tailored for imaging whole mice with no need of remounting (Extended Data Fig. 2) was built by updating the published version. The updated microscope has a larger (100 × 200 × 100 mm) *XYZ* travel range, uses imaging cuvettes of 30 × 30 × 120 mm or 40 × 40 × 120 mm and has an easy strategy to mount the samples on the basis of self-centering magnets (Extended Data Fig. 7). To reduce the number of required tiles while retaining micrometer-level sampling, an integrated CMOS camera with 3.75× more pixels compared with the previous version (15 MP versus 4 MP) was added in the system. The modified mesoSPIM allows us to perform two channel acquisitions of whole mice with 4.7 × 4.7 × 10 µm sampling within 9 h.

Regarding the data collection, raw images are collected as grayscale TIFF stacks with a pixel intensity range of 16 bits in order to resolve details in images with high contrast in intensity. Scans are saved as Zeiss CZI files if from Zeiss microscopes. In the latter case, the single images constituting a stack can then be exported as TIFF files as well.

Data processing and analysis

The data generated by vDISCO span from hundreds of gigabytes for individual organs to several terabytes for a single mouse. To handle these data, first, the size can be reduced by simply compressing the raw TIFF files with a lossless compression algorithm: we suggest Lempel-Ziv-Welch (LZW)[55], which is widely supported by common scientific software. Some commercial software for image rendering and analysis might have their own data structure that includes streams of compressed data (e.g., HDF5 in the IMS format from Bitplane Imaris or the SIS format of Arivis Vision4D). We convert our stacks to these structures for a fast loading of the files while also keeping a copy of the raw data.

Since almost all our data were generated as tiling scans, a stitching step is needed to reconstruct the final image. 2D image tiles generated by AxioZoom were manually aligned in the *XY* axes with each other on the basis of visual inspection and merged together with Adobe Photoshop CS6 using its 'Photomerge' function[56–58]. It should be noted that this procedure converts the 16-bit images to 8-bit RGB images irreversibly in addition to disabling single-channel viewing; therefore, it should be used only for the purpose of visualization of representative data. Alternative tools that work on 16-bit images include Fiji stitching plugins such as the more advanced 'BigStitcher'[59], which provides the advantages of flexible tile positioning, handling missing tiles, being open source and scriptable. Tiling scans saved in CZI format were automatically stitched by the Zen (Zeiss) acquisition software immediately after completing the acquisition. Tiling scans saved as TIFF stacks were stitched using Fiji[60] (ImageJ)'s stitching plugin[61] (Supplementary Fig. 1); optionally, the removal of acquisition errors/shifting can be done by using Fiji's TrakEM2 plugin and Imglib2library. Alternatively, tiling errors in the *XY* and *Z* dimensions can be corrected by using TeraStitcher[62] (v.1.10; https://abria.github.io/TeraStitcher/). Whole-mouse stitching/reconstruction processes can be heavily impaired by insufficient RAM. However, this can be overcome by using read on demand and caching implementations/code as we did in the Volume Fusion module of the Vision4D (Arivis) to stitch the whole mouse scan (Supplementary Figs. 2 and 3).

Data visualization and simple processing including filtering, equalization, histogram adjustments and contrast enhancement can be performed with several software tools: Fiji, Amira (FEI Visualization Sciences Group), Imaris (Bitplane) and Vision4D. The latter three were also used for 3D rendering of the scans. In particular, we used Fiji for fluorescent signal characterizations, while Imaris was applied to produce most of the 3D volume renderings and videos. All the above-mentioned software packages include tools for segmentation, tracing, quantification and manual annotation. For more specialized applications, software such as Neurolucida[63] or NeuroGPS-Tree[32] are available to analyze the morphology and quantify the features of the neurites[23] in neurons, or ClearMap[53] to automatically count, register and annotate cells with distinguishable round soma to the Allen Mouse Brain Atlas. All mentioned software tools offer a diverse degree of automation in analysis: for instance, one can either manually segment all the cell processes in a scan with the selection tools in Fiji or rely on the automated segmentation function of NeuroGPS-Tree. However, all the computer programs listed so far have limitations. First, the data size that they can handle is determined either by the RAM of the computer or by an intrinsic characteristic of the software; for example, NeuroGPS-Tree can only run data smaller than 1 gigabyte. Second, although some of these tools can perform automated analysis, all of them rely on traditional analytical approaches based on explicit preprocessing and recognition with filters, of which parameters must be adjusted by the human operator based on the characteristics of each individual dataset[53]. Since fully automated data analysis is greatly

desired owing to the complexity and the amount of data produced by the vDISCO pipeline, new computational tools based on artificial intelligence have now started solving these bottlenecks. In fact, the high-contrast images that vDISCO is able to provide represent suitable data that can be analyzed using deep learning algorithms. These algorithms are able to learn from the information provided by human experts and adjust their criteria in a dynamic and autonomous way depending on the characteristics of the new dataset[64,65]. This results in a reliable processing of large information in a very fast, accurate and unsupervised manner[66]. For instance, we developed a deep learning algorithm called DeepMACT to be run on vDISCO cleared animals to automatically detect, segment, quantify and annotate single metastasis in intact mice of cancer models[1].

Computational power, data storing and backing up

For the analysis of data generated via vDISCO, we used different standalone workstations: an HP Z820 with 196 GB RAM and with eight-core Xeon processor and nVidia Quadro k5000 graphics card, an HP Z840 dual Xeon 256 GB DDR4 RAM and with nVidia Quadro M5000 8GB graphic card, and an HP Z840 with 512 GB RAM and with Intel Xeon E5-2640 v4 @ 2.40GHz x 40 combined with a Quadro P5000 graphic card. All workstations can support Windows and Linux operating systems (OS) in dual boot mode. Windows can be used for standard or commercially available software, while Linux is the ideal OS for machine learning and deep learning algorithm coding. In general, RAM should be at least 256 GB and at least one SSD drive should be dedicated to the OS. In addition, we used multiple Promise Technology Pegasus2NAS (network attached storage with 96 TB capacity) devices to store the data collected daily and a couple of Synology RS2418 NAS (with 200 TB capacity) devices as backup and long-term storage system on 10-Gbit/s-Ethernet layout.

A promising option to obtain high computational power is to adopt cloud computing, which recently has been adopted in private sectors and in some labs[67]. In small labs, it is possible to start with an implementation of this strategy using local workstations. As the need for computing power arises with more data, another alternative is to migrate the workload to cloud platforms such as Digital Ocean, Amazon Web Services (AWS), Google Cloud Platform (GCP) and Microsoft Azure, where a cluster of high-performing interconnected computers can run data-crunching software in a distributed manner.

Finally, the data from the microscope should not be collected directly in a network drive while acquiring the image, because a failure of the connection in the network would jeopardize the whole scan. Rather, data should be stored on a hard drive with a redundant array of independent disks (RAID) configuration for speed and redundancy (depending on implemented local policy).

Materials

Reagents

Samples

Samples should be chosen from animals expressing fluorescent proteins that have been shown to be compatible with a particular nanobody according to the nanobody data sheet. The sample can express the fluorescent protein also with viral strategies. Alternatively, a sample coming from animals transplanted or injected with fluorescent-protein-expressing cells can be used. The following mouse lines are examples of suitable strains to use: Thy1-GFPM[36] (and Thy1-YFPH), CX3CR1$^{GFP/+}$ (B6.129P-Cx3cr1tm1Litt/J; Jackson Laboratory strain code 005582[27]), Prox1-EGFP (Tg(Prox1-EGFP) KY221Gsat/Mmucd; Mutant Mouse Resource and Research Centers strain code 031006-UCD) and PDGFRb-EGFP (Mouse Genome Informatics strain code 4847307) are shown in this study; LySM-GFP (Lyz2tm1.1^{Graf}, Mouse Genome Informatics strain code 2654931), CCR2$^{RFP/+}$ (B6.129(Cg)-Ccr2tm2.1Ifc/J; Jackson Laboratory strain code 017586) and CD68-GFP (C57BL/6-Tg(CD68-EGFP) 1Drg/j; Jackson Laboratory strain code 026827) were published before[23]. Other examples used here are: a C57BL/6 mouse transplanted with murine syngeneic R254 pancreatic cancer cells expressing eGFP for 38 d, and an adult Emx1-Cre × RΦGT mouse[68,69] injected with EnvA-pseudotyped G-deleted rabies virus expressing GFP (SADB19 (ref. [70])) in the neocortex. ▲ **CRITICAL** Animal experimentation must be in accordance with all the relevant governmental and institutional regulations. The animal housing and experiments in this work were conducted conforming to the institutional guidelines indicated in the figure legends.

Reagents for sample preparation

- 10× phosphate-buffered saline (PBS), 0.1 M, 10× stock solution (Invitrogen, cat. no. AM9625)
- Double-distilled water (ddH_2O)
- MMF triple combination anesthetics: midazolam, medetomidine and fentanyl (1 ml per 100 g body mass for mice; intraperitoneal) (Fentanyl, Panpharma, 0,5mg/10ml, Midazolam, Braun, 5mg/5ml, Dorbene vet, Zoetis, 1mg/ml) ▲ **CRITICAL** Follow the regulations of your institution regarding the drugs used for anesthesia.
- Heparin, 5,000 U/ml (Ratiopharm, cat. no N68542.03)
- 4% paraformaldehyde (PFA) in 1× PBS solution, 4% (wt/vol); pH 7.4 (Morphisto, cat. no. 11762.01000) ! **CAUTION** Toxic reagent ▲ **CRITICAL** Store at 4 °C and in dark, and use it within expiration period only.
- Sodium azide (Sigma-Aldrich, cat. no. 71290) ! **CAUTION** Very toxic reagent.

Reagents for decolorization, decalcification and immunostaining

- Urea (Carl Roth, cat. no. 3941.3)
- 10× PBS
- ddH_2O
- Quadrol, also known as *N*,*N*,*N*′,*N*′-tetrakis (2-hydroxypropyl)ethylenediamine (Sigma-Aldrich, cat. no. 122262)
- Triton X-100 (AppliChem, cat. no. A4975,1000)
- EDTA (Carl Roth, cat. no. 8040)
- Sodium hydroxide (NaOH; Sigma-Aldrich, cat. no. 71687)
- Goat serum (Gibco, cat. no. 16210072)
- Methyl-β-cyclodextrin (Sigma, cat. no. 332615)
- *trans*-1-acetyl-4-hydroxy-L-proline, also known as *N*-acetyl-L-hydroxyproline (Sigma-Aldrich, cat. no. 441562)
- PI (Sigma-Aldrich, cat. no. P4864 or Invitrogen cat. no. P3566)
- Nanobody (Table 1)

Reagents for clearing

- THF (Sigma-Aldrich, cat. no. 186562)
- DCM (Sigma-Aldrich, cat. no. 270997)
- Benzyl alcohol (Sigma-Aldrich, cat. no. 24122)
- Benzyl benzoate (Sigma-Aldrich, cat. no. W213802)

Equipment

General equipment and supplies

- Perfusion system One system (Leica, model Perfusion One), used for the initial fixation step ▲ **CRITICAL** This perfusion system can be replaced with other perfusion methods/set ups.
- Disposable 30 ml syringes (any; we used B. Braun, cat. no. 4616308F)
- Disposable 1 ml syringes (B. Braun, cat. no. 9166017V)
- Disposable 1 ml syringes with 25 G needle (B. Braun, model Injekt-F, cat. no. 9166033V)
- Micro-Fine Ultra needles 12.7 mm, 0.3 mm 29 G (BD, cat. no. 09372884)
- Microlance 3 needles 0.3 mm, 13 mm 30 G (BD, cat. no. 304000)
- Surgery scissors (FST, cat. no. 14958-11)
- Large surgical tweezers (FST, cat. no. 11000-20)
- Fine surgical tweezers (FST, cat. no. 11252-40)
- Razor blade (Personna, cat. no. 604305-001001)
- (Optional) Hair removal cream (Veet, Hair Removal Cream Normal)
- 5 ml tubes (Eppendorf, cat. no. 0030 119.401) ▲ **CRITICAL** These particular tubes are resistant to the clearing solutions.
- 50 ml tubes (Thermo Fisher Scientific, cat. no. 339653) ▲ **CRITICAL** These particular tubes are resistant to the clearing solutions. 50 ml tubes from Falcon brand (cat. no. 352070) are also resistant to the clearing solutions, but prone to leak BABB. 15 ml Falcon tubes are not recommended owing to the easy-to-break lid.
- 24-Multiwell plates (Falcon, cat. no. 353504) ▲ **CRITICAL** Multiwell and cell culture plastic are generally made from polystyrene, which is not resistant to the clearing solutions. Use these containers for all the steps before clearing, but not for clearing.
- 35 mm glass-bottom Petri dishes (MatTek, cat. no. P35G-0-14-C)

- 5 ml disposable Pasteur plastic pipettes (Alpha Laboratories, cat. no. LW4728), resistant to the clearing solutions
- Pipette boy (any; we used Roth, model accu-jet pro, cat. no. NA55.1)
- 50 ml serological pipettes (Corning Costar Stripette, cat. no. CORN4490) ▲ **CRITICAL** Not resistant to the clearing solutions.
- 10 or 25 serological pipettes (we used Corning Costar 25mL Stripette, cat. no. 4489) ▲ **CRITICAL** Not resistant to the clearing solutions.
- 300 ml glass chamber with lid (Omnilab, cat. no. 5163279)
- Glass jars for histological staining with lids (any; we used the ones from vwr: staining jar, Hellendahl, with enlargement, cat. no. 631-0698)
- Glass Petri dishes (any; we used VWR, cat. no. 391-2025)
- 1 L glass beakers (any; we used DURAN, cat. no. 211075409)
- 1 L glass bottles (any; we used DURAN, cat. no. DU218015455)
- 2 L glass bottles (any; we used DURAN, cat. no. 218016357)
- 500 ml glass bottles (any; we used DURAN, cat. no. DU218014459)
- (Optional) One Büchner flask or vacuum glass flask with a rubber stopper (any; we used VWR, 511-0047)
- Polytetrafluoroethylene (PFTE) also known as Teflon covered magnetic stirring bars (any; we used IKAFLON, cat. no. IKAA4488700)
- Hot magnetic stirrer (any; we used IKA, model RCT basic B-5000, cat no. 0003810000)
- Aluminum foil (any; we used Korff AG, cat.no. 60050)
- Parafilm (Bemis, cat. no. PM-992)
- Transparent sticky tape (any)
- Electrical black insulation sticky tape (any, we used SoundOriginal, available from Amazon.com)
- Liquid Superglue (Pattex, cat. no. PSK1C or Toolcraft, Superglue rapid 200, cat. no. 886515)
- Maxi-Cure Super Glue, CA (Bob Smith Industries, cat. no. BSI-113)
- Insta-Set, CA Accelerator (Bob Smith Industries, cat. no. BSI-152)
- Kleenex or adsorbent kitchen paper (any)
- White precision wipes (Kimtech Science, cat no. 05511)
- Permanent ink labeling pens (any; we used Edding, cat. no. 140003)
- Any sample and tube holders with the shape as in Fig. 3a
- 0.22 µm syringe filters (Sartorius, cat. no. 16532)
- Perfusion needle (Leica, cat. no. 39471024)
- Peristaltic pump (ISMATEC, REGLO Digital MS-4/8 ISM 834)
- Reference tubing for the ISMATEC peristaltic pump (ISMATEC, cat. no. SC0266)
- Hose tubing connectors for 3–5 mm diameter (Omnilab, cat. no. 5434482 or 8700-0406)
- PVC tubing (Omnilab, cat. no. 5437920)
- Infrared lamp (Beuer, cat. no. IL21)
- pH meter (any; we used WTW, model pH7110)
- Vibratome (any; we used Leica, model VT1200S)
- Incubator (Memmert, model UN160), or any incubator that can hold a shaker inside at 37 °C
- Cordless multi-tool with a thin rotary blade, 0.2 mm (Dremel, model 8200)
- Shaking rocker (IKA, model 2D digital)
- Shaker (IKA, model KS 260 basic)
- Fume hood

Zeiss AxioZoom EMS3/SyCoP3 fluorescence stereomicroscope with

- 1× air objective (Plan Z ×1, 0.25 NA, WD 56 mm)

LaVision-Miltenyi BioTec Ultramicroscope II light-sheet microscope with

- Filter sets: Ex 470/40 nm, Em 535/50 nm; Ex 545/25 nm, Em 605/70 nm; Ex 560/30 nm, Em 609/54 nm; Ex 580/25 nm, Em 625/30 nm; Ex 640/40 nm, Em 690/50 nm
- Andor sCMOS camera Neo 5.5 (Andor, mod. no. DC-152Q-C00-FI)
- SuperK EXTREME/FIANIUM supercontinuum white light laser (NKT Photonics, model SuperK EXTREME EXW-12)
- Olympus MVX10 zoom body (zoom range 0.63–6.3×)
- Olympus revolving zoom body unit (U-TVCAC)
- 1× air objective (Olympus MV PLAPO ×1/0.25 NA, WD 65 mm)
- 2× immersion objective (Olympus MVPLAPO2XC/0.5 NA, WD 6 mm)

- 4× immersion objective (Olympus XLFLUOR340 ×4 corrected/0.28 NA, WD 10 mm),
- 20× immersion objective (Zeiss ×20 Clr Plan-Neofluar/1.0 NA, WD 5.6 mm)
- 12× objective (LaVision-Miltenyi BioTec MI PLAN ×12/0.53 NA, WD 10 mm with dipping cap for organic solvents)

LaVision-Miltenyi Biotec Ultramicroscope Blaze light-sheet microscope with

- Filter sets: Ex 488 nm, Em 525/50 nm; Ex 561 nm, Em 595/40 nm; Ex 640 nm, Em 680/30 nm; Ex 785 nm, Em 845/55 nm
- sCMOS camera 4.2 Megapixel
- LaVision laser beam combiner with laser lines 488,561,639
- Single-arm sample holder (Extended Data Fig. 6k-r)
- Customized large imaging chamber (25 ×7 × 9 cm length–width–height)
- 1.1× objective (LaVision-Miltenyi BioTec MI PLAN ×1.1/0.1 NA, WD 17 mm)
- 12× objective (LaVision-Miltenyi BioTec MI PLAN ×12/0.53 NA, WD 10 mm with dipping cap for organic solvents)

Zeiss Lightsheet Z.1 light-sheet microscope

- Detection objective: 5× air objective (Zeiss EC Plan-Neofluar ×5/0,16 NA, WD 10.5 mm) compatible with water-based and clearing solutions $n = 1.45$
- Illumination: Zeiss LSFM ×5/0.1 NA objectives (for dual side illumination), illumination in Pivot mode for stripe reduction
- Cameras: two pco.edge 4.2 sCMOS cameras
- Filter set: (1) SBS LP 490, EF BP 420-470, EF BP 505-545, (2) SBS LP, 560 EF BP 505-545, EF LP 660, (3) SBS LP 510, EF BP 420-470, EF BP 575-615, (4) SBS LP 560, EF BP 505-545, EF BP 575-615, (5) SBS LP 560, EF BP 505-545, EF LP 585, (6) SBS LP 640, EF BP 575-615, EF LP 660
- Chamber: 5× clearing chamber for sample size of 1 × 1 × 2 cm
- Excitation lasers: 405 nm, 445 nm, 488 nm, 515 nm, 561 nm, 638 nm

Modified mesoSPIM light-sheet microscope with

- Omicron SOLE-6 laser combiner with 405 nm, 488 nm, 515 nm, 561 nm, 594 nm, and 647 nm laser lines and two output fibers
- AHF QuadLine Rejectionband ZET405/488/561/640 emission filter with 50 mm diameter
- Sample *XYZ* and rotation stages composed of two Steinmayer Mechatronik PMT-160-DC stages with 100 and 200 mm travel range for *XY* movements and a combination of Physik Instrumente M-406.4PD and M-061.PD stages for *Z* movements and rotation, respectively
- Physik Instrumente M-605 stage for focusing the detection path
- Edmund Optics F-Mount PlatinumTL Telecentric lens with 0.9× magnification and lens clamp
- Teledyne Photometrics Iris 15 camera with 15-megapixel resolution
- Optomechanical architecture and electronic controlling system of mesoSPIM (https://github.com/mesoSPIM/mesoSPIM-hardware-documentation)
- Custom 40 mm × 40 mm × 120 mm cuvette for mounting samples (Portmann Instruments)
- Magnetic holder for 40 × 40 cuvettes (https://github.com/mesoSPIM/mesoSPIM-hardware-documentation/blob/master/mesoSPIM_V5/drawings/Large-cuvette-mount-40mm-V3.pdf)
- mesoSPIM software (https://github.com/mesoSPIM/mesoSPIM-control)

Zeiss LSM 880 inverted laser-scanning confocal microscope coupled with

- 25× water-immersion objective (Leica Fluotar Visir, ×25/0.95 NA, WD 2.5 mm) mounted with a custom mounting thread

Data processing and analysis tools/software

- Vision4D (v.3.0.1 ×64, Arivis)
- Arivis converter (v.2.12.6, Arivis)
- Amira (v.6.3.0, FEI Visualization Sciences Group)
- Imaris (v.9.1, Bitplane)
- Fiji[60] (ImageJ2, v.1.51, https://fiji.sc/)
- (Optional) TeraStitcher[62] (v.1.10, https://abria.github.io/TeraStitcher/)
- (Optional) Total Commander (v. 8.52a ×64, https://www.ghisler.com/)
- Photoshop CS6 (v. 13.0, Adobe)

Box 2 | Clearing reagents toxicity and safety issues

Of the solvents used for vDISCO, only a few represent a health issue for the operator, and only if they are not handled properly. In particular, according to PubChem, THF represents a hazard owing to its explosivity and high flammability, and irritation caused to the eyes and skin. It is classified as a moderate toxic agent in acute exposure and suspect carcinogen in chronic exposure at least in rodents, while data in humans are limited. In the same database, DCM is reported as a health hazard in certain conditions: it is inflammable, causes severe irritation to the eyes and to the respiratory tract, and is responsible for moderate skin irritation up to chemical burns under prolonged exposure. DCM has mutagenic and carcinogenic effects in animals, while no confirmation of such effects was obtained in humans. The inhalation of THF or DCM can cause headaches, dizziness, nausea and anesthesia. Handling and storing DCM and THF must follow dispositions for hazardous, inflammable, explosive and toxic substances; in particular, handling must be performed in fume hoods, while wearing safety goggles, nitrile gloves (preferably double layer) and a lab coat.

According to the safety data sheet, benzyl alcohol has fulfilled the 'Safer Choice Criteria' as a relatively safe compound. It can irritate skin, eyes and respiratory tract. It is not listed among the carcinogenic agents.

Finally, benzyl benzoate is considered an irritant and a harmful substance if swallowed. According to the Hazardous Substances Data Bank, it is an irritant to the eyes and skin. There is no evidence of its carcinogenic effects in either animals or humans. It is considered an environmental hazard that can affect aquatic life. Both benzyl alcohol and benzyl benzoate are combustible but not inflammable and explosive. The prolonged inhalation of benzyl alcohol or benzyl benzoate can cause coughing and dizziness. According to the US Food and Drug Administration, these compounds can be used in minimum quantity as food additives or as cosmetic ingredients for human use and consumption. Handling both benzyl alcohol and benzyl benzoate should be performed in a well-ventilated environment, possibly in a fume hood or under an aspiration system, and wearing safety goggles, double nitrile gloves and a lab coat. Operators must follow all the safety and disposal dispositions for all the chemicals used in vDISCO. More information and data are available at https://pubchem.ncbi.nlm.nih.gov/.

- ClearMap[53],
- DeepMACT[1]
- NeuroGPS-Tree[32]

Reagent setup

! CAUTION All the reagents prepared for vDISCO must be discarded according to institutional regulations. All personnel must have adequate safety training and equipment (lab coat, safety goggles, fume hood, etc.) for working with hazardous (flammable, toxic, volatile, irritant, environmentally harmful) materials. Considerations about clearing reagents toxicity can be found in Box 2.

1× (0.01 M) PBS

Dilute 10× PBS with ddH_2O to obtain 1× PBS. 1× PBS solution can be stored at room temperature (18–25 °C) for several months.

Heparinized PBS

Dilute the stock solution of heparin (5,000 U/ml) into 1 L of 1× PBS to reach final concentration of heparin 25 U/ml. This solution is used during the perfusion for the sample preparation step to help flush the blood out of the body. This solution can be kept for several weeks at 4 °C.

4% (wt/vol) PFA

This solution is used as fixative solution for the perfusion and the post-fixation of the animal during the sample preparation step. We purchase 4% pH 7.4 PFA ready-to-use solution directly from the supplier (see 'Materials' section). Otherwise, any 4% PFA in 1× PBS for perfusion is usable. **! CAUTION** Toxic reagent. Avoid inhalation or contact with skin and eyes. Handle it in a fume hood.

PBS + sodium azide

Dissolve the sodium azide in powder into 1× PBS reaching a final concentration of 0.05% (wt/vol). This solution is used as storing solution for unprocessed samples obtained from the sample preparation step. It can be stored at RT for several months. **! CAUTION** This solution is toxic. Avoid contact with skin and eyes.

Decolorization solution

Stock solution preparation: in a 1.5–2 L beaker mix 25 wt% urea, 25 wt% Quadrol and 15 wt% Triton X-100 in ddH_2O. To facilitate the dissolution, stir with a magnetic stirring bar while heating up the stirrer up to 60 °C. While stirring, cover the beaker with aluminum foil to prevent water evaporation. When the solution turns completely transparent and with no aggregates inside, pour it in a glass bottle and let it cool down at RT. The stock solution can be stored for 2–3 months at RT. 1–2 L of the stock is sufficient for one or two animals. **▲ CRITICAL** Avoid boiling the stock solution when stirring.

Owing to the high amount of detergent, be careful not to generate too many bubbles or foam when mixing.

Final decolorization solution preparation: dilute the stock solution 20–30% (vol/vol) with 1× PBS (for whole-body active vDISCO, use 25%). Mix well until the final solution turns homogeneous and transparent. 1 L should be enough to process one animal with whole-body vDISCO. It is optional to use this solution in passive-vDISCO.

Decalcification solution

Dissolve 10% (wt/vol) EDTA in 1× PBS by stirring with a magnetic stirring bar and by adding NaOH in powder until no aggregates are visible and the pH reaches ~8. The NaOH is necessary to help the EDTA dissolve. Heating the solution is not recommended, because the reaction already generates heat and the pH should be measured when the solution has cooled down to RT. 1 L of solution is enough for whole-body vDISCO of three or four animals. The decalcification solution can be stored at 4 °C for several months. This solution can be skipped if applying passive-vDISCO on not calcified tissues.

Permeabilization/staining solution

The permeabilization/staining solution is used in both the permeabilization step and staining step (it contains the dyes in the staining step). Prepare it by mixing 1.5% (vol/vol) goat serum, 0.5% (vol/vol) Triton X-100, 0.5 mM of methyl-β-cyclodextrin, 0.2% (wt/vol) *trans*-1-acetyl-4-hydroxy-l-proline and 0.05% (wt/vol) sodium azide in 1× PBS. 600–700 ml is enough to process one animal with whole-body vDISCO. ▲ **CRITICAL** Prepare fresh solution before starting the experiment, it can be stored for a few days at 4 °C.

Mild staining/washing solution

The mild staining/washing solution is used as washing solution in standard vDISCO, while it is used as both staining solution and washing solution in mild-vDISCO. Prepare it by mixing 1.5% (vol/vol) goat serum, 0.5% (vol/vol) Triton X-100 and 0.05% (wt/vol) sodium azide in 1× PBS. 600–700 ml is enough to process one animal with whole-body vDISCO. ▲ **CRITICAL** Prepare fresh solution before starting the experiment; it can be stored for a few days at 4 °C.

Dehydration solutions

Transfer 500 ml (this amount might be decreased to 100 ml for small samples) of 100% THF from the stock bottle into a glass bottle to limit repetitive opening of stock bottles. This solution will be used as the last dehydration treatment during the clearing procedure. Then, prepare 50%, 70% and 80% (vol/vol) THF dilutions by mixing and gently shaking pure 100% THF with ddH2O. 250 ml of each dilution is sufficient to treat one whole body. All solutions can be stored in glass bottles with a solvent-resistant lid at RT in the dark for several weeks. ! **CAUTION** For information on THF toxicity, see Box 2. THF tends to form peroxides over time, being an explosive hazard if stored for months or years. Purchase THF in max 2 L bottles and avoid stocking up unused THF in the lab for long periods. THF containing a stabilizer such as 250 ppm BHT (see 'Reagents' section) has reduced formation of peroxides. Both open and unopened/new bottles of THF should be kept at RT in a safety cabinet for flammable and explosive substances. Follow the guidelines for peroxide-forming compounds carefully: (https://www.sigmaaldrich.com/chemistry/solvents/learning-center/peroxide-formation.html).

Delipidation solution

The delipidation solution consists of 100% DCM. Since whole-body vDISCO needs at least 250 ml of pure DCM per animal, at the delipidation step the DCM can be poured into the clearing chamber directly from the stock bottle. However, if working with small dissected tissue pieces, then transfer 200 ml of 100% DCM from the stock bottle into a glass bottle with a solvent-resistant lid to avoid repetitive opening of stock bottles. Use the transferred solution within 1 month. ! **CAUTION** DCM is toxic and highly volatile. For further information about toxicity and handling of DCM, see Box 2. Store all DCM solutions in the dark and in well-sealed bottles at RT in a safety cabinet for solvents.

Refractive Index matching solution: BABB

Mix one volume of 100% benzyl alcohol with two volumes of 100% benzyl benzoate. 300–350 ml of BABB is sufficient for one animal. BABB can be stored for some months at RT in the dark in glass bottles sealed with lids resistant to solvents. ! **CAUTION** For information on the toxicity of BABB components, see Box 2.

Equipment setup

Transcardial-circulatory perfusion system

In whole-body active vDISCO, the setting up of the transcardial-circulatory perfusion system is required for decolorization, decalcification and staining, and it is established by using the Ismatec peristaltic pump as shown in Fig. 3. This pump can hold four pumping channels with one setup/tube per channel (Fig. 3b, left); therefore, four animals can be processed at the same time. For the sake of simplicity, here we describe the procedure to set up one channel with a single reference tube (Fig. 3b, right and Fig. 3c, blue arrow). Insert the hose tubing connectors at both ends of the reference tube (Fig. 3c, red dashed rectangles). Through the tubing connectors, connect the reference tube with two additional PVC tubes at each side of the reference tube (Fig. 3c, magenta arrows), to extend the total length of the reference tube. Use parafilm to seal the connecting parts (Fig. 3c, red boxed insert). Next, cut the tip of the 1 ml Braun syringe and use this tip to connect one end of the tube, which will represent the outflow end during the experiment, with the perfusion needle (Fig. 3c, yellow insert and Fig. 3d). When starting the protocol, the needle will inject the vDISCO solutions into the circulatory system of the animal through the left ventricle of the heart. ▲ **CRITICAL** All the connections must be stable. Check and test the integrity of all the components and the absence of leaking points by pumping some water.

Procedure

Sample preparation with PBS and PFA perfusion ● Timing 14 h to 1 d

1 Deeply anesthetize the animal by intraperitoneally injecting the MMF triple combination 1 ml per 100 g body mass for mouse. Wait some minutes to let the anesthesia set in. Check the pedal reflex of the animal to evaluate the success of the anesthesia.

(a) If using the Leica Perfusion One system to perfuse the animal:

(i) Fill one of its pumping tanks with RT heparinized PBS (alternatively ice cold) and a second pumping tank with RT 4% (wt/vol) PFA (alternatively ice cold).

(ii) Start pumping for 1–2 min with the heparinized PBS to fill up the pumping tube and to push out all the air bubbles.

▲ **CRITICAL STEP** Avoid formation of air bubbles in the tubing because they can impair the subsequent circulation of the solutions (for fixation and later for staining) in the vasculature of the animal.

(b) Other possible perfusion methods:

(i) Use an electric peristaltic pump.

(ii) Manually push the solutions in the heart with syringes or using gravity perfusion systems.

It is up to the operator to choose the perfusion strategy that the operator is most familiar with.

2 At RT, intracardially perfuse the anesthetized animal at pressure ~110 mmHg with the heparinized PBS for 5–10 min until the blood is flushed out.

3 Switch the perfusion with the 4% PFA solution for 10–20 min until the animal gets fixed.

▲ **CRITICAL STEP** The perfusion step must run flawlessly; otherwise, the whole-body vDISCO immunolabeling might be impaired. To assess the success of the perfusion in this step, visually check if the liver starts turning yellow (Extended Data Fig. 1a, cyan dashed line) and the perfusate drains clear from the right atrium. Moreover, the animal should become rigid and stiff starting from the second or third minute of perfusion with 4% PFA (usually after 25 ml of PFA).

? TROUBLESHOOTING

Passive-vDISCO staining ● Timing 2–23 d (excluding the optional decolorization and decalcification treatments: for timing details, see Table 2).

4 After perfusing with 4% PFA, dissect out the tissue or organ of interest from the animal.

▲ **CRITICAL STEP** Since the gut content cannot be cleared, the gut should be emptied at this stage either by flushing the content through small incisions made in the tissue with a syringe filled with 1× PBS or by gently and manually squeezing it out through the incisions (Extended Data Fig. 1b and Supplementary Videos 1 and 2).

5 Post-fix the dissected organs/tissues in appropriately sized tube in 4% PFA overnight at 4 °C.

▲ **CRITICAL STEP** The sample must be completely immersed in at least five sample volumes of 4% PFA solution. Avoid overfixation because it can increase the tissue autofluorescence. Label the tubes

with solvent-resistant ink (permanent pen, graphite pencil) and further cover the label with transparent tape, because all the solutions that will be used from now on can dissolve the labels.

6 Set up a rocker or a shaker that can hold the sample containers for gentle shaking. Set an incubator that must be able to hold the rocker or the shaker for the incubations at 37 °C.

7 After post-fixation, wash the samples with 1× PBS three times for 20 min for smaller samples, up to 2 h for the larger samples (Table 2), at RT and with gentle shaking.

■ PAUSE POINT Washed samples can be stored at 4 °C in PBS for up to 4 weeks or in PBS + 0.05% sodium azide for up to 1–2 years.

! CAUTION Do not use samples where bacteria or fungal contamination is observed in the storing solution.

8 (Optional) Cut the sample in 500 µm or 1 mm sections using a vibratome and leave them in PBS for immediate use or in PBS + 0.05% sodium azide at 4 °C for longer storage (up to 2–3 months).

9 (Optional) Straighten dissected spinal cords or whole central nervous systems (brain and spinal cord) with the strategy described in Extended Data Fig. 4 by using plastic Pasteur pipettes cut in half and fine needles.

10 (Optional) Decolorization. For samples that cannot be efficiently flushed from blood in the PBS/PFA perfusion step (e.g., spleen or liver), perform the decolorization step by incubating the sample in the decolorization solution at RT with gentle shaking until the heme is eluted out. The sample will turn a lighter color, and the solution will turn yellow (Table 2). For a faster decolorization, the incubation can be performed at 37 °C. Refresh the decolorization solution two to three times (e.g., every 3–8 h) until the sample appears lighter in color and the solution does not turn yellow anymore.

! CAUTION This treatment can reduce the overall tissue clearing performance of the sample; hence, carefully adjust the timing of this step and the concentration of the decolorization solution (Table 2). Preliminary tests with different timings and concentrations can help optimize the decolorization step.

11 Wash thorough at least five times with 1× PBS at RT to eliminate any traces of decolorization solution.

■ PAUSE POINT One of the washings in PBS can be extended to overnight.

12 (Optional) Decalcification. Decalcify samples (e.g., bones) by incubation in the decalcification solution at RT with gentle shaking until the sample becomes soft and flexible.

▲ CRITICAL STEP The decalcification step can decrease the staining performance.

13 Wash five times with 1× PBS at RT to eliminate any traces of decalcification solution.

■ PAUSE POINT One of the washings in PBS can be extended to overnight.

14 Permeabilization. Treat the sample with the permeabilization solution (adjusted to sample size) at 37 °C with gentle shaking for 3 h to 2 d (for timing details, see Table 2).

15 Staining. Incubate the sample in the staining solution containing the dyes of interest at 37 °C with gentle shaking and protected from light for 3 h to 21 d. The concentration of the dyes, the final volume and the timing used for the incubation must be adjusted to the expression of the target and to the size of sample as shown in Tables 1 and 2.

▲ CRITICAL STEP For nanobodies that have stability issues as indicated in Table 1, mild-vDISCO protocol should be used: at this step, wash the permeabilized samples with the washing solution 30 min three times at RT. Then incubate in the mild-staining solution to which the dyes were added (Table 3). The sample containers must be tightly sealed (e.g., wrapping the lid container with parafilm) to prevent evaporation.

▲ CRITICAL STEP The nanobody must be previously validated (Box 1).

16 Wash the sample with the washing solution 3 times (adjusted to the sample size) at RT, protected from light and with gentle shaking for 10 min to 1 h.

■ PAUSE POINT One of the washing steps can be extended to overnight.

17 Wash the samples with 1× PBS three times for 10 min to 1 h (adjusted to sample size) at RT, protected from light and with gentle shaking.

■ PAUSE POINT Stained samples can be stored in PBS at 4 °C protected from light for up to 1 d.

Whole-body active vDISCO staining ● Timing 12–16 d

Sample preparation

18 After the PBS–PFA perfusion of the animal, remove the skin and the eyes (Extended Data Fig. 1c; see also Table 4).

▲ CRITICAL STEP Since the gut content cannot be cleared, the gut should be emptied at this stage either by flushing the content through small incisions made in the tissue with a syringe filled with 1

PBS or by gently and manually squeezing it out through the incisions (Extended Data Fig. 1b and Supplementary Videos 1 and 2). For clearing the non-nude whole mice with intact skin, remove the hair by shaving it off with a razor blade or by applying a commercial hair removal cream (Extended Data Fig. 1d).

19 Wash the whole body extensively with PBS to clean the body from hair and digested food as much as possible.

▲ **CRITICAL STEP** A large amount of hair and gut content residues can clog the pumping system that will be used later in the staining procedure.

20 Post-fix the specimen in 4% PFA at 4 °C in 50 ml tubes or bigger plastic containers for 1 d.

▲ **CRITICAL STEP** The sample must be completely immersed in the 4% PFA solution. Avoid overfixation because it can increase the tissue autofluorescence.

21 After post-fixation, wash the samples with 1× PBS three times each at RT and with gentle shaking for 1 h.

■ **PAUSE POINT** Washed bodies can be stored at 4 °C in PBS for up to 4 weeks and in PBS + 0.05% sodium azide for up to 1–2 years.

! **CAUTION** Do not use samples where bacteria or fungal contamination is observed.

Sample and perfusion system setup

22 Put the body of the animal in the 300 ml glass chamber (Fig. 3e) and place it close to the peristaltic pump (Fig. 3f).

23 Place the sucking end of the pumping tube inside the glass chamber until the tip touches the bottom of the chamber (Fig. 3e, bottom, black arrow).

24 Fill the chamber with 1× PBS with an amount that can cover the body.

25 Start the pumping for 2–3 min to make sure that the entire tube is filled with PBS with no air bubbles.

26 Using the sample/tube holders from Fig. 3a, fix the whole pumping tube with an angle that has the perfusion needle directed into the glass chamber (Fig. 3f).

27 Insert the perfusion needle (which was placed onto the outflow end of the tube) inside the same entry point hole that was created during the PBS–PFA perfusion step at the level of the left ventricle (Fig. 3g,h).

▲ **CRITICAL STEP** Be extremely gentle pushing the needle inside the hole. Do not force the needle and do not push it too hard or too deep to prevent damaging or breaking the tissue around the hole or the heart. The hole must be just big enough for the blunt tip of the perfusion needle to get in. If the hole becomes too big, the perfusion solution can immediately leak out from the hole, resulting in insufficient circulation in the vasculature.

? TROUBLESHOOTING

28 (Optional) Remove some PBS from the chamber to expose only the heart to the air. While doing this, make sure that the sucking end (inflow end) of the tube is constantly immersed in PBS. Add one to two drops of the liquid Pattex or Toolcraft superglue onto the point where the needle goes into the heart in order to fix the needle in place, to seal the hole and keep the perfusion pressure constant (Fig. 3i, left). Let the glue dry for a few minutes (Fig. 3i, right). Then, cover the animal back with 1× PBS.

▲ **CRITICAL STEP** This step is indicated as optional at this point, because later the perfusion with the decolorization solution might detach the glue from the heart. However, the solidified glue will still hold onto the needle and can act as a cover on the hole to keep the pressure. If the pressure does not seem to be kept well while pumping (e.g., a lot of flow is coming out directly from the hole), then the glue can be added just before the staining step (Step 39).

? TROUBLESHOOTING

Decolorization

29 Set the peristaltic pump with a pumping rate of 45–60 rpm, which is 160–230 mmHg.

30 Start the pumping and perfuse the animal with the 1× PBS contained in the chamber for 2–3 h two times (one washing with PBS can be left overnight) at RT. The perfusion will work as follows: the needle (outflow) injects the PBS into the body, while the other ending of the perfusion tube (inflow) collects the solution exiting from the mouse body, pumping it back into the animal in a closed recirculation loop.

! CAUTION Always protect skin and eyes from bursts when handling the pumping system. You may adjust the pressure on the basis of the feedback from the body of the animal (smaller animals require less pressure). When the pressure is too high, it can damage the vasculature by creating leaking points or burst the heart and lungs, or the solution might spurt out from the openings of the animal. In these circumstances, stop the pumping immediately. Before turning on the pump again, you can reduce the pumping pressure or make a bigger cut on the right ventricle (Fig. 3j).

31 From this point, refresh 'the pumping reference tube slot' every day. To do this, note that the reference tube has two slots for pumping. The pumping can work on either one of the two slots (Fig. 3k, top).

▲ CRITICAL STEP After many hours of pumping at high pressure, the running slot can get deformed by the movement of the gearwheel of the pump, thus reducing the pumping. Therefore, alternate the slots every 8–16 h (Fig. 3k, middle and bottom and Supplementary Video 3).

32 After washing with PBS, the perfusion should continue with the next solution. In general, the exchange of the perfusion solution is performed without touching the perfusion setup or the animal: first, stop the pumping, then completely suck out the PBS with a 50 ml serological pipette (Fig. 3l).

▲ CRITICAL STEP This operation must be done by avoiding the formation of bubbles inside the perfusion tube. To this end, do not accidentally touch the sucking tube, and make sure that it is well pushed into the chamber with the sucking end touching the bottom of the chamber. In this way after removing the PBS, some remaining PBS with its surface tension will prevent the formation of air bubbles (Fig. 3e, bottom).

33 Pour the decolorization solution inside the glass chamber, covering the animal. Start the pumping with the same pressure optimized in the previous step and perfuse for 2 d at RT. In between, exchange the decolorization solution whenever it turns into a strong yellow color (every ~12 h, Fig. 4a), indicating that the heme is being successfully eluted out from the body. On the last exchange, the solution will stay colorless or turn pale yellow; in both cases, the sample is ready for the next step.

▲ CRITICAL STEP The perfusion of the decolorization solution is a good indicator of the performance of the whole-body perfusion system: after 2 d of decolorization, the spleen should become pale beige color (Fig. 4b) and the body whiter.

? TROUBLESHOOTING

Decalcification

34 Following the decolorization, exchange the solution with 1× PBS and perfuse three times at RT for 2–3 h to wash the decolorization solution out from the body.

■ PAUSE POINT Animal bodies can be perfused with 1× PBS for up to 2 d.

35 After washing, exchange the PBS with the decalcification solution in the same way as described before and perfuse with the decalcification solution for 2 d at RT. The refreshing of the decalcification solution is not required.

▲ CRITICAL STEP To assess the success of the decalcification process, check if the body of the animal and its skeleton bend easily: test by bending one of the limbs with a pair of tweezers.

? TROUBLESHOOTING

36 After decalcification, wash again by perfusing with 1× PBS three times for 2–3 h at RT.

■ PAUSE POINT Bodies can be perfused with 1× PBS for a maximum of 2 d.

Permeabilization and staining

37 Replace the PBS with the permeabilization solution and perfuse with the permeabilization solution at RT for half a day.

38 After permeabilization, turn off the pump, take a 0.22 μm filter and wet it with some permeabilization solution using a syringe to reduce the formation of bubbles later in the pumping tube, Fig. 4c. Then take the sucking (inflow) end of the perfusion tube and connect it to the filter (Fig. 4d). Finally place the tube filter inside the chamber (Fig. 4e).

▲ CRITICAL STEP The filter prevents the accumulation of dye aggregates into the sample by filtering the staining solution. Periodically check if the filter still functions. If clogging is observed after extended perfusion, replace the filter.

? TROUBLESHOOTING

39 With the pump still turned off, replace the old permeabilization solution with fresh permeabilization solution (Fig. 3l). From now on, this fresh permeabilization solution will be called staining solution since it will contain the dyes.
▲ **CRITICAL STEP** At this point, if the liquid superglue was already applied as indicated in the optional point of the sample and perfusion system setup section, Step 28, and the glues still holds well, proceed with covering the whole animal with 250 ml of staining solution. If the glue was not applied yet, initially pour an amount of staining solution that does not cover the heart and apply the super glue by following the procedure described in Step 28: briefly add one to two drops of superglue onto the point where the needle goes into the heart, let the glue dry and add staining solution to completely immerse the animal. Last, make an incision in the right ventricle (Fig. 3i,j).

40 Add the dyes into the staining solution (Fig. 4f) with a pipette. For nanobody concentrations, see Table 1. Optionally, perform counterstain of nuclei by adding a nucleus dye: for example, add 290 µl of PI from the stock bottle into the staining solution.
▲ **CRITICAL STEP** The nanobody must be previously validated in sections.

41 Cover the chamber with aluminum foil to minimize light exposure (Fig. 4g).

42 Turn on the pump and perfuse the animal for at least 6 d with the staining solution. During this step place the infrared lamp at a distance of 20–30 cm from the chamber and direct the infrared light to it (Fig. 4g). The infrared light will heat up the solution to ~28–30 °C, to increase the molecular movement of the dyes for a better staining. Alternatively, place the pump and the whole setting in a temperature controlled warm room (~28–30 °C) or onto a hot plate. The temperature of the hot plate should be adjusted in order to warm up the solution in the chamber to ~28–30 °C. If the PI is added, different organs of the body such as intestine, lymph nodes and thymus will turn pink (Fig. 4h).
! **CAUTION** The infrared lamp can overheat after continuous usage for many hours. Switch the lamp off after 10–12 h to let it cool down.
▲ **CRITICAL STEP** During daily checks, if the level of the solution in the chamber decreases due to evaporation, fill it back with distilled water only.
? TROUBLESHOOTING

43 After 6 d, remove the perfusion tube with the needle from the heart, by delicately detaching the glue. Place the body in a 50 ml tube or in a bigger plastic container with a lid. Fill the tube or the container with fresh staining solution and add 5 µl of nanobody (2.5–5 µg in the 50 ml tube) (Fig. 4i).

44 Passively incubate the tube at 37 °C or at RT for 1–2 d with gentle shaking and protected from light for additional staining and propagation of the dyes into the tissue. The choice of the temperature for this step is based on the stability of the nanobody (Table 1); for example, we recommend RT incubation for nanobodies that would normally require passive mild-vDISCO for the staining of dissected organs.

45 Meanwhile, discard the filter and the solution left in the glass chamber. Wash the now empty container and the pump tubing by pumping two to three times for 30 min with distilled water and then with PBS using the same pumping setup.

46 After 1–2 d, place the animal back into the glass chamber of the (now) clean perfusion system and wash the body by perfusing it with the washing solution two times at RT for 2–3 h. From this step, the filter is not needed anymore.

47 In the end, wash the body by perfusing it with 1× PBS two times at RT for 3 h.
■ **PAUSE POINT** Stained samples can be stored in PBS for up to 1 d at 4 °C protected from light.

? TROUBLESHOOTING

Clearing ● Timing 1–4 d

48 After staining, place the samples immersed in 1× PBS into containers resistant to organic solvents (tubes for small samples and glass chambers for whole bodies as shown in Fig. 4k) that will be used for clearing.

49 Remove the PBS and dehydrate and delipidate the samples by incubating with a series of THF dilutions (50%, 70%, 80% and two times 100%) and 100% DCM with gentle shaking, at RT, with the container lids sealed with parafilm and protected from light (Fig. 4k). Tables 2 and 4 include the incubation times and the dilutions of the organic solvents based on the samples size. For samples in small tubes (e.g., 5 ml tubes), the exchange of the solutions can be performed with a plastic Pasteur

pipette. For samples in bigger containers (e.g., 50 ml tubes or glass chambers), the exchange is done by directly pouring the previous solution into a big beaker for waste, and adding the next solution into the container. The amount of the clearing solution at each step must almost fill the plastic tube (e.g., 4–4.5 ml into 5 ml tubes) or cover the whole body in the glass chamber (~200–250 ml).

▲ **CRITICAL STEP** Use a set of Pasteur pipettes dedicated to each kind of solvent and its dilutions (e.g., one pipette for THF dilutions, one for THF waste, one for DCM, etc.) to prevent contamination.

50 Exchange the DCM with the RI matching solution BABB. The sample must be completely immersed. Incubate for 20 min to 12 h with gentle shaking, at RT and protected from light, until the sample becomes visually transparent (Fig. 4l).

■ **PAUSE POINT** Store the cleared samples in BABB at RT and protected from light. Unimaged whole bodies can be kept for some weeks in the glass chambers used for clearing. However, for long-term storage, the bodies should be moved into plastic containers filled with BABB (e.g., 50 ml tubes). Small samples can be stored in BABB in the same tubes used for clearing.

▲ **CRITICAL STEP** Label the tubes with permanent pens and cover the text with transparent sticky tape to protect the label from solvents.

? TROUBLESHOOTING

51 *Imaging*. Imaging options should be chosen on the basis of the desired application:

2D epifluorescence microscope (AxioZoom) imaging ● Timing 5–15 min

(i) Use an adequate imaging container that allows the sample to be completely immersed in BABB. For example, small samples can be placed in smaller solvent resistant transparent containers with a flat bottom (e.g., glass Petri dishes) (Extended Data Fig. 5a–c), while the whole cleared body can be placed in the same glass chamber used for clearing (Extended Data Fig. 5d).

! CAUTION Perform all the next imaging steps wearing nitrile gloves and safety goggles.

(ii) Put the container with the sample and without the lid under the epifluorescence microscope coupled with the 1× objective (Extended Data Fig. 5b–d).

(iii) Place the sample in the chamber as straight as possible and avoid accidental movements of the sample.

? TROUBLESHOOTING

(iv) Focus on a part of the sample where it is expected to detect fluorescence signal.

? TROUBLESHOOTING

(v) Adjust the zoom on the basis of the details that need to be visualized. For example, select a zoom factor ×7 for the 2D whole-body reconstruction. Normally, small cells such as microglia can be imaged with a zoom about ×63 or higher.

(vi) Start scanning by taking individual 2D images over the sample. Proceed by covering the entire sample.

▲ **CRITICAL STEP** Move the chamber in *XY* directions very slowly to prevent any accidental sample movement.

▲ **CRITICAL STEP** Consecutive 2D images must have overlapping regions at the edges of the images to facilitate the stitching.

(vii) Save each scan as a multichannel scan if doing multicolor imaging.

Light-sheet LaVision-Miltenyi Biotec Ultramicroscope II imaging ● Timing 2–12 h

(i) Mount a zoom body unit onto the microscope by following the manufacturer's instructions.

! CAUTION Perform all the next imaging steps wearing nitrile gloves and safety goggles.

(ii) Pour BABB into the imaging chamber, filling half of the chamber.

(iii) Mount the sample onto the sample holder: small samples such as brains can be simply mounted using the screwing system provided by the microscope manufacturer (Extended Data Fig. 6a) or plunged onto Micro-Fine Ultra needles attached to the sample holder[16] (Extended Data Fig. 6b–e). Bigger samples such as the chest or the abdomen can be mounted on the sample holder using the suggested superglue (which does not affect the imaging) (Extended Data Fig. 6f–j). For using superglue: attach a piece of black sticky tape onto the surface of the sample holder (Extended Data Fig. 6g), apply one drop of Maxi-Cure super glue onto the tape (Extended Data Fig. 6h), inject 30–40 µl of the Insta-Set Accelerator over the super glue using a 1 ml syringe + needle (Extended Data Fig. 6i), lightly wipe the sample two to three times on a paper tissue (e.g., Kleenex) to remove some BABB, place the sample onto the glue and hold it for 1 min until it is

stabilized (Extended Data Fig. 6j). In this way, the removal of the glue after the scan can be easily done by detaching the tape, without leaving any glue residue on the sample holder.

▲ **CRITICAL STEP** Mounting of the samples should be carried out as fast as possible because air can go into the tissue that it is not soaked in BABB, creating air bubbles. Be gentle while grabbing the samples with tweezers and do not squeeze them to avoid the accumulation of air bubbles inside. For the removal of bubbles, see Extended Data Fig. 6p–r.

? TROUBLESHOOTING

(iv) Place the sample holder with the sample inside the imaging chamber and align it to the chamber.

(v) Pour additional BABB into the imaging chamber to cover the sample.

! CAUTION Do not fill the chamber completely to avoid overflowing of BABB, which can damage the mechanical components of the microscope.

(vi) Select the correct filter set for the fluorophore in the software.

(vii) Turn on the excitation light and move the sample in the *Z* direction until the upper surface of the sample is illuminated by the light sheet.

(viii) Mount the objective of interest. We use the 4× immersion objective for the scan of organs that can fit in a tiling scan of maximum 3 × 4 (e.g., samples smaller or equal to a whole brain), the 2× immersion objective for other body parts (e.g., limbs, chest), the 12× and the 20× immersion objectives to detect very small structures such as single cancer cells, dendritic spines or microglia ramifications.

(ix) By using the lowest zoom provided by the zoom body, slowly lower the objective towards the sample until the structures of the sample appear on the computer screen.

! CAUTION If using immersion objectives, make sure that while lowering the objective into BABB the solution does not overflow; otherwise, use a Pasteur pipette to suck out some BABB from the imaging chamber. Water immersion objectives such as Zeiss 20× can be compatible with BABB, but in general, the compatibility of objectives must be checked in advance with the manufacturer or with preliminary tests.

(x) Move the objective slightly up and down to adjust the focus.

? TROUBLESHOOTING

(xi) Adjust the microscope settings on the basis of the sample. For example, for a Thy1-GFPM brain we used a *Z*-step of 4 µm, double-sided light sheet, NA 0.025, light-sheet width 60%, exposure time 100.00 ms, tile scan 3 × 3 with 13% of overlap and 5,000 µm of *Z*-range.

▲ **CRITICAL STEP** The laser power and the exposure time should be optimized to never reach the saturation of the camera.

? TROUBLESHOOTING

(xii) Adjust the alignment of the two sides of the light sheet. For small or thin samples such as a spinal cord, one-sided light sheet is sufficient to cover the entire sample.

(xiii) Adjust the laser power and the chromatic correction focus of the autofocus box for the other channels, when performing multichannel imaging.

(xiv) Select two-sided light sheet or one-sided light sheet on the basis of the size of the sample. For small or thin samples such as a spinal cord, one-sided light sheet is sufficient to cover the entire sample.

(xv) Take a screenshot of the Imspector software with the 'info' icon switched on to record the settings after checking all the parameters. Then, start the scan without touching the light-sheet microscope or running other software in the hosting computer to avoid potential interruptions. Wait until the scanning and imaging recording is completed.

Light-sheet imaging with the LaVision-Miltenyi Biotec Blaze microscope ● Timing 6–7 d

(i) Pour BABB into the imaging chamber, by filling half of the chamber.

! CAUTION Perform all the next imaging steps wearing nitrile gloves and safety goggles.

(ii) Mount the sample onto the sample holder with the Maxi-Cure superglue + accelerator as shown in Extended Data Fig. 6k–o. In case of a whole body, you can start mounting the body either in prone position (facing down) or in supine position (facing up). First, attach two pieces of black sticky tape onto the surface of the sample holder (Extended Data Fig. 6k, l). Suck 50–70 µl of the Insta-Set Accelerator solution with a 1 ml syringe and keep it for later. Apply three to five drops of Maxi-Cure super glue onto both pieces of the tape (Extended Data Fig. 6m). After that, inject ~20–30 µl of the Insta-Set Accelerator into each drop of the glue (Extended Data Fig. 6n) in a fast manner. Place the body onto the sample holder and hold it for few minutes until the glue cures

(Extended Data Fig. 6o). The removal of the glue after the scan will be easily done by detaching the tape.

▲ **CRITICAL STEP** Avoid leaving the sample outside of BABB for too long, and perform the sample mounting fast. Otherwise, air can go into the sample and create air bubbles within the tissue. Be gentle while grabbing the samples with tweezers and do not squeeze them to avoid the accumulation of air bubbles inside the sample. For the removal of air bubbles, see Extended Data Fig. 6p–r.

? TROUBLESHOOTING

(iii) Follow steps (iv)–(vii) of the 'Light-sheet LaVision-Miltenyi Biotec Ultramicroscope II imaging' section.

(iv) Select the objective of interest. We use the 1.1× objective to image whole bodies, and the 12× objective to capture details.

(v) Lower the objective towards the sample until the structures of the sample appear on the computer screen.

! CAUTION Make sure that while lowering the objective into BABB the solution does not overflow; otherwise, use a Pasteur pipette to suck out some BABB from the imaging chamber.

(vi) Move the objective slightly up and down to adjust the focus.

? TROUBLESHOOTING

(vii) Adjust the microscope settings. For example, to cover a whole adult mouse, set 3 × 8 tiles of scans with 35% of overlap, two-sided light sheet, laser power 10–15%, *Z*-step 6 µm, light-sheet NA 0.035, light-sheet width 80–100%, exposure time 80.0–120.0 ms and 11 mm of *Z*-range. Settings can be adjusted on the basis of the characteristics of the sample.

▲ **CRITICAL STEP** The laser power and the exposure time should be optimized to never reach the saturation of the camera, while the number of tiles should be set on the basis of the sample size.

? TROUBLESHOOTING

(viii) Adjust the laser power and the chromatic correction focus for the other channels, if performing multichannel imaging. Start the scanning.

(ix) After imaging one half side (ventral or dorsal) of the entire body (or sample), remove the body from the sample holder, discard the black tape and clean the sample holder surface by wiping with a Kleenex and 80% ethanol.

(x) Flip the body or sample and mount it onto the sample holder with the super glue + accelerator method indicated before.

▲ **CRITICAL STEP** When in prone position, the animal might appear tilted in *Z* because the thickness of the head of the animal including the snout is higher than the thickness of the belly.

(xi) Scan the other side in the same way as described in steps (iii)–(ix) of this section.

Light-sheet imaging with a modified mesoSPIM ● Timing 10 h to 2 d

(i) Switch on the mesoSPIM and start the mesoSPIM-control software.

(ii) Lower the sample into the cuvette and fill it with BABB solution.

(iii) To stabilize the sample inside the cuvette, insert an appropriately sized (e.g., 40.5 mm for a 40 mm cuvette) crossbar between the cuvette walls above the sample and gently press it down onto the sample. The crossbar should be made from BABB-resistant material, e.g., 3D-printed from nylon (PA-2200) (Extended Data Fig. 7d).

(iv) Attach the lid of the sample cuvette (Extended Data Fig. 7c).

(v) Insert the sample into the microscope by attaching the lid magnet to the rotation stage (Extended Data Fig. 7e).

! CAUTION Be careful when moving the sample in *XYZ* to avoid crashing into microscope components. The magnetic sample holders usually provide a safety zone; when touching microscope components such as the scan lens mounts, the cuvette will first gently tilt before cracking. By slowly reversing the movement, it is thus possible to return the sample cuvette to a safe location.

(vi) Adjust the position of the sample by translating the sample via the mesoSPIM-control software until the fluorescent image can be acquired by the camera.

▲ **CRITICAL STEP** Be aware that, when translating the sample in *Z*, the detection focus needs to be changed as well to keep the light sheet in focus.

(vii) Test the range of motion for the intended scan by moving the sample around to ensure that the sample and the sample holder will not collide with the imaging chamber during the scan and tiling.

(viii) Before starting the acquisition, the rotation of the cuvette needs to be aligned to minimize the offset of the illumination from the left and the right side. If the cuvette walls are not perpendicular to the light sheet, the refraction will lead to the left and right light sheets illuminating different parts of the sample. To make the cuvette wall perpendicular to the light-sheet propagation direction, use a white piece of paper (e.g., a business card) to check where the back-reflection from the cuvette wall enters the scan lens. Then, rotate the cuvette using the rotation controls in mesoSPIM-control software to superimpose the back-reflection with the excitation beam. If different sample rotation angles are required for the left and right patch, co-align the light sheets according to the mesoSPIM wiki (https://github.com/mesoSPIM/mesoSPIM-hardware-documentation/wiki/mesoSPIM_coalignment).

(ix) Run the tiling wizard in the mesoSPIM-control software, following the instructions to set up the range of image scanning, filters, lasers and to specify the filenames and path for saving data. For the 0.9× objective, typical *X* and *Y* offsets between adjacent tiles are 12,000 µm and 20,000 µm, respectively. For each channel, you need to set a start and end focus. When acquiring a *Z*-stack, mesoSPIM-control will linearly interpolate the focus position between the start and end points.

(x) For whole-body stacks, it is often not possible to properly focus the detection path at the start and end points as both are commonly located outside of the sample. Therefore, mesoSPIM-control provides a focus-tracking wizard that allows to extrapolate the correct focus trajectory from two points inside the sample. After setting up the tiling pattern, preview a tile using the corresponding button in the acquisition manager window. Then, run the focus tracking wizard and move to a first *Z*-position inside the sample, manually focus the detection path in live mode and mark the position. Repeat the same procedure at a second *Z*-position. The wizard then allows you to apply the calculated focus trajectory to a selected subset of stacks (for example only to stacks using a specific excitation wavelength).

(xi) Use the preview button in the acquisition manager to check whether individual tiles in the acquisition manager are set up properly.
▲ **CRITICAL STEP** It is advisable to check if the laser intensity is set up correctly to avoid saturated regions of the sample. Ideally, the brightest sample regions are known from previous acquisitions. In addition, the tunable lens parameters (ETL parameter tab in the main window) should be checked to ensure that the light sheet is configured to be as thin as possible.

(xii) Toggle the 'Run acquisition list' button to start the scanning. The mesoSPIM-control software will show two progress bars: the top one shows the progress of the currently running stack and the bottom one the progress of the whole tiling scan. The predicted time estimate for the whole tiling scan will be continuously updated.

(xiii) If desired, rotate the sample by 90° or 180° to perform a multiview acquisition.

Lightsheet Z.1 microscope imaging ● Timing 10–30 min

(i) Switch on the microscope, start the ZEN software and mount the objectives required for the image acquisition.

(ii) Glue the cleared sample to the Lightsheet Z.1 sample holder (Extended Data Fig. 8a) and mount the sample holder into the microscope. Drive the sample holder to the upper-most position to avoid a collision of the chamber with the sample.

(iii) Fill the chamber with the clearing solution (e.g., BABB) and insert it into the microscope.

(iv) Lower the sample and position it in front of the detection objective, rotate the sample to the desired angle (Extended Data Fig. 8b). It is most convenient when the horizontal plane of the brain is in the *XY* plane of the microscope (directions are indicated in the ZEN software). Monitor the movement of the sample with the integrated door camera.

(v) Find the focus in the sample using the Near-IR pseudo-bright-field mode and readjust the rotational position, if there is need for refinement (Extended Data Fig. 8c).

(vi) Set up tracks for imaging by adjusting the laser intensity, exposure time, zoom and activate the Pivot scanner to maximally reduce the stripe artefacts in the images. Use simultaneous two channel imaging to reduce the total time of the experiment.

(vii) Define the *Z*-stack and the Tile scan for the entire brain.

(viii) Start the image acquisition.

(ix) Save the data for further processing.

Inverted confocal microscope imaging ● Timing 1–3 h

(i) Cut the sample and place it onto the glass slide of a glass bottom dish (Extended Data Fig. 5e, f).

(ii) Cover the sample with a few drops of BABB (Extended Data Fig. 5e, f). Complete immersion of the sample in BABB is not necessary, as long as the interface between the sample and the glass has BABB. Closing or sealing of the Petri dish is not required, because BABB has a high evaporation point and does not dry out for several days.

(iii) Mount the glass-bottom dish onto the sample holder of the microscope (Extended Data Fig. 5g).
! CAUTION MatTek glass bottom dishes are relatively resistant to BABB, even when BABB touches the plastic of the dish or the glue that seals the plastic part with the glass dish. MatTek glass-bottom dishes are able to stand the BABB for more than 4–5 h of imaging without leaking. However, BABB will eventually melt the plastic after some time. The resistance of the glass bottom dishes with BABB should be tested before mounting them onto the microscope. Strictly avoid leakage or spillage of BABB onto the microscope because BABB can severely damage the objectives and the mechanical parts of the microscope.

(iv) Select the desired objective. A long-WD objective such as the 25× Leica (used here) can be used to cover large depths in transparent samples.

(v) Adjust the settings of the scan: channel, gain and laser power, speed, averaging, bits, frame size, tiles, Z-stack limits, etc.

(vi) Activate the online stitching.

(vii) Start the scan.

(viii) Save the scan in CZI format, which will store all the metadata available.

52 Image processing and visualization steps will depend on the microscope method used:

Processing of 2D epifluorescence microscope (AxioZoom) scans ● Timing 30 min to 1 h

(i) From each scan, export the single 2D image.

(ii) In Adobe Photoshop CS6 software go to 'File' → 'Automate' → 'Photomerge'.

(iii) Select 'Reposition' and import all the files (previously exported images) representing your tiles.

(iv) Stitch the final image by repositioning the tiles and by changing their opacity whenever merging the overlapping regions.

(v) Group the stitched tiles in a single Photoshop layer.

(vi) Save the stitched file in Photoshop format such as.PDD, *.PSD. Then the stitched image can be exported as .jpeg or .tiff file and loaded in Fiji for visualization, analysis and the separation of the individual channels.

Processing of light-sheet microscope (Miltenyi Biotec) scans ● Timing 2 h to 6 d

(i) The Miltenyi Biotec light-sheet microscopes (Step 51B,C) save the scans as series of TIFF files in separate/not stitched sequences in one folder. Stitch the different tiles from one scan/folder with Fiji using the function located in 'Plugins' → 'Stitching' → 'deprecated' → 'Stitch Sequence of Grids of Images' (Supplementary Fig. 1a).

(ii) Fill the 'Stitch Image Grid Sequence' with the information about grid size, overlap, input directory, output directory and start positions (Supplementary Fig. 1b).

(iii) In 'file names': copy the name of one of the images from the scan and replace [00 ×00] with [{yy} x {xx}] and Z0000 with Z{zzzz}.

(iv) To have a first preliminary check of the result of the stitching, select the option 'create only preview', and set 'grid size z' = 1, 'start x' = 0, 'start y' = 0, 'start z' = a number of an optical slice deep in the tissue that contains data from each tile. This will yield the correct parameters for all tiles.

(v) If the stitched result looks fine, generate the first stitched image by unclicking 'create only preview' and start stitching.
▲ CRITICAL STEP If there are mistakes in *XY* dimensions, manually correct the positioning of the tiles in 2D, by using the TrakEM2 plugin of Fiji.
▲ CRITICAL STEP Stitching for all sections can be performed with this plugin by simply changing 'grid size z' to the total number of *Z*-stack +1 and 'start z' = 0. However, this option may lead to faulty stitching, and we recommend completing this procedure with steps (vi)–(vii).

(vi) Immediately after starting the stitching, the parameters and coordinates of the tiles will be saved in an automatically created file called 'TileConfiguration_{zzz}.txt.registered' in the input folder. This file will be used to stitch the other channels as well (Supplementary Fig. 1c). Rename the

automatically created file by deleting the '.registered' and change all tiles of the *Z*-panel numbers back to 0000 and set the new channel number that you want to stitch (e.g., C00_xyz-Table Z0100 into C01_xyz-Table Z0000). Do not change the coordinates. Save the file and move it into a new folder for stitching another channel. Each channel requires its own .txt file with the same coordinates; only C0x should change (Supplementary Fig. 1c, d).

(vii) In Fiji, open the macro for stitching called 'Stitching-old-just_txtFile.py' (available in http://discotechnologies.org/) and click on 'Run'. Load the .txt file that was just created in the previous step, which contains the stitching parameters for each channel and input the 'Number of images', which is the total number of optical slices of the scan (Supplementary Fig. 1e).

(viii) Click 'OK' and start stitching the first channel. Conduct the same steps for each channel.
▲ **CRITICAL STEP** Stitching can also be performed by other algorithms: for example, using TeraStitcher[62] (v.1.10; https://abria.github.io/TeraStitcher/), especially for correction of the shifting of the tiles in the *XYZ* directions.

(ix) Now, to stitch different tiling scans already individually stitched previously (for example, to obtain the whole mouse from different tiling scans of single individual body parts), proceed by using Vision4D from Arivis (version 3.4.0) (Supplementary Figs. 2 and 3).

(x) Rename the single .tiff files (for example, that compose the ventral side of a whole body), which you previously obtained from stitching in Fiji, by using the multi-Rename tool of an orthodox file manager software such as 'Total Commander'. The name of each single .tiff image must indicate the information about the channel (e.g., C00, C01, etc.) and the position of the panel/image in *Z* in four digits (e.g., for the channel C00, new name of the files: C00-Z0000.tif, C00-Z0001 and so on as shown in Supplementary Fig. 2a).

(xi) Save all the renamed images from different channels into the same folder (i.e., C00-C01-C02) (Supplementary Fig. 2a, last panel).

(xii) Drag your files composed of all channels and Z-stacks into the Vision4D software and proceed with the import steps. Press 'Yes' when 'Assume same structure for all files?' comes up (Supplementary Fig. 2b).
▲ **CRITICAL STEP** Open the software called ‚Arivis converter' to convert all the renamed images of the scan folder into a single file in .sis Arivis format in case the application is occupied. Click on 'add files'.

(xiii) Select 'custom import'. Select the output folder and give a name to the file (e.g. GFPM34-dorsal.sis). Then, click 'more options' and match the target pixel type to the one of your .tif files (in our case, 16-bit integer). Click 'OK' (Supplementary Fig. 2b).
▲ **CRITICAL STEP** All the images must be in the same format (for example, either compressed or not compressed, 16-bit and same number of *Z*-panels).

(xiv) A new window called 'manual import map' will pop up. Go to 'Selection' and 'pattern matching', to check whether Arivis identifies which part of the image name contains the information about the channel and the *Z*-panel, respectively (Supplementary Fig. 2b).

(xv) Check if the output name is correct and confirm the setting.

(xvi) Start the conversion: Arivis/Arivis converter will create a .sis file of your scan.
▲ **CRITICAL STEP** This .sis file must be saved in a final folder that must be located into the local drive of the computer. Do not save it in the network drive, as an interruption in the network would terminate the process.

(xvii) After the first image set is converted and imported, the second volume (e.g., the other side of the whole body) to be fused must be added. Drag the second folder into the software. The same prompter will pop up. Assume the same structure for all images and follow the steps (xii)–(xvi) as before except for choosing a 'New image set' instead of 'New file'. After the conversion and the import is finished with the second image set, make sure to save the .sis file. If you were using a converter so far, start Vision4D and open the first .sis file you want to consider by clicking 'File' → 'open' or by double clicking on the .sis file. Then, to open the second .sis file that has to be stitched to the first one you have to import it as 'New Image Set' in Vision4D.
▲ **CRITICAL STEP** Ensure that the second .sis file and all the others match the pixel type of the original images by clicking in 'Target Pixel Type' (e.g., 16-bit). Make sure to have enough gigabytes in the local drive to later save the final stitched file. You must decide from the beginning how many channels to stitch. Extra channels cannot be added later.

(xviii) Set the correct pixel size in μm for each volume by going to 'Data' → 'pixel size' and do this for all the volumes. The system is flexible, and it is not necessary to have same pixel size for all volumes.

(xix) In 'Extra' → 'Preferences', select the desired quality of rendering. If dealing with large datasets (in the range of 800–900 GB), reducing the quality of rendering helps increase the speed.

(xx) Adjust the brightness and contrast and scroll in 2D to take a better look of the data

(xxi) If necessary, flip one of the volumes to match the orientation of another volume, by clicking 'Data' → 'Transformation Gallery' → 'Flipping'. In 'Flipping Properties' you can choose to flip the volume around a different axis. For example, to stitch the dorsal scan with the ventral scan of the whole mouse, select 'Flip X-Axis' + 'Flip Z-Axis' for the dorsal volume. Wait until the image set is flipped and press 'Save'. This can take up to 1–1.5 d depending on the data size. After checking that the flipping has worked correctly in the multiview window, close the original version that was not flipped.

▲ **CRITICAL STEP** Create a .docx/.doc or a .txt file to keep track of how the volumes were flipped and the order that the different volumes were stitched to each other. This record will be important in case you want to repeat the process.

(xxii) Using the 2D visualization modality, look for three landmarks in the different volumes. A landmark consists of a single pixel in a structure of the tissue that appears in both or more volumes that have to be stitched together. The purpose is to get the coordinates of this landmark/pixel.

▲ **CRITICAL STEP** The landmarks should be structures deep into the tissue, for example, bone cracks, holes or junctions. They should be fixed structures that do not move during the mounting of the sample, and they should be as far as possible apart from each other in *XYZ*. It is possible to flip the volumes as explained in the previous point to ease the finding of the same landmark in different volumes. We generally use bones and not internal organs as landmarks.

(xxiii) To highlight the selected landmark of interest, click on the icon 'Place New Object/Marker' and click on the icon 'Marker', then, click on the landmark of interest for each image set. Then, match the names of the corresponding landmarks through 'Show objects Table' (Supplementary Fig. 2c).

(xxiv) To get the *XYZ* coordinates of the indicated landmarks, click on 'Annotation' icon and go in 'Properties' → 'Marker locations'. Record the landmarks and their coordinates in the .docx or .txt file (in case you want to reuse them in the future). You can rename each landmark appearing in all volumes using the same name (e.g., LM1). Save after each step.

(xxv) Click on 'Data' → 'Volume Fusion'. A new prompter will open; indicate which volume you want to specify as 'Base image Set' and which as 'Moving Image Set'. During stitching, the coordinates of the 'Base Image Set' will be kept fixed, while the coordinates of the 'Moving Image Set' will be changed. This will transform the whole 'Moving Image Set' to stitch it to the Base Image Set. We normally keep the ventral scan as 'Base Image Set', and we indicate the flipped dorsal scan as 'Moving Image Set' (Supplementary Fig. 3a).

(xxvi) Choose 'New File' to save the fused volume as that will be generated and select '10% of Scale' (at this stage we do a first preview by scaling down) and give a name to the volume that will result from stitching (Supplementary Fig. 3a).

(xxvii) In 'Transformation' → 'Landmark Registration' window, click 'Add all annotations as Landmarks' for both 'Base Image Set' and 'Moving Image Set'. By doing so, the list of landmarks will appear as two lists in this window.

▲ **CRITICAL STEP** Make sure that the order of landmarks is the same in both image sets. Their locations are displayed in the volumes on the right side of the window (Supplementary Fig. 3a).

(xxviii) Click run to automatically fuse the two volumes/image sets. This step will take several minutes depending on the power of the computer.

(xxix) After fusing, a new .sis file will be created. Open it using Vision4D (without closing the previous one which was used to start the stitching) and check the quality of fusion by scrolling it in 2D, by moving it in 3D and by changing the brightness and contrast.

(xxx) If the result is satisfactory, go back to the previous Vision4D window that was used to set the landmarks. The preview window can be closed and deleted.

? TROUBLESHOOTING

(xxxi) Set the scale to '100%'. Click run. This process will take 1–2 d and will create a .sis file consisting of the volumes now stitched together (Supplementary Fig. 3b).

(xxxii) Export the .sis file into a series of .tiff images using 'tiff exporter' function of the software. This process will take a few hours, depending on the size of the data.

▲ **CRITICAL STEP** Vision4D names the exported .tiff files with the *Z*-panel information before the channel information. Renaming might be necessary if a specific pattern of labeling is needed for further analysis.

Now it is possible to visualize, render and analyze this stitched image series in different software such as Fiji, Imaris and Amira or published algorithms such as ClearMap, DeepMACT and NeuroGPS-Tree.

Troubleshooting

Troubleshooting advice can be found in Table 5.

Table 5 | Troubleshooting table

Step	Problem	Potential cause	Suggested solution
2, 3	The liver does not turn partially or completely yellow	The angle with which the PBS goes inside the heart from the needle is not optimal	Change the position or the angle of the needle Make sure the right atrium is not covered or clogged
	The animal does not become rigid and stiff with PFA perfusion	The angle with which the PFA goes inside the heart from the needle is not optimal	Change position or the angle of the needle
27	The needle does not go into the hole	The tip of the needle might be too large or the hole too small	Change the angle of the needle Slightly enlarge the hole with a larger normal needle until the size is sufficiently big for the perfusion needle
28	The glue detaches at some point during perfusion	A movement caused displacement	Glue it again
33	The decolorization solution is still yellow at the end of this step	More heme has to be extracted	Repeat one or more round of decolorization solution
35	When pumping the decalcification solution, the solution turns from transparent to milky	Insufficient wash of the decolorization solution from the previous step	Wash the sample again by pumping with PBS and restart the decalcification step
38	Presence of bubbles in the perfusion tubing	While connecting the filter to the perfusion tubing, air bubbles entered the tube	Temporarily displace the ending of the tube that holds the needle in order to remove the needle from the heart. Switch on the pump for some minutes to push all the bubbles out from the tubing through the needle. When all the bubbles are removed, place the needle back into the hole on the heart. Pump for some minutes, ensuring that the system is still working properly, and switch off the pump again for the next step
42	The perfusion system starts pumping a lot of bubbles	The filter might be obstructed for example by hair	Change the filter with a new one and repeat the operation of removing the bubbles from the tubing when the new filter is connected to the tube
47	The organs are too widespread	The abdominal cavity may have been opened too much during perfusion and fixation step	Push the organs back inside the abdominal cavity and if necessary, use surgical sutures to stitch up the body with a couple of stitches before clearing
50	The sample is blurry or not sufficiently transparent	Insufficient clearing	Increase the incubation time and/or volume of the clearing solutions and the refractive index matching solution
51A(iii)	Sample moves during epifluorescence imaging	Sample is not adequately fixed in the glass chamber	Try to put the lid of the glass chamber diagonally inside the chamber as a wall to restrain the sample
51A(iv)	No signal visible	Animal does not express the fluorescence signal in some regions or at all	Check the genotype of the animal and make sure there were no mistakes Choose another body region to image
51B(iii) and C(ii)	Presence of bubbles in the sample	Air trapped inside the sample	Gently tap the sample inside the imaging chamber with tweezers to push the bubbles out Use a syringe with a fine needle to suck the bubbles out (if you decide to inject the bubbles with BABB, sprays of BABB can reach your eyes! Wear protection) Wait for some hours until bubbles will disappear by themselves. This might take even some days; therefore, you can place the sample back into BABB into the storing container while doing this. Mount the sample again back to the microscope

Table continued

Table 5 (continued)

Step	Problem	Potential cause	Suggested solution
51B(x) and C(vi)	Sample not visible during the imaging	Out of focus	Move the stage in *X*–*Y* to find bright halos that might be the sample. Move the objective to the highest level and start lowering again very slowly while continuously adjusting the contrast on the computer screen until focus is reached
	Distortion in the image during imaging	Presence of a bubble between the sample and the objective	Move the objective up out of the BABB, wipe the lens of the objective once with a piece of tissue to get rid of the bubble. Lower the objective back into the BABB
51B(xi) and C(vii)	Tiles in mosaic scan do not seem to have proper overlap	The sample moved during the imaging	Remount the sample more firmly by, for example, increasing the glue amount
52B(xxx)	Result of stitching is not satisfactory	Landmarks that were chosen were not optimal	Replace the landmarks with new ones, by observing the preview and identifying the region that shows problems in the fusion, then change the landmark that was inside this region

Timing

Steps 1–3, sample preparation with PBS and PFA perfusion: 14 h to 1 d
Steps 4–47, passive-vDISCO: 2–23 d, whole-body active vDISCO: 12–16 d
Steps 48–50, clearing, 1–4 d
Step 51, imaging:
Option A, epifluorescence imaging: 5–15 min
Option B, light-sheet imaging with Ultramicroscope II: 2–12 h
Option C, light-sheet imaging with Blaze: 6–7 d
Option D, light-sheet imaging with the modified mesoSPIM: 10 h to 2 d
Option E, light-sheet imaging with Z.1: 10–30 min
Option C, confocal imaging: 1–3 h
Step 52: image processing:
Option A, processing of 2D epifluorescence microscope (AxioZoom) scans: 30 min to 1 h
Option B, processing of light-sheet microscope (Miltenyi Biotec) scans: 2 h to 6 d

Anticipated results

By developing a reproducible, straightforward and rapid pipeline that combines different steps that have the purpose to decrease the tissue background, increase and stabilize the fluorescent signal and clear very large specimens, we are able to obtain high-resolution 3D imaging data of an entire rodent.

Previously, one of the applications of vDISCO was to detect and localize all metastases at single-cell resolution in animal models of cancer: the data shown in Fig. 2 represent a typical imaging result obtained by vDISCO for a mouse bearing pancreatic cancer, where single metastatic cells are visible from the whole imaged body (but are not visible in bioluminescence imaging in Fig. 2a,b). This kind of data can be analyzed using artificial intelligence algorithms that are able to provide the location, number and distribution of all cancer cells and their targeting by therapeutic antibodies[1].

Here, we also show the possibility of analyzing other biological structures that span from head to toe: Fig. 8 represents the 3D reconstruction of the *Prox1*+ lymphatic system where details of lymphatic vessels are visible in different organs (Supplementary Video 4). Such data can become highly valuable for studies of whole-body inflammatory responses from local diseases. For example, on the one hand our light-sheet data reveal the intricate lymphatic vasculature in the lungs (Fig. 8i, red arrows); on the other hand, our confocal data magnify a single connected lymphatic vessel (Fig. 8j). It has been shown that patients with moderate chronic obstructive pulmonary disease bear de novo lymphatic vessel formation in lungs[71]. vDISCO can help systematically assess changes (e.g., connectivity, diameter and length of the vessels) in the lymphatic vasculature of the disease mouse model not only in the organ affected by the disease but also in other peripheral organs. In addition to the widely known presence of *Prox1* expression in lymphatic vessels[72], our technology underlines the less known cells where *Prox1* is also expressed, such as the satellite cells in muscle tissue (Fig. 8g,k, green arrows)[73] and granule cells in the hippocampus[74]. On the basis of this unbiased screening, it is

possible to analyze the different patterns of expressions and how this pattern may change under specific circumstances.

Thus, vDISCO can be applied in synergy with many different fluorescent imaging systems, including epifluorescence microscopes, confocal microscopes and different kinds of light-sheet microscopes (Figs. 2 and 5–9 and Extended Data Figs. 2, 3 and 5–8).

The versatility of vDISCO is also demonstrated by the fact that it can be applied on single dissected organs composed of different kinds of tissues. This is achieved by using a simplified version of the method that relies on passive incubation of the nanobody (Figs. 6, 7 and 9 and Extended Data Fig. 3). The application of vDISCO on dissected organs can substantially further simplify and speed up the whole immunolabeling procedure, while still yielding high-quality data: for example, in Fig. 6 the distribution of monocytes/macrophages is visible in different organs and in Fig. 9d–h all brain pericytes are visible with such detail that we can observe the single cells wrapping the brain vasculature.

Last, we show that vDISCO can be used to trace viral spread in tissue: in Fig. 9a–c, the increase and stabilization of the fluorescent signal expressed by viral vectors after vDISCO allows us to detect neurites including single axons (Fig. 9b,c, red and cyan arrowheads, and Supplementary Video 5).

Overall, vDISCO can be broadly applied to various studies. We think vDISCO may be used in future work to elucidate how peripheral symptoms originate from brain insults or to investigate alterations in the neuronal circuitry in neurodegenerative and psychiatric diseases. Other possible future applications include the study of whole-body inflammatory phenomena, the crosstalk between microbiota and host, and the screening of infectious agents, stem cells or therapeutic cells (e.g., CAR-T cells). The ability to comprehensively and unbiasedly analyze whole organs and bodies represents a tool for biomedical researchers to address a broad spectrum of scientific questions that require single-cell resolution with a systems-biology approach.

Reporting summary

Further information on research design is available in the Nature Portfolio Reporting Summary linked to this article.

Data availability

The main data discussed in this protocol are available in the supporting primary research papers (https://www.nature.com/articles/s41593-018-0301-3 and https://www.cell.com/cell/fulltext/S0092-8674(19)31269-3?_returnURL=https%3A%2F%2Flinkinghub.elsevier.com%2Fretrieve%2Fpii%2FS0092867419312693%3Fshowall%3Dtrue). The raw datasets of the main data and of the additional new data shown in this work are too large to be publicly shared but are available for research purposes from the corresponding authors upon reasonable request.

References

1. Pan, C. et al. Deep learning reveals cancer metastasis and therapeutic antibody targeting in the entire body. *Cell* **179**, 1661–1676.e19 (2019).
2. Ntziachristos, V. Going deeper than microscopy: the optical imaging frontier in biology. *Nat. Methods* **7**, 603–614 (2010).
3. James, M. L. & Gambhir, S. S. A molecular imaging primer: modalities, imaging agents, and applications. *Physiol. Rev.* **92**, 897–965 (2012).
4. Timpson, P., McGhee, E. J. & Anderson, K. I. Imaging molecular dynamics in vivo—from cell biology to animal models. *J. Cell Sci.* **124**, 2877–2890 (2011).
5. Erturk, A. et al. Three-dimensional imaging of the unsectioned adult spinal cord to assess axon regeneration and glial responses after injury. *Nat. Med.* **18**, 166–171 (2012).
6. Hama, H. et al. Scale: a chemical approach for fluorescence imaging and reconstruction of transparent mouse brain. *Nat. Neurosci.* **14**, 1481–1488 (2011).
7. Chung, K. et al. Structural and molecular interrogation of intact biological systems. *Nature* **497**, 332–337 (2013).
8. Susaki, E. A. et al. Whole-brain imaging with single-cell resolution using chemical cocktails and computational analysis. *Cell* **157**, 726–739 (2014).
9. Ke, M.-T., Fujimoto, S. & Imai, T. SeeDB: a simple and morphology-preserving optical clearing agent for neuronal circuit reconstruction. *Nat. Neurosci.* **16**, 1154–1161 (2013).
10. Hama, H. et al. ScaleS: an optical clearing palette for biological imaging. *Nat. Neurosci.* **18**, 1518–1529 (2015).
11. Renier, N. et al. iDISCO: a simple, rapid method to immunolabel large tissue samples for volume imaging. *Cell* **159**, 896–910 (2014).

12. Belle, M. et al. Tridimensional visualization and analysis of early human development. *Cell* **169**, 161–173.e12 (2017).
13. Belle, M. et al. A simple method for 3D analysis of immunolabeled axonal tracts in a transparent nervous system. *Cell Rep.* **9**, 1191–1201 (2014).
14. Murray, E. et al. Simple, scalable proteomic imaging for high-dimensional profiling of intact systems. *Cell* **163**, 1500–1514 (2015).
15. Dodt, H.-U. et al. Ultramicroscopy: three-dimensional visualization of neuronal networks in the whole mouse brain. *Nat. Methods* **4**, 331–336 (2007).
16. Pan, C. et al. Shrinkage-mediated imaging of entire organs and organisms using uDISCO. *Nat. Methods* **13**, 859–867 (2016).
17. Susaki, E. A. et al. Advanced CUBIC protocols for whole-brain and whole-body clearing and imaging. *Nat. Protoc.* **10**, 1709–1727 (2015).
18. Tainaka, K. et al. Whole-body imaging with single-cell resolution by tissue decolorization. *Cell* **159**, 911–924 (2014).
19. Kubota, S. I. et al. Whole-body profiling of cancer metastasis with single-cell resolution. *Cell Rep.* **20**, 236–250 (2017).
20. Yang, B. et al. Single-cell phenotyping within transparent intact tissue through whole-body clearing. *Cell* **158**, 945–958 (2014).
21. Treweek, J. B. et al. Whole-body tissue stabilization and selective extractions via tissue–hydrogel hybrids for high-resolution intact circuit mapping and phenotyping. *Nat. Protoc.* **10**, 1860–1896 (2015).
22. Jing, D. et al. Tissue clearing of both hard and soft tissue organs with the PEGASOS method. *Cell Res.* **28**, 803–818 (2018).
23. Cai, R. et al. Panoptic imaging of transparent mice reveals whole-body neuronal projections and skull–meninges connections. *Nat. Neurosci.* **22**, 317–327 (2019).
24. Muyldermans, S. Single domain camel antibodies: current status. *Rev. Mol. Biotechnol.* **74**, 277–302 (2001).
25. Muyldermans, S. Nanobodies: natural single-domain antibodies. *Annu. Rev. Biochem.* **82**, 775–797 (2013).
26. Schumacher, D., Helma, J., Schneider, A. F. L., Leonhardt, H. & Hackenberger, C. P. R. Nanobodies: chemical functionalization strategies and intracellular applications. *Angew. Chem. Int. Ed.* **57**, 2314–2333 (2018).
27. Niess, J. H. et al. CX3CR1-mediated dendritic cell access to the intestinal lumen and bacterial clearance. *Science* **307**, 254–258 (2005).
28. Gage, G. J., Kipke, D. R. & Shain, W. Whole animal perfusion fixation for rodents. *J. Vis. Exp.* https://doi.org/10.3791/3564 (2012).
29. Wang, X. et al. An ocular glymphatic clearance system removes β-amyloid from the rodent eye. *Sci. Transl. Med.* **12,** eaaw3210 (2020).
30. Louveau, A. et al. Structural and functional features of central nervous system lymphatic vessels. *Nature* **523**, 337–341 (2015).
31. Hong, G., Antaris, A. L. & Dai, H. Near-infrared fluorophores for biomedical imaging. *Nat. Biomed. Eng.* **1**, 0010 (2017).
32. Quan, T. et al. NeuroGPS-Tree: automatic reconstruction of large-scale neuronal populations with dense neurites. *Nat. Methods* **13**, 51–54 (2016).
33. Li, A. et al. Micro-optical sectioning tomography to obtain a high-resolution atlas of the mouse brain. *Science* **330**, 1404–1408 (2010).
34. Qi, X. et al. Fluorescence micro-optical sectioning tomography using acousto-optical deflector-based confocal scheme. *Neurophotonics* **2**, 041406–041406 (2015).
35. Ragan, T. et al. Serial two-photon tomography for automated ex vivo mouse brain imaging. *Nat. Methods* **9**, 255–258 (2012).
36. Feng, G. et al. Imaging neuronal subsets in transgenic mice expressing multiple spectral variants of GFP. *Neuron* **28**, 41–51 (2000).
37. Zhao, S. et al. Cellular and molecular probing of intact human organs. *Cell* **180**, 796–812.e19 (2020).
38. Richardson, D. S. et al. Tissue clearing. *Nat. Rev. Methods Primer* **1**, 1–24 (2021).
39. Erturk, A. et al. Three-dimensional imaging of solvent-cleared organs using 3DISCO. *Nat. Protoc.* **7**, 1983–1995 (2012).
40. Rothbauer, U. et al. Targeting and tracing antigens in live cells with fluorescent nanobodies. *Nat. Methods* **3**, 887–889 (2006).
41. Horecker, B. L. The absorption spectra of hemoglobin and its derivatives in the visible and near infra-red regions. *J. Biol. Chem.* **148**, 173–183 (1943).
42. Tainaka, K., Kuno, A., Kubota, S. I., Murakami, T. & Ueda, H. R. Chemical principles in tissue clearing and staining protocols for whole-body cell profiling. *Annu. Rev. Cell Dev. Biol.* **32**, 713–741 (2016).
43. Tuchin, V. V. Tissue optics and photonics: light–tissue interaction. *J. Biomed. Photonics Eng.* **1**, 98–134 (2015).
44. Tainaka, K. et al. Chemical landscape for tissue clearing based on hydrophilic reagents. *Cell Rep.* **24**, 2196–2210.e9 (2018).
45. Kristinsson, H. G. & Hultin, H. O. Changes in trout hemoglobin conformations and solubility after exposure to acid and alkali pH. *J. Agric. Food Chem.* **52**, 3633–3643 (2004).
46. Alnuami, A. A., Zeedi, B., Qadri, S. M. & Ashraf, S. S. Oxyradical-induced GFP damage and loss of fluorescence. *Int. J. Biol. Macromol.* **43**, 182–186 (2008).

47. Fagan, J. M., Sleczka, B. G. & Sohar, I. Quantitation of oxidative damage to tissue proteins. *Int. J. Biochem. Cell Biol.* **31**, 751–757 (1999).
48. Acar, M. et al. Deep imaging of bone marrow shows non-dividing stem cells are mainly perisinusoidal. *Nature* **526**, 126–130 (2015).
49. Greenbaum, A. et al. Bone CLARITY: clearing, imaging, and computational analysis of osteoprogenitors within intact bone marrow. *Sci. Transl. Med.* **9**, eaah6518 (2017).
50. Gonzalez-Chavez, S. A., Pacheco-Tena, C., Macias-Vazquez, C. E. & Luevano-Flores, E. Assessment of different decalcifying protocols on osteopontin and osteocalcin immunostaining in whole bone specimens of arthritis rat model by confocal immunofluorescence. *Int. J. Clin. Exp. Pathol.* **6**, 1972–1983 (2013).
51. Xiao, X. et al. Antibody incubation at 37°C improves fluorescent immunolabeling in free-floating thick tissue sections. *Biotechniques* **62**, 115–122 (2017).
52. Weiss, K. R., Voigt, F. F., Shepherd, D. P. & Huisken, J. Tutorial: practical considerations for tissue clearing and imaging. *Nat. Protoc.* **16**, 2732–2748 (2021).
53. Renier, N. et al. Mapping of brain activity by automated volume analysis of immediate early genes. *Cell* **165**, 1789–1802 (2016).
54. Voigt, F. F. et al. The mesoSPIM initiative: open-source light-sheet microscopes for imaging cleared tissue. *Nat. Methods* **16**, 1105–1108 (2019).
55. Welch, A. Technique for high-performance data compression. *Computer* **17**, 8–19 (1984).
56. Ma, B. et al. A fast algorithm for material image sequential stitching. *Comput. Mater. Sci.* **158**, 1–13 (2019).
57. Dellatorre, G. & Gadens, G. A. Wide area digital dermoscopy applied to basal cell carcinoma. *An. Bras. Dermatol.* **95**, 379–382 (2020).
58. Boatright, J. H. et al. Methodologies for analysis of patterning in the mouse RPE sheet. *Mol. Vis.* **21**, 40–60 (2015).
59. Hörl, D. et al. BigStitcher: reconstructing high-resolution image datasets of cleared and expanded samples. *Nat. Methods* **16**, 870–874 (2019).
60. Schindelin, J. et al. Fiji: an open-source platform for biological-image analysis. *Nat. Methods* **9**, 676–682 (2012).
61. Pietzsch, T., Preibisch, S., Tomancak, P. & Saalfeld, S. ImgLib2-generic image processing in Java. *Bioinformatics* **28**, 3009–3011 (2012).
62. Bria, A. & Iannello, G. TeraStitcher—a tool for fast automatic 3D-stitching of teravoxel-sized microscopy images. *BMC Bioinformatics* **13**, 316 (2012).
63. Glaser, J. R. & Glaser, E. M. Neuron imaging with neurolucida—a PC-based system for image combining microscopy. *Comput. Med. Imaging Graph.* **14**, 307–317 (1990).
64. Belthangady, C. & Royer, L. A. Applications, promises, and pitfalls of deep learning for fluorescence image reconstruction. *Nat. Methods* https://doi.org/10.1038/s41592-019-0458-z (2019).
65. Moen, E. et al. Deep learning for cellular image analysis. *Nat. Methods* https://doi.org/10.1038/s41592-019-0403-1 (2019).
66. Zhou, H. et al. 3D high resolution generative deep-learning network for fluorescence microscopy imaging. *Opt. Lett.* **45**, 1695–1698 (2020).
67. Mano, T. et al. CUBIC-Cloud provides an integrative computational framework toward community-driven whole-mouse-brain mapping. *Cell Rep. Methods* **1**, 100038 (2021).
68. Iwasato, T. et al. Cortex-restricted disruption of NMDAR1 impairs neuronal patterns in the barrel cortex. *Nature* **406**, 726–731 (2000).
69. Takatoh, J. et al. New modules are added to vibrissal premotor circuitry with the emergence of exploratory whisking. *Neuron* **77**, 346–360 (2013).
70. Wickersham, I. R. et al. Monosynaptic restriction of transsynaptic tracing from single, genetically targeted neurons. *Neuron* **53**, 639–647 (2007).
71. Reed, H. O. et al. Lymphatic impairment leads to pulmonary tertiary lymphoid organ formation and alveolar damage. *J. Clin. Invest.* **129**, 2514–2526 (2019).
72. Wigle, J. T. et al. An essential role for Prox1 in the induction of the lymphatic endothelial cell phenotype. *EMBO J.* **21**, 1505–1513 (2002).
73. Kivelä, R. et al. The transcription factor Prox1 is essential for satellite cell differentiation and muscle fibre-type regulation. *Nat. Commun.* **7**, 13124 (2016).
74. Iwano, T., Masuda, A., Kiyonari, H., Enomoto, H. & Matsuzaki, F. Prox1 postmitotically defines dentate gyrus cells by specifying granule cell identity over CA3 pyramidal cell fate in the hippocampus. *Dev. Camb. Engl.* **139**, 3051–3062 (2012).

Acknowledgements

This work was supported by the Vascular Dementia Research Foundation, Deutsche Forschungsgemeinschaft (DFG, German Research Foundation) under Germany's Excellence Strategy within the framework of the Munich Cluster for Systems Neurology (EXC 2145 SyNergy, ID 390857198), the ERC Consolidator Grant (AE, 865323), and the Nomis Heart Atlas Project Grant (Nomis Foundation). H.M. is also supported by the China Scholarship Council (CSC) (no. 201806780034). M.M. is supported by the Turkish Ministry of Education for her PhD studies. We thank K. Sleiman, C. Veltkamp and D. Saur for providing the animal bearing pancreatic cancer; M. Voll (Zeiss Microscopy GmbH, Germany) and the Zeiss Microscopy Customer Center Europe for performing the image acquisition with the Lightsheet Z.1; J. Thomas, S. Grade and M. Götz for providing the virus traced sample; J. Shrouder and N. Plesnila for providing the PDGFRb-EGFP mice; A. Ghasemigharagoz, A. Parra-Damas and F.P. Quacquarelli for help during the initial optimization and method development; M. Bralo and B. Forstera for help during the testing of some nanobodies; F. Hellal for critical reading of the manuscript. A.E. and Z.I.K. are members of the Graduate School of Systemic Neurosciences at the Ludwig Maximilian University of Munich.

Author contributions

A.E. and R.C. initiated the project. R.C. and C.P. developed the original vDISCO method. R.C. designed the experiments. R.C. and Z.I.K. performed most of the experiments. C.P. provided data for the cancer mouse. H.M. and S.Z. provided data for the PDGFRb-EGFP pericyte-labeled brains. F.F.V., M.M., T.-L.O. and F.H. provided mesoSPIM data. C.V. and J.A.V.G. provided the custom-made nanobodies anti-GFP. D.K. contributed to the imaging, and M.I.T helped with the stitching of the Prox1-EGFP sample. R.C. and Z.I.K. supervised the experiments. A.E. supervised the project. R.C. and Z.I.K. wrote the manuscript. All authors edited the manuscript.

Competing interests

A.E., R.C., C.P. and S.Z. have filed a patent related to vDISCO.

Additional information

Extended data is available for this paper at https://doi.org/10.1038/s41596-022-00788-2.

Supplementary information The online version contains supplementary material available at https://doi.org/10.1038/s41596-022-00788-2.

Correspondence and requests for materials should be addressed to Ali Ertürk.

Peer review information *Nature Protocols* thanks Nicolas Renier and the other, anonymous, reviewer(s) for their contribution to the peer review of this work.

Reprints and permissions information is available at www.nature.com/reprints.

Publisher's note Springer Nature remains neutral with regard to jurisdictional claims in published maps and institutional affiliations.

Received: 29 September 2021; Accepted: 20 October 2022;
Published online: 25 January 2023

Related Links
Key references using this protocol
Cai, R. et al. *Nat. Neurosci.* **22**, 317–327 (2019): https://doi.org/10.1038/s41593-018-0301-3
Pan, C. et al. *Cell* **179**, 1661–1676.e19 (2019): https://doi.org/10.1016/j.cell.2019.11.013

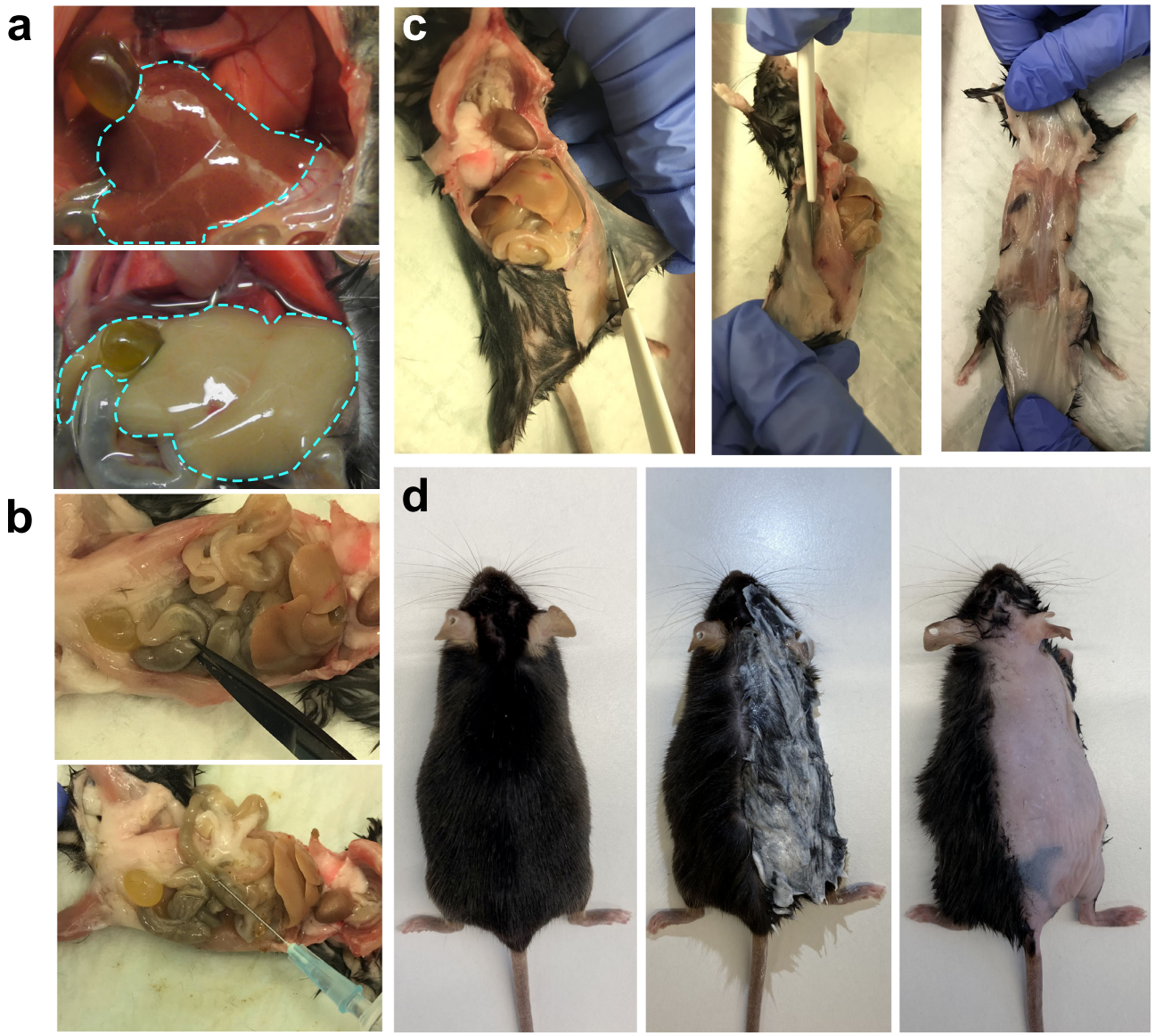

Extended Data Fig. 1 | Sample preparation for whole-body active-vDISCO. a, During the 1× PBS perfusion step of the anesthetized animal, the color of the liver (cyan dashed line) turns yellow as indication of proper drainage of the blood from the body. **b**, Some cuts in the gut are necessary to flush out the gut content and the feces with a syringe. **c**, Pictures showing the procedure of skinning the body of the animal using a blade. **d**, In case the animal is needed with intact skin, commercial hair removal creams may be used as illustrated. The cream should be applied to region of interest and removed with water after 3–5 min. Steps can be repeated until the desired quality of hair removal is achieved. Animal experiments followed European directive 2010/63/EU for animal research, reported according to the Animal Research: Reporting of In Vivo Experiments (ARRIVE) criteria, complied with the '3Rs' measure and were approved by the ethical review board of the government of Upper Bavaria (Regierung von Oberbayern, Munich, Germany) and conformed to institutional guidelines of Klinikum der Universität München/Ludwig Maximilian University of Munich). The severity of the procedure was low.

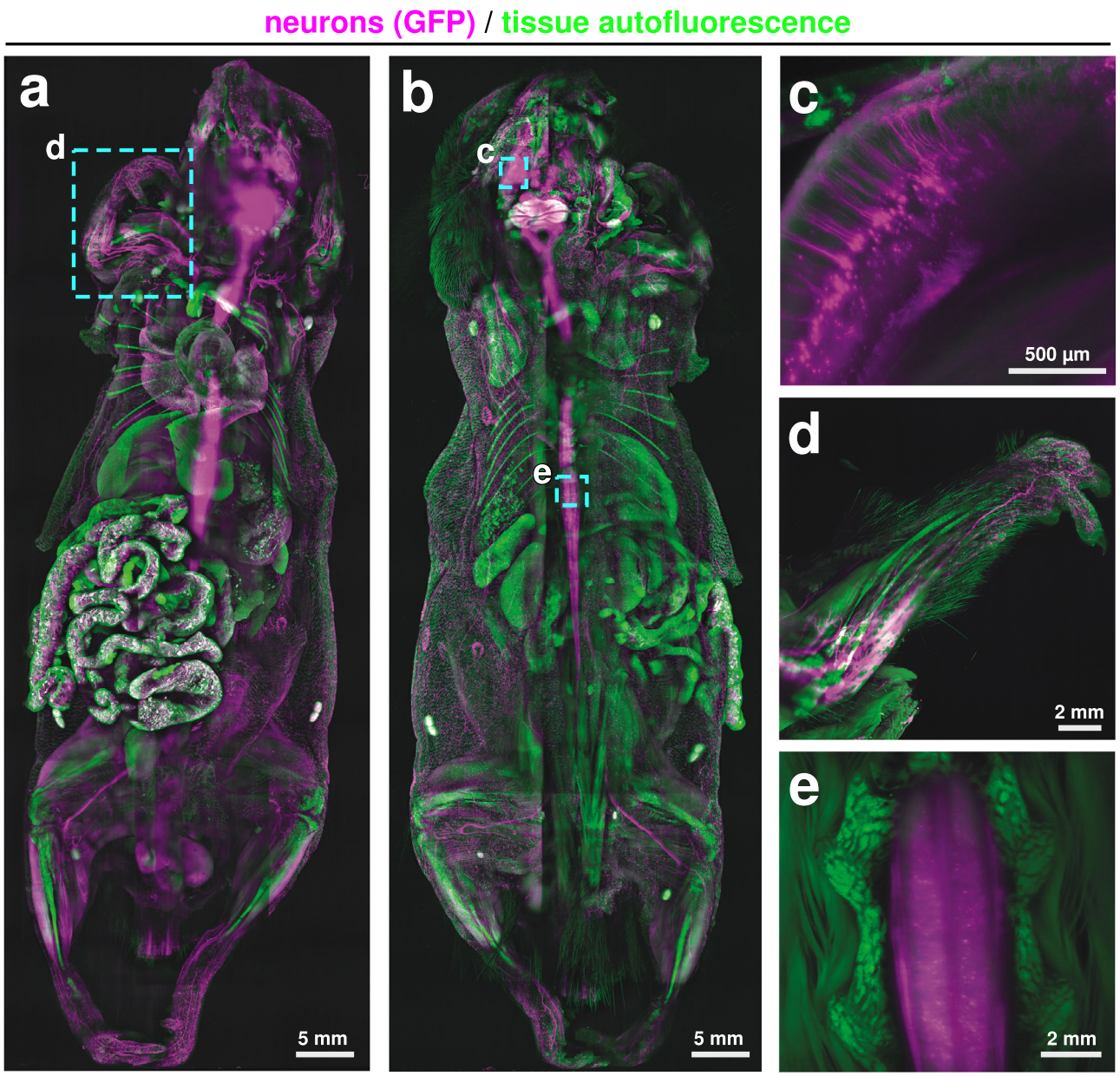

Extended Data Fig. 2 | Whole-body imaging of a sample with intact skin using a modified mesoSPIM light-sheet microscope. a, Maximum projection of an adult Thy1-GFPM mouse with intact skin imaged with a modified mesoSPIM light-sheet microscope from the ventral side. Autofluorescence excited at 488 nm is shown in green, GFP in magenta. **b**, Maximum projection of the same sample imaged from the dorsal side (rotated by 180°). **c**, Layer 5 pyramidal neurons in the brain. **d**, Peripheral nerves and skin of the forepaw imaged from the lateral direction (90° rotation). **e**, Detail of the spinal cord and vertebrae. Images in **a**, **b**, **d** and **e** were taken at 0.9× magnification whereas image in **c** was imaged at 4× magnification. Animal experiments followed European directive 2010/63/EU for animal research, reported according to the Animal Research: Reporting of In Vivo Experiments (ARRIVE) criteria, complied with the '3Rs' measure and were approved by the ethical review board of the government of Upper Bavaria (Regierung von Oberbayern, Munich, Germany) and conformed to institutional guidelines of Klinikum der Universität München/Ludwig Maximilian University of Munich). The severity of the procedure was low.

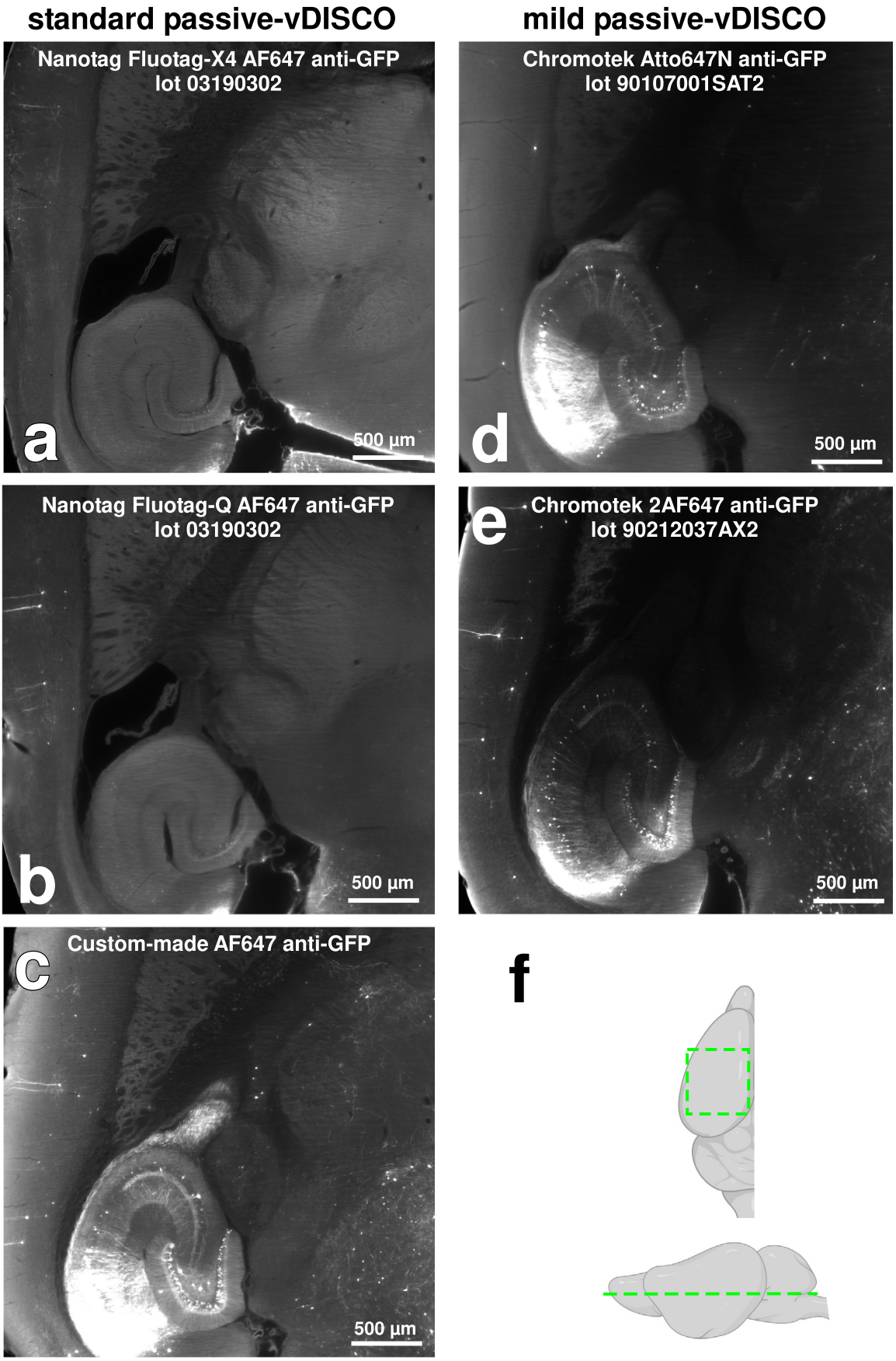
standard passive-vDISCO
mild passive-vDISCO
Nanotag Fluotag-X4 AF647 anti-GFP
lot 03190302
a
500 µm
Chromotek Atto647N anti-GFP
lot 90107001SAT2
d
500 µm
Nanotag Fluotag-Q AF647 anti-GFP
lot 03190302
b
500 µm
e
Chromotek 2AF647 anti-GFP
lot 90212037AX2
500 µm
c
Custom-made AF647 anti-GFP
500 µm
f

◀ **Extended Data Fig. 3 | Performances of different kinds of nanobodies in passive-vDISCO for Thy1-GFPM line. a**–**e**, Light-sheet microscopy images of half mouse brains from Thy1-GFPM lines showing the performances of different batches of nanobodies from different sources and companies using standard passive-vDISCO (**a**–**c**) and mild passive-vDISCO (**d** and **e**). The used nanobody is indicated in the panel title. **f**, Illustration indicating the anatomic region of the brain (green dashed) that was displayed in **a**–**e**. Note that the imaging was taken either on the right or on the left hemisphere; right hemisphere images were flipped to ease the comparison between the different nanobodies. All the results in this figure were similarly observed in at least two independent experiments for each kind of nanobody. Animal experiments followed European directive 2010/63/EU for animal research, reported according to the Animal Research: Reporting of In Vivo Experiments (ARRIVE) criteria, complied with the '3Rs' measure and were approved by the ethical review board of the government of Upper Bavaria (Regierung von Oberbayern, Munich, Germany) and conformed to institutional guidelines of Klinikum der Universität München/Ludwig Maximilian University of Munich). The severity of the procedure was low.

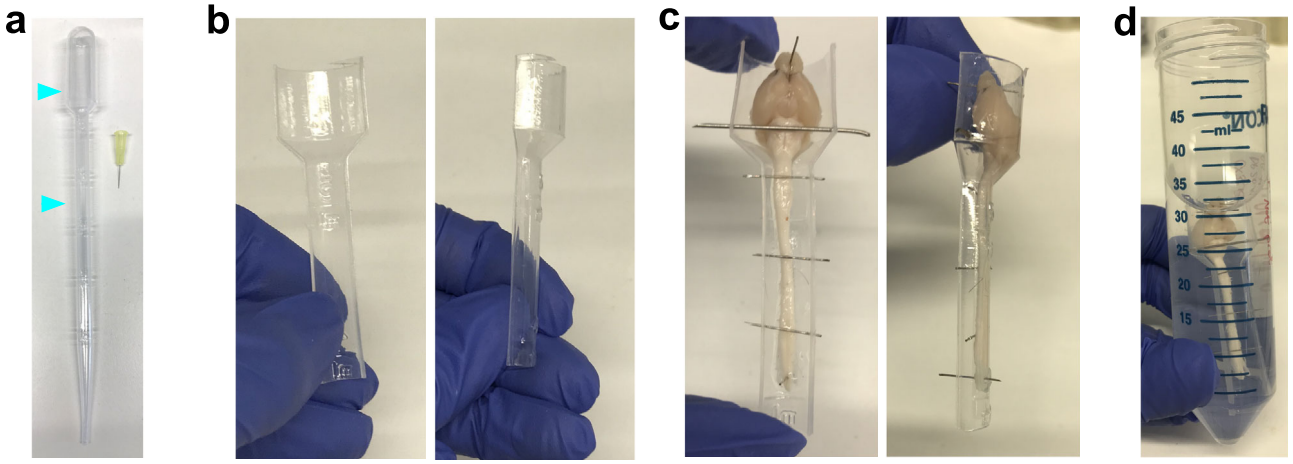

Extended Data Fig. 4 | Strategy to make spinal cord straight for passive-vDISCO. a, Required materials: a plastic Pasteur pipette and some fine needles. The cyan arrowheads indicate the cutting points. **b**, The plastic Pasteur pipette is then longitudinally cut in half. **c**, Positioning of the needles to constrain the brain with the spinal cord inside one of the halves of the pipette. **d**, The whole setting is put into a container such as a 50 ml tube for passive-vDISCO protocol. Animal experiments followed European directive 2010/63/EU for animal research, reported according to the Animal Research: Reporting of In Vivo Experiments (ARRIVE) criteria, complied with the '3Rs' measure and were approved by the ethical review board of the government of Upper Bavaria (Regierung von Oberbayern, Munich, Germany) and conformed to institutional guidelines of Klinikum der Universität München/Ludwig Maximilian University of Munich). The severity of the procedure was low.

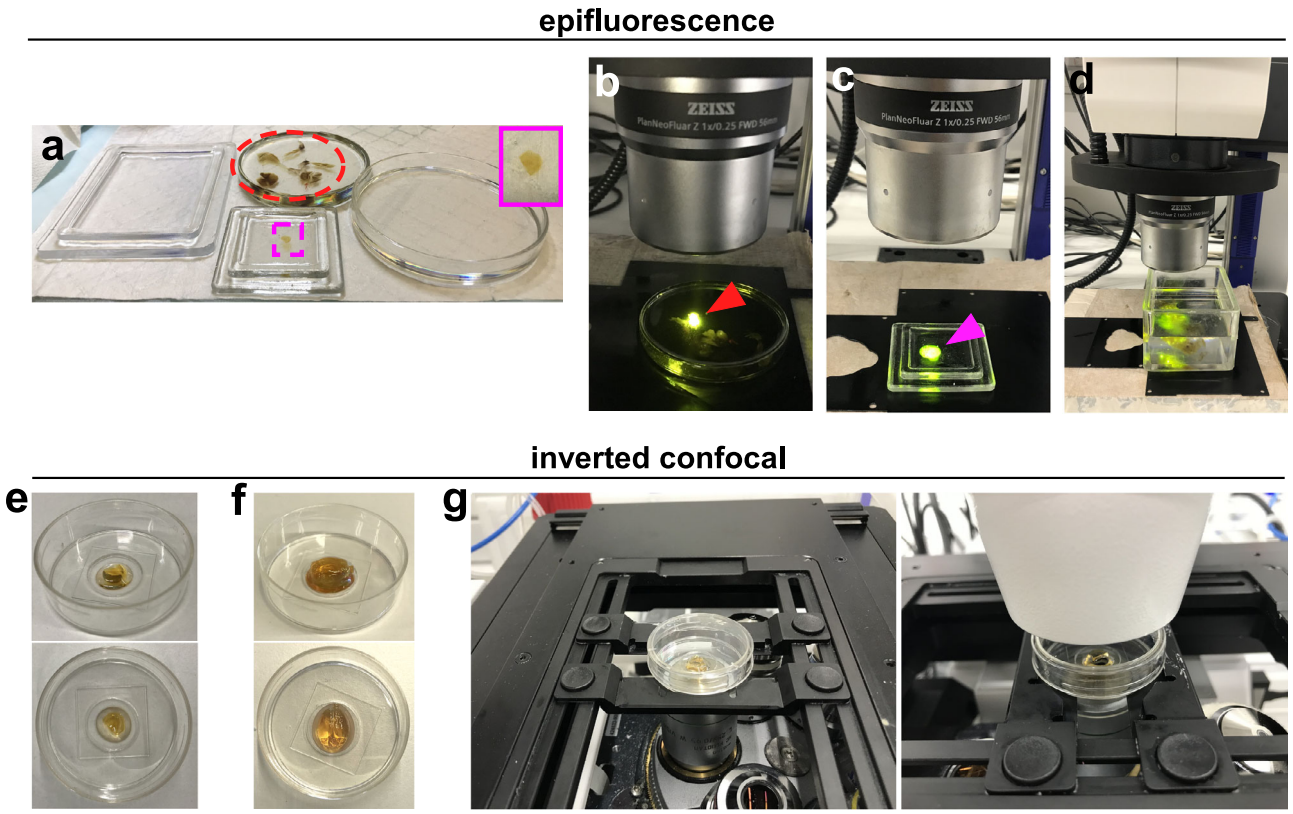

Extended Data Fig. 5 | Mounting of cleared samples for epifluorescence imaging and inverted confocal imaging. a–d, Mounting of different samples for AxioZoom epifluorescence imaging: different glass containers used to mount cleared organs (red dashed circle) and slices (magenta boxes) for AxioZoom epifluorescence imaging (**a**); epifluorescence imaging of dissected organs (red arrowhead) and slices (magenta arrowhead) with the AxioZoom microscope (**b** and **c**); epifluorescence imaging of the whole body with the AxioZoom microscope (**d**). **e–g**, Mounting of different samples for inverted confocal microscope imaging: a slice (**e**) and a whole brain (**f**) are placed onto a glass-bottom dish, then the dish with the lid is positioned onto the stage of the microscope (**g**). Animal experiments followed European directive 2010/63/EU for animal research, reported according to the Animal Research: Reporting of In Vivo Experiments (ARRIVE) criteria, complied with the '3Rs' measure and were approved by the ethical review board of the government of Upper Bavaria (Regierung von Oberbayern, Munich, Germany) and conformed to institutional guidelines of Klinikum der Universität München/Ludwig Maximilian University of Munich). The severity of the procedure was low.

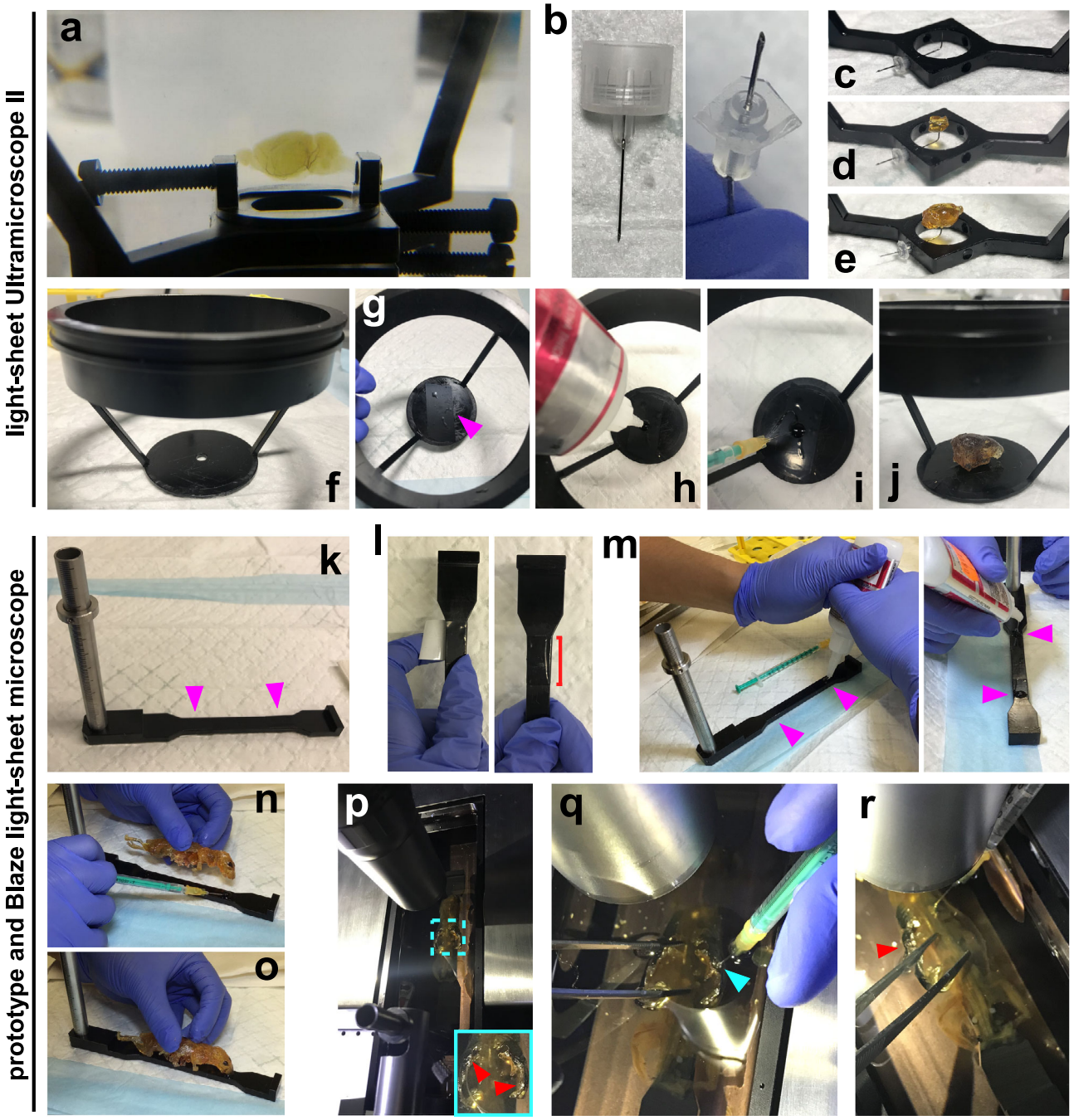

Extended Data Fig. 6 | Mounting of cleared samples for light-sheet imaging. a–j, Various strategies to mount different samples for LaVision-Miltenyi light-sheet Ultramicroscope II imaging. A whole brain is mounted using the screw system provided by the microscope supplier (**a**); a slice (**d**) and a whole brain (**e**) are mounted using Micro-Fine Ultra needles (**b**) attached to the sample holder (**c–e**). To mount a whole head using a flat sample holder (**f**), a piece of black tape is stuck to the flat surface (**g**, magenta arrowhead), then by adding super glue (**h**) and accelerator (**i**) the head is stabilized onto the tape (**j**). **k–o**, Mounting of a whole-body sample for light-sheet imaging using the Blaze microscope: two pieces of black tape are sticked onto the mounting region of the samples holder (**k** and **l**, magenta arrowheads), superglue is applied onto the black tapes (**m**, magenta arrowheads), accelerator is injected into the superglue (**n**) and the animal is positioned onto the sample holder at the level of the tapes (**o**). **p–r**, Strategy to remove air bubbles (**p** and **r**, red arrowheads) from the samples (e.g., a whole body) by inserting a fine needle into the bubble (**q**, cyan arrowhead) and sucking the bubble out with the syringe (**r**). Animal experiments followed European directive 2010/63/EU for animal research, reported according to the Animal Research: Reporting of In Vivo Experiments (ARRIVE) criteria, complied with the '3Rs' measure and were approved by the ethical review board of the government of Upper Bavaria (Regierung von Oberbayern, Munich, Germany) and conformed to institutional guidelines of Klinikum der Universität München/Ludwig Maximilian University of Munich). The severity of the procedure was low.

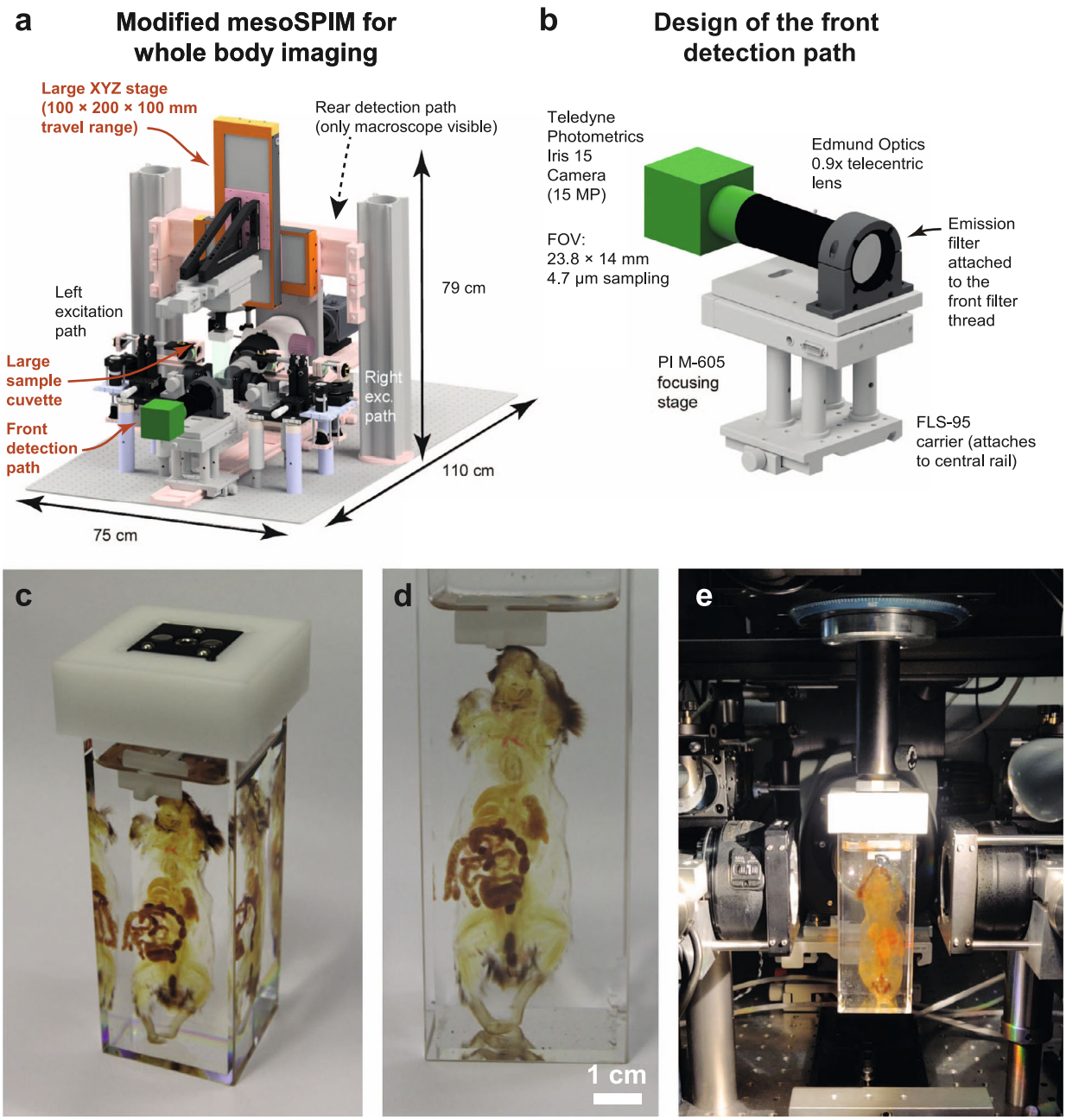

Extended Data Fig. 7 | Whole-body imaging with a mesoSPIM: setup modifications and sample handling. a, Overview of the modified mesoSPIM setup: an existing mesoSPIM was modified by replacing the sample *XYZ* translation stages with stages with larger travel range and by adding a second detection path in the front of the setup. **b**, Design of the modified detection path with a telecentric detection lens with fixed magnification and a camera with high pixel count. **c**, The sample was mounted in a custom 40 × 40 × 120 mm^3 quartz cuvette. The cuvette was closed with a custom lid that includes a kinematic mount with magnets that attach to the *XYZ* stages. **d**, To stabilize the sample inside the cuvette, a 3D-printed crossbar with 40 mm length was inserted above the sample and gently pressed down. **e**, View of the sample between the mesoSPIM excitation lenses before the front detection path was inserted. Animal experiments followed European directive 2010/63/EU for animal research, reported according to the Animal Research: Reporting of In Vivo Experiments (ARRIVE) criteria, complied with the '3Rs' measure and were approved by the ethical review board of the government of Upper Bavaria (Regierung von Oberbayern, Munich, Germany) and conformed to institutional guidelines of Klinikum der Universität München/Ludwig Maximilian University of Munich). The severity of the procedure was low.

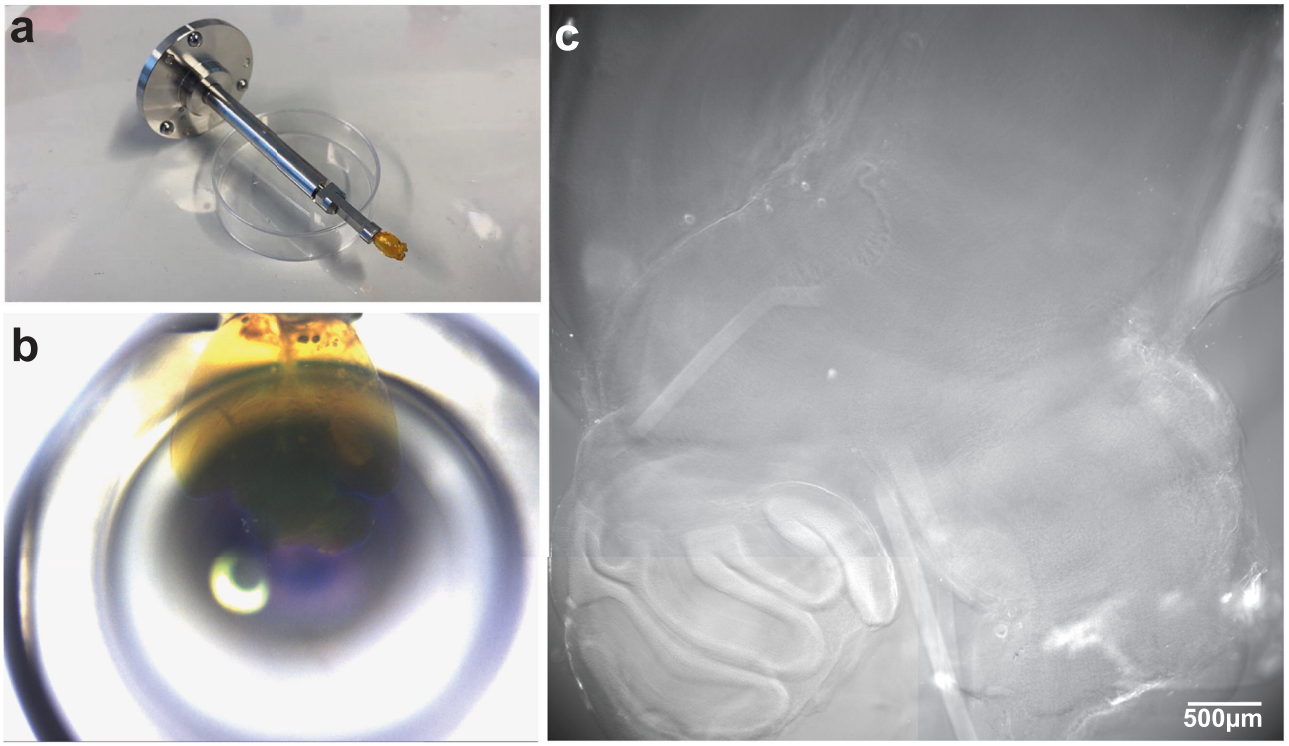

Extended Data Fig. 8 | Whole-brain imaging with Zeiss Lightsheet Z.1. a, The cleared brain sample is glued to the Lightsheet Z.1 rotatable sample holder. **b**, After mounting the sample holder into the microscope and inserting the imaging chamber containing the clearing solution, the sample is positioned in front of the detection objective. The right position in *X*, *Y*, *Z* and the rotation angle are monitored via the door camera of the microscope. **c**, The focus plane is adjusted using Near-IR pseudo-bright-field illumination. Animal experiments followed European directive 2010/63/EU for animal research, reported according to the Animal Research: Reporting of In Vivo Experiments (ARRIVE) criteria, complied with the '3Rs' measure and were approved by the ethical review board of the government of Upper Bavaria (Regierung von Oberbayern, Munich, Germany) and conformed to institutional guidelines of Klinikum der Universität München/Ludwig Maximilian University of Munich). The severity of the procedure was low.

nature portfolio

Corresponding author(s): Ali Erturk

Last updated by author(s): 2022-10-18

Reporting Summary

Nature Portfolio wishes to improve the reproducibility of the work that we publish. This form provides structure for consistency and transparency in reporting. For further information on Nature Portfolio policies, see our Editorial Policies and the Editorial Policy Checklist.

Statistics

For all statistical analyses, confirm that the following items are present in the figure legend, table legend, main text, or Methods section.

n/a	Confirmed	
X	☐	The exact sample size (*n*) for each experimental group/condition, given as a discrete number and unit of measurement
X	☐	A statement on whether measurements were taken from distinct samples or whether the same sample was measured repeatedly
X	☐	The statistical test(s) used AND whether they are one- or two-sided *Only common tests should be described solely by name; describe more complex techniques in the Methods section.*
X	☐	A description of all covariates tested
X	☐	A description of any assumptions or corrections, such as tests of normality and adjustment for multiple comparisons
X	☐	A full description of the statistical parameters including central tendency (e.g. means) or other basic estimates (e.g. regression coefficient) AND variation (e.g. standard deviation) or associated estimates of uncertainty (e.g. confidence intervals)
X	☐	For null hypothesis testing, the test statistic (e.g. *F*, *t*, *r*) with confidence intervals, effect sizes, degrees of freedom and *P* value noted *Give P values as exact values whenever suitable.*
X	☐	For Bayesian analysis, information on the choice of priors and Markov chain Monte Carlo settings
X	☐	For hierarchical and complex designs, identification of the appropriate level for tests and full reporting of outcomes
X	☐	Estimates of effect sizes (e.g. Cohen's *d*, Pearson's *r*), indicating how they were calculated

Our web collection on statistics for biologists contains articles on many of the points above.

Software and code

Policy information about availability of computer code

Data collection	*Code and software versions and descriptions used to collect the data in this study are listed in the section "Data processing and analysis tools/software" of the article*
Data analysis	*Code and software versions and descriptions used to analyze the data in this study are listed in the section "Data processing and analysis tools/software" of the article.*

For manuscripts utilizing custom algorithms or software that are central to the research but not yet described in published literature, software must be made available to editors and reviewers. We strongly encourage code deposition in a community repository (e.g. GitHub). See the Nature Portfolio guidelines for submitting code & software for further information.

Data

Policy information about availability of data

All manuscripts must include a data availability statement. This statement should provide the following information, where applicable:

- Accession codes, unique identifiers, or web links for publicly available datasets
- A description of any restrictions on data availability
- For clinical datasets or third party data, please ensure that the statement adheres to our policy

The data shown in this study including all the raw imaging scans are available from the corresponding author upon request.

Field-specific reporting

Please select the one below that is the best fit for your research. If you are not sure, read the appropriate sections before making your selection.

☒ Life sciences ☐ Behavioural & social sciences ☐ Ecological, evolutionary & environmental sciences

For a reference copy of the document with all sections, see nature.com/documents/nr-reporting-summary-flat.pdf

Life sciences study design

All studies must disclose on these points even when the disclosure is negative.

Sample size	*not applicable*
Data exclusions	*Animals that were negative for the expression of the fluorescent proteins after genotyping were excluded from the study.*
Replication	*The data shown in the study which are obtained by the described protocol were replicated at least 3 times and by at least 3 different operators.*
Randomization	*not applicable*
Blinding	*not applicable*

Behavioural & social sciences study design

All studies must disclose on these points even when the disclosure is negative.

Study description	
Research sample	
Sampling strategy	
Data collection	
Timing	
Data exclusions	
Non-participation	
Randomization	

Ecological, evolutionary & environmental sciences study design

All studies must disclose on these points even when the disclosure is negative.

Study description	
Research sample	

Research sample	
Sampling strategy	
Data collection	
Timing and spatial scale	
Data exclusions	
Reproducibility	
Randomization	
Blinding	

Did the study involve field work? ☐ Yes ☐ No

Field work, collection and transport

Field conditions	
Location	
Access & import/export	
Disturbance	

Reporting for specific materials, systems and methods

We require information from authors about some types of materials, experimental systems and methods used in many studies. Here, indicate whether each material, system or method listed is relevant to your study. If you are not sure if a list item applies to your research, read the appropriate section before selecting a response.

Materials & experimental systems

n/a	Involved in the study
☐	☒ Antibodies
☒	☐ Eukaryotic cell lines
☒	☐ Palaeontology and archaeology
☐	☒ Animals and other organisms
☒	☐ Human research participants
☒	☐ Clinical data
☒	☐ Dual use research of concern

Methods

n/a	Involved in the study
☒	☐ ChIP-seq
☒	☐ Flow cytometry
☒	☐ MRI-based neuroimaging

Antibodies

Antibodies used	*All nanobodies used in this study are shown in Table 1 with their RRID that includes all relevant information. Used nanobodies are*
Validation	*tested at least 3 times and by 3 different operators. A protocol used to validate the nanobodies are described in Box 1 of the article.*

Eukaryotic cell lines

Policy information about cell lines

Cell line source(s)	

Authentication

Mycoplasma contamination

Commonly misidentified lines
(See ICLAC register)

Palaeontology and Archaeology

Specimen provenance

Specimen deposition

Dating methods

☐ Tick this box to confirm that the raw and calibrated dates are available in the paper or in Supplementary Information.

Ethics oversight

Note that full information on the approval of the study protocol must also be provided in the manuscript.

Animals and other organisms

Policy information about studies involving animals; ARRIVE guidelines recommended for reporting animal research

Laboratory animals

Young mixed gender mice of the following lines are used in this study:Thy1-GFPM37 (and Thy1-Y FPH), CX 3CR1GFPI+ (B6.129 P-Cx3cr1tm1LittlJ ; Jackson Laboratory strain code 00558 228), Prox1-EGFP (Tg(Prox1-EGFP)KY 221GsatIMmucd; Mutant Mouse Resource and Research Centers strain code 031006-UCD) and PDGFRb-EGFP (Mouse Genome Informatics strain code 4847 307), C57 BLI 6 mouse transplanted with murine syngeneic R254 pancreatic cancer cells expressing eGFP for 38 days, an adult Emx1-Cre x RΦ GT. mice64 ,65 inj ected with EnvA-pseudotyped G-deleted rabies virus expressing GFP (SADB19 66) in the neocortex.

Wild animals

This study does not involve wild animals

Field-collected samples

This study does not involve Field-collected samples

Ethics oversight

Animal experiments followed European directive 2010I63IEU for animal research and were approved by the Institutional Animal Care and Use Committees (IACUC) of Technische Universität München and the ethical review board of the government of Upper Bavaria (Regierung von Oberbayern, Munich, Germany) and UK Home office. Experiments were conformed to Institutional guidelines in Klinikum der Universität München/Ludwig Maximilian University of Munich).

Note that full information on the approval of the study protocol must also be provided in the manuscript.

Human research participants

Population characteristics

Policy information about studies involving human research participants

Recruitment

Ethics oversight

Note that full information on the approval of the study protocol must also be provided in the manuscript.

Clinical data

Policy information about clinical studies

All manuscripts should comply with the ICMJE guidelines for publication of clinical research and a completed CONSORT checklist must be included with all submissions.

Clinical trial registration

Study protocol

Data collection

Outcomes

Dual use research of concern

Policy information about dual use research of concern

Hazards

Could the accidental, deliberate or reckless misuse of agents or technologies generated in the work, or the application of information presented in the manuscript, pose a threat to:

No	Yes	
[x]	[ ]	Public health
[x]	[ ]	National security
[x]	[ ]	Crops and/or livestock
[x]	[ ]	Ecosystems
[x]	[ ]	Any other significant area

Experiments of concern

Does the work involve any of these experiments of concern:

No	Yes	
[x]	[ ]	Demonstrate how to render a vaccine ineffective
[x]	[ ]	Confer resistance to therapeutically useful antibiotics or antiviral agents
[x]	[ ]	Enhance the virulence of a pathogen or render a nonpathogen virulent
[x]	[ ]	Increase transmissibility of a pathogen
[x]	[ ]	Alter the host range of a pathogen
[x]	[ ]	Enable evasion of diagnostic/detection modalities
[x]	[ ]	Enable the weaponization of a biological agent or toxin
[x]	[ ]	Any other potentially harmful combination of experiments and agents

ChIP-seq

Data deposition

[ ] Confirm that both raw and final processed data have been deposited in a public database such as GEO.

[ ] Confirm that you have deposited or provided access to graph files (e.g. BED files) for the called peaks.

Data access links
May remain private before publication.

Files in database submission

Genome browser session
(e.g. UCSC)

Methodology

Replicates

Sequencing depth

Antibodies

Peak calling parameters

Data quality

Software

Flow Cytometry

Plots

Confirm that:

☐ The axis labels state the marker and fluorochrome used (e.g. CD4-FITC).

☐ The axis scales are clearly visible. Include numbers along axes only for bottom left plot of group (a 'group' is an analysis of identical markers).

☐ All plots are contour plots with outliers or pseudocolor plots.

☐ A numerical value for number of cells or percentage (with statistics) is provided.

Methodology

Sample preparation

Instrument

Software

Cell population abundance

Gating strategy

☐ Tick this box to confirm that a figure exemplifying the gating strategy is provided in the Supplementary Information.

Magnetic resonance imaging

Experimental design

Design type

Design specifications

Behavioral performance measures

Acquisition

Imaging type(s)

Field strength

Sequence & imaging parameters

Area of acquisition

Diffusion MRI ☐ Used ☐ Not used

Preprocessing

Preprocessing software

Normalization

Normalization template

Noise and artifact removal

Volume censoring

Statistical modeling & inference

Model type and settings

Effect(s) tested

Specify type of analysis: ☐ Whole brain ☐ ROI-based ☐ Both

Statistic type for inference (See Eklund et al. 2016)

Correction

Models & analysis

n/a	Involved in the study
☐	☐ Functional and/or effective connectivity
☐	☐ Graph analysis
☐	☐ Multivariate modeling or predictive analysis

Functional and/or effective connectivity

Graph analysis

Multivariate modeling and predictive analysis

4. GENERAL DISCUSSION

In this thesis, I showed how to address systems biology questions. Apart from leading the path to uncovering the potential role of the skull bone marrow in brain diseases[1,115,116], we optimized and shared vDISCO whole mouse clearing and imaging protocol, which enabled many questions to be asked and answered previously out of the scope of technology. Currently, a modified version of vDISCO technology addresses TSPO-PET cellular sources in experimental glioblastoma[117] and bridges our imaging-based understanding to protein-level understanding, devising DISCO-MS (although only employing the 3DISCO part of the protocol)[19].

4.1. Main findings

Using several cutting-edge technologies such as scRNAseq, mass-spec based proteomics, tissue clearing and 3D imaging, and TSPO-PET imaging, we examined the mouse and human skull on the molecular and structural level and its diagnostic and therapeutic potential for brain diseases[1]. Our primary data revealed that the skull has a distinct molecular profile on the transcriptomic and proteomic levels, with neutrophil-related pathways driving the distinction. Additionally, we showed that the human skull is immensely interconnected with the meninges harboring numerous connections that allow immune cell trafficking between the two compartments. We achieved showing the connected nature of the skull to the dura by optimizing the already devised vDISCO protocol that we expanded and the SHANEL protocol[17] used for clearing human bones. Lastly, we demonstrated that the skull responds to various neurological disorders spatially and temporally in terms of its neuroinflammatory phenotype.

With our protocol paper, we attempted to reflect the protocol's flexibility for both whole-body level understanding and the protocol's effectiveness for tissue pieces and whole organs. We demonstrated various microscopes vDISCO is compatible with, depending on the nature of the tissue, to make the protocol accessible. We also showed how the whole-body lymphatic system can be visualized using Prox1-eGFP animals, how pericytes look on the whole brain level, and how virus tracing can be visualized on the whole brain level. These broad applications make vDISCO a powerful technique. Lastly, by combining vDISCO and SHANEL protocols, I developed an improved clearing protocol to perform both vDISCO boosting strategy and SHANEL antibody labeling. We used modified vDISCO and SHANEL protocol to address TSPO-PET cellular sources in experimental glioblastoma[117].

4.2. Key implications

4.2.1 Bone marrow cell composition in the skull differs from other bones in mice and humans

Our initial question was whether the skull's molecular landscape differed from other bone marrow. We aimed to answer this question on the transcriptomic and proteomic levels. Although our hypothesis was supported on both levels, we could not report specific genes or proteins that made the skull unique. However, our data suggested that skull neutrophils contributed to a distinct signature showing late-neutrophil phenotype with downregulated neutrophil degranulation pathways in both mice and humans. Our human proteomics and transcriptomics data analyses also suggested decreased mRNA processing. Although we found a very inflammatory milieu compared to other bones in naïve and after-stroke conditions on the transcriptomic level, we could not recapitulate this phenotype on the protein level.

Our results reveal several key details about the skull compared to other bones in its naïve state and after a brain injury. First, the fact that the focus of the manuscript was on immune cells might restrict our understanding of what makes the skull unique. Extracellular matrix and other cell types such as endothelial cells, fibroblasts, and stromal cells are recently shown to be involved in immune regulation, especially in brain immune regulation[118]. Moreover, the fact that gene-level and protein-level differences do not yield a vast difference can be observed for three reasons. First, perhaps all bone marrow depends on each other simultaneously to an extent, although no previous literature has specifically investigated different bone marrow reactions to a specific disease. Our results suggest that they do not vary so much. Second, different bone marrow may specialize in different tasks based on shape and size. The skull's role is not to provide an immune reservoir for the whole body but to closely monitor the brain's immunological state, hence keeping a lower mRNA processing phenotype and harboring inflammatory cells in case they are needed in the brain. The immune reservoir hypothesis is more plausible due to inherent structural differences of different bone marrow in the body, such as the proportion of compact vs. spongy bone or the ratio of yellow to red marrow[119]. Third, perhaps more considerable changes occur on the epigenome level or after protein modifications. It has been shown numerous times that epigenetics[120–122] and protein modifications[123,124] affect the homeostasis of bone or the progression of the disease. However, a comparison of how different bone marrow react to the same injury has been made. For example, recent research suggested skull is shaped via post-transcriptional regulation of a master bone gene called RUNX2 and concluded that single nucleotide polymorphisms within the skull-specific RUNX2 enhancers must be investigated in future studies. While underlining the role of epigenetics for

bones, unfortunately, the study did not include any other bones[125]. Moreover, some studies have shown epigenetic control of skull morphogenesis again in a limited manner that underlines the importance of epigenetics without providing a bigger picture[126]. It is also likely that all three options are on action partially without mutual exclusivity.

4.2.1.1 Unique aspects of human skull proteome

A striking result we have gathered is from our human proteomics data. In this dataset, we had 20 individuals from a significant age range with various causes of death. Comparing the skull, vertebra, and pelvis, we saw that regardless of the set of causes of death we exhibit in our dataset, the skull showed the most distinct proteome compared to the two other bones. Although we would have expected more similarity between the vertebra and the skull due to their proximity to CNS tissue, we saw that the vertebra was more similar to the pelvis than to the skull. Since the pelvis is also a flat bone-like skull, a similarity between the pelvis and skull could also be explained by this commonality. However, neither closeness to CNS tissue nor bone type seems to drive the overall proteomic signature in the human bone marrow. So far, one article has provided supporting evidence that CNS proximal bone marrow reacts to a CNS injury, spinal cord injury. However, no comparison to a non-CNS proximal bone in the disease setting was provided in the study[63]. Herrison et al., on the other hand, only provided a comparison between the skull and the femur and not the vertebra[11].

Hence, whether and how CNS proximal bones are affected by the brain remains to be addressed. We also detected unique proteins from each bone we sampled in the same dataset. These proteins included SYP, a small synaptic vesicle membrane protein[127], SYN3, a phosphoprotein associated with the cytoplasmic surface of synaptic vesicles[128], and SNAP25, a presynaptic plasma membrane protein which is involved in the regulation of neurotransmitter release[129]. We did not detect many unique proteins from the vertebra and pelvis, but we did detect over 100 unique proteins in the skull samples. As a result, we performed a pathway enrichment analysis and found many pathways related to pre-synapse. The unique proteins detected in the skull were striking because pre-synaptic sites are found in the brain, spinal cord, peripheral nerves, autonomic ganglia, and neuromuscular junctions at the end of axons[130]. They release neurotransmitters into the synaptic cleft, which is then picked up via postsynaptic neurons, relaying the nerve impulse. In neuromuscular junctions, motor neurons innervating the skeletal muscle allow muscle contraction via neurotransmitter release onto the synaptic cleft[131]. However, previous studies have not shown axons in the bone marrow. Therefore, detecting these proteins only in the skull allowed us to speculate another communication layer via the

peripheral nerves. Another potential explanation could be that there are no axons, but via the tightly connected nature of the skull with the meninges, perhaps some brain antigens are getting stuck in the bone marrow during waste clearance pathways via the CSF through meningeal lymphatic vessels. The potential exchange between the skull and the brain might also give brain-antigen privilege to the skull bone marrow niche. Another hypothesis we considered was that the immune cells in the skull may have engulfed brain antigens during potential waste clearance pathways again[132,133]. To understand whether the unique synaptic proteins found in the dataset are innately transcribed and translated from the immune cells, we sampled one human skull for scRNAseq and checked for the expression of unique synaptic markers we found in our proteomics dataset. Only six of the 256 unique synapse-relevant genes were detected in the scRNAseq dataset, expressed primarily on fibroblasts. It allowed us to rule out immune cells as the source of the synapse-related terms, meaning that brain antigens might be engulfed in the skull or the meninges and brought back to the skull, allowing antigen sampling. This hypothesis aligns well with the current literature on CSF-skull interaction[63,64]. Although future work is necessary to decipher the innervation landscape of the skull and how it differs from other bone marrow, the mechanism by which synaptic proteins end up in the skull, in addition to cytokines and immune cells, nervous system-related cells, and neurotransmitters, are also essential to examine further.

4.2.1.2 Human skull is highly connected with the meningeal layers through SMCs

Similar connections have been reported in the vertebra, as well as in the long bones[58,92]. The channels in the vertebra have not been studied elaborately. However, the connections in the long bones have been shown to participate in the neutrophil egression into the bloodstream, even providing more cells than the bloodstream[92]. In the case of the skull, neutrophil egression apart from the bloodstream might also be the case, yet, this would still make the skull relevant to the neuroimmune axis and not the bloodstream, as the cells that are trafficked out of the skull enter the dura mater, a central hub for brain's immune regulation. Moreover, the recent studies underlining CSF exchange in the skull connections also provide additional layers to how the skull communicates with the brain fluid much faster than any other immune reservoir[63,64].

Thus, due to the strategic location of the skull being so close to the brain, we aimed to identify if there were regional heterogeneity among channels. In this regard, we quantified the number of channels in three different brain regions and the diameter of the interface between the skull and the dura mater. In previous literature, human channel quantification has only been done once, where 60 channels from three patients have been counted with microCT[11]. Although the

quantification of 60 channels allowed the authors to quantify the diameter and the number of the channels, we now validated these findings in terms of diameter and expanded the spatial understanding by quantifying over 500 channels from seven post-mortem samples. One patient from our samples had Parkinson's disease before deceasing.

Interestingly, in the Parkinson's disease sample, we observed the highest number of channels in the parietal bone compared to the two other samples. The frontal bone of the same sample did not differ from other samples. It is hard to draw any solid conclusions from one sample. However, the high number of channels could suggest that patients with neurological deficits may exhibit more connections in certain skull regions, allowing further communication between the nervous and immune systems. If the number of channels increases upon a neurological insult, such as Parkinson's disease, in this case, that might also suggest bone remodeling after the disease. Literature suggests a critical connection between osteoporosis, a disorder of bone and mineral metabolism, often increasing patients' vulnerability to bone fractures[134–136]. Some studies also show the contrary for other neurological insults, demonstrating that a damaged brain contributes to bone healing[137]. Both aspects underline the undeniable connection between the skeletal and nervous systems, although skull-specificity or the exact influence a damaged brain has on SMC dynamics is far from being known. Moreover, current literature on when channels develop, whether their numbers are stable in humans, or whether they are dynamic structures that can form upon a neurological deficit is also nonexistent.

To start closing this gap, using tissue clearing, we could show that these connections do not stop at the dural interface but often cross the dura, opening up to the arachnoid granulation in the sub-dural space. CSF is known to be exposed to the meninges' dural layer, although the precise route and mechanism are unknown[138]. Therefore, these connections starting from the skull bone marrow transversing the dura and opening up to the sub-dural space, firstly provide an alternative explanation of CSF exposure to the dura and, secondly, also allows us to speculate that CSF exposure to skull bone marrow happens via the connections as shown in mice[63,64], and partially in humans[42]. The connection opening from the skull bone marrow transversing to the dura indeed underlines the strategic location of the skull and its potential privilege in sampling brain fluid faster than any other compartment in the body.

4.2.1.3 Structural detail of human SMCs

Upon examining the highly interconnected nature of the skull using tissue clearing, 3D imaging, and segmentation of the skull architecture, we aimed to characterize the anatomical structure of the connections to a greater extent. So far, no characterization in human channels has been made. In mice, these connections have been referred to as ossified structures and vascular channels that were positive for Osteosense and CD31[11]. Based on the present data on mice, we also utilized a vessel marker, lectin, to characterize these connections. We coupled lectin with either propidium iodide, which labels all cell nuclei, or a pan-myeloid marker, Lyz2, as the myeloid cell population was molecularly distinct in the skull compared to other bones based on our omics analysis. As a result, we observed several interesting phenomena. First was that Lyz2 labeling was very abundant in the bone marrow as expected and surrounding the channels. We expected Lyz2+ myeloid cells within the channel outside the blood vessel. In addition to seeing these cells outside of the blood vessel, we also observed these cells in the walls of connections surrounding the blood vessel. Observing the Lyz2+ cells on the connections surrounding the blood vessels meant that skull bone marrow harboring the immune cells is not confined to the marrow area per se but is distributed in the overall bone. This observation also aligns with our 2-photon skull live imaging experiments in mice, where we recorded the dynamic changes in regions of skull bone marrow after stroke. Over the time of imaging (72 hours), the LysM+ cell (pan-myeloid) pools constantly moved and were relocated around the blood vessels. The presence, amount, and dynamics of Lyz2+ cells suggest that skull bone marrow is a highly dynamic site.

Second, we observed these connections not only on the dural interface but all connections connecting the skull bone marrow, with the vessels inside to be surrounded by hollow tubes in our light sheet images. These hollow tubes often had immune cells but no clear structure. To further explore the structural detail of the skull bone marrow, we performed scanning electron microscopy on a channel at the dura-skull interface. sEM allowed us to visualize the lipid layer surrounding the blood vessel within a channel. The lipid layer surrounding the blood vessel was perhaps missed due to the limitations of the techniques used[11,58,59,64]. Both tissue clearing and immunohistochemistry rely on detergents and other solvents that dissolve lipids. Hence, these channels were deprived of these molecules and were missed. The presence of fat might serve as an energy source for the traveling immune cells along the skull connections. For example, a similar mechanism is known for sperm where seminal plasma, the fluid portion of semen, is composed of high concentrations of fructose, which serves as an energy source for sperm and helps with motility [139]. It is already known that fat is used as an energy source for immune

cells[140–142]. The reserve in the skull bone marrow might therefore be critical to immune cell trafficking outside the bloodstream.

It is noteworthy that it is also known that fat percentage increases in bone marrow over age[143], and here we were limited to aged deceased patients. For example, only one group reported EM images from mouse channels, where the lipids were not observable[11,64]. The presence of lipids within the SMCs in humans and mice could be an interspecies difference and affected during processing. Thus, the precise structure of the channels, therefore, might be different for old and young people, which may have different implications. For example, the involvement of the skull in waste clearance might be affected by age via the lipids deposited in the channels. Therefore, it would be critical to increase the sample size for EM from ranging ages and perhaps to perform lipidomics to understand the constituents of the lipid layer. At the current state, it is too premature to make any conclusions. Additionally, as the scope of this research was the skull, it is unclear how these findings translate to other bones. It would be interesting to examine the presence of this lipid layer in other bones with channels, such as the vertebra and the tibia.

In addition to the lipids discovered within the channels, we could also see the immune cells within the extracellular matrix, as observed in our tissue clearing and light sheet experiments. We also observed fibroblast lining, which we confirmed with immunohistochemistry using PDGFRB+ as a marker. Fibroblasts are critical structural cells that are known to be involved in the immune response: they are also known as antigen-presenting cells[144]. Finding fibroblasts in the region where we expect CSF flow suggests that brain antigen sampling starts at the beginning of these channels. It would be interesting to utilize different fibroblast markers to more precisely define their role and identify whether these fibroblasts are perhaps different from other fibroblasts, such as dural fibroblasts. The previously mentioned interconnected structure of the dura and the skull, in addition to the dura's known involvement in brain immunity, thus makes the skull an active player in the neuroimmune response[40].

4.2.1.4 Optimized pipeline for bone processing and clearing

In order to achieve clearing the notoriously hard human bone, we significantly optimized the tissue clearing protocol and, more specifically, the decalcification process for the human skull, human skull+dura, and human skull+dura+brain samples. We utilized different decalcification treatments depending on the sample type. For example, skull pieces were kept at 37 degrees on a shaker for faster decalcification, whereas the samples connected to the brain were strictly decalcified at 4 degrees without any movement. Some samples were not decalcified and cut using an electric saw to overrule any side effect clearing that might introduce the visualization

of the SMCs. Moreover, the protocol timing was adjusted based on the sample size. We are enthusiastic to have developed an extended protocol that enables the effective clearing of complex tissue, such as skull-dura-brain, encompassing different tissue types and overcoming the challenges posed by human bone tissue.

4.2.1.5 Skull TSPO-PET imaging: A proof-of-concept for mirroring brain inflammation

Setting up the transcriptomic and proteomic profile of the skull and characterizing its highly interconnected nature to other neuroimmune players, we were curious if we could capture the skull's reaction to a neurological disorder. Since neuroinflammation is the brain's typical reaction after a neurological insult, we found TSPO-PET imaging an excellent candidate to reflect the potential skull response to a neurological disorder[145]. Quantification of skull TSPO-PET signal in stroke, AD, 4RT, PPMS, and RRMS patients, we found spatially distinct neuroinflammatory phenotype. Following up this phenotype longitudinally in stroke and AD patients, we observed that stroke inflammation resolves over time, whereas AD increases, just as it does in the brain. The longitudinal phenotype was a significant finding because it not only showed that we could detect brain response through skull response, but it also meant that we expanded the research into clinical aspects. Although it is too early to make strong claims, upon extensive research, we may be able to use the skull as a new site to monitor the progression of brain diseases and judge how well a therapy works. Using the skull as a new site to monitor brain disease progression depends on devising further markers that reflect neuroinflammation, which could be detected in non-invasive, accessible methods. Lastly, although diagnosis and therapy may be an option in the future, these two aspects require another set of extensive studies exploring various aspects of the skull response.

4.2.2 vDISCO whole-body immunolabeling, clearing, and imaging pipeline

On the other hand, our protocol paper presented as the second study in this thesis elaborately describes how to stain, clear, and image an entire mouse while leaving all systems intact. Our protocol paper gives tremendous power to systems biology research, circumventing the significant challenges in the field, such as dealing with a variety of tissues or the necessity to section and hence alter the innate state of the tissue. Our findings here provide a solid ground to tackle any systems biology question ranging from investigating a particular cell type, cellular response, conditional changes, or an entire system using transgenic mouse models, cell tracking using viral tracers, or simply observing structural changes upon a disease model or a physiological process. We showcase examples for the abovementioned applications by visualizing the entire mouse lymphatic system, whole brain pericyte labeling, and virus tracing

in the mouse brain. Another great advantage of the vDISCO optical tissue clearing technology is that it can generate or validate a particular proven hypothesis, again underlining its versatility. Additionally, we demonstrate different microscopes that can be utilized for cleared samples, expanding their usability and providing solutions for potential errors in the protocol.

4.3. Limitations

4.3.1 Technical limitations

As with any study, there are inherent limitations that should be acknowledged. The two papers presented in this thesis are no exception. I want to begin with methodological limitations, specifically tissue-clearing method-based ones. Firstly, while the vDISCO protocol is a robust technique, it is designed for fixed samples, making longitudinal studies within the same sample unfeasible. Consequently, assessing *in vivo* phenotypes becomes impossible, thereby restricting the scope of functional conclusions that can be drawn. Additional functional assays may be required to overcome the fixed sample limitation to provide conclusive mechanistic results. A potential solution to the fixed sample problem may be to achieve tissue clearing *in vivo*. However, *in vivo*, tissue clearing remains challenging due to factors such as tissue pigmentation, the presence of blood, or the need for naturally transparent animals. Even with transparent animals, their physiology may differ from non-transparent animals, limiting the generalizability of conclusions drawn from specific model organisms.

Efforts have been made to address these limitations, such as the attempts to develop *in vivo* tissue clearing techniques, including the tissue clearing of the skull using bio-compatible reagents, enabling skull, meninges, and deeper brain imaging in mice, as well as tissue clearing of the skin for monitoring blood flow in specific regions[146–148]. However, it should be noted that these advancements are still in progress and are not free of their limitations.

Another limitation of the vDISCO technique is the lack of molecular insight obtained from processed specimens. To overcome the lack of molecular insight one can get using vDISCO, we devised a new protocol called DISCO-MS to extract proteins and proteomic measurements on cleared tissues[19]. However, extracting RNA-level information from cleared tissue remains a significant milestone yet to be achieved.

The limitations also extend to the application of vDISCO in the first study. Since the DISCO-MS pipeline was unavailable during the generation of clearing data in the first study, additional experiments were required to generate proteomics samples for mice and humans. Similarly, the

inability to perform *in vivo* examination of cleared samples necessitated the use of 2-photon live imaging to assess the dynamic reaction of the skull to brain injuries in mice. The ability to assess deep-tissue dynamics, such as cerebrospinal fluid (CSF) flow, would provide valuable insights into skull-brain communication. However, assessing the deep-tissue dynamics was not feasible with the current state of technology. A 3-photon microscope might have been able to address depth limitations.

In addition to the limitations associated with tissue clearing, other technologies employed in the first study have their limitations that should be considered when interpreting the results. While providing extensive data, single-cell technologies often have limitations regarding sample size due to cost and practical constraints. Therefore, they serve as valuable tools for hypothesis generation or validation, but they alone may not be sufficient to answer a scientific question.

4.3.2 Biological limitations

Additionally, from a biological perspective, these limitations in clearing protocols may have influenced the results obtained from human SMCs. For example, we are examining the entire skull and quantifying all channels in the three specified regions and other regions, such as the occipital region or the skull base. However, even if clearing an entire skull, in theory, could be performed, imaging the entire skull would not be possible due to the size of the imaging chamber. Furthermore, including different groups, such as post-mortem samples with neurological disorders versus non-neurological disorders cohorts, would enable the assessment of potential differences in the quantity or regionality of these channels. It is important to note that these limitations are inherent to working with human tissue rather than being solely limitations of tissue-clearing techniques.

Additionally, the contribution of immune cells originating from the skull versus those from the periphery is still poorly understood. Conducting KikGR photoconversion experiments on a larger sample size, not limited to the skull but also including other distant bones like the femur, could help determine the proportion of skull-specific contributions.

Furthermore, as RNA is relatively more dynamic than proteins, various experimental parameters, such as different settings, times of the day, or even the scientist processing the data, may influence the results[107]. Hence, orthogonal validations are essential for this dataset which we could provide to a certain extent. Furthermore, proteomic analysis is based on relative

abundance, which can introduce variability depending on the specific tissue being processed. Therefore, while omics protocols, including RNA and protein analysis, allow us to paint a comprehensive picture of samples and assess their molecular phenotypes, it is crucial to interpret the results while considering these limitations.

Another notable limitation of the first study is its focus on immune cells. Recent studies have highlighted the significance of structural cells, such as fibroblasts and stromal cells, in immune regulation[118]. Thus, it is critical to examine immune cells within the bone marrow and explore other cell types present in the bone to gain a more comprehensive understanding of the immune system.

Lastly, it is crucial to recognize that the sample size for the TSPO-PET study should be expanded to enhance the generalizability of the reported skull TSPO tracer uptake. Acknowledging that the skull imaging approach may benefit from exploring different tracers in future studies is essential. Translating the skull imaging approach into clinical settings will require numerous prior investigations. It will also be necessary to examine bone-specific and sex-specific uptake patterns of skull TSPO tracers in various neurological diseases. While this study included several neurological disorders, it is imperative to include neurodevelopmental and neuropsychiatric diseases and brain tumors in future research endeavors. By broadening the scope of the study to encompass a broader range of conditions, a more comprehensive understanding of the skull TSPO tracer uptake can be achieved, facilitating its potential clinical applications.

In conclusion, it is essential to recognize the limitations inherent in the methodologies and approaches utilized in these studies. The inability to perform longitudinal studies on fixed samples, the challenge of assessing *in vivo* phenotypes, and the ongoing developments *in vivo* tissue clearing techniques are significant considerations. Additionally, the lack of molecular insight from processed specimens and the limitations associated with single-cell technologies and proteomic analysis should be considered. Finally, expanding the scope beyond immune cells to include other cell types within the bone can provide a more holistic view of the immune system's functioning.

Acknowledging these limitations and their potential impact on the results allows for a more comprehensive and accurate interpretation of the findings presented in this thesis.

4.4. Future directions

4.4.1. Leveraging Skull in monitoring brain pathologies in Humans

This study was designed to provide our foundation on skull biology, emphasizing how it is connected to the brain and the brain's immune regulation. As a result of many datasets and approaches, we enabled the generation of many new hypotheses and functional study opportunities. On the short-term questions such as whether the skull is more innervated, whether its epigenome is distinct compared to other bone marrow, whether it is metabolically less active, and whether other cell types in the skull have functional relevance to the brain's immune regulation may be addressed with a new set of experiments.

We should also decipher whether skull cells are damaging or healing by setting up experiments such as irradiation of the skull in various neurological disorders and assessing whether the disease worsens. Determining whether the cells are healing or damaging will allow future research to be shaped: damaging cells could be inhibited, or healing cells may be targeted to be enhanced using genetic engineering tools. Furthermore, the interesting population of neutrophils, and some relevant genes, such as *Nr4a1*, can be tested for functional studies. These may provide essential drug targets to lessen neuroinflammation, for example.

It would also be interesting to assess the distribution and the numbers of SMCs in a cohort with neurological disorders. A hypothesis could be that more channels form in patients with brain inflammation over time; blocking these channels may resolve the inflammation. It might also be that channels are getting looser or leakier upon aging, causing potentially pro-inflammatory immune cell flow into the dura. These experiments may provide key findings when assessing routes of immune cell trafficking after a particular neurological insult and perhaps even when considering designing drug targets, i.e., aiming to block the channels to perturb skull cell flow into the parenchyma. Integration of several other omics approaches, such as metabolomics and epigenomics, both in mice and humans, may also provide new insights into new biomarkers for drug design. However, integrating other omics approaches may be challenging for humans.

Lastly, as a long-term outlook, studies must be designed to use the skull to read out brain health. Dissecting brain health using skull readouts requires further research on biomarkers reflecting brain health change status in the skull. Then, these biomarkers must be used as a read-out of newly-devised hand-held non-invasive imaging tools. The multi-omic approaches would greatly help to improve this aspect of skull-brain axis research.

Overall, the research presented in this thesis lays the foundation for future investigations into the intricate connections between the skull, meninges, and central nervous system. By further exploring these areas, we can gain deeper insights into the neuroimmune axis, develop new therapeutic strategies, and advance our understanding of brain health and neurological disorders.

4.4.2. Using vDISCO clearing technology to assess whole-body pathology response in mice

The research on using vDISCO clearing technology to assess whole-body pathology response in mice also opens up several exciting avenues for future exploration. Since vDISCO is a methodology, it can easily be applied to various biological systems. Diseases that affect the whole body can be precisely assessed with our protocol. Some examples are metastasized cancer, obesity, systemic sclerosis, and viral infections. Upon establishing imaging-based assessments of systemic disorders, we can combine them with proteomic analysis, bridging the images to specific molecules. The bridge between molecular and spatial understanding is essential in generating new drug targets that are tissue specific.

By pursuing these future directions, researchers can continue to expand our understanding of systems biology, uncover the complex interactions between different organs and tissues, and advance the development of innovative diagnostic and therapeutic approaches for systemic diseases.

4.5. Conclusion

This thesis presents a wealth of groundbreaking information, employing a systems biology approach in both studies. The first study delves into biological discoveries using diverse modalities, including scRNAseq, mass-spectrometry-based proteomics, TSPO-PET imaging, tissue clearing, and LSFM. These modalities explored the skull's distinctive role in the body's overall communication with the brain.

As a result of using cutting mentioned above edge technologies, our findings reveal that the skull possesses a unique molecular profile and powerfully connects with the brain's immunomodulatory sites. Moreover, our study demonstrates parallel patterns of skull-brain inflammation in various neurological disorders. Consequently, we propose that further research is imperative to utilize the skull to enhance our understanding of the brain's immune status.

In the first study, we employ and expand upon the vDISCO applications, using this protocol to quantify skull cell intensity in whole mouse heads. The second study comprehensively describes how the vDISCO protocol can be applied and adapted for various other applications.

To conclude, I aimed to decipher novel biological insights in both studies by harnessing cutting-edge technologies. I genuinely hope these two studies will serve as valuable resources for fellow researchers, facilitating the expansion of their investigations and broadening our understanding of the intricacies of the remarkable and closely interconnected neuroimmune system.

The Craniology, also called Phrenology, theorizes that the skull reveals human character, and capability may not be so wacky after all[149,150]. Although the skull might not exactly reveal personality traits, the presented research demonstrates the benefits of focusing on the skull to understand brain health status[1].

5. REFERENCES OF INTRODUCTION AND GENERAL DISCUSSION

1. Kolabas, Z.I., Kuemmerle, L.B., Perneczky, R., Förstera, B., Ulukaya, S., Ali, M., Kapoor, S., Bartos, L.M., Büttner, M., Caliskan, O.S., et al. (2023). Distinct molecular profiles of skull bone marrow in health and neurological disorders. Cell *186*, 3706-3725.e29. 10.1016/j.cell.2023.07.009.

2. Cai, R., Kolabas, Z.I., Pan, C., Mai, H., Zhao, S., Kaltenecker, D., Voigt, F.F., Molbay, M., Ohn, T., Vincke, C., et al. (2023). Whole-mouse clearing and imaging at the cellular level with vDISCO. Nat. Protoc., 1–55. 10.1038/s41596-022-00788-2.

3. Benakis, C., Brea, D., Caballero, S., Faraco, G., Moore, J., Murphy, M., Sita, G., Racchumi, G., Ling, L., Pamer, E.G., et al. (2016). Commensal microbiota affects ischemic stroke outcome by regulating intestinal gammadelta T cells. Nat Med *22*, 516–523. 10.1038/nm.4068.

4. Shi, K., Li, H., Chang, T., He, W., Kong, Y., Qi, C., Li, R., Huang, H., Zhu, Z., Zheng, P., et al. (2022). Bone marrow hematopoiesis drives multiple sclerosis progression. Cell *185*, 2234-2247.e17. 10.1016/j.cell.2022.05.020.

5. Shi, S.X., Shi, K., and Liu, Q. (2021). Brain injury instructs bone marrow cellular lineage destination to reduce neuroinflammation. Sci. Transl. Med. *13*, eabc7029. 10.1126/scitranslmed.abc7029.

6. Carson, M.J., Doose, J.M., Melchior, B., Schmid, C.D., and Ploix, C.C. (2006). CNS immune privilege: hiding in plain sight. Immunol. Rev. *213*, 48–65. 10.1111/j.1600-065X.2006.00441.x.

7. Luissint, A.-C., Artus, C., Glacial, F., Ganeshamoorthy, K., and Couraud, P.-O. (2012). Tight junctions at the blood brain barrier: physiological architecture and disease-associated dysregulation. Fluids Barriers CNS *9*, 23. 10.1186/2045-8118-9-23.

8. Kratzer, I., Ek, J., and Stolp, H. (2020). The molecular anatomy and functions of the choroid plexus in healthy and diseased brain. Biochim. Biophys. Acta BBA - Biomembr. *1862*, 183430. 10.1016/j.bbamem.2020.183430.

9. Decimo, I., Fumagalli, G., Berton, V., Krampera, M., and Bifari, F. (2012). Meninges: from protective membrane to stem cell niche. Am. J. Stem Cells *1*, 92–105.

10. Cai, R., Pan, C., Ghasemigharagoz, A., Todorov, M.I., Förstera, B., Zhao, S., Bhatia, H.S., Parra-Damas, A., Mrowka, L., Theodorou, D., et al. (2019). Panoptic imaging of transparent mice reveals whole-body neuronal projections and skull–meninges connections. Nat. Neurosci. *22*, 317–327. 10.1038/s41593-018-0301-3.

11. Herisson, F., Frodermann, V., Courties, G., Rohde, D., Sun, Y., Vandoorne, K., Wojtkiewicz, G.R., Masson, G.S., Vinegoni, C., Kim, J., et al. (2018). Direct vascular channels connect skull bone marrow and the brain surface enabling myeloid cell migration. Nat. Neurosci. *21*, 1209–1217. 10.1038/s41593-018-0213-2.

12. Themes, U.F.O. (2022). Imaging Modalities for Central Nervous System Tumors. Radiol. Key. https://radiologykey.com/imaging-modalities-for-central-nervous-system-tumors/.

13. Dodt, H.-U., Leischner, U., Schierloh, A., Jährling, N., Mauch, C.P., Deininger, K., Deussing, J.M., Eder, M., Zieglgänsberger, W., and Becker, K. (2007). Ultramicroscopy: three-dimensional visualization of neuronal networks in the whole mouse brain. Nat. Methods *4*, 331–336. 10.1038/nmeth1036.

14. Kubota, S.I., Takahashi, K., Nishida, J., Morishita, Y., Ehata, S., Tainaka, K., Miyazono, K., and Ueda, H.R. (2017). Whole-Body Profiling of Cancer Metastasis with Single-Cell Resolution. Cell Rep. *20*, 236–250. 10.1016/j.celrep.2017.06.010.

15. Pan, C., Schoppe, O., Parra-Damas, A., Cai, R., Todorov, M.I., Gondi, G., von Neubeck, B., Böğürcü-Seidel, N., Seidel, S., Sleiman, K., et al. (2019). Deep Learning Reveals Cancer Metastasis and Therapeutic Antibody Targeting in the Entire Body. Cell *179*, 1661-1676.e19. 10.1016/j.cell.2019.11.013.

16. Molbay, M., Kolabas, Z.I., Todorov, M.I., Ohn, T.-L., and Ertürk, A. (2021). A guidebook for DISCO tissue clearing. Mol. Syst. Biol. *17*, e9807. 10.15252/msb.20209807.

17. Zhao, S., Todorov, M.I., Cai, R., -Maskari, R.A., Steinke, H., Kemter, E., Mai, H., Rong, Z., Warmer, M., Stanic, K., et al. (2020). Cellular and Molecular Probing of Intact Human Organs. Cell *180*, 796-812.e19. 10.1016/j.cell.2020.01.030.

18. Todorov, M.I., Paetzold, J.C., Schoppe, O., Tetteh, G., Shit, S., Efremov, V., Todorov-Völgyi, K., Düring, M., Dichgans, M., Piraud, M., et al. (2020). Machine learning analysis of whole mouse brain vasculature. Nat. Methods. 10.1038/s41592-020-0792-1.

19. Bhatia, H.S., Brunner, A.-D., Öztürk, F., Kapoor, S., Rong, Z., Mai, H., Thielert, M., Ali, M., Al-Maskari, R., Paetzold, J.C., et al. (2022). Spatial proteomics in three-dimensional intact specimens. Cell *185*, 5040-5058.e19. 10.1016/j.cell.2022.11.021.

20. Baysoy, A., Bai, Z., Satija, R., and Fan, R. (2023). The technological landscape and applications of single-cell multi-omics. Nat. Rev. Mol. Cell Biol., 1–19. 10.1038/s41580-023-00615-w.

21. Allan, S.M., and Rothwell, N.J. (2003). Inflammation in central nervous system injury. Philos. Trans. R. Soc. B-Biol. Sci. *358*, 1669–1677. 10.1098/rstb.2003.1358.

22. Chen, G.Y., and Nuñez, G. (2010). Sterile inflammation: sensing and reacting to damage. Nat. Rev. Immunol. *10*, 826–837. 10.1038/nri2873.

23. Casanova, J.-L., and Abel, L. (2021). Mechanisms of viral inflammation and disease in humans. Science *374*, 1080–1086. 10.1126/science.abj7965.

24. Leimkühler, N.B., and Schneider, R.K. (2019). Inflammatory bone marrow microenvironment. Hematol. Am. Soc. Hematol. Educ. Program *2019*, 294–302. 10.1182/hematology.2019000045.

25. Roh, J.S., and Sohn, D.H. (2018). Damage-Associated Molecular Patterns in Inflammatory Diseases. Immune Netw. *18*, e27. 10.4110/in.2018.18.e27.

26. Li, D., and Wu, M. (2021). Pattern recognition receptors in health and diseases. Signal Transduct. Target. Ther. *6*, 1–24. 10.1038/s41392-021-00687-0.

27. Silva-Gomes, S., Decout, A., and Nigou, J. (2015). Pathogen-Associated Molecular Patterns (PAMPs). In Encyclopedia of Inflammatory Diseases, M. Parnham, ed. (Springer), pp. 1–16. 10.1007/978-3-0348-0620-6_35-1.

28. Alberts, B., Johnson, A., Lewis, J., Raff, M., Roberts, K., and Walter, P. (2002). The Adaptive Immune System. In Molecular Biology of the Cell. 4th edition (Garland Science).

29. Charles A Janeway, J., Travers, P., Walport, M., and Shlomchik, M.J. (2001). The importance of immunological memory in fixing adaptive immunity in the genome. In Immunobiology: The Immune System in Health and Disease. 5th edition (Garland Science).

30. Davies, L.C., Jenkins, S.J., Allen, J.E., and Taylor, P.R. (2013). Tissue-resident macrophages. Nat. Immunol. *14*, 986–995. 10.1038/ni.2705.

31. Italiani, P., and Boraschi, D. (2015). New Insights Into Tissue Macrophages: From Their Origin to the Development of Memory. Immune Netw. *15*, 167–176. 10.4110/in.2015.15.4.167.

32. Lenz, K.M., and Nelson, L.H. (2018). Microglia and Beyond: Innate Immune Cells As Regulators of Brain Development and Behavioral Function. Front. Immunol. *9*, 698. 10.3389/fimmu.2018.00698.

33. Rustenhoven, J., and Kipnis, J. (2022). Brain borders at the central stage of neuroimmunology. Nature *612*, 417–429. 10.1038/s41586-022-05474-7.

34. Louveau, A., Smirnov, I., Keyes, T.J., Eccles, J.D., Rouhani, S.J., Peske, J.D., Derecki, N.C., Castle, D., Mandell, J.W., Lee, K.S., et al. (2015). Structural and functional features of central nervous system lymphatic vessels. Nature *523*, 337–341. 10.1038/nature14432.

35. Engelhardt, B. (2021). Private immune protection at the border of the central nervous system. Nature. 10.1038/d41586-021-01962-4.

36. Hattori, Y., Kato, D., Murayama, F., Koike, S., Naito, Y., Kawaguchi, A., Wake, H., and Miyata, T. (2022). Border-associated macrophages transventricularly infiltrate the early embryonic cerebral wall to differentiate into microglia. 2022.07.27.501563. 10.1101/2022.07.27.501563.

37. Schonhoff, A.M., Figge, D.A., Williams, G.P., Jurkuvenaite, A., Gallups, N.J., Childers, G.M., Webster, J.M., Standaert, D.G., Goldman, J.E., and Harms, A.S. (2023). Border-associated macrophages mediate the neuroinflammatory response in an alpha-synuclein model of Parkinson disease. Nat. Commun. *14*, 3754. 10.1038/s41467-023-39060-w.

38. Ajami, B., Bennett, J.L., Krieger, C., Tetzlaff, W., and Rossi, F.M. (2007). Local self-renewal can sustain CNS microglia maintenance and function throughout adult life. Nat Neurosci *10*, 1538–1543. 10.1038/nn2014.

39. Pan, J., Ma, N., Zhong, J., Yu, B., Wan, J., and Zhang, W. (2021). Age-associated changes in microglia and astrocytes ameliorate blood-brain barrier dysfunction. Mol. Ther. - Nucleic Acids *26*, 970–986. 10.1016/j.omtn.2021.08.030.

40. Rustenhoven, J., Drieu, A., Mamuladze, T., de Lima, K.A., Dykstra, T., Wall, M., Papadopoulos, Z., Kanamori, M., Salvador, A.F., Baker, W., et al. (2021). Functional

characterization of the dural sinuses as a neuroimmune interface. Cell *184*, 1000-1016.e27. 10.1016/j.cell.2020.12.040.

41. McKnight, C.D., Rouleau, R.M., Donahue, M.J., and Claassen, D.O. (2020). The regulation of cerebral spinal fluid flow and its relevance to the glymphatic system. Curr. Neurol. Neurosci. Rep. *20*, 58. 10.1007/s11910-020-01077-9.

42. Ringstad, G., and Eide, P.K. (2022). Molecular trans-dural efflux to skull bone marrow in humans with CSF disorders. Brain *145*, 1464–1472. 10.1093/brain/awab388.

43. Bothwell, S.W., Janigro, D., and Patabendige, A. (2019). Cerebrospinal fluid dynamics and intracranial pressure elevation in neurological diseases. Fluids Barriers CNS *16*, 9. 10.1186/s12987-019-0129-6.

44. Louveau, A., Plog, B.A., Antila, S., Alitalo, K., Nedergaard, M., and Kipnis, J. (2017). Understanding the functions and relationships of the glymphatic system and meningeal lymphatics. J. Clin. Invest. *127*, 3210–3219. 10.1172/JCI90603.

45. Jessen, N.A., Munk, A.S.F., Lundgaard, I., and Nedergaard, M. (2015). The Glymphatic System – A Beginner's Guide. Neurochem. Res. *40*, 2583–2599. 10.1007/s11064-015-1581-6.

46. Møllgård, K., Beinlich, F.R.M., Kusk, P., Miyakoshi, L.M., Delle, C., Plá, V., Hauglund, N.L., Esmail, T., Rasmussen, M.K., Gomolka, R.S., et al. (2023). A mesothelium divides the subarachnoid space into functional compartments. Science *379*, 84–88. 10.1126/science.adc8810.

47. Alves de Lima, K., Rustenhoven, J., and Kipnis, J. (2020). Meningeal Immunity and Its Function in Maintenance of the Central Nervous System in Health and Disease. Annu. Rev. Immunol. *38*, 597–620. 10.1146/annurev-immunol-102319-103410.

48. The top 10 causes of death https://www.who.int/news-room/fact-sheets/detail/the-top-10-causes-of-death.

49. Katan, M., and Luft, A. (2018). Global Burden of Stroke. Semin. Neurol. *38*, 208–211. 10.1055/s-0038-1649503.

50. Kemp, W.L., Burns, D.K., and Brown, T.G. (2008). Chapter 11. Neuropathology. In Pathology: The Big Picture (The McGraw-Hill Companies).

51. Nussinov, R., Tsai, C.-J., and Jang, H. (2022). Neurodevelopmental disorders, immunity, and cancer are connected. iScience *25*, 104492. 10.1016/j.isci.2022.104492.

52. Diaz-Aparicio, I., Paris, I., Sierra-Torre, V., Plaza-Zabala, A., Rodríguez-Iglesias, N., Márquez-Ropero, M., Beccari, S., Huguet, P., Abiega, O., Alberdi, E., et al. (2020). Microglia Actively Remodel Adult Hippocampal Neurogenesis through the Phagocytosis Secretome. J. Neurosci. *40*, 1453–1482. 10.1523/JNEUROSCI.0993-19.2019.

53. Irvine, G.B., El-Agnaf, O.M., Shankar, G.M., and Walsh, D.M. (2008). Protein Aggregation in the Brain: The Molecular Basis for Alzheimer's and Parkinson's Diseases. Mol. Med. *14*, 451–464. 10.2119/2007-00100.Irvine.

54. Finnie, J.W. (2013). Neuroinflammation: beneficial and detrimental effects after traumatic brain injury. Inflammopharmacology *21*, 309–320. 10.1007/s10787-012-0164-2.

55. Welcome, M.O. (2020). Neuroinflammation in CNS diseases: Molecular mechanisms and the therapeutic potential of plant derived bioactive molecules. PharmaNutrition *11*, 100176. 10.1016/j.phanu.2020.100176.

56. França, K., and Lotti, T.M. (2017). Psycho-Neuro-Endocrine-Immunology: A Psychobiological Concept. Adv. Exp. Med. Biol. *996*, 123–134. 10.1007/978-3-319-56017-5_11.

57. Sanada, F., Taniyama, Y., Muratsu, J., Otsu, R., Shimizu, H., Rakugi, H., and Morishita, R. (2018). Source of Chronic Inflammation in Aging. Front. Cardiovasc. Med. *5*, 12. 10.3389/fcvm.2018.00012.

58. Cugurra, A., Mamuladze, T., Rustenhoven, J., Dykstra, T., Beroshvili, G., Greenberg, Z.J., Baker, W., Papadopoulos, Z., Drieu, A., Blackburn, S., et al. (2021). Skull and vertebral bone marrow are myeloid cell reservoirs for the meninges and CNS parenchyma. Science. 10.1126/science.abf7844.

59. Brioschi, S., Wang, W.-L., Peng, V., Wang, M., Shchukina, I., Greenberg, Z.J., Bando, J.K., Jaeger, N., Czepielewski, R.S., Swain, A., et al. (2021). Heterogeneity of meningeal B cells reveals a lymphopoietic niche at the CNS borders. Science. 10.1126/science.abf9277.

60. Cheng, X., Wang, H., Zhang, X., Zhao, S., Zhou, Z., Mu, X., Zhao, C., and Teng, W. (2017). The Role of SDF-1/CXCR4/CXCR7 in Neuronal Regeneration after Cerebral Ischemia. Front. Neurosci. *11*, 590. 10.3389/fnins.2017.00590.

61. Abbott, J.D., Ball, G., Boumpas, D., Bridges, S.L., Chatham, W., Curtis, J., Daniel, C., Hughes, L.B., Kao, A.H., Langford, C., et al. eds. (2004). B cell tolerance. In Rheumatology and Immunology Therapy (Springer), pp. 147–147. 10.1007/3-540-29662-X_402.

62. Wang, Y., Chen, D., Xu, D., Huang, C., Xing, R., He, D., and Xu, H. (2021). Early developing B cells undergo negative selection by central nervous system-specific antigens in the meninges. Immunity, S1074761321004015. 10.1016/j.immuni.2021.09.016.

63. Mazzitelli, J.A., Smyth, L.C.D., Cross, K.A., Dykstra, T., Sun, J., Du, S., Mamuladze, T., Smirnov, I., Rustenhoven, J., and Kipnis, J. (2022). Cerebrospinal fluid regulates skull bone marrow niches via direct access through dural channels. Nat. Neurosci. *25*, 555–560. 10.1038/s41593-022-01029-1.

64. Pulous, F.E., Cruz-Hernández, J.C., Yang, C., Kaya, Z., Paccalet, A., Wojtkiewicz, G., Capen, D., Brown, D., Wu, J.W., Schloss, M.J., et al. (2022). Cerebrospinal fluid can exit into the skull bone marrow and instruct cranial hematopoiesis in mice with bacterial meningitis. Nat. Neurosci. *25*, 567–576. 10.1038/s41593-022-01060-2.

65. Alcolea, D., Beeri, M.S., Rojas, J.C., Gardner, R.C., and Lleó, A. (2023). Blood Biomarkers in Neurodegenerative Diseases: Implications for the Clinical Neurologist. Neurology. 10.1212/WNL.0000000000207193.

66. Peltz, C.B., Kenney, K., Gill, J., Diaz-Arrastia, R., Gardner, R.C., and Yaffe, K. (2020). Blood biomarkers of traumatic brain injury and cognitive impairment in older veterans. Neurology *95*, e1126–e1133. 10.1212/WNL.0000000000010087.

67. Saunders, T.S., Pozzolo, F.E., Heslegrave, A., King, D., McGeachan, R.I., Spires-Jones, M.P., Harris, S.E., Ritchie, C., Muniz-Terrera, G., Deary, I.J., et al. (2023). Predictive blood biomarkers and brain changes associated with age-related cognitive decline. Brain Commun. *5*, fcad113. 10.1093/braincomms/fcad113.

68. Hansson, O., Lehmann, S., Otto, M., Zetterberg, H., and Lewczuk, P. (2019). Advantages and disadvantages of the use of the CSF Amyloid β (Aβ) 42/40 ratio in the diagnosis of Alzheimer's Disease. Alzheimers Res. Ther. *11*, 34. 10.1186/s13195-019-0485-0.

69. Vos, P.E., Jacobs, B., Andriessen, T.M.J.C., Lamers, K.J.B., Borm, G.F., Beems, T., Edwards, M., Rosmalen, C.F., and Vissers, J.L.M. (2010). GFAP and S100B are biomarkers of traumatic brain injury: An observational cohort study. Neurology *75*, 1786–1793. 10.1212/WNL.0b013e3181fd62d2.

70. Kwong, R.Y., and Yucel, E.K. (2003). Computed Tomography Scan and Magnetic Resonance Imaging. Circulation *108*, e104–e106. 10.1161/01.CIR.0000086899.32832.EC.

71. Villanueva-Meyer, J.E., Mabray, M.C., and Cha, S. (2017). Current Clinical Brain Tumor Imaging. Neurosurgery *81*, 397–415. 10.1093/neuros/nyx103.

72. van de Pol, L.A., Hensel, A., van der Flier, W.M., Visser, P., Pijnenburg, Y.A.L., Barkhof, F., Gertz, H.J., and Scheltens, P. (2006). Hippocampal atrophy on MRI in frontotemporal lobar degeneration and Alzheimer's disease. J. Neurol. Neurosurg. Psychiatry *77*, 439–442. 10.1136/jnnp.2005.075341.

73. Kothapalli, S.V.V.N., Benzinger, T.L., Aschenbrenner, A.J., Perrin, R.J., Hildebolt, C.F., Goyal, M.S., Fagan, A.M., Raichle, M.E., Morris, J.C., and Yablonskiy, D.A. (2022). Quantitative Gradient Echo MRI Identifies Dark Matter as a New Imaging Biomarker of Neurodegeneration that Precedes Tissue Atrophy in Early Alzheimer's Disease. J. Alzheimers Dis. *85*, 905–924. 10.3233/JAD-210503.

74. Lyra, V., Parissis, J., Kallergi, M., Rizos, E., Filippatos, G., Kremastinos, D., and Chatziioannou, S. (2020). 18 F-FDG PET/CT brain glucose metabolism as a marker of different types of depression comorbidity in chronic heart failure patients with impaired systolic function. Eur. J. Heart Fail. *22*, 2138–2146. 10.1002/ejhf.1866.

75. Ismail, R., Parbo, P., Madsen, L.S., Hansen, A.K., Hansen, K.V., Schaldemose, J.L., Kjeldsen, P.L., Stokholm, M.G., Gottrup, H., Eskildsen, S.F., et al. (2020). The relationships between neuroinflammation, beta-amyloid and tau deposition in Alzheimer's disease: a longitudinal PET study. J. Neuroinflammation *17*, 151. 10.1186/s12974-020-01820-6.

76. van Waarde, A., Marcolini, S., de Deyn, P.P., and Dierckx, R.A.J.O. (2021). PET Agents in Dementia: An Overview. Semin. Nucl. Med. *51*, 196–229. 10.1053/j.semnuclmed.2020.12.008.

77. Kumar, J.S.D., and Mann, J.J. (2014). PET Tracers for Serotonin Receptors and Their Applications. Cent. Nerv. Syst. Agents Med. Chem. *14*, 96–112.

78. Zhang, L., Hu, K., Shao, T., Hou, L., Zhang, S., Ye, W., Josephson, L., Meyer, J.H., Zhang, M.-R., Vasdev, N., et al. (2021). Recent developments on PET radiotracers for TSPO and their applications in neuroimaging. Acta Pharm. Sin. B *11*, 373–393. 10.1016/j.apsb.2020.08.006.

79. Lazzari, G., Vinciguerra, D., Balasso, A., Nicolas, V., Goudin, N., Garfa-Traore, M., Fehér, A., Dinnyés, A., Nicolas, J., Couvreur, P., et al. (2019). Light sheet fluorescence microscopy versus confocal microscopy: in quest of a suitable tool to assess drug and nanomedicine penetration into multicellular tumor spheroids. Eur. J. Pharm. Biopharm. *142*, 195–203. 10.1016/j.ejpb.2019.06.019.

80. Hama, H., Kurokawa, H., Kawano, H., Ando, R., Shimogori, T., Noda, H., Fukami, K., Sakaue-Sawano, A., and Miyawaki, A. (2011). Scale: a chemical approach for fluorescence imaging and reconstruction of transparent mouse brain. Nat. Neurosci. *14*, 1481–1488. 10.1038/nn.2928.

81. Chung, K., Wallace, J., Kim, S.-Y., Kalyanasundaram, S., Andalman, A.S., Davidson, T.J., Mirzabekov, J.J., Zalocusky, K.A., Mattis, J., Denisin, A.K., et al. (2013). Structural and molecular interrogation of intact biological systems. Nature *497*, 332–337. 10.1038/nature12107.

82. Renier, N., Wu, Z., Simon, D.J., Yang, J., Ariel, P., and Tessier-Lavigne, M. (2014). iDISCO: A Simple, Rapid Method to Immunolabel Large Tissue Samples for Volume Imaging. Cell *159*, 896–910. 10.1016/j.cell.2014.10.010.

83. Neckel, P.H., Mattheus, U., Hirt, B., Just, L., and Mack, A.F. (2016). Large-scale tissue clearing (PACT): Technical evaluation and new perspectives in immunofluorescence, histology and ultrastructure. Sci. Rep. *6*, 34331. 10.1038/srep34331.

84. Yang, B., Treweek, J.B., Kulkarni, R.P., Deverman, B.E., Chen, C.-K., Lubeck, E., Shah, S., Cai, L., and Gradinaru, V. (2014). Single-Cell Phenotyping within Transparent Intact Tissue through Whole-Body Clearing. Cell *158*, 945–958. 10.1016/j.cell.2014.07.017.

85. Ueda, H.R., Ertürk, A., Chung, K., Gradinaru, V., Chédotal, A., Tomancak, P., and Keller, P.J. (2020). Tissue clearing and its applications in neuroscience. Nat. Rev. Neurosci. *21*, 61–79. 10.1038/s41583-019-0250-1.

86. Ke, M.-T., Fujimoto, S., and Imai, T. (2013). SeeDB: a simple and morphology-preserving optical clearing agent for neuronal circuit reconstruction. Nat. Neurosci. *16*, 1154–1161. 10.1038/nn.3447.

87. Tainaka, K., Kubota, S.I., Suyama, T.Q., Susaki, E.A., Perrin, D., Ukai-Tadenuma, M., Ukai, H., and Ueda, H.R. (2014). Whole-Body Imaging with Single-Cell Resolution by Tissue Decolorization. Cell *159*, 911–924. 10.1016/j.cell.2014.10.034.

88. Pan, C., Cai, R., Quacquarelli, F.P., Ghasemigharagoz, A., Lourbopoulos, A., Matryba, P., Plesnila, N., Dichgans, M., Hellal, F., and Ertürk, A. (2016). Shrinkage-mediated imaging of entire organs and organisms using uDISCO. Nat. Methods *13*, 859–867. 10.1038/nmeth.3964.

89. Ertürk, A., Becker, K., Jährling, N., Mauch, C.P., Hojer, C.D., Egen, J.G., Hellal, F., Bradke, F., Sheng, M., and Dodt, H.-U. (2012). Three-dimensional imaging of solvent-cleared organs using 3DISCO. Nat. Protoc. *7*, 1983–1995. 10.1038/nprot.2012.119.

90. Klingberg, A., Hasenberg, A., Ludwig-Portugall, I., Medyukhina, A., Männ, L., Brenzel, A., Engel, D.R., Figge, M.T., Kurts, C., and Gunzer, M. (2017). Fully Automated Evaluation of Total Glomerular Number and Capillary Tuft Size in Nephritic Kidneys Using Lightsheet Microscopy. J. Am. Soc. Nephrol. *28*, 452–459. 10.1681/ASN.2016020232.

91. Jing, D., Zhang, S., Luo, W., Gao, X., Men, Y., Ma, C., Liu, X., Yi, Y., Bugde, A., Zhou, B.O., et al. (2018). Tissue clearing of both hard and soft tissue organs with the PEGASOS method. Cell Res. *28*, 803–818. 10.1038/s41422-018-0049-z.

92. Grüneboom, A., Hawwari, I., Weidner, D., Culemann, S., Müller, S., Henneberg, S., Brenzel, A., Merz, S., Bornemann, L., Zec, K., et al. (2019). A network of trans-cortical capillaries as mainstay for blood circulation in long bones. Nat. Metab. *1*, 236–250. 10.1038/s42255-018-0016-5.

93. General (US), O. of the S. (2004). The Basics of Bone in Health and Disease. In Bone Health and Osteoporosis: A Report of the Surgeon General (Office of the Surgeon General (US)).

94. Hwang, J.S., and Cummins, H.Z. (1982). Dynamic light scattering studies of collagen. J. Chem. Phys. *77*, 616–621. 10.1063/1.443926.

95. Zwirner, J., Scholze, M., Waddell, J.N., Ondruschka, B., and Hammer, N. (2019). Mechanical Properties of Human Dura Mater in Tension – An Analysis at an Age Range of 2 to 94 Years. Sci. Rep. *9*, 16655. 10.1038/s41598-019-52836-9.

96. Sanjai, K., Kumarswamy, J., Patil, A., Papaiah, L., Jayaram, S., and Krishnan, L. (2012). Evaluation and comparison of decalcification agents on the human teeth. J. Oral Maxillofac. Pathol. JOMFP *16*, 222–227. 10.4103/0973-029X.99070.

97. Choi, S.-E., Hong, S.W., and Yoon, S.O. (2015). Proposal of an Appropriate Decalcification Method of Bone Marrow Biopsy Specimens in the Era of Expanding Genetic Molecular Study. J. Pathol. Transl. Med. *49*, 236–242. 10.4132/jptm.2015.03.16.

98. Hsueh, B., Burns, V.M., Pauerstein, P., Holzem, K., Ye, L., Engberg, K., Wang, A.-C., Gu, X., Chakravarthy, H., Arda, H.E., et al. (2017). Pathways to clinical CLARITY: volumetric analysis of irregular, soft, and heterogeneous tissues in development and disease. Sci. Rep. *7*, 5899. 10.1038/s41598-017-05614-4.

99. Ertürk, A., Mauch, C.P., Hellal, F., Förstner, F., Keck, T., Becker, K., Jährling, N., Steffens, H., Richter, M., Hübener, M., et al. (2012). Three-dimensional imaging of the unsectioned adult spinal cord to assess axon regeneration and glial responses after injury. Nat. Med. *18*, 166–171. 10.1038/nm.2600.

100. Shekhar, K., and Menon, V. (2019). Identification of Cell Types from Single-Cell Transcriptomic Data. Methods Mol. Biol. Clifton NJ *1935*, 45–77. 10.1007/978-1-4939-9057-3_4.

101. Jagadeesh, K.A., Dey, K.K., Montoro, D.T., Mohan, R., Gazal, S., Engreitz, J.M., Xavier, R.J., Price, A.L., and Regev, A. (2022). Identifying disease-critical cell types and cellular processes by integrating single-cell RNA-sequencing and human genetics. Nat. Genet. *54*, 1479–1492. 10.1038/s41588-022-01187-9.

102. Haber, A.L., Biton, M., Rogel, N., Herbst, R.H., Shekhar, K., Smillie, C., Burgin, G., Delorey, T.M., Howitt, M.R., Katz, Y., et al. (2017). A single-cell survey of the small intestinal epithelium. Nature *551*, 333–339. 10.1038/nature24489.

103. Al-Amrani, S., Al-Jabri, Z., Al-Zaabi, A., Alshekaili, J., and Al-Khabori, M. (2021). Proteomics: Concepts and applications in human medicine. World J. Biol. Chem. *12*, 57–69. 10.4331/wjbc.v12.i5.57.

104. Adan, A., Alizada, G., Kiraz, Y., Baran, Y., and Nalbant, A. (2017). Flow cytometry: basic principles and applications. Crit. Rev. Biotechnol. *37*, 163–176. 10.3109/07388551.2015.1128876.

105. Petersen, A.-K., Zeilinger, S., Kastenmüller, G., Römisch-Margl, W., Brugger, M., Peters, A., Meisinger, C., Strauch, K., Hengstenberg, C., Pagel, P., et al. (2014). Epigenetics meets metabolomics: an epigenome-wide association study with blood serum metabolic traits. Hum. Mol. Genet. *23*, 534–545. 10.1093/hmg/ddt430.

106. Van den Berge, K., Hembach, K.M., Soneson, C., Tiberi, S., Clement, L., Love, M.I., Patro, R., and Robinson, M.D. (2019). RNA Sequencing Data: Hitchhiker's Guide to Expression Analysis. Annu. Rev. Biomed. Data Sci. *2*, 139–173. 10.1146/annurev-biodatasci-072018-021255.

107. Luecken, M.D., and Theis, F.J. (2019). Current best practices in single-cell RNA-seq analysis: a tutorial. Mol. Syst. Biol. *15*, e8746. 10.15252/msb.20188746.

108. Raudvere, U., Kolberg, L., Kuzmin, I., Arak, T., Adler, P., Peterson, H., and Vilo, J. (2019). g:Profiler: a web server for functional enrichment analysis and conversions of gene lists (2019 update). Nucleic Acids Res. *47*, W191–W198. 10.1093/nar/gkz369.

109. Wolf, F.A., Angerer, P., and Theis, F.J. (2018). SCANPY: large-scale single-cell gene expression data analysis. Genome Biol. *19*, 15. 10.1186/s13059-017-1382-0.

110. Satija, R., Farrell, J.A., Gennert, D., Schier, A.F., and Regev, A. (2015). Spatial reconstruction of single-cell gene expression data. Nat. Biotechnol. *33*, 495–502. 10.1038/nbt.3192.

111. Cox, J., Neuhauser, N., Michalski, A., Scheltema, R.A., Olsen, J.V., and Mann, M. (2011). Andromeda: a peptide search engine integrated into the MaxQuant environment. J. Proteome Res. *10*, 1794–1805. 10.1021/pr101065j.

112. Kuleshov, M.V., Jones, M.R., Rouillard, A.D., Fernandez, N.F., Duan, Q., Wang, Z., Koplev, S., Jenkins, S.L., Jagodnik, K.M., Lachmann, A., et al. (2016). Enrichr: a comprehensive gene set enrichment analysis web server 2016 update. Nucleic Acids Res. *44*, W90. 10.1093/nar/gkw377.

113. Tyanova, S., Temu, T., Sinitcyn, P., Carlson, A., Hein, M.Y., Geiger, T., Mann, M., and Cox, J. (2016). The Perseus computational platform for comprehensive analysis of (prote)omics data. Nat. Methods *13*, 731–740. 10.1038/nmeth.3901.

114. Mai, H., Luo, J., Hoeher, L., Al-Maskari, R., Horvath, I., Chen, Y., Kofler, F., Piraud, M., Paetzold, J.C., Modamio, J., et al. (2023). Whole-body cellular mapping in mouse using standard IgG antibodies. Nat. Biotechnol., 1–11. 10.1038/s41587-023-01846-0.

115. Kolabas, Z.I., Kuemmerle, L.B., Perneczky, R., Förstera, B., Büttner, M., Caliskan, O.S., Ali, M., Rong, Z., Mai, H., Hummel, S., et al. (2021). Multi-omics and 3D-imaging reveal bone heterogeneity and unique calvaria cells in neuroinflammation. 2021.12.24.473988. 10.1101/2021.12.24.473988.

116. Rong, Z., Mai, H., Kapoor, S., Puelles, V.G., Czogalla, J., Schädler, J., Vering, J., Delbridge, C., Steinke, H., Frenzel, H., et al. (2023). SARS-CoV-2 Spike Protein Accumulation in the Skull-Meninges-Brain Axis: Potential Implications for Long-Term Neurological Complications in post-COVID-19. 2023.04.04.535604. 10.1101/2023.04.04.535604.

117. Bartos, L.M., Kirchleitner, S.V., Kolabas, Z.I., Quach, S., Blobner, J., Mueller, S.A., Ulukaya, S., Hoeher, L., Horvath, I., Wind-Mark, K., et al. (2023). Deciphering sources of PET signals in the tumor microenvironment of glioblastoma at cellular resolution. 2023.01.26.522174. 10.1101/2023.01.26.522174.

118. Krausgruber, T., Fortelny, N., Fife-Gernedl, V., Senekowitsch, M., Schuster, L.C., Lercher, A., Nemc, A., Schmidl, C., Rendeiro, A.F., Bergthaler, A., et al. (2020). Structural cells are key regulators of organ-specific immune responses. Nature *583*, 296–302. 10.1038/s41586-020-2424-4.

119. Clarke, B. (2008). Normal Bone Anatomy and Physiology. Clin. J. Am. Soc. Nephrol. CJASN *3*, S131–S139. 10.2215/CJN.04151206.

120. Chen, Y., Sun, Y., Xue, X., and Ma, H. (2023). Comprehensive analysis of epigenetics mechanisms in osteoporosis. Front. Genet. *14*.

121. Cakouros, D., and Gronthos, S. (2019). Epigenetic Regulation of Bone Marrow Stem Cell Aging: Revealing Epigenetic Signatures associated with Hematopoietic and Mesenchymal Stem Cell Aging. Aging Dis. *10*, 174–189. 10.14336/AD.2017.1213.

122. Xu, F., Li, W., Yang, X., Na, L., Chen, L., and Liu, G. (2021). The Roles of Epigenetics Regulation in Bone Metabolism and Osteoporosis. Front. Cell Dev. Biol. *8*.

123. You, Y., Liu, J., Zhang, L., Li, X., Sun, Z., Dai, Z., Ma, J., Jiao, G., and Chen, Y. (2023). WTAP-mediated m6A modification modulates bone marrow mesenchymal stem cells differentiation potential and osteoporosis. Cell Death Dis. *14*, 1–14. 10.1038/s41419-023-05565-x.

124. Zhang, Z., Huang, Z., Awad, M., Elsalanty, M., Cray, J., Ball, L.E., Maynard, J.C., Burlingame, A.L., Zeng, H., Mansky, K.C., et al. (2023). O-GlcNAc glycosylation orchestrates fate decision and niche function of bone marrow stromal progenitors. eLife *12*, e85464. 10.7554/eLife.85464.

125. Di Pietro, L., Barba, M., Palacios, D., Tiberio, F., Prampolini, C., Baranzini, M., Parolini, O., Arcovito, A., and Lattanzi, W. (2021). Shaping modern human skull through epigenetic, transcriptional and post-transcriptional regulation of the RUNX2 master bone gene. Sci. Rep. *11*, 21316. 10.1038/s41598-021-00511-3.

126. Haberland, M., Mokalled, M.H., Montgomery, R.L., and Olson, E.N. (2009). Epigenetic control of skull morphogenesis by histone deacetylase 8. Genes Dev. *23*, 1625–1630. 10.1101/gad.1809209.

127. SYP synaptophysin [Homo sapiens (human)] - Gene - NCBI https://www.ncbi.nlm.nih.gov/gene/6855.

128. SYN3 synapsin III [Homo sapiens (human)] - Gene - NCBI https://www.ncbi.nlm.nih.gov/gene/8224.

129. SNAP25 synaptosome associated protein 25 [Homo sapiens (human)] - Gene - NCBI https://www.ncbi.nlm.nih.gov/gene/6616.

130. Presynaptic Membrane - an overview | ScienceDirect Topics https://www.sciencedirect.com/topics/neuroscience/presynaptic-membrane.

131. Synaptic Transmission at the Skeletal Neuromuscular Junction (Section 1, Chapter 4) Neuroscience Online: An Electronic Textbook for the Neurosciences | Department of Neurobiology and Anatomy - The University of Texas Medical School at Houston https://nba.uth.tmc.edu/neuroscience/m/s1/chapter04.html.

132. Dhaiban, S., Al-Ani, M., Elemam, N.M., Al-Aawad, M.H., Al-Rawi, Z., and Maghazachi, A.A. (2021). Role of Peripheral Immune Cells in Multiple Sclerosis and Experimental Autoimmune Encephalomyelitis. Sci *3*, 12. 10.3390/sci3010012.

133. Yang, Q., Wang, G., and Zhang, F. (2020). Role of Peripheral Immune Cells-Mediated Inflammation on the Process of Neurodegenerative Diseases. Front. Immunol. *11*, 582825. 10.3389/fimmu.2020.582825.

134. Xiong, L., Pan, J.-X., Guo, H., Mei, L., and Xiong, W.-C. (2021). Parkinson's in the bone. Cell Biosci. *11*, 190. 10.1186/s13578-021-00702-5.

135. Handa, K., Kiyohara, S., Yamakawa, T., Ishikawa, K., Hosonuma, M., Sakai, N., Karakawa, A., Chatani, M., Tsuji, M., Inagaki, K., et al. (2019). Bone loss caused by dopaminergic degeneration and levodopa treatment in Parkinson's disease model mice. Sci. Rep. *9*, 13768. 10.1038/s41598-019-50336-4.

136. Gao, H., Wei, X., Liao, J., Wang, R., Xu, J., Liu, X., Pan, X., Li, Z., Li, Z., Xia, Y., et al. (2015). Lower Bone Mineral Density in Patients with Parkinson's Disease: A Cross-Sectional Study from Chinese Mainland. Front. Aging Neurosci. *7*.

137. Xia, W., Xie, J., Cai, Z., Liu, X., Wen, J., Cui, Z.-K., Zhao, R., Zhou, X., Chen, J., Mao, X., et al. (2021). Damaged brain accelerates bone healing by releasing small extracellular vesicles that target osteoprogenitors. Nat. Commun. *12*, 6043. 10.1038/s41467-021-26302-y.

138. Proulx, S.T. (2021). Cerebrospinal fluid outflow: a review of the historical and contemporary evidence for arachnoid villi, perineural routes, and dural lymphatics. Cell. Mol. Life Sci. *78*, 2429–2457. 10.1007/s00018-020-03706-5.

139. Toragall, M.M., Satapathy, S.K., Kadadevaru, G.G., and Hiremath, M.B. (2019). Evaluation of Seminal Fructose and Citric Acid Levels in Men with Fertility Problem. J. Hum. Reprod. Sci. *12*, 199–203. 10.4103/jhrs.JHRS_155_18.

140. Wang, H., Leng, Y., and Gong, Y. (2018). Bone Marrow Fat and Hematopoiesis. Front. Endocrinol. *9*.

141. Robles, H., Park, S., Joens, M.S., Fitzpatrick, J.A.J., Craft, C.S., and Scheller, E.L. (2019). Characterization of the bone marrow adipocyte niche with three-dimensional electron microscopy. Bone *118*, 89–98. 10.1016/j.bone.2018.01.020.

142. Tratwal, J., Rojas-Sutterlin, S., Bataclan, C., Blum, S., and Naveiras, O. (2021). Bone marrow adiposity and the hematopoietic niche: A historical perspective of reciprocity,

heterogeneity, and lineage commitment. Best Pract. Res. Clin. Endocrinol. Metab. *35*, 101564. 10.1016/j.beem.2021.101564.

143. Ganguly, P., El-Jawhari, J.J., Giannoudis, P.V., Burska, A.N., Ponchel, F., and Jones, E.A. (2017). Age-related Changes in Bone Marrow Mesenchymal Stromal Cells. Cell Transplant. *26*, 1520–1529. 10.1177/0963689717721201.

144. Kündig, T.M., Bachmann, M.F., DiPaolo, C., Simard, J.J.L., Battegay, M., Lother, H., Gessner, A., Kühlcke, K., Ohashi, P.S., Hengartner, H., et al. (1995). Fibroblasts as Efficient Antigen-Presenting Cells in Lymphoid Organs. Science *268*, 1343–1347. 10.1126/science.7761853.

145. Guilarte, T.R., Rodichkin, A.N., McGlothan, J.L., Acanda De La Rocha, A.M., and Azzam, D.J. (2022). Imaging neuroinflammation with TSPO: A new perspective on the cellular sources and subcellular localization. Pharmacol. Ther. *234*, 108048. 10.1016/j.pharmthera.2021.108048.

146. Costantini, I., Cicchi, R., Silvestri, L., Vanzi, F., and Pavone, F.S. (2019). In-vivo and ex-vivo optical clearing methods for biological tissues: review. Biomed. Opt. Express *10*, 5251–5267. 10.1364/BOE.10.005251.

147. Deng, Z., Jing, L., Wu, N., Lv, P., Jiang, X., Ren, Q., and Li, C. (2014). Viscous optical clearing agent for in vivo optical imaging. J. Biomed. Opt. *19*, 076019. 10.1117/1.JBO.19.7.076019.

148. Iijima, K., Oshima, T., Kawakami, R., and Nemoto, T. (2021). Optical clearing of living brains with MAGICAL to extend i n vivo imaging. iScience *24*, 101888. 10.1016/j.isci.2020.101888.

149. Greenblatt, S.H. (1995). Phrenology in the Science and Culture of the 19th Century. Neurosurgery *37*, 790.

150. Bilal, M., Edwards, B., Loukas, M., Oskouian, R.J., Tubbs, R.S., Bilal, M., Edwards, B., Loukas, M., Oskouian, R.J., and Tubbs, R.S. (2017). Johann Gaspar Spurzheim: A Life Dedicated to Phrenology. Cureus *9*. 10.7759/cureus.1295.

ACKNOWLEDGEMENTS

I am deeply grateful to many individuals who have made these years the most challenging yet transformative experience, shaping my identity.

First and foremost, I would like to express my heartfelt gratitude to Ali for recognizing my potential and continuously pushing me beyond my limits. His trust in me has allowed me to accomplish things I never imagined possible, despite my limited experience in science and being in a foreign country.

I would also like to extend my sincere thanks to Farida for her exceptional foresight and support, always offering comfort during difficult times.

My journey would not have been the same without the past and current members of the lab who have had a profound impact. Special thanks go to Selin, Muge, Furkan, Louis, Izabela, Denise, Markus, Harsh, Marika and all those who have contributed to this endeavor. Throughout my PhD, I not only encountered scientific challenges but also faced extraordinary events that tested my resilience, such as the pandemic, lab relocation, and even a cyber-attack, to name just a few. Their support, guidance, and collaboration have been instrumental in shaping my research experience and overcoming these hurdles.

I extend my heartfelt appreciation to each member of my Thesis Advisory Committee for their contributions. I am thankful for the invaluable time and feedback generously provided by Prof. Dr. Nikolaus Plesnila, Prof. Dr. Ilona Grunwald-Kadow, and Dr. Cristina Garcica Cacares.

I am truly grateful for the invaluable collaborations and the students I have had throughout this journey. The contributions of my collaborators, Laura Bartos, Matthias Brendel, Anna Kopzcak, and my students: Selin, Laura and Constanze have enriched my research, my supervision skills, and broadened my horizons.

I appreciate the support from the GSN team throughout my PhD. I would also like to thank LMU Amgen Scholar Programme director Raluca Goron for providing me with an amazing opportunity back in 2016 that led me here today, I am a proud LMU Amgen Scholar and Supervisor Alumni.

On a more personal level, I am eternally grateful to my parents, Tevfik and Canan Kolabas, for their firm support that goes beyond what words can convey. They have not only invested in my education but also wholeheartedly believed in me and encouraged me to chase my dreams. I

would also like to extend a special thanks to Idil, whose mere presence unknowingly pushes me to become a better person and serves as a constant reminder to set a positive example for her. They have been and will forever remain my source of support and strength.

Daniel, you are the hidden force that has propelled me forward in this journey. Your support, encouragement, and understanding have been the anchor of my success. Thank you for being my rock, my confidant, and my constant pillar of support.

Lastly, I would like to acknowledge myself for always finding the motivation to persevere and continue, even in the face of adversity. I am proud of the resilience I have shown.

I consider myself incredibly fortunate to be surrounded by people who enable me to pursue my passion. With their unwavering support, I am filled with excitement and anticipation for what the future holds.

All illustrations in this thesis have been generated using BioRender.com. The manuscript “Whole-mouse clearing and imaging at the cellular level with vDISCO” has been reproduced with permission from Springer Nature. The manuscript “Distinct molecular profiles of skull bone marrow in health and neurological disorders” has been reproduced with permission from Elsevier.

CURRICULUM VITAE

Education

Since 10/2019	PhD candidate
	Graduate School of Systemic Neurosciences,
	Ludwig-Maximilians-University, Munich, Germany
09/2017 – 08/2019	Cognitive Neuroscience, MSc
	Minor, Neurophiloshophy
	Donders Institute for Brain, Cognition and Behavior
	Radboud University, Nijmegen, The Netherlands
09/2023 – 07/2017	Molecular Biology, Genetics and Bioengineering, BSc
	Minor, Psychology
	Sabanci University, Istanbul, Turkiye
01/2017 – 06/2017	Semester abroad
	Hong Kong University of Science and Technology, Hong Kong

Research Experience

Since 10/2019	Research associate
	Institute for Tissue Engineering and Regenerative Medicine,
	Helmholtz Center Munich, Munich, Germany
06/2023 – 09/2023	Intern
	Cellular and Tissue Genomics Department
	Genentech Inc., South San Francisco, California, USA
09/2018 – 09/2019	Research assistant
	Ali Erturk Lab,
	Institute for Stroke and Dementia Research, Munich, Germany
09/2013 – 07/2017	Research assistant
	Batu Erman Lab,
	Sabanci University, Istanbul, Turkiye

LIST OF PUBLICATIONS

Accepted for publication

Z. I. Kolabas*, L. B. Kuemmerle*, R. Perneczky*, B. Förstera*, S. Ulukaya, M. Ali, S. Kapoor, L. M. Bartos, M. Büttner, O. S. Caliskan, Z. Rong, H. Mai, L. Höher, D. Jeridi, M. Molbay, I. Khalin, I. K. Deligiannis, M. Negwer, K. Roberts, A. Simats, O. Carofiglio, M. I. Todorov, I. Horvath, F. Ozturk, S. Hummel, G. Biechele, A. Zatcepin, M. Unterrainer, J. Gnörich, J. Roodselaar, J. Shrouder, P. Khosravani, B. Tast, L. Richter, L. Díaz-Marugán, D. Kaltenecker, L. Lux, Y. Chen, S. Zhao, B.-S. Rauchmann, M. Sterr, I. Kunze, K. Stanic, V. W. Y. Kan, S. Besson-Girard, S. Katzdobler, C. Palleis, J. Schädler, J. C. Paetzold, S. Liebscher, A. E. Hauser, O. Gokce, H. Lickert, H. Steinke, C. Benakis, C. Braun, C. P. Martinez-Jimenez, K. Buerger, N. L. Albert, G. Höglinger, J. Levin, C. Haass, A. Kopczak, M. Dichgans, J. Havla, T. Kümpfel, M. Kerschensteiner, M. Schifferer, M. Simons, A. Liesz, N. Krahmer, O. A. Bayraktar, N. Franzmeier, N. Plesnila, S. Erener, V. G. Puelles, C. Delbridge, H. S. Bhatia, F. Hellal, M. Elsner, I. Bechmann, B. Ondruschka, M. Brendel, F. J. Theis, A. Erturk, Distinct molecular profiles of skull bone marrow in health and neurological disorders. *Cell*, 186, 3706-3725.e29. 10.1016/j.cell.2023.07.009 (2023). *Equally contributed

R. Cai*, **Z. I. Kolabas***, C. Pan, H. Mai, S. Zhao, D. Kaltenecker, F. F. Voigt, M. Molbay, T. Ohn, C. Vincke, M. I. Todorov, F. Helmchen, J. A. Van Ginderachter, A. Ertürk, Whole-mouse clearing and imaging at the cellular level with vDISCO. Nat. Protoc., 1–55 (2023). *Equally contributed

H. S. Bhatia*, A.-D. Brunner*, F. Öztürk*, S. Kapoor, Z. Rong, H. Mai, M. Thielert, M. Ali, R. Al-Maskari, J. C. Paetzold, F. Kofler, M. I. Todorov, M. Molbay, **Z. I. Kolabas**, M. Negwer, L. Hoeher, H. Steinke, A. Dima, B. Gupta, D. Kaltenecker, Ö. S. Caliskan, D. Brandt, N. Krahmer, S. Müller, S. F. Lichtenthaler, F. Hellal, I. Bechmann, B. Menze, F. Theis, M. Mann, A. Ertürk, Spatial proteomics in three-dimensional intact specimens. *Cell*. 185, 5040-5058.e19 (2022). *Equally contributed

L. M. Bartos, S. V. Kirchleitner, J. Blobner, K. Wind, L. H. Kunze, A. Holzgreve, L. Gold, A. Zatcepin, **Z. I. Kolabas**, S. Ulukaya, L. Weidner, S. Quach, D. Messerer, P. Bartenstein, J. C. Tonn, M. J. Riemenschneider, S. Ziegler, L. von Baumgarten, N. L. Albert, M. Brendel, 18 kDa translocator protein positron emission tomography facilitates early and robust tumor detection in the immunocompetent SB28 glioblastoma mouse model. *Front. Med.* 9, 992993 (2022).

M. Molbay*, **Z. I. Kolabas***, M. I. Todorov, T.-L. Ohn, A. Ertürk, A guidebook for DISCO tissue clearing. *Mol. Syst. Biol.* 17, e9807 (2021). *Equally contributed

Submitted for publication

Z. Rong, H. Mai, S. Kapoor, V. G. Puelles, J. Czogalla, J. Schädler, J. Vering, C. Delbridge, H. Steinke, H. Frenzel, K. Schmidt, Ö. S. Caliskan, J. M. Wettengel, F. Cherif, M. Ali, **Z. I. Kolabas**, S. Ulukaya, I. Horvath, S. Zhao, N. Krahmer, S. Tahirovic, A. Ö. Yildirim, T. B. Huber, B. Ondruschka, I. Bechmann, G. Ebert, U. Protzer, H. S. Bhatia, F. Hellal, A. Ertürk, SARS-CoV-2 Spike Protein Accumulation in the Skull-Meninges-Brain Axis: Potential Implications for Long-Term Neurological Complications in post-COVID-19 (2023), p. 2023.04.04.535604, , doi:10.1101/2023.04.04.535604. (in revision)

L. M. Bartos, S. V. Kirchleitner, **Z. I. Kolabas**, S. Quach, J. Blobner, S. A. Mueller, S. Ulukaya, L. Hoeher, I. Horvath, K. Wind-Mark, A. Holzgreve, V. C. Ruf, L. Gold, L. H. Kunze, S. T. Kunte, P. Beumers, M. Antons, A. Zatcepin, N. Briel, L. Hoermann, D. Messerer, P. Bartenstein, M. J. Riemenschneider, S. Lindner, S. Ziegler, J. Herms, S. F. Lichtenthaler, A. Ertürk, J. C. Tonn, L. von Baumgarten, N. L. Albert, M. Brendel, Deciphering sources of PET signals in the tumor microenvironment of glioblastoma at cellular resolution (2023), p. 2023.01.26.522174, , doi:10.1101/2023.01.26.522174. (in revision)

AFFIDAVIT

I hereby confirm that the dissertation “Skull bone marrow emerges as a key neuroimmune player utilizing disco-clearing and multi-omics” is the result of my own work and that I have only used sources or materials listed and specified in the dissertation.

Hiermit versichere ich an Eides statt, dass ich die vorliegende Dissertation “ Skull emerges as a key neuroimmune player utilizing disco-clearing and multi-omics” selbstständig angefertigt habe, mich außer der angegebenen keiner weiteren Hilfsmittel bedient und alle Erkenntnisse, die aus dem Schrifttum ganz oder annähernd übernommen sind, als solche kenntlich gemacht und nach ihrer Herkunft unter Bezeichnung der Fundstelle einzeln nachgewiesen habe.

San Francisco, August 15, 2023 Zeynep Ilgın Kolabaş

DECLARATION OF AUTHOR CONTRIBUTIONS

Study I: (Kolabas et al., 2023, *Cell*) "Distinct molecular profiles of skull bone marrow in health and neurological disorders"

Authors: *Zeynep Ilgin Kolabas, Louis B. Kuemmerle, Robert Perneczky, Benjamin Förstera, Selin Ulukaya, Mayar Ali, Saketh Kapoor, Laura M. Bartos, Maren Büttner, Ozum Sehnaz Caliskan, Zhouyi Rong, Hongcheng Mai, Luciano Höher, Denise Jeridi, Muge Molbay, Igor Khalin, Ioannis K. Deligiannis, Moritz Negwer, Kenny Roberts, Alba Simats, Olga Carofiglio, Mihail I. Todorov, Izabela Horvath, Furkan Ozturk, Selina Hummel, Gloria Biechele, Artem Zatcepin, Marcus Unterrainer, Johannes Gnörich, Jay Roodselaar, Joshua Shrouder, Pardis Khosravani, Benjamin Tast, Lisa Richter, Laura Díaz-Marugan, Doris Kaltenecker, Laurin Lux, Ying Chen, Shan Zhao,Vanessa W.Y. Kan, Sabine Liebscher, Boris-Stephan Rauchmann, Michael Sterr, Ines Kunze, Karen Stanic, Vanessa W.Y. Kan, Simon Besson-Girard, Sabrina Katzdobler, Carla Palleis, Julia Schädler, Johannes C. Paetzold, Sabine Liebscher, Anja E. Hauser, Ozgun Gokce, Heiko Lickert, Hanno Steinke, Corinne Benakis, Christian Braun, Celia P. Martinez-Jimenez, Katharina Buerger, Nathalie L. Albert, Günter Höglinger, Johannes Levin, Christian Haass, Anna Kopczak, Martin Dichgans, Joachim Havla, Tania Kümpfel, Martin Kerschensteiner, Martina Schifferer, Mikael Simons, Arthur Liesz, Natalie Krahmer, Omer A. Bayraktar, Nicolai Franzmeier, Nikolaus Plesnila, Suheda Erener, Victor G. Puelles, Claire Delbridge, Harsharan Singh Bhatia, Farida Hellal, Markus Elsner, Ingo Bechmann, Benjamin Ondruschka, Matthias Brendel, Fabian J. Theis and Ali Erturk*

Contribution of authors: L.B.K., Mar.B., M.A., Z.I.K. and F.J.T. performed the single-cell RNA sequencing bioinformatic analysis. R.P. provided ActiGliA clinical data and TSPO-PET scans. B.F. designed, coordinated and performed experiments in the project's initial phase and performed the initial MCAo and sham surgeries. H.S.B co-organized experiments in the initial phase of the project. S.K., S.U., O.S.C., Z.I.K. and N.K. performed mass-spectrometry experiment and analysis. M.A. performed the mass-spectrometry analysis. Z.I.K., B.F., H.S.B., S.U., D.J., Z.R., H.M., M.M., K.S., F.H., S.B.G. and O.G. contributed to RNA sequencing and mass spectrometry collection. Ig.K., N.P., performed 2-photon imaging experiment. I.H., M.N., M.T., J.C.P., S.U., L.B.K. and Z.I.K. performed image analysis. S.U. and Z.I.K. labeled, cleared and imaged human samples. L.H. and Z.I.K. quantified the SMCs. Z.I.K., S.U., D.J., M.M., F.O., J.S., J.R., A.E.H., S.Z., D.K., V.W.Y.K., S.L. performed experiments. K.R. and O.B. performed RNAscope experiment. Z.I.K., A.S., O.C., L.D.M., Co.B., A.L., performed photoconversion experiments. P.K. acquired flow cytometry measurements for proportions,

B.T and L.R. designed the panel. M.S., In.K., H.L., I.D., C.M.J. performed cDNA synthesis and library construction for single-cell RNA sequencing. Mar.S. performed sEM experiments. V.W.Y.K., S.L. performed pilot 2-photon experiments. N.L.A., G.H., M.U., J.G., S.K., C.P., A.K., K.B., J.L., C.H., Mi.S., M.D., J.H., T.K., M.K., R.P., Mat.B. organized, recruited, and conducted the human TSPO-PET study. G.B., L.M.B. S.H., J.G. and Mat.B. analyzed human TSPO-PET scans. L.M.B. performed the serial analysis of TSPO-PET scans. A.Z. produced 3D projections. N.F. performed skull brain correlation analysis. H.S., I.B., Ch.B., C.D., Ju.S., B.O., V.P. provided human skull sample. F.H., S.E., H.S.B., M.E. and A.E. supervised the project. Z.I.K., S.E. and M.E. provided the first draft of the manuscript, F.H., H.S.B., L.B.K. helped write the manuscript. A.E, Z.I.K. and M.E. cowrote the final manuscript. A.E conceived the project and led all aspects of the project.

My contribution to this publication detail: I designed, performed, and analyzed most experiments. I supervised all analyses in the study, interpreted the data, revised the manuscript, and co-wrote the final manuscript with Markus Elsner.

Herewith, I confirm the contributions to the manuscripts.

San Francisco, August 15, 2023

Zeynep Ilgin Kolabas (1st author)

Louis B. Kuemmerle (1st author)

Robert Perneczky (1st author)

Benjamin Forstera (1st author)

Ali Erturk (1st supervisor)

Study II: (Cai, Kolabas et al., 2023, *Nature Protocols*) "Whole-mouse clearing and imaging at the cellular level with vDISCO"

Authors: *Ruiyao Cai, Zeynep Ilgin Kolabas, Chenchen Pan, Hongcheng Mai, Shan Zhao, Doris Kaltenecker, Fabian F. Voigt, Muge Molbay, Tzu-lun Ohn, Cécile Vincke, Mihail I. Todorov, Fritjof Helmchen, Jo A. Van Ginderachter, and Ali Ertürk*

Contribution of authors: A.E. and R.C. initiated the project. R.C. and C.P. developed the original vDISCO method. R.C. designed the experiments, R.C. and Z.I.K. performed most of and supervised all of the experiments. C.P. provided data for the cancer mouse. H.M. and S.Z. provided data for the PDGFRb-EGFP pericyte-labeled brains. F.F.V., M.M., T.-L.O. and F.H. provided mesoSPIM data. C.V. and J.A.V.G. provided the custom-made nanobodies anti-GFP. D.K. contributed to the imaging, and M.I.T helped with the stitching of the Prox1-EGFP sample. A.E. supervised the project. All authors edited the manuscript.

My contribution to this publication detail: together with my co-first author Ruiyao Cai, I performed most of the experiments and supervised all that I did not perform. I co-wrote the manuscript with Ruiyao Cai and performed the revision of the manuscript.

Herewith, I confirm the contributions to the manuscripts.

San Francisco, August 15, 2023

Zeynep Ilgin Kolabas (1st author)

Ruiyao Cai (1st author)

Ali Erturk (1st supervisor)